CORA Cork Open Research Archive
Cartlann Taighde Oscailte Chorcaí

Title	New materials via combinatorial atomic layer deposition
Authors	Doyle, Shóna
Publication date	2022-01
Original Citation	Doyle, S. 2022. New materials via combinatorial atomic layer deposition. PhD Thesis, University College Cork.
Type of publication	Doctoral thesis
Rights	© 2022, Shóna Doyle. - https://creativecommons.org/licenses/by-nc-nd/4.0/
Download date	2024-04-19 10:24:36
Item downloaded from	https://hdl.handle.net/10468/13206

UCC
University College Cork, Ireland
Coláiste na hOllscoile Corcaigh

Ollscoil na hÉireann, Corcaigh
NATIONAL UNIVERSITY OF IRELAND, CORK

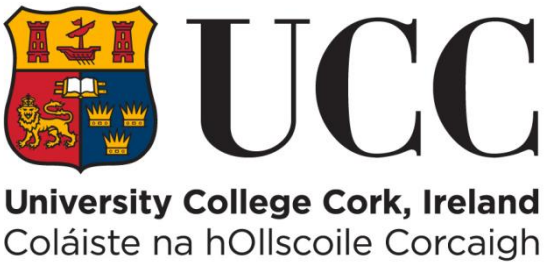

New Materials via Combinatorial Atomic Layer Deposition

A thesis presented to

The National University of Ireland

For the degree of Doctor of Philosophy

by

Shóna Doyle B.Sc. M.Sc.

School of Chemistry

Tyndall National Institute,

University College Cork, Ireland

January 2022

Supervisor: Professor Martyn Pemble and Dr Ian Povey

Head of School of Chemistry: Dr Humphrey Moynihan

Table of Contents

Declaration……vii

List of Figures……...viii

List of Tables……xvi

Acronyms……...xix

Acknowledgements……..….xxiv

Abstract……..…xxv

Chapter 1: Introduction……1

1.1 Thin Film Nanotechnologies……1

1.2 Nanolaminates - Definitions and Potential Applications……..4

1.2.1 Chemically-based methods for nanolaminate synthesis……..6

1.2.2 Physical methods for nanolaminate synthesis……12

1.3 ALD for the synthesis of nanolaminates……....18

1.3.1 History and Development of ALD……18

1.3.2 Principles and Mechanisms of ALD……..19

1.3.2.1 ALD principles……...19

1.3.3 ALD Processes……...25

1.3.4 ALD Growth of ZnO……..27

1.3.5 ALD Growth of TiO_2……..31

1.3.6 ALD Growth of Al_2O_3……36

1.4 Properties and applications of nanolaminates of Al_2O_3, TiO_2 and ZnO……38

1.4.1 Electronic applications of nanolaminates of Al_2O_3, TiO_2 and ZnO……38

1.4.2 Mechanical properties of nanolaminates of Al_2O_3, TiO_2 and ZnO……41

1.4.3 Optical properties of nanolaminates of Al_2O_3, TiO_2 and ZnO……43

1.4.4 The use of nanolaminates of Al_2O_3, TiO_2 and ZnO for encapsulation and passivation……44

1.4.5 TiO_2/ZnO nanolaminates……47

1.5 Doping of ZnO thin films……...50

1.5.1 Advantages of doping by ALD……...50

1.5.2 ALD Doping of ZnO - distribution and efficiency of the added dopant ions….51

1.5.3 ALD growth of Al-doped ZnO……54

1.5.4 ALD growth of Sn-doped ZnO……...59

1.5.5 ALD growth of Ti-doped ZnO……60

1.5.6 ALD growth of Ga-doped ZnO……...62

1.5.7 ALD growth of In-doped ZnO……64

1.6 Summary of the contents of the thesis……68

References……70

Chapter 2: Experimental Methods……...148

2.1 Substrate cleaning……149

2.2 ALD growths……...149

2.2.1 Preparations of TiO_2/ZnO composites……....…….149

2.2.2 Preparation of ZnO thin films……...152

2.2.3 Preparation of doped ZnO thin films……154

2.2.4 Preparation of ZnO-based ternary thin films……156

2.3 Methods of Analysis……160

2.3.1 Scanning Electron Microscopy……160

2.3.2 Transmission Electron Microscopy……..162

2.3.3 X-ray Diffraction……..164

2.3.4 X-ray Photoelectron Spectroscopy……...166

2.3.5 UV/Visible Spectroscopy……167

2.3.6 Contact Angle Measurement……170

2.3.7 Evaluation of Photocatalytic Activity……...171

2.3.8 The Hall Effect and Hall Measurements……...173

References……..……178

Chapter 3: Combinatorial ALD for the Growth of ZnO/TiO_2 Nanolaminates and Mixed ZnO/TiO_2 Nanostructured Films……185

Abstract……..185

3.1 Introduction……186

3.2 Experimental……... 190

3.2.1 Preparation of TiO_2/ZnO composites……190

3.2.2 Characterization techniques……..……190

3.2.3 Evaluation of Photocatalytic Activity……...191

3.3 Results and discussion……..192

3.3.1 The surface morphologies and structural properties of TiO_2/ZnO films……..192

3.3.2 Optical Properties……211

3.3.3 Contact angle and photocatalytic activity……..…212

3.4 Conclusions…….……219

References…….……..…220

Chapter 4: A Comparative Study of the Growth of ZnO on Si (100) and Glass Substrates by both Thermal and Remote Plasma-Assisted ALD……231

Abstract……..231

4.1 Introduction…….…232

4.2 Experimental……...234

4.2.1 Preparation of ZnO films…….234

4.2.2 Characterisation techniques…….235

4.3 Results and Discussion…….……...236

4.3.1 The surface morphologies, growth rate and structural properties of ZnO films……....236

4.3.2 Optical Properties…….....248

4.3.3 Electrical Properties…….....250

4.4 Conclusion…….....255

References……..256

Chapter 5: The Growth of Nanolaminate Doped ZnO binaries by ALD…….……...262

Abstract……..262

5.1 Introduction…….263

5.2 Experimental……...…265

5.2.1 Preparation of doped ZnO films……...…265

5.2.2 Film Characterisation……..266

5.3 Results and discussion……....267

5.3.1 The morphologies, growth rate and structural properties of doped ZnO films……...…267

5.3.2 Optical Properties……...…….300

5.3.3 Electrical Properties……....308

5.4 Conclusions……....313

References…….315

Chapter 6: A Study of the Growth of Ternary Compounds Based on ZnO by Plasma-Assisted ALD.....329

Abstract.....329

6.1 Introduction.....329

6.2 Experimental.....330

6.2.1 Preparation of ZnO ternary films.....330

6.2.2 Characterisation techniques.....331

6.3 Results and discussion.....331

6.3.1 X-ray Diffraction.....331

6.3.2 Hall Effect Measurements.....336

6.4 Conclusions.....339

References.....340

Chapter 7: Conclusion and Suggestions for Future Work.....342

Appendix I.....349

Appendix II.....350

Declaration

I hereby declare that I have written this thesis independently along with the advice of my supervisor and colleagues. I have also been assisted with other sources to further my knowledge which has all been accredited for in the reference section. This work has not been submitted for another degree, either at University College Cork or elsewhere.

Shóna Doyle

January 2022

List of Figures

Figure 1.1: (a) 0D naocluster, (b) 1D nanorod, (c) 2D thin film, (d) 3D polycrystal

Figure 1.2: Typical nanolaminate structure

Figure 1.3: Graphic of a multi-layered organic electronic device including a metal-oxide buffer layer in which the oxide/organic and oxide/electrode interfaces are highlighted. Adapted from Greiner et al.

Figure 1.4: Graphic displaying the potential templating effect of nanolaminate films in which amorphous TiO_2 is influenced by the crystalline ZnO underneath to form a crystalline TiO_2 layer

Figure 1.5: Schematic of CVD process

Figure 1.6: Schematic of electrochemical deposition process

Figure 1.7: Schematic of Langmuir-Blodgett process

Figure 1.8: Schematic of layer-by-layer process

Figure 1.9: Schematic of magnetron sputtering process

Figure 1.10: Schematic of pulsed laser deposition process

Figure 1.11: Schematic of thermal evaporation process

Figure 1.12: ALD schematic

Figure 1.13: Growth per cycle vs temperature curve displaying the ALD window (Adapted from Suntola)

Figure 1.14: (a) Direct plasma schematic, (b) Remote plasma schematic

Figure 1.15: ZnO/TiO_2 nanolaminates for use as ultra-long-life anode material for lithium-ion batteries adapted from Cao et al.

Figure 1.16: Bar chart displaying the number of papers versus the dopant element used. Al is the most frequently studied dopant followed by Ga, N, Ti, and In

Figure 2.1: The Cambridge Nanotech Fiji 200 ALD deposition system at the Tyndall National Institute

Figure 2.2: (a) ZnO and TiO_2 bilayer laminate, (b) TiO_2 and ZnO bilayer laminate, (c) TiO_2, (d) ZnO, (e) ZnO and TiO_2 multilayers laminate (4 nm ZnO + 4 nm TiO_2) x5 and (f) Standard ZnO/TiO_2 1:1 laminate

Figure 2.3: The Picosun™ R200 ALD deposition system at the Tyndall National Institute

Figure 2.4: Supercycle method schematic for doped ZnO thin films in which X = Al, Ga, In, Ti and Sn

Figure 2.5: Supercycle recipe for the deposition of PE-ALD ZnO-based quaternary with 9:1 dopant 1 and 19:1 dopant 2 ratios using the Picosun™ R200

Figure 2.6: Supercycle recipe for the deposition of PE-ALD ZnO-based quaternary with 19:1 dopant 1 and 9:1 dopant 2 ratios using the Picosun™ R200

Figure 2.7: Supercycle recipe for the deposition of PE-ALD ZnO-based quaternary with 19:1 dopant 1 and 19:1 dopant 2 ratios using the Picosun™ R200

Figure 2.8: Schematic of components of a Scanning Electron Microscope

Figure 2.9: Schematic of components of a Transmission Electron Microscope

Figure 2.10: X-ray diffraction schematic. Adapted from He et al.

Figure 2.11: Schematic of the components of a UV/Visible Spectrometer

Figure 2.12: Understanding Contact Angle

Figure 2.13: Contact angles associated with hydrophilic and hydrophobic surfaces

Figure 2.14: Chemical structure of basic blue 66

Figure 2.15: Schematic representation of the Hall Effect

Figure 2.16: Schematic representations of a) Van der Pauw resistivity measurement configuration (one of the eight possible configurations) and b) The Hall Effect measurement configuration

Figure 3.1: Schematic of the TiO_2/ZnO nanolaminates

Figure 3.2: Schematic of the true ZnO: TiO_2 1:1 nanolaminate

Figure 3.3 GIXRD patterns recorded from TiO_2 (light blue), ZnO (pink), TiO_2 on ZnO (dark blue) and ZnO on TiO_2 (green), ZnO-TiO_2 x5 bilayer (red) and ZnO: TiO_2 1:1 (black) grown on (a), an oxide-covered Si (100) substrate and (b), glass substrates. See insert caption for detail

Figure 3.4: SEM images following ALD growth on Si (100) substrates: (a) TiO_2 (b) ZnO (c) TiO_2 on ZnO and (d) ZnO on TiO_2

Figure 3.5: SEM images following ALD growth glass substrates: (a) TiO_2 (b) ZnO (c) TiO_2 on ZnO and (d) ZnO on TiO_2

Figure 3.6 (a) TEM images of (a) the Si (100)/ZnO/TiO_2 and (b) the Si (100)/TiO_2/ZnO bilayer structures grown on the naturally-oxidized Si (100) substrates. Note the differences in layer thickness for the darker, ZnO layers when comparing both structures

Figure 3.7: TEM images of ZnO and TiO_2 multilayers laminate (4 nm ZnO + 4 nm TiO_2) x5 at (a) 20 nm and (b) 10 nm

Figure 3.8: TEM images of the mixed 1:1 $ZnOTiO_2$ (1:1) layer (a) before and (b) after, annealing at 400 °C for 60 minutes in air

Figure 3.9: TEM image of the annealed mixed ZnO/TiO_2 layer focusing on one of the deposits that appear at the surface of the layer after annealing at 400 °C for 60 minutes in air

Figure 3.10: AFM images of TiO_2

Figure 3.11: AFM images of ZnO

Figure 3.12: AFM images of ZnO on TiO_2

Figure 3.13: AFM images of TiO_2 on ZnO

Figure 3.14: AFM images the mixed ZnO: TiO_2 (1:1) layers

Figure 3.15: AFM images of the x5 bilayers

Figure 3.16: Ti 2p XPS spectra for TiO_2, TiO_2 on ZnO, ZnO on TiO_2, ZnO/TiO_2 x5 and ZnO: TiO_2 (1:1) on a Si (100) substrate

Figure 3.17: Zn 2p XPS spectra for ZnO, TiO_2 on ZnO, ZnO on TiO_2, ZnO/TiO_2 x5 and ZnO: TiO_2 (1:1) on a Si (100) substrate

Figure 3.18: O 1s XPS spectra for TiO_2, ZnO, TiO_2 on ZnO, ZnO on TiO_2, ZnO/TiO_2 x5 and ZnO: TiO_2 (1:1) on a Si (100) substrate

Figure 3.19: Transmittance spectra of the ZnO: TiO_2 (1:1), ZnO/TiO_2 (x5 bilayer), ZnO/TiO_2 bilayer nanolaminate structures grown on glass

Figure 3.20: Contact angle measurements for TiO_2 and TiO_2 on ZnO grown on both Si (100) and glass substrates, after annealing at 400 °C for 1 hour in air and then exposed to UV radiation, as a function of time

Figure 3.21: Contact angle measurements for ZnO/TiO_2 (x5 bilayers) and ZnO: TiO_2 (1:1) grown on both Si (100) and glass substrates, after annealing at 400 °C for 1 hour in air and then exposed to UV radiation, as a function of time

Figure 3.22: Images of the samples before and after 150 minutes UV irradiation on glass substrate: (a) TiO_2 (b) ZnO (c) TiO_2 on ZnO (d) ZnO on TiO_2 (e) ZnO/TiO_2 x5 (f) ZnO: TiO_2 $(1:1)^+$

Figure 4.1: A schematic representation of the thermal and plasma ZnO ALD recipes used in this work

Figure 4.2: Graph of growth rate per cycle vs. temperature for thermal and PE-ALD ZnO on (a) Si and (b) glass substrate at 100 °C, 150 °C and 200 °C

Figure 4.3: Plan-view SEM of (a) - (c) thermal ZnO and (d) - (f) plasma ZnO at various temperatures on Si (100) substrate

Figure 4.4 Plan-view SEM of (a) - (c) thermal ZnO and (d) - (f) plasma ZnO at various temperatures on glass substrate

Figure 4.5 XRD patterns of (a) thermal ALD ZnO on Si, (b) PE-ALD ZnO on Si, (c) thermal ALD ZnO on glass and (d) PE-ALD ZnO on glass

Figure 4.6 UV/Visible Spectroscopy transmittance spectra for 900 cycles (a) ZnO thermal ALD and (b) PE-ALD films at 100 °C 150 °C and 200 °C on glass substrates

Figure 4.7: Resistivity of thermal and PE-ALD ZnO deposited on glass substrates as a function of substrate temperature

Figure 5.1: The supercycle method schematic for doped ZnO thin films in which X = Al, Ga, In, Ti and Sn

Figure 5.2: Plan-view SEM images of thermal ALD (a) AZO, (b) GZO, (c) SZO and (d) TZO (19:1) films deposited at 150 °C on glass substrates, Au-coated

Figure 5.3: Plan-view SEM images of PE-ALD (a) AZO, (b) GZO, (c) SZO and (d) TZO (19:1) films deposited at 150 °C on glass substrates, Au-coated

Figure 5.4: Plan-view SEM images of thermal ALD (a) AZO, (b) GZO, (c) SZO and (d) TZO (19:1) films deposited at 150 °C on Si (100) substrates, Au-coated

Figure 5.5: Plan-view SEM images of PE-ALD (a) AZO, (b) GZO, (c) SZO and (d) TZO (19:1) films deposited at 150 °C Si (100) substrates, Au-coated

Figure 5.6: Plan-view SEM images of as-grown ZnO on Si (100) substrates, Au-coated by (a) thermal ALD and (b) PE-ALD, and on glass substrates by (c) thermal ALD and (d) PE-ALD deposited at 150 °C

Figure 5.7: TEM image of thermal AZO at scale of (a) 10 nm (b) 20 nm and (c) 50 nm on Si (100) substrates

Figure 5.8: TEM image of PE-ALD AZO at scale of (a) 20 nm (b) 50 nm and (c) 100 nm on Si (100) substrates

Figure 5.9: TEM image and FFT images of PE-ALD AZO confirming the presence of ZnO in hexagonal wurtzite structure on a Si (100) substrate

Figure 5.10: TEM images of thermal ALD GZO at scales of (a) 5 nm (b) 10 nm and (c) 20 nm on Si (100) substrates

Figure 5.11: TEM images of PE-ALD GZO at scales of (a) 10 nm (b) 20 nm and (c) 50 nm on Si (100) substrates

Figure 5.12: TEM images of thermal ALD SZO at scales of (a) 10 nm (b) 50 nm and (c) 200 nm on Si (100) substrates

Figure 5.13: TEM images of PE-ALD SZO at scales of (a) 10 nm (b) 20 nm and (c) 50 nm on Si (100) substrates

Figure 5.14: TEM images of thermal ALD TZO at scales of (a) 10 nm (b) 20 nm and (c) 50 nm on Si (100) substrates

Figure 5.15: TEM images of PE-ALD TZO at scales of (a) 50 nm, (b) 5 nm and (c) 20 nm in which the film-substrate interface is highlighted on Si (100) substrates

Figure 5.16: TEM images of PE-ALD TZO in which the film-substrate interface is highlighted at (a) 2 nm and (b) 20 nm on a Si (100) substrate

Figure 5.17: EDS elemental mapping of thermal ALD (a) AZO, (b) GZO and (c) SZO on Si (100) substrates

Figure 5.18: EDS elemental mapping of PE-ALD (a) AZO, (b) GZO, (c) SZO and (d) TZO on Si (100) substrates

Figure 5.19: XRD patterns of as-grown ZnO films deposited at 150 °C on (a) glass substrates and (b) Si (100) substrates

Figure 5.20: XRD patterns of thermal ALD AZO, GZO, SZO and TZO (9:1) films deposited at 150 °C on (a), glass substrates and (b) Si (100) substrates

Figure 5.21: XRD patterns of thermal ALD AZO, GZO, SZO and TZO (19:1) films deposited at 150 °C on (a) glass substrates and (b) Si (100) substrates

Figure 5.22: XRD patterns of PE-ALD AZO, GZO, SZO and TZO (9:1) films deposited at 150 °C on (a) glass substrates and (b) Si (100) substrates

Figure 5.23: XRD patterns of PE-ALD AZO, GZO, SZO and TZO (19:1) films deposited at 150 °C on (a) glass substrates and (b) Si (100) substrates

Figure 5.24: XPS spectra of the O 1s region for (a) thermal and (b) PE-ALD AZO at a depth of 0-36 nm. The oxygen peak was composed of two components with different binding energies

Figure 5.25: UV/visible spectra of thermal and PE-ALD ZnO films deposited at 150 °C on glass substrates

Figure 5.26: UV/visible spectra of (a), thermal and (b), PE-ALD AZO, GZO, SZO and TZO (9:1) films deposited at 150 °C on glass substrates

Figure 5.27: UV/visible spectra of (a), thermal and (b), PE-ALD AZO, GZO, SZO and TZO (19:1) films deposited at 150 °C on glass substrates

Figure 5.28: Band gap energies calculated via Tauc plot method for thermal ALD 19:1 AZO, SZO and TZO on glass substrates

Figure 6.1: XRD patterns of ZnO: Ga_2O_3: Al_2O_3 materials deposited using various dopant ratios at 150 °C on (a) glass substrates and (b) Si (100) substrates

Figure 6.2: XRD patterns of ZnO: SnO_2: Al_2O_3 materials deposited using various dopant ratios at 150 °C on (a) glass substrates and (b) Si (100) substrates

Figure 6.3: XRD patterns of ZnO: TiO_2: Al_2O_3 materials deposited using various dopant ratios at 150 °C on (a) glass substrates and (b) Si (100) substrates

List of Tables

Table 1.1: Summary of CVD processes

Table 1.2: Summary of ZnO ALD processes

Table 1.3: Summary of TiO_2 ALD processes

Table 1.4: Residual stresses, Young's modulus and tensile strength obtained by bulge and MEMS shaft-loading techniques

Table 1.5: Lifetimes of nanolaminate materials for encapsulation and passivation applications

Table 1.6: Previous work on ZnO/TiO_2 laminates via E-beam evaporation, sol-gel, ALD and spatial-ALD deposition methods

Table 1.7: Temperature study by Baji et al. showing growth directions for intrinsic ZnO and 4.9at% Al-doped ZnO

Table 1.8: Listing of cation dopants used in ALD doped ZnO along with the dopant precursors, oxidants, growth temperature and deposition rate. The Zn precursor in all cases is diethyl zinc

Table 2.1: Plasma growth process details using Litmas® RPS 3001 by Advanced Energy™

Table 2.2: Carrier gas flow rate, precursor pulse, purge times and temperatures for TMA, TMG, TDMASn and TDMAT

Table 2.3: Dopant ratios used for the growth of ternary films

Table 2.4: Characteristic wavelength ranges for UV, Visible and IR regions

Table 3.1: Comparison of crystallite size calculated by the Scherrer equation and the intercept method along to ZnO (002) crystal plane

Table 3.2: RMS roughness values for the various films produced here as a function of substrate type

Table 3.3: Percentages of Ti^{3+} present in the various nanolaminate films studied

Table 3.4: Times to bleach for TiO_2, ZnO, ZnO on TiO_2, TiO_2 on ZnO, ZnO/TiO_2 x5 and ZnO: TiO_2 (1:1) films

Table 4.1: A comparison of the GPC values recorded for ZnO ALD on both Si (100) wafers and glass substrates as a function of substrate temperature and growth mode

Table 4.2: Comparison of crystallite size calculated by the Scherrer equation for thermal and plasma ALD deposited ZnO on both Si (100) and glass along to ZnO (002) crystal plane

Table 4.3: Hall mobility, carrier concentration and sheet resistance measurements for 900 cycles thermal and PE-ALD ZnO films at 100 °C, 150 °C and 200 °C

Table 4.4: Hall mobility, carrier concentration and sheet resistance measurements for 900 cycles PE-ALD ZnO films at 150 °C, PE-ALD ZnO deposited with a reduced plasma power and PE-ALD ZnO deposited with a reduced plasma pulse

Table 5.1: Comparison of crystallite size as determined by both the Scherrer equation and the intercept method for both thermal and PE-ALD 19:1 AZO, GZO, SZO and TZO on Si (100) and glass substrates

Table 5.2: Estimated and measured thickness for thermal and PE-ALD 19:1 AZO, GZO, SZO and TZO on Si (100) substrates

Table 5.3: Quantification of high resolution XPS data for both thermal ALD and plasma ALD grown ZnO at 600 s etch time, equivalent to 24 nm depth profiling

Table 5.4: Quantification of high resolution XPS data for both thermal ALD and plasma ALD-grown AZO, GZO, SZO and TZO (19:1) samples at 900 s etch time, equivalent to 36 nm depth profiling.

Table 5.5: Nominal dopant atomic percentage (at%) for thermal and PE-ALD AZO, GZO, SZO and TZO calculated based on GPC values using equation 5.2, dopant ratio 19:1

Table 5.6: Band gap energies calculated via Tauc plot method for 19:1 thermal and PE-ALD AZO, GZO, SZO and TZO on glass substrates

Table 5.7: Electrical properties of AZO, GZO, SZO and TZO (9:1) deposited by thermal and PE-ALD at 150 °C on glass substrates

Table 5.8: Electrical properties of AZO, GZO, SZO and TZO (19:1) deposited by thermal and PE-ALD at 150 °C on glass substrates

Table 6.1: Dopant ratios used for the growth of ternary films

Table 6.2: Electrical properties of ZnO: Ga_2O_3: Al_2O_3, ZnO: SnO_2: Al_2O_3 and ZnO: TiO_2: Al_2O_3 deposited by PE-ALD at 150 °C on glass substrates

Acronyms

0D - Zero dimensional

1D - One dimensional

2D - Two dimensional

3D - Three dimensional

AC - Alternating current

AFM - Atomic force microscopy

AIP - Aluminium isopropoxide

ALD - Atomic layer deposition

ALE - Atomic layer epitaxy

AZO - Aluminium zinc oxide

BB66 - Basic blue 66

C-ALD - Combinatorial atomic layer deposition

CA - Contact angle

CMOS - Complementary metal–oxide–semiconductor

CR - Cycle ratio

CVD - Chemical vapour deposition

DC - Direct current

DEZn - Diethyl zinc

DMAIP - Dimethylaluminium isopropoxide

DMLDMIn - dimethylamino- dimethyl indium

DMZ - Dimethyl zinc

DSSC - Dye-sensitised solar cell

EDS - Energy-dispersive X-ray spectroscopy

EELS - Electron energy loss spectroscopy

EIS - Electrochemical impedance spectroscopy

FEG - Field emission gun

FEI - Field Electron and Ion Company

FFT - Fast Fourier transform

FIB - Focused Ion Beam

FOLED - Flexible organic light-emitting diodes

FTIR - Fourier transform infrared spectroscopy

FWHM - Full width at half maximum height

GIXRD - Grazing incidence x-ray diffraction

GPC - Growth per cycle

GZO - Gallium zinc oxide

HAADF – High-angle annular dark-field imaging

HF - Hydrogen fluoride

HSS - High speed steel

IC - Integrated circuit

InCA-1 - 1, 1, 1-trimethyl-*N*-(trimethylsilyl)silanaminato]-indium

IPA - Isopropyl alcohol

IR - Infrared

ITO - Indium tin oxide

IZO - Indium zinc oxide

JCPDS - Joint Committee on the Powder Diffraction Standard

LbL - Layer-by-layer

LIB - Lithium-ion battery

MEMS - Mirco-electro-mechanical system

MB - Methylene blue

MO - Methyl orange

MZI - Methyl zinc isopropoxide

NMR - Nuclear magnetic resonance

OFET - Organic field-effect transistor

OLED - Organic light emitting diode

OTFT - Organic thin films transistors

PE-ALD - Plasma enhanced – atomic layer deposition

PLD - Pulsed laser deposition

PSC - Perovskite solar cell

PV - Photovoltaic

PVD - Physical vapour deposition

RF - Radio frequency

RI - Refractive index

RMS - Root mean square

ROM - Rule of mixtures

RT - Room temperature

Rz - Resazurin

SA - Stearic acid

SAM - Self-assembled monolayer

SED - Sacrificial electron donor

SE - Secondary electron

SEI - Solid electrolyte interface

SEM - Scanning electron microscopy

STEM - Scanning transmission electron microscopy

SZO - Tin zinc oxide

TCO - Transparent conducting oxide

TDEAT - Tetrakis(diethylamido)titanium

TDMASn - Tetrakis-dimethylamido tin

TDMAT - Tetrakis(dimethylamido)titanium

TEG - Triethyl gallium

TEM - Transmission electron microscopy

TMA - Trimethyl Aluminium

TMD - Transition metal dichalcogenide

TMG - Trimethyl Gallium

TMI - Trimethyl indium

TTIP - Titanium tetraisopropoxide

TZO - Titanium zinc oxide

UV - Ultraviolet

XPS - X-ray photoelectron spectroscopy

XRD - X-ray diffraction

ZTO - Zinc tin oxide

Acknowledgements

I would like to thank my supervisor Professor Martyn Pemble for providing me with the opportunity to pursue postgraduate studies within the Advanced Materials and Surfaces Group at Tyndall National Institute. I greatly appreciate the encouragement and guidance I received throughout the years. I also would like to thank my supervisor Dr Ian Povey for the constant guidance through lab work and especially for making me realise my potential.

I would like to extend my gratitude to my colleagues at Tyndall National Institute and beyond whose contributions were invaluable. Namely, Dr Mircea Modreanu, Paul Tassie, Dr Jun Lin, Dr Scott Monaghan, Vince Lodge, Dr Michael Schmidt, Dr Brendan Sheehan, Dr Shane O'Brien, Dr Trevor Carey, Dr Ian O'Connor, Dr Aoife O'Sullivan, Dr Karrina McNamara, Dr Fathima Laffir and Dr Michele Conroy. Thank you to the members of the Advanced Materials and Surfaces group, past and present especially Catherine, Jan, Harry and Will.

A very special thanks to my friend Jen who has been with me all the way through our undergraduate years at UCC to now. I found a friend for life through Chemistry.

Thank you to my family for always believing in me, especially my parents and my brother, Stephen. To my Granny Maureen – I hope I can be as tenacious as you are. To my grandparents that I have lost since I started this thesis, Grandad Mick, Grandad Paddy and Nana Helene – yes, I have finally finished school. To my forever best friend Bear, I truly believe dogs help us calm and heal in a way nothing else can – I miss you. Finally, thank you to my partner, Cillian for always being there for me.

Abstract

In recent years, hybrid nanolaminate materials have generated great interest due to the physical and chemical properties that 2D nanosheets possess that their bulk counterparts do not. Thin films and nanostructured materials offer unique and potential benefits that could positively impact the areas of communications, electronics and energy arising from the fact that the properties of atoms, groups of atoms and ultra-thin layers are exploited rather than bulk materials. The applications of hybrid films are almost endless, ranging from use as capacitors, dielectrics and insulators, encapsulation layers/ protective coatings, lubricants and optical waveguides. By definition, nanolaminates are multicomponent systems consisting of alternating layers of materials such as metals and metal oxides. Each individual layer has an associated thickness on the nanometre scale. By mixing a wide variety of materials, it may be possible to fine-tune a desirable material in terms of its composition, properties and structure.

In this thesis, the growth of nanolaminate structures of ZnO and TiO_2 were studied using a C-ALD (combinatorial atomic layer deposition) approach. The specific aim of this study was to combine the photocatalytic properties and robustness of TiO_2 with the transparent conducting behaviour and photoactivity of ZnO. Mixed nanolaminate structures containing ZnO/TiO_2 layers were fabricated by deliberately under-dosing during the metal precursor parts of the ALD cycle. The ZnO/TiO_2 nanolaminate films were deposited at 200 °C.

Building upon this nanolaminate study, a fundamental study of ZnO deposited by both thermal and PE-ALD (plasma- enhanced ALD) was employed, focusing on the crystallinity and morphology of the films as well as optical and electrical performance. The same reactor, a Picosun™ R200 ALD reactor, was used for both sets of experiments so as to minimise the influence of reactor design on the nature of the deposited films.

Next, doped ZnO films were deposited via thermal and PE-ALD with the intention of improving the electrical properties. ZnO thin films were doped with Al, Ga, Sn and Ti dopants. The introduction of dopants into a host material allows for the manipulation of the composition and structure that can impact both electrical and optical properties of the material.

Lastly, ZnO: Ga_2O_3: Al_2O_3, ZnO: SnO_2: Al_2O_3 and ZnO: TiO_2: Al_2O_3 ternaries were deposited via PE-ALD at 150 °C in order to study the electrical, optical and structural properties. Ternaries are inherently more complex which provides more opportunities to fine tune the composition and both the atomic and electronic structures.

Chapter 1: Introduction

1.1 Thin Film Nanotechnologies

The earliest documented inorganic thin films date back to more than 5000 years ago during the Bronze Age in which the ancient Egyptians produced gold thin films (<3000 Å) chemo-mechanically. These gold films were made for decorative purposes such as gold-coated copper and brass statues and jewelry. Evidence of such has been found in ancient tombs in Cairo, Egypt[1].

Speed up to 1870 when the deposition of a metal thin film on glass was documented[2] while in 1880, a thin film metal film was fabricated for use as a sensory element in a bolometer[3]. The first electrical characterization of a thin film was reported in 1898[4]. Then, in 1900, Longden et al. reported on the novel deposition method named "cathode discharge" which is now known as sputtering[5, 6].

The development of solid-state transistors dramatically accelerated interest in thin film nanotechnology. Germanium-based transistors were first[7], followed by silicon[8, 9]. In 1960, the fabrication of an integrated circuit (IC) also further increased the interest in thin film nanotechnology[10]. ICs cannot be mentioned without making reference to Moore's Law. In 1965, the co-founder and Chairman Emeritus of Intel Corporation, Gordon Moore, made the observation that every year the number of transistors per square inch of an integrated circuit had doubled since the first invention. This phenomenon became known as Moore's law. In 1975, the law was revised to doubling every two years[11]. In order to keep up with Moore's

Law, it is desirable to fabricate new or improved materials that can outperform traditional silicon in the semiconductor industry which is why research is constantly ongoing in this area. Thin film nanotechnology is an essential area of research that involves the manipulation and utilization of a layer(s) of atoms and molecules at the nanoscale (10^{-9} nm)[12]. It is relevant to a myriad of applications. Principle application areas benefitting specifically from thin film nanotechnology include advanced complementary metal–oxide–semiconductor (CMOS) technology, antimicrobial coatings, environmental and medical applications[13], memory and data storage and photovoltaics[14]. Enabling thin film nanotechnology allows for the fabrication of novel materials and devices with remarkable chemical and physical properties as it is possible to precisely control the architecture and microstructure at the nanometre scale.

Based on the quantity of dimensions the material possesses outside of the nanoscale (>100 nm), they may be classified as either zero dimensional (0D), one dimensional (1D), two dimensional (2D) or three dimensional (3D). Consequently, 0D nanomaterials have all dimensions within the nanometre scale as the electrons are confined within all 3 dimensions. This includes nanoclusters, nanodots and the well-studied fullerenes. 1D materials have 1 dimension outside of the nanometre scale. This includes nanoribbons, nanorods and nanowires. 2D materials have 2 dimensions outside of the nanometre scale. These layered materials include graphene and transition metal dichalcogenides (TMDs). Finally, 3D materials have no dimensions within the nanometre scale. This include bulk powders and bundles of nanocones, nanocoils and nanoflowers[15]. A diagram of each nanomaterial can be seen in figure 1.1 (a)-(d) below.

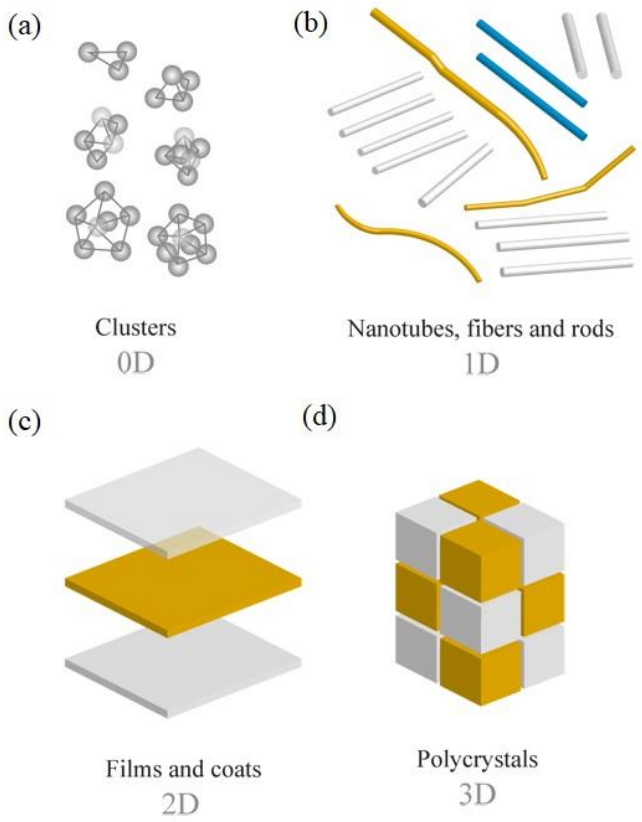

Figure 1.1: (a) 0D nanocluster, (b) 1D nanorod, (c) 2D thin film, (d) 3D polycrystal[16]

1.2 Nanolaminates - Definitions and Potential Applications

To define, nanolaminates are multicomponent systems consisting of alternating layers of specific materials such as metals and metal oxides. Each individual layer has an associated thickness present on the nanoscale[17]. Combining a variety of layers of different materials makes it potentially possible to fine-tune a nanolaminate thin film in terms of its properties such as composition and structure[18]. Nanolaminate films can be prepared by various chemical and physical deposition methods which are discussed in sections 1.2.1 and 1.2.2. The unique conformity and precision of thin films produced by atomic layer deposition (ALD) enables sub-nanometre design and control of these true nanolaminates[19]. In particular, when utilized in a combinatorial sense using multiple precursors, the possibility of combinations of material is infinitely large and presents a very interesting area of research.

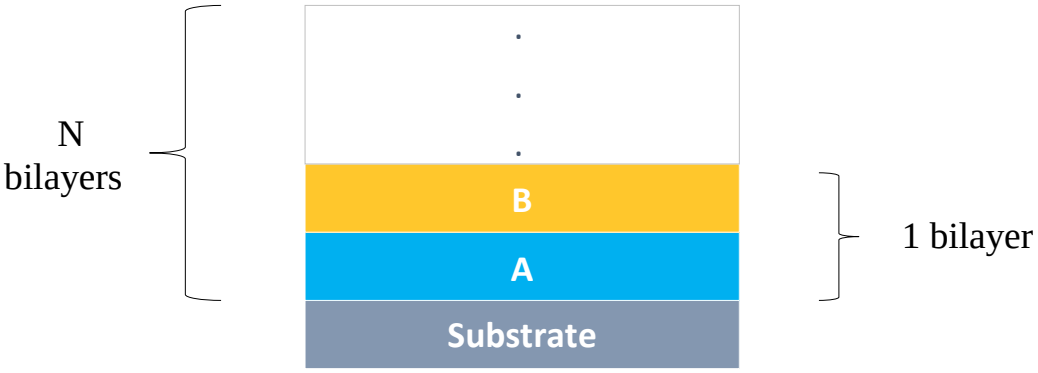

Figure 1.2: Typical nanolaminate structure

Hybrid nanolaminate films have attracted much attention in recent years due to the physical and chemical properties that 2D nanosheets and nanofilms possess that their corresponding bulk counterparts do not, such as electrical[20, 21], mechanical[22], optical[23-25] and thermal properties[26]. Numerous publications exist on the topic and the number of publications is predicted to continue to increase[27]. Notable reviews on the topic also exist which explore the

fundamentals of these materials[19, 27, 28] and also review with a focus on specific application fields[29]. The applications of hybrid films are almost limitless, ranging from use as capacitors[30-33], dielectrics and insulators[34-43], encapsulation layers/ protective coatings[44-52], lubricants[53] and optical waveguides[54]. Figure 1.3 displays an application of nanolaminates in electronic devices; a multi-layered organic electronic device with a metal-oxide buffer layer[55]. Figure 1.4 depicts the possible capability of nanolaminates in terms of templating effects. This idea will be explored in chapter 3.

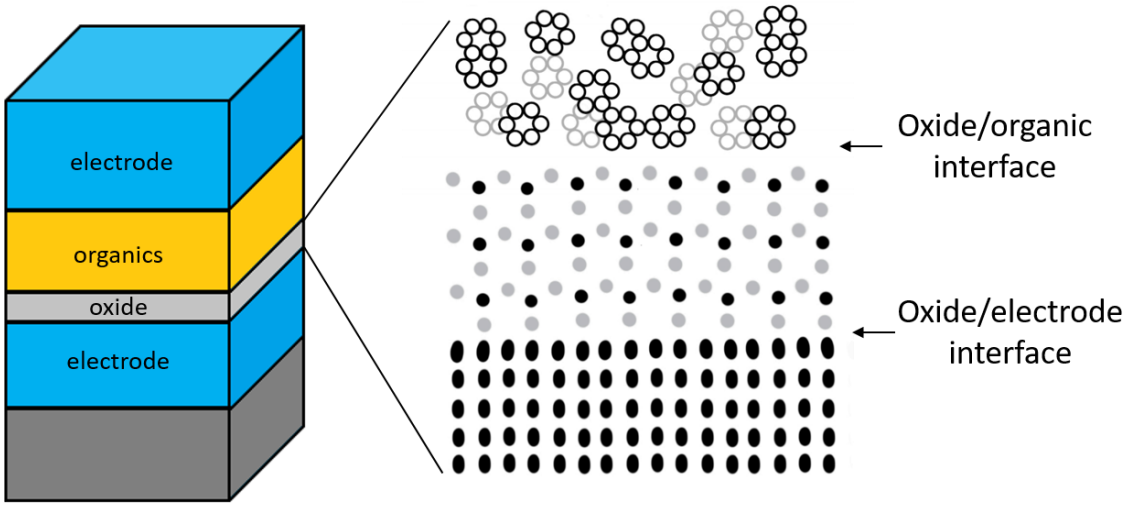

Figure 1.3: Graphic of a multi-layered organic electronic device including a metal-oxide buffer layer in which the oxide/organic and oxide/electrode interfaces are highlighted. Adapted from Greiner et al.[55]

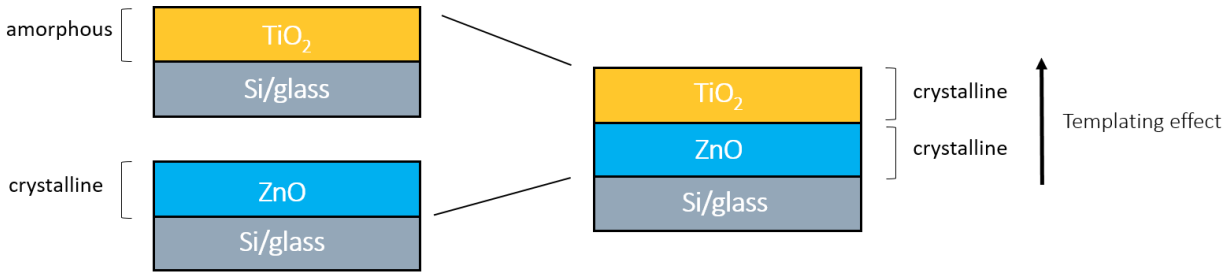

Figure 1.4: Graphic displaying the potential templating effect of nanolaminate films in which amorphous TiO_2 is influenced by the crystalline ZnO underneath to form a crystalline TiO_2 layer

The following sections describe both chemical and physical methods for the fabrication of nanolaminate materials. Both methods may be thought of as bottom-up methods whereby the material is built from the bottom up and the deposition continues until the desired film is complete. Atoms or molecules are deposited on a substrate and it is necessary to understand the individual components in order to build a complete structure[56, 57].

1.2.1 Chemically-based methods for nanolaminate synthesis

The use of chemical techniques for the deposition of thin films aids the fabrication of highly homogeneous films as mixing of materials at a molecular level can be studied[58]. This is the huge advantage of chemical methods as compared to physical methods. However, a common drawback associated with chemical methods is the need to utilise toxic reagents and solvents[59] while the integration of such methods into a commercially-viable process flow can also be problematic.

1.2.1.1 Chemical Vapour Deposition

Chemical vapour deposition (CVD) is a vapour phase chemical technique in which solid material is deposited onto the surface of substrates that are usually heated. During the CVD

process, precursor molecules enter the deposition chamber at the same time in order for deposition to occur. It is possible to control the thickness, crystalline structure, surface morphology and the film composition by altering the growth conditions. Parameters such as deposition temperature, gas flow patterns, pressure and composition of reactant gases can be readily modified. CVD is capable of producing dense, high-quality films with high performance. However, the process has relatively low deposition rates (μm/hr) and may produce potentially toxic gaseous by-products[60, 61]. Several variations of the CVD process exist as seen in Table 1.1.

Process name	**Acronym**	**References**
Aerosol-assisted CVD	AACVD	62-84
Atomic layer CVD	ALCVD	85-101
Atmospheric pressure CVD	APCVD	102-147
Direct liquid injection CVD	DLICVD	148-153
Hybrid physical CVD	HPCVD	154-170
Hot wire CVD	HWCVD	171-183
Low-pressure CVD	LPCVD	157, 184-193
Metal-organic CVD	MOCVD	194-205
Microwave plasma-assisted CVD	MPCVD	206-215
Remote plasma-enhanced CVD	RPECVD	216-226
Rapid thermal CVD	RTCVD	227-235
Ultra-high vacuum CVD	UHCVD	236-242

Table 1.1: Summary of CVD processes[60]

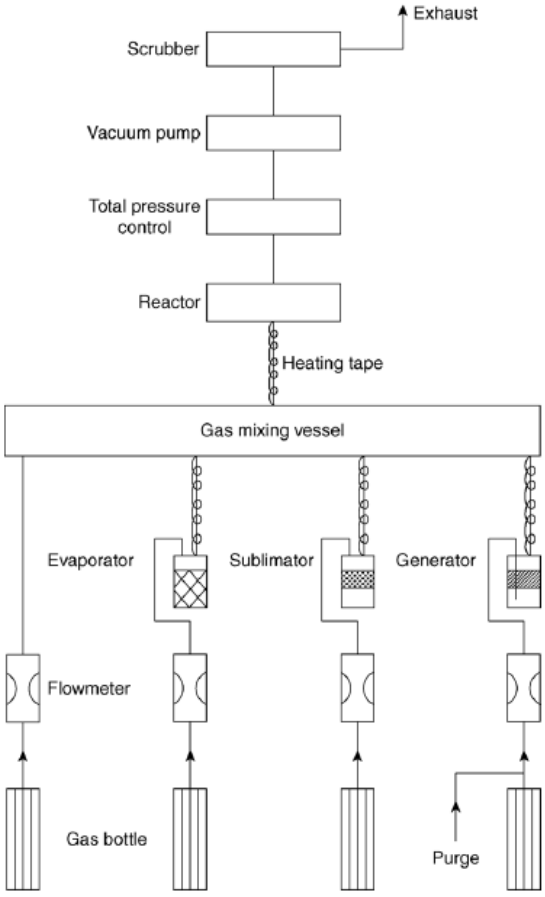

Figure 1.5: Schematic of a typical CVD process consisting of a reaction gas dispensing system, a reactor, including components for defining gas flows and an exhaust system containing a total pressure controller, vacuum pump, scrubber/or reactant recycling system[243]

1.2.1.2 Electrochemical Deposition

Electrochemical deposition, also known as cathodic deposition, electrolytic deposition or electrodeposition is a relatively simple technique[244]. A thin coating of a metal or a metal-oxide can be deposited on to a conducting substrate by means of electrochemical reaction. A solution containing the desired metal ion or complex undergoes electrochemical reaction, usually reduction, in order for deposition to occur[245]. The equipment used can consist of either a two or three electrode arrangement. Electrodeposition is an inexpensive technique and has been

used to deposit nanostructured films and substrates and also for the functionalization of nanostructured templates[246]. It is suitable for covering large areas and can be performed at room temperature (RT) and atmospheric pressure. The method has been used for the deposition of nanolaminates such as platinum on alloys (Co-super alloy, Inconel, pure Al, Al-Ti alloy, graphite) for applications in batteries, capacitors and fuel cells[247].

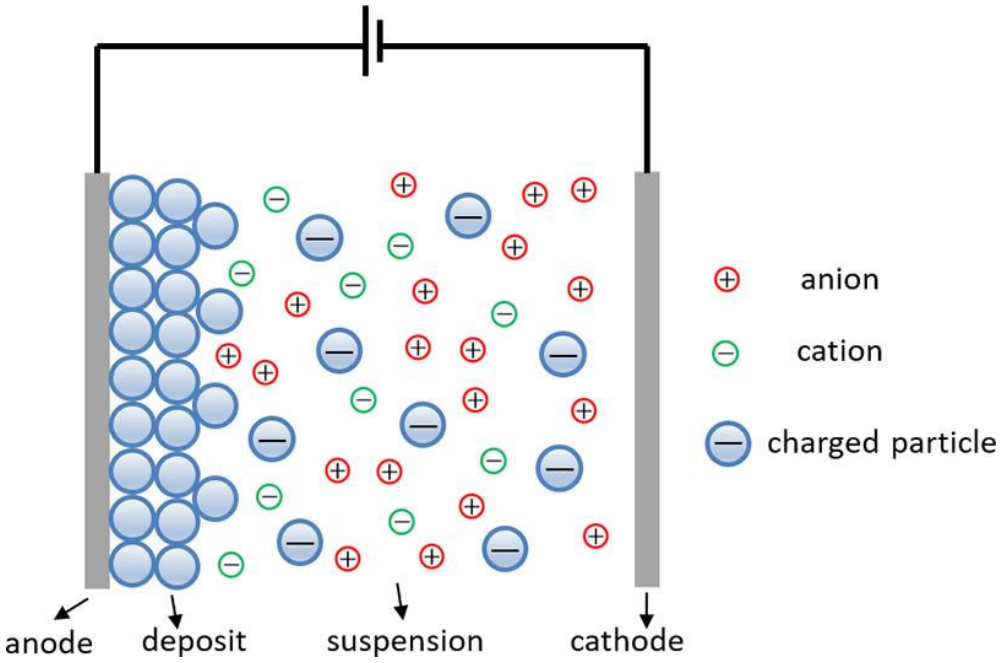

Figure 1.6: Schematic of electrochemical deposition process in which an electric field is applied and the ionically charged particles suspended in the suspension move to the oppositely charged electrode and then deposit onto it[248]

1.2.1.3 Molecular self-assembly & Langmuir-Blodgett film formation

A Langmuir film is formed by the self-assembly of a monolayer of amphiphilic molecules usually on the surface of a liquid. Self-assembled monolayers (SAMs) then follow as the simultaneous formation of monolayers occurs via surface adsorption and organisation of ordered domains[249]. These methods combined allow for the deposition of organised multilayers that are densely and closely packed, for the surface immobilisation of functional molecules[250] and for the use of some area-selective growth processes[251, 252]. However, the method is very time consuming, expensive and requires special equipment. The molecules used must be amphiphilic which limits the choice of what can be used. The films produced are not particularly stable under ambient conditions due the weak molecular interactions occurring between the film and substrate[249].

Nanolaminates films utilising the self-assembly approach have been formed using p-type oligo (p-phenylenevinylene)s and n-type perylenebisimides films for photovoltaic applications and gold-polypyrrole amphiphiles for use as chemical sensors, electrocatalysts and microelectronic devices[253]. Nanolaminate Langmuir Blodgett films have been applied in biological membranes[254] and glucose sensors[255].

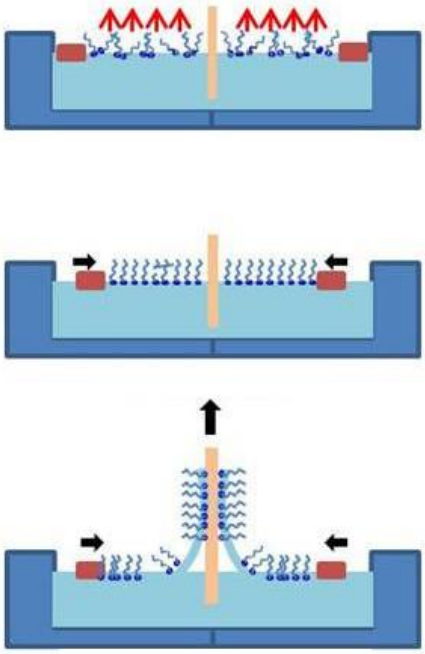

Figure 1.7: Schematic of a Langmuir-Blodgett process in which lipids are dissolved in a solvent mixture, nanostructured mica are then immersed in water perpendicular to the interface. The lipid solution is spread at the air-water interface using a Hamilton syringe. After evaporation of solvents, lipids are compressed continuously until a certain surface pressure is reached. Once stabilization of the monolayer is complete, the mica surface is removed from the subphase using an automatic dipper[256]

1.2.1.4 Layer-by-layer assembly

The layer-by-layer assembly (LbL) approach utilises the consecutive adsorption of multivalent molecules present on a surface which gives rise to both electrostatic and non-electrostatic interactions. Multilayer films fabricated by this method can have their thickness, composition, structure, properties and functionalities tailored[250]. The method itself has many advantages such as reproducibility, robustness and flexibility. In order to prevent contamination from the previous adsorption, washings are required between each multilayer growth[257]. Increasing the

length of washings can lead to a more regular build-up of layers[250]. The most widely used LbL processes are dip-coating[258], spin-coating[259, 260] and spraying[258, 260, 261]. Nanolaminate films have been fabricated using these techniques for use as super-capacitors and sensors[262].

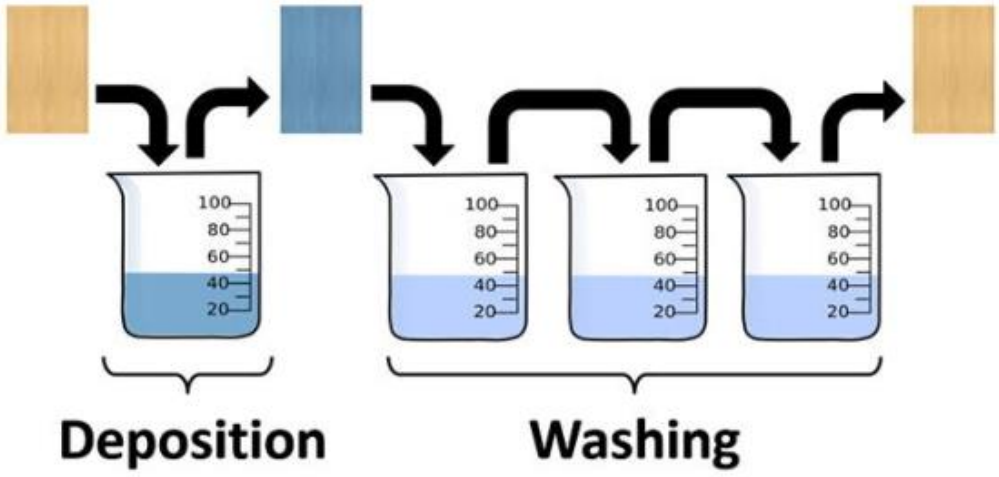

Figure 1.8: Schematic of layer-by-layer process in which a substrate is subsequently exposed to solutions of oppositely charged polyelectrolytes to allow for stacking of multiple layers of material. Numerous washings between layers prevent contamination[257]

1.2.2 Physical methods for nanolaminate synthesis

Physical deposition methods involve techniques such as evaporation and sputtering. They are perceived as more environmentally friendly than chemical methods as they do not call for the use of toxic solvents and reagents while they are also compatible with current semiconductor processing and as such may be readily scaled to commercial levels.

Although not all physical methods incur it, line-of-sight transfer is the main drawback of this approach as it can lead to poor coverage of complex surfaces and lack of uniformity in thickness[263].

1.2.2.1 Magnetron Sputtering

Many sputtering techniques exist including ion-assisted and ion-beam assisted deposition of which with magnetron sputtering is the most common for the fabrication of nanolayered materials. In the vapour phase, a collision process between incident particles and a source material/target occurs. The incident particle transmits energy to a target atom, which can then collide with other target atoms to start a cascading process. Target atoms near the surface gain sufficient momentum for ejection to occur causing deposition of material on the substrate. As ions are charged particles, their velocities can be controlled using a magnetic field[264, 265]. Accordingly, magnets are used to confine the ions in the plasma or close to the surface of the target[266]. This effect enhances the efficiency of the ionization process, improves the plasma density and results in faster deposition rates. It also reduces the possibility of damage that may be caused by the direct impact of these electrons with the film or substrate. Magnetron sputtering may be direct current (DC) or radio frequency (RF)[264] sputtering and has been utilised to fabricate nanolaminate structures such as Nd-doped SnO_2 solar cells[267] and Al/CuO micro-electro-mechanical system (MEMS) energy sources[268].

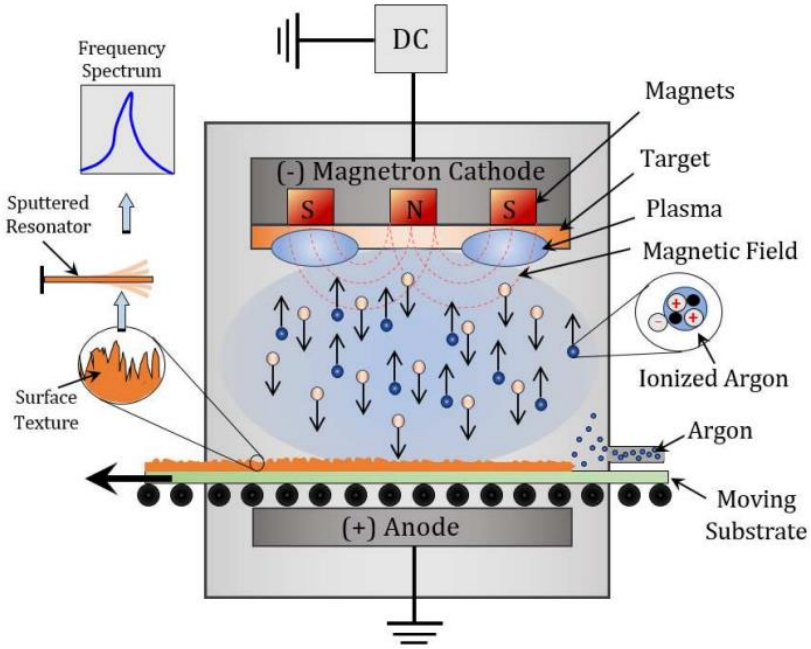

Figure 1.9: Schematic of magnetron sputtering process which shows the cathode target material and the anode substrate. A sputtering gas is supplied and a plasma is created which emits positively charged ions. These ions are accelerated by a DC electrical field which is generated between the cathode target and the anode substrate. A magnetic field around the target material is used to trap the ions. Argon atoms collide with the ions and ionized argon molecules are generated which are then driven towards and hit the target material. Target atoms are sputtered off and condense on the substrate forming the thin film[269]

1.2.2.2 Pulsed Laser Deposition

Pulsed laser deposition (PLD) is a physical deposition process that occurs in the gas phase. In an ultra-high vacuum chamber, a pulsed laser is used to vaporise a target material which can then interact with a reagent gas such as oxygen to form an oxide[270, 271]. Following the ablation, condensation of the material and subsequent deposition onto a substrate takes place in order to form a thin film[272]. Typically an excimer laser is used such as KrF or a solid state laser such as Nd:YAG[273]. High power pulses in the range of 108 Wcm^{-2} are used. The use of an external energy source, i.e. the laser makes PLD a clean process and allows for reagent gases to be either inert or reactive. PLD is capable of producing high quality films with exact stoichiometric transfer from the target material. This fact makes it possible to reproduce extremely complex materials[274]. The target material is placed on a carousel meaning multiple target materials can be placed within the chamber to allow for the deposition of multilayer films. The formation of droplets that may be seen on the surface of the material is a drawback of PLD as this can lead to the formation of a rough surface. The plasma plume is highly forward-directed which in turn means deposition is not uniform and composition across the film may vary[275]. PLD deposited Ti_3AlC_2 nanolaminates have potential as next-generation biomechanical touch sensors for energy harvesting[276].

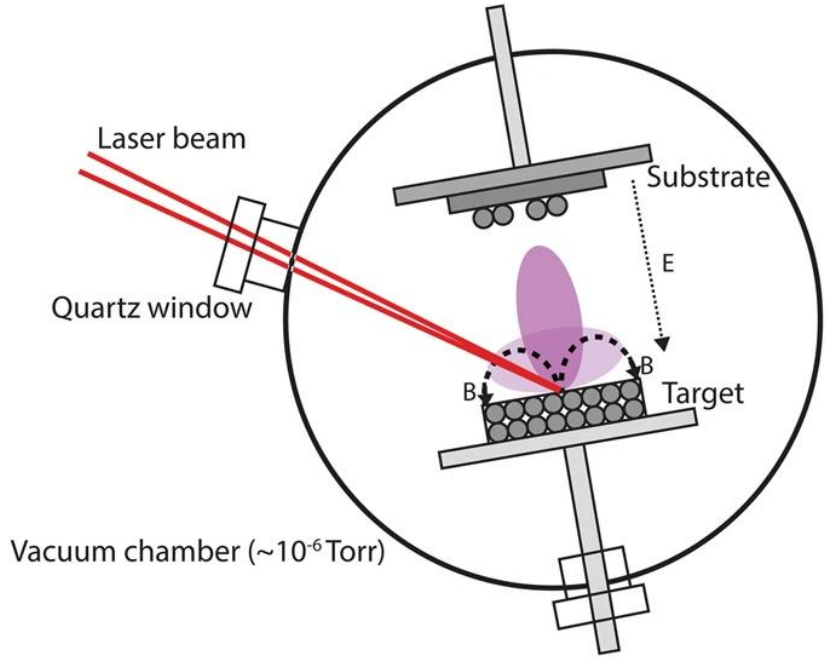

Figure 1.10: Schematic of pulsed laser deposition process in which the target is exposed to the PLD laser which vaporises the target material which can then interact with a reagent gas. Condensation of the material follows the ablation and subsequent deposition onto a substrate takes place in order to form a thin film. B represents the magnetic field and E represents the electric field[277]

1.2.2.3 Thermal evaporation deposition

Thermal evaporation deposition, also known as vacuum deposition, was first reported by Faraday in the 1850s. By placing metal wires in a vacuum and effectively exploding them, Faraday deposited metallic thin films[278]. The technique itself involves the evaporation of a source material under conditions of low pressure (10^{-5}-10^{-6} Torr) so that atoms are lost from the surface of the source material. A vacuum environment is required to prevent reactions occurring between the vapour and any species present in the ambient atmosphere. For example oxide formation may occur if any atmospheric oxygen was present. Collisions with any species

that may be present would also slow down the rate of the evaporation process. Generally for this process film adhesion is poor and films with low densities are often obtained. However, the method is simple and inexpensive and films may possess high levels of purity[265, 279, 280].

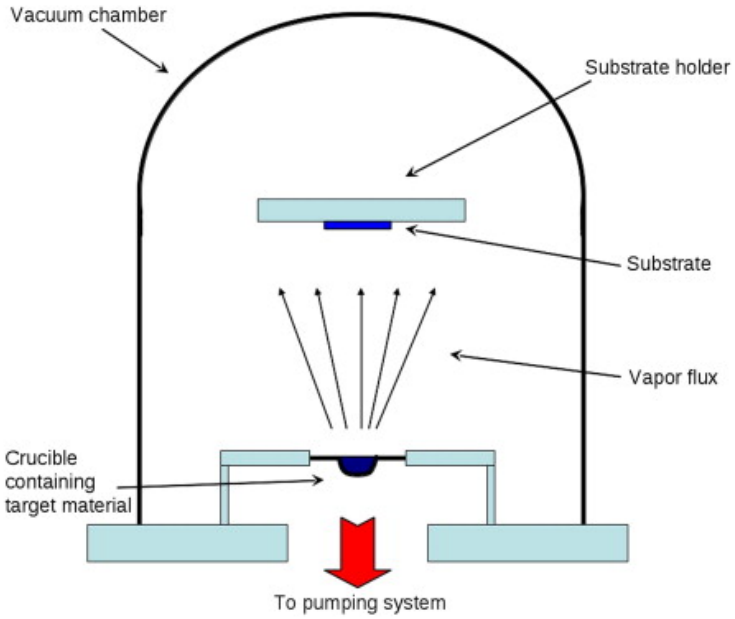

Figure 1.11: Schematic of thermal evaporation process in which the target material contained in a crucible is placed in a vacuum chamber and then heated in order to generate a vapour flux. The vapour flux condenses on a substrate to deposit material[281]

1.3 ALD for the synthesis of nanolaminates

1.3.1 History and Development of ALD

Atomic layer deposition (ALD) is a vapour phase technique that allows for sequential self-limiting growth of thin films. Originally, the method was referred to as atomic layer epitaxy (ALE). As a result of the self-limiting nature of the approach, only one atomic or molecular layer can be deposited per cycle. During the deposition process, the surface of the activated substrate becomes saturated with precursor molecules. Owing to this fact, ALD is potentially the best method for achieving growth of films with precisely controlled thickness in the nanometre and sub-nanometre range[282].

ALD is a relatively new method of thin film deposition and interestingly has been discovered twice, independently. In the 1960s, scientist Valentin Borisovich Aleskovsky[283] and his co-workers developed a technique which they called "molecular layering" in Leningrad (Lensovet) Technological Institute in the Soviet Union. Secondly, Finnish scientist Tuomo Suntola[284] and his team developed "atomic layer epitaxy" in the 1970s. Suntola and his colleagues originally developed the method with the intention of producing electroluminescent (EL) flat panel displays. The first thin film produced by this process was zinc sulfide (ZnS)[285]. This was patented by Suntola and Antson in 1977[285]. The first literature paper on the topic was published in Thin Solid Films in 1980[286]. The first commercial ALE reactor was the F-120 by ASM Microchemistry. From the years of 1983-1998, an EL display fabricated by ALE operated at Helsinki Airport[287]. This was the first public display of an ALE device. The method continued to grow in popularity in the 1980s which saw a rapid expansion of research in this area combined with the publication of many papers. When compared to other deposition methods, ALD has a relatively slow deposition rate. While some may see this as a drawback, it is a definite advantage for the miniaturisation of devices. Excellent reviews exist on ALD, notably by the researchers Professor Steven George[287] at the University of Colorado and

Professors Markku Leskelä and Mikko Ritala[288] at the University of Helsinki- all experts in the field of ALD.

1.3.2 Principles and Mechanisms of ALD

1.3.2.1 ALD principles

ALD can be considered as a modified version of CVD[287]. ALD and CVD are both very similar processes. However, the main differentiating factor between ALD and CVD is the alternate pulsing of the precursor doses in ALD which is one of the most characteristic features of the deposition technique. In CVD, the predefined mix of precursors or single precursor are introduced into the reaction chamber at exactly the same time for deposition to take place.

ALD has many advantages over other deposition methods for thin films. The self-limiting feature allows for accurate and precise thickness control of the film. Excellent conformal growth is also achievable due to this. The process can be scaled up and is capable of large-area deposition. Excellent reproducibility is seen from film to film meaning recipes can be saved and carried out numerous times. Low temperature deposition is also possible by means of plasma-enhanced ALD, meaning delicate and high quality materials can be utilised without damaging the substrate or film. Multilayer structures (nanolaminates) which possess clearly defined interfaces between the layers can be fabricated in a continuous process such as roll-to-roll ALD.

Typically in ALD, growth occurs in a cyclic manner. Gas phase precursors of choice, are introduced into the deposition chamber in order to saturate the surface. Surface species on the surface of the substrate then react with the precursor molecules in order to form new bonds. It is important to note that the precursor molecules do not react with each other. As a result of this, theoretically only one molecular layer is deposited on the substrate as steric hindrance must be taken into consideration. At this stage of the process, precursor molecules have been chemically bonded to the substrate. An inert purge gas or carrier gas then enters the chamber

in order to remove any surplus precursor or reaction by-products. The purge also prevents any unwanted gas phase reactions from taking place in the flow tubes. The process is repeated and the desired precursor is then reintroduced into the deposition chamber where it can react with the activated surface present. Note that the precursor may be the same or different to the precursor previously used which allows for growth of different materials within the one chamber and growth process. This is then repeated until the desired amount of layers with appropriate thickness has been reached. Growth should occur at temperatures which are below the gas phase thermal decomposition temperature of the precursor used. Figure 1.12 below shows a simple schematic describing the ALD process.

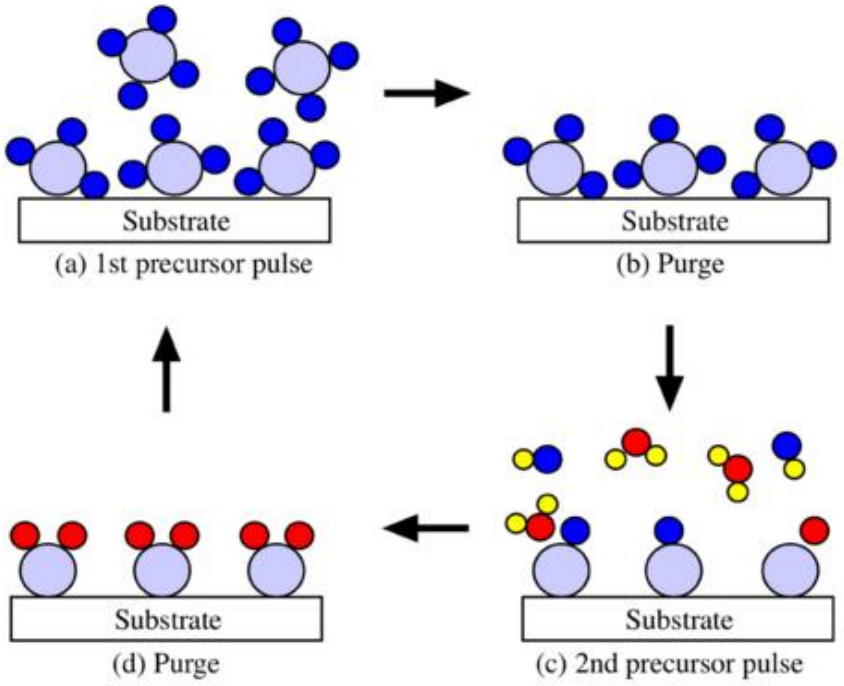

Figure 1.12: A schematic of a typical ALD process taken from reference[289]

1.3.2.2 Surface adsorption

Typical ALD models describe the growth process as successive adsorptions of precursor onto a surface. In order for an ALD process to be considered a true ALD process, the growth must occur in a cyclic, self-limiting manner. For gas-solid phase reactions, in order for the desired

self-limiting reaction and surface saturation to occur, reactants should not be capable of forming multiple layers. The saturation point of a surface is related to the chemical equilibrium associated with chemisorption in that at this point the number of chemisorbed reactant species does not increase with time. The kinetics of the surface reactions do not influence the position of the equilibrium but can affect the speed at which the equilibrium is reached. Adsorption of precursor molecules occurs via both chemisorption and physisorption mechanisms. Chemisorbed species bond with reactive surface sites. Any excess precursors that may be present can physisorb on to the chemisorbed species. A purge can be applied to break the weak physisorbed bonds and remove the unwanted physisorbed species. In an ideal ALD adsorption process only one monolayer of chemisorbed species remains and any physisorbed species are re-evaporated and extracted. There are two types of chemisorption process that generally occurs during the ALD process; (i) ligand exchange and (ii) dissociation and/or association[290].

In the equations below, *-a* is the surface group ML_n represents the precursor molecule, *M* is the central atom and *L* represents the ligands. Typically these ligands are alkyls, halides, alkoxides and β-diketones. Ultimately, MZ_x is the grown material in which Z atom of the former is provided by a second reactant such as a non-metal hydride (H_2O, H_2S or NH_3) or an oxidiser (O_2 or O_3).The symbol ‖ denotes the surface.

(i) Ligand exchange

In ligand exchange chemisorption, the reactant molecule (ML_n) is split and a ligand (L) bonds to a surface group (-a) to form a volatile gaseous by-product that is released.

$$\| - a(s) + ML_n(g) \rightleftarrows \| - ML_{n-1}(s) + aL\ (g) \tag{1.1}$$

This type of reaction can also occur in the presence of nearby active sites which results in multiple precursor-surface bonds (aL). No additional metal centres are bonded to the surface.

$$\| - a(s) + ML_{n-y-1}(g) \rightleftarrows \ \| - ML_{n-y-1} - \|(s) + aL\ (g) \qquad (1.2)$$

Ligand exchange tends to be the most favourable chemisorption mechanism as equilibrium can be driven forward towards the products as gaseous by-products are removed[290].

(ii) Dissociation and association mechanisms

In a dissociative mechanism, all fragments of precursor are either chemisorbed onto the surface or alternatively, one or more of the dissociated the fragments does not chemisorb to the surface but desorbs into the gas phase. The reactant molecule ($ML_{n)}$ is split onto the surface reactive $M' - Z$ sites.

$$\|M' - Z\|(s) + ML_n(g) \rightleftarrows \ \|M' - L(s) + \ \|Z - ML_{n-1}(s) \qquad (1.3)$$

Associative chemisorption is considered to be the rarest of the possible mechanisms. Here, a bond is formed with the precursor and the surface and no other bonds are broken. The reactant molecule (ML_n) usually forms a coordinative or dative bond with the reactive site on the surface. This bonding does not result in the release of ligands[290].

$$\| + ML_n(g) \rightleftarrows \ \| \cdots ML_n\ (\mathrm{s}) \qquad (1.4)$$

1.3.2.3 Growth per cycle

Growth per cycle (GPC) is a term used to describe the thickness achieved per deposition cycle. It is calculated by dividing the film thickness (in Angstroms (Å) or nanometres) by the number of deposition cycles. This is shown in equation 1.5 below.

$$GPC\ (nm/cycle) = \frac{film\ thickness\ (nm)}{number\ of\ cycles} \quad (1.5)$$

The GPC is determined by many contributing factors including, the deposition temperature, the partial pressure of the precursors, the number of reactive sites available, the exposure/pulse time of the precursors, the length of purge employed to remove redundant ligands and by-products and the type of substrate used. Typically growth rates of between 0.1 and 1 Å per ALD cycle are possible[288]. It is perceived that ALD growth occurs in a layer-by-layer manner with exactly one monolayer of material deposited per cycle. This is a very common misconception and often only a fraction of a monolayer is deposited per cycle. Reasons for this may be due to a limited number of reactive sites present on the surface or steric hindrance caused by bulky precursor ligands[291]. A bulky precursor with large ligands may hinder growth as it can prevent adjacent sites from reacting by blocking the active sites. Steric hindrance can cause an incomplete monolayer growth as the number of chemisorbed species is too low.

1.3.2.4 The ALD Window

Another important characteristic of the ALD deposition process is a term referred to as the ALD window. This "window" is a temperature range in which the deposition rate, as measured by the GPC, is constant. Knowing the ALD window for a given process is beneficial as it can increase the reproducibility of the thin films and also improve quality. At temperatures below this range where ideal ALD behaviour occurs, precursor molecules may condense on the surface of the substrate leading to an increase in GPC or alternatively the precursor molecules

may not have sufficient energy for the reaction to reach completion. Whereas above the ALD window temperature range, precursor molecules and also surface species may decompose and desorb leading to a decrease in GPC or alternatively CVD-type processes may occur leading to an increase in GPC[292]. Under these latter conditions the film may have impurities present. Figure 1.13 shows schematically the possible variation in GPC with temperature, adapted from Suntola[284]. In order for the identification of the ALD temperature window for a process, the film should be deposited across a range of temperatures while also varying the precursor pulse length and purge. At a fixed temperature, once the precursor pulse completely saturates the surface the GPC should cease to increase further even with an increase in the precursor pulse duration. The film thickness should also linearly increase with an increase in the number of ALD cycles. Outside of the ALD window, non-conformal and non-uniform films result.

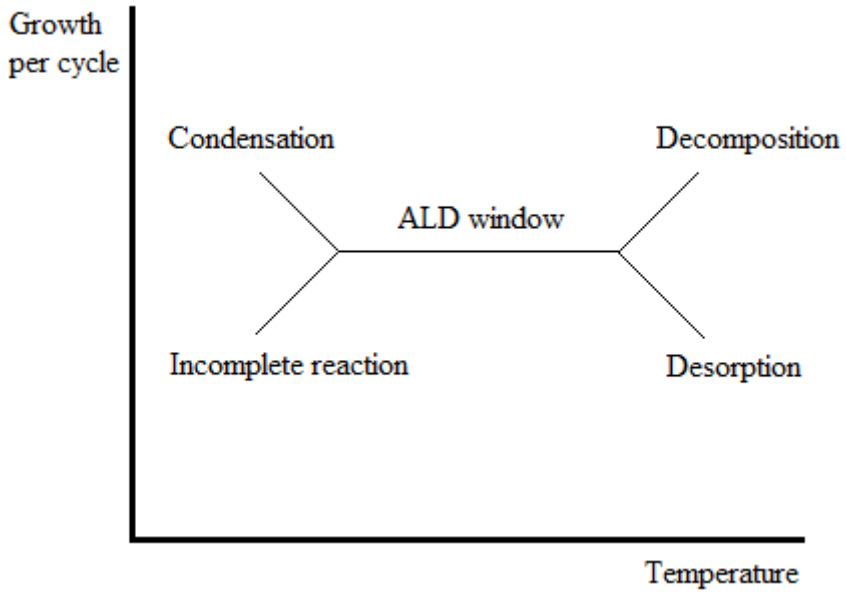

Figure 1.13: Growth per cycle vs temperature curve displaying the ALD window (Adapted from Suntola[284])

1.3.3 ALD Processes

1.3.3.1 Thermal ALD

Thermal ALD is the most reported and most used method of ALD. The definitive characteristic of thermal ALD is that the surface reactions are solely driven by thermal energy[293]. Both the reaction chamber and substrate are heated to a temperature of choice which provides the required energy for the surface reactions to take place. Typical co-reactants used are H_2O as an oxygen source to produce metal oxides and NH_3 to deposit metal nitrides. Other sources of oxygen have also been reported such as H_2O_2 and O_3 which is a particularly strong oxidant. Both hot and cold-wall reactors are utilised for thermal ALD. A hot-wall reactor, as the name suggests has a heated chamber wall, substrate and flow lines. In a cold-wall reactor, the chamber walls are not heated. The substrate and flow lines are heated however, in order to prevent condensation of precursor[287].

The thermal ALD processes for the growth of ZnO and TiO_2 are shown in equations 1.6 and 1.7 and their corresponding thermal enthalpies are given which allow for deposition to occur at various temperatures without the need for a plasma source. These reactions have negative values for the heats of reaction[287].

ZnO: $Zn(CH_2CH_3)_2 + H_2O \rightarrow ZnO + 2C_2H_6$ $\Delta H = -293$ kJ (1.6)

TiO_2: $TiCl_4 + 2H_2O \rightarrow TiO_2 + 4HCl$ $\Delta H = -67$ kJ (1.7)

1.3.3.2 Plasma Enhanced ALD

As previously discussed, thermal ALD may be the most documented variant of ALD and its mechanism has been described above. However, with the demand for improved quality of thin films and a reduction of the deposition temperature for specific applications, another branch of ALD has emerged- plasma enhanced ALD or PE-ALD. This is an atomic layer deposition

method which is rapidly gaining popularity. It allows for lower temperature processes while still providing self-limiting growth and maintaining thickness control[294]. It also allows for the elimination of H_2O from the process. This method caters for in-situ surface activation- e.g. making an otherwise inert surface such as a polymer, active towards the chemically reactive species that take part in ALD- and also allows for the use of very delicate substrates, e.g. polymers, textiles etc. A lower temperature may be required if the substrate is particularly temperature sensitive[295]. The energy to break the bonds in the substrate to chemically activate it is provided by the plasma and excluding the need for a high growth temperature. The desired precursor can then bond to the activated surface. The plasma may be applied in two ways; direct or remote. Direct plasmas (figure 1.14 a) are generated from a low pressure gas source situated in between two parallel electrodes that are placed a few centimetres apart. A voltage is applied to the top electrode and the substrate sits on the lower, counter electrode. The plasma that is generated is in extremely close proximity to the substrate. Gas is fed into the chamber containing the plasma through a gas distributor in order to improve the uniformity of the plasma. In contrast, when remote plasmas are utilised (figure 1.14 b) the plasma does not come into contact with the substrate during the reaction process[296]. Argon (Ar) or oxygen (O_2) plasma are commonly employed in such processes[297].

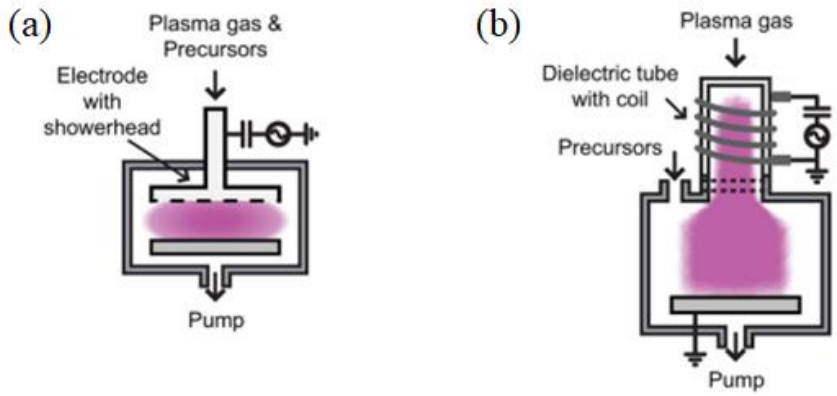

Figure 1.14: (a) Direct plasma schematic, (b) Remote plasma schematic[296]

This thesis is mainly concerned with the growth of ZnO, TiO_2 and Al_2O_3. In the following sections the properties of these materials will be summarised and previous work in the area of their deposition by ALD will be described.

1.3.4 ALD Growth of ZnO

The first material of interest, ZnO, is a wide band gap (3.37 eV) semiconductor that exists as two main crystalline structures; wurtzite (hexagonal) and zinc blende (cubic). Under ambient conditions it is the wurtzite form of ZnO that is the most stable. It is possible to stabilize the zinc blende structure by depositing the ZnO on a substrate that also has a cubic structure. The geometry for both forms has the zinc and the oxygen atoms positioned within tetrahedral centres[298]. Owing to its excellent electrical and optical properties, ZnO is utilised in many applications including thin film transistors (TFTs) and photovoltaic (PV) devices[299-311], solar cell buffer layers[312-317], organic PVs[318-324], dye-sensitised solar cells[325-327] (DSSCs) and in optoelectronic applications such LEDs in which fabrication of p-n junctions are possible with ZnO as the n-type part and GaN as the p-type part[328-336]. ZnO is an intrinsically n-type material. This was originally attributed to the presence of oxygen vacancies and zinc interstitials. More recent results have shown it is caused by other, unintentional impurities that are incorporated during film growth[337-339]. Due to the strong nature of the n-type character, it is extremely difficult to induce p-type conductivity into ZnO. The lack of p-type characteristics of ZnO hinders its use in applications such as p-n junctions that are solely fabricated with ZnO. ALD ZnO-coated SiO_2 nanoparticles have also been reported to act as a current blocking layer between junctions[328, 329, 332]. The piezoelectric properties of ZnO allow for it to be used as chemical and gas sensors[340-344]. ZnO has a large exciton binding energy of 60 meV at room temperature which makes it attractive for optoelectronic applications[345].

Doping of ZnO by ALD for the fabrication of transparent conducting oxides (TCOs) in order to improve the resistivity of the material is widely reported. TCOs are electrically conductive

materials with a comparably low absorption of light. Indium Tin Oxide (ITO) is typically used but it is limited by scarcity of Indium. ZnO is a promising material for TCOs. It is a wide band gap semiconductor and its constituent materials are abundant therefore it offers a cost effective alternative to ITO. Due to its wide band gap, doping of ZnO causes the creation of excess charge carriers[346, 347]. Albeit, one of the key requirements for TCOs in many applications is possession of a film resistivity on the order of 1 mΩ cm or lower[348]. This can be achieved with ZnO if the material undergoes cation doping from elements from group III, IV and V.

The structure of ZnO can be controlled by the deposition temperature used. Studies have shown that at deposition temperatures <70 °C, the growth is along the c-axis[349, 350]. At temperatures >100 °C, the (100) peaks becomes more evident and from 160-200 °C, (100) becomes the preferred orientation[350-354]. At temperatures above 220 °C, the preferred orientation switches to the (002) direction[353]. The ALD temperature window for ZnO can vary, even for the same precursors[345, 355, 356]. This introduces the idea that variation in reactor design plays a significant role. The precursor sequence also influences the structure of the film[357]. By having an O_2 pulse before the H_2O pulse in a DEZn/H_2O ALD process, it has been shown that the preferred orientation switches from (100) to (002)[357]. In terms of type of ALD process, for PE-ALD the GPC is more sensitive to plasma exposure and O_2 plasma is more reactive than H_2O resulting in more stoichiometric films[358]. The following sections discuss different Zn precursors for the deposition of ALD ZnO.

The first report of ZnO deposited by ALD was by Tammenmaa et al. involving zinc acetate ($Zn(CH_3CO_2)_2$) (ZnAc) and H_2O[359]. The reported GPC for ZnO deposited on soda lime glass substrate was 0.9-1.2 Å/cycle over a temperature range of 290-350 °C. ZnAc is not very volatile and requires heating up to 230-250 °C prior to deposition[360]. Lengthening the purge time to allow for element diffusion resulted in ZnO films with a (002) preference. A GPC of 0.4-3 Å/cycle was obtained on sapphire (0001) deposited at 350 °C[361].

The ZnAc/H_2O reaction proceeds as follows;

- $Zn(CH_3COO)_2^* + H_2O\ (g) \rightarrow ZnO^* + 2CH_3COOH\ (g)$ (1.8)

The symbol * denotes a surface species.

Diethyl zinc ($Zn(C_2H_5)_2$) (DEZn) is the most commonly used ALD Zn precursor. Numerous co-reagents used in conjunction with DEZn have been studied such as H_2O[349-355, 358, 362-390], O_2[357, 381, 391, 392], O_2 plasma[358, 393-397], O_3[398, 399], N_2O[400-403], H_2O plasma[396, 404, 405] and H_2O_2[390, 406]. The DEZn/H_2O reaction is exothermic and a lower deposition temperature is required than that for the ZnAc/H_2O process. An ALD window of 110-170 °C has been reported. A GPC of 1.8-2.0 Å/cycle can be achieved[382, 383, 407]. The interplanar distances for the resulting ZnO films have been reported for the (001), (002) and (100) peaks respectively as 2.48, 2.60 and 2.82 Å[351].

The DEZn/H_2O reaction proceeds as follows;

- $Zn(C_5H_5)_2^* + H_2O\ (g) \rightarrow ZnO^* + 2C_2H_6\ (g)$ (1.9)

The dimethyl zinc ($Zn(CH_3)_2$) (DMZ)/H_2O ALD process closely resembles the DEZn/H_2O process. The ALD temperature window is similar to that of DEZn although the limit of the ALD window is lower for DMZ. The GPC has been reported to be higher for DMZ than DEZn[408] at some 1.3-1.4 Å/cycle with an ALD window in the range of 120-170 °C on glass substrates. These films had a higher resistivity than films deposited using DEZn which was attributed to the presence of residual impurities incorporated into the film during deposition[354]. ZnO films deposited on Si, glass, sapphire and GaAs substrates had GPCs ranging from 1.8-1.9 Å/cycle with an ALD window of 110-180 °C[371]. The DMZ/O_2 plasma process had a higher GPC of 2.9 Å/cycle on a Si (100) substrate. The growth rate was constant between 85-120 °C. As temperature increased, (002) emerged as the preferred orientation[372].

The DMZ/H_2O reaction proceeds as follows;

- $Zn(CH_3)_2^* + H_2O\ (g) \rightarrow ZnO^* + 2CH_4\ (g)$ (1.10)

The use of zinc chloride ($ZnCl_2$) in ZnO has been found to require much higher deposition temperatures as compared to the various organic-based precursors and shows much lower deposition rates and for these reasons it is not widely used[409]. Studies have found that the $ZnCl_2$ must be heated to 390 °C while a substrate temperature of ca. 500 °C[410, 411] was required. Despite this extremely high deposition temperature, very flat and smooth films have been deposited with root mean square (RMS) values of 0.52 nm[410]. The smooth surfaces may be as a consequence of the HCl by-product that is capable of etching the surface of the film. On GaN/sapphire substrates, monocrystalline growth was observed[410]. Whereas, on soda lime glass, sapphire and Si (001) or (111) polycrystalline growth has been observed[411].

The $ZnCl_2/H_2O$ reaction proceeds as follows;

- $ZnCl_2 + H_2O \rightarrow ZnO + 2HCl$ (1.11)

ZnO films deposited by methyl zinc isopropoxide $(CH_3)Zn(OCH(CH_3)_2)$ (MZI) have required the use of a low deposition temperature yet it was found that relatively high growth rates were still achievable. However, only one study exists on this ALD process. This study reported a GPC of 1.9-2.0 Å/cycle within an ALD window of 160-200 °C[412].

Table 1.2 summarises the growth of ZnO with different precursors.

Precursor	ALD window (°C)	Growth per cycle (Å/cycle)	Reference
zinc acetate	290-350	0.9-1.2	[359]
diethyl zinc	110-170	1.8-2.0	[382, 383, 407]
dimethyl zinc	120-150	1.4	[371]
methyl zinc isopropoxide	160-200	1.9-2.0	[412]

Table 1.2: Summary of ZnO ALD processes

1.3.5 ALD Growth of TiO_2

Titanium dioxide (TiO_2), a thermodynamically stable material exists as three main crystalline polymorphs; rutile, anatase and brookite. Both anatase and brookite are metastable, whereas rutile is stable. Anatase consists of a tetragonal structure with octahedrons that share four edges forming a 4-fold axis. Rutile also has a tetragonal structure. Anatase and rutile possess band gap energies of 3.2 eV and 3.0 eV respectively[413]. TiO_2 is a well-known photocatalyst. Anatase possesses a slightly larger band gap than rutile which may be used to explain why anatase TiO_2 is a more active photocatalyst than rutile TiO_2. The larger band gap of anatase as compared to rutile also helps to improve the ability of the material to oxidise surface species when irradiated with light of energy equal to or greater than the band gap as the photogenerated holes will migrate to the surface where they can accept electrons from adsorbed species[414]. TiO_2 has been extensively studied as it is widely used in industry as a pigments in white paint and coatings[415].

The first report of ALD TiO_2 dates back to 1985 in which TiO_2-Al_2O_3 was fabricated for use as dielectrics[416]. Later work by Lakomaa et al. in 1992[417] and Ritala et al. in 1993[418] studied the growth mechanism for TiO_2 ALD. A wide variety of Ti precursors exist for the deposition of TiO_2. The use of halides such as chlorides, bromides and iodides are suitable due to their small size and low steric hindrance[282]. A drawback to their small size means they can easily be

incorporated in the growing film and therefore introduce impurities which compromises the quality of the film and also act as an unintentional dopants. The by-products released by the use of halide precursors tend to be reactive and corrosive in nature. A highly reactive by-product such as HCl may etch the surface of the film, thereby reducing the GPC. TiI_4 has been used as a Ti precursor as it has a lower bond energy[419] than $TiCl_4$ and releases ligands more readily[420-425]. Precursors with alkoxide ligands such as $Ti(OMe)_4$[426-428], $Ti(OEt)_4$[429-433] and $Ti(OiPr)_4$[434-440] have been employed. The use of metal alkylamides is also common being TDMAT[441-446] and tetrakis(diethylamido) titanium (TDEAT)[447, 448].

Titanium isopropoxide $Ti(OCH(CH_3)_2)_4$ (TTIP) is the most volatile of the reported Ti precursors for ALD[449]. The reaction between TTIP and H_2O is a self-limiting reaction within the temperature range of 200-250 °C. The reaction of TTIP and an alternative oxygen source H_2O_2 results in self-limiting growth in the wide temperature window of 100-250 °C[435]. A constant growth rate of 0.3 Å/cycle has been reported at 250-325 °C[449]. However, this study also showed that an increase in the H_2O dose resulted in an increase in growth rate to 0.6 Å/cycle[435, 450]. Above 325 °C, the precursor showed evidence of self-decomposition in the form of a departure from self-limited growth[449]. Studies have showed that during the reaction process, on average 2.2-2.5 ligands per TTIP molecule are released i.e. each TTIP molecule reacts with two hydroxyl groups during adsorption onto the film surface[435].

The TTIP/H_2O reaction proceeds as follows;

- $Ti(OCH(CH_3)_2)_4 + 2H_2O(g) \rightarrow TiO_2 + 4((CH_3)_2CHOH)(g)$ (1.12)

Metal amide precursors are more favourable for ALD reactions when compared to metal halide precursors as the bond energy of the latter is much stronger than metal amides[446]. This results in a higher reactivity for metal amides. Tetrakis(dimethylamido)titanium (TDMAT) is more reactive than titanium TTIP which allows for enhanced coverage that approaches monolayer

growth at lower deposition temperatures[443]. In contrast to this, at higher deposition temperatures, TDMAT undergoes decomposition[446]. The TDMAT/H_2O process has a reported ALD temperature window of 100-250 °C. The TDMAT ALD process with both H_2O and O_3 have a reported GPC of 0.46 Å/cycle[446, 451].

The TDMAT/H_2O reaction proceeds as follows[443];

- $Ti(N(CH_3)_2)_4 + 2H_2O(g) \rightarrow \ TiO_2 + \ 4NH(CH_3)_2(g)$ (1.13)

Titanium tetrachloride ($TiCl_4$) is a highly reactive Ti source. $TiCl_4$ is extremely reactive towards H_2O and hydroxyl groups which allows for deposition to occur over a wide range of temperatures. The mechanism for the reaction is suspected to follow that of TMA. $TiCl_4$ chemisorbs onto the film surface and undergoes irreversible exchange reactions[418].

The $TiCl_4$/H_2O reaction proceeds as follows[418];

- $TiCl_4 \ + \ 2H_2O(g) \rightarrow \ TiO_2 + 4HCl\ (g)$ (1.14)

The amphoteric nature of TiO_2 allows for the formation of both bridging and terminal hydroxyl groups. Bridging hydroxyl groups are more acidic due to polarization of cations whereas terminal hydroxyls are basic[418, 452, 453].

Reactions involving bridging Ti may also occur;

- $TiCl_4\ (g) + Ti(-O-)_2Ti\ (s) \leftrightarrow \ Ti(Cl) - O - Ti(OTiCl_3)(s)$ (1.15)

In the above reaction in equation (1.15) there is no release of gaseous product. Entropically, this reaction is less favourable. The reaction is reversible due to the proximity of the products of the reaction[454].

In addition to the reaction of hydroxyl groups with $TiCl_4$, hydroxyl groups may condense on the film surface with each other[452].

- $Ti(OH) - O - Ti(OH)(s) \rightarrow Ti(-O-)_2Ti(s) + H_2O\ (g)$ (1.16)
- $2 - Ti(OH)\ (s) \rightarrow Ti - O(s) + -Ti(s) + H_2O\ (g)$ (1.17)

The reaction in equation 1.16 occurs at low temperatures when adjacent hydroxyl groups undergo hydrogen bonding[452]. The resulting product involves the coordination of oxygen to two cations. In equation 1.17, the hydroxyl groups are isolated. The oxygen coordinates to one cation and is co-ordinately unsaturated. This reaction is less favourable as it requires proton migration to occur before dihydroxylation can take place[452]. This explains to some extent why the reactivity of $TiCl_4$ is found to be temperature dependent as various configurations and densities of hydroxyl groups exist at different temperatures[452].

It has been reported that the adsorption of HCl onto the surface of the film further complicates the reaction mechanism as competitive, simultaneous reactions are occurring[455].

- $Ti - OH(s) + HCl\ (g) \leftrightarrow Ti(H_2O) - Cl\ (s)$

  $\leftrightarrow TiCl(s) + H_2O\ (g)$ (1.18)

- $Ti(-O-)_n(s) + HCl\ (g) \leftrightarrow Ti(OH) - O - Ti - Cl(s)$ (1.19)

$(n = 1 - 3)$

For the above reactions (equations) 1.18 and 1.19, the equilibria shown are believed to occur at lower temperatures for a rutile TiO_2 surface[455]. At low temperatures, residual Cl has been reported to increase the surface adsorption of H_2O. In contrast, at high temperatures residual Cl assists the dihydroxylation process[453].

The titanium ethoxide ($Ti(OEt)_4$)/H_2O ALD reaction proceeds as follows[429];

- $Ti(OCH_2CH_3)_4 + 2H_2O\ (g) \rightarrow\ TiO_2 +\ 4CH_3CH_2OH(g)$ (1.20)

It is also thought that the ethanol formed may undergo dehydration[429].

An alternative mechanism involves the chemisorption of $Ti(OEt)_4$ followed by hydrolysis after the introduction of water causes complete dehydroxylation of the surface[456], as shown below:

- $Ti(OCH_2CH_3)_4(g)\ \rightarrow\ Ti(OCH_2CH_3)_4(s)$ (1.21)

- $Ti(OCH_2CH_3)_4(s) + 2H_2O\ (g)$

$\rightarrow\ TiO_2(s) +\ CH_3CH_2OH(g)$ (1.22)

Table 1.3 summarises the growth of TiO_2 with different precursors.

Precursor	ALD window (°C)	Growth per cycle (Å/cycle)	Reference
titanium isopropoxide	200-250	0.3	[449]
tetrakis(dimethylamido) titanium	100-250	0.46	[446, 451]
titanium tetrachloride	100-150	0.07	[418]
titanium ethoxide	300	0.03-0.04	[429]

Table 1.3: Summary of TiO_2 ALD processes

1.3.6 ALD Growth of Al_2O_3

Al_2O_3, commonly called alumina is an electrical insulator with a relatively high thermal conductivity for a ceramic material of 30 $Wm^{-1}K^{-1}$. It exists naturally as various minerals including corundum, which is thermally stable and bauxite which is considered as the principal aluminium ore[457]. Due to the materials bio-inertness, chemical properties and hardness, Al_2O_3 is used widely across a myriad of medical applications including bearings for hip replacements, bionic implants, dental implants and prostheses[457].

The most commonly used Al precursor in ALD is TMA. The ALD chemistry of this precursor is the most studied and documented in literature. The precursor itself is cheap and readily available. Puurunen has published an extensive review particularly studying the TMA/water ALD process[291]. The reaction is understood as two successive "half reactions" as shown below in equation (1.23) and (1.24).

$$\| Al - OH(s) + Al(CH_3)_3(g) \rightarrow \| Al - O - Al(CH_3)_2(s) + CH_4(g) \quad (1.23)$$

$$\| Al - CH_3(s) + H_2O(g) \rightarrow \| Al - OH(s) + CH_4(g) \quad (1.24)$$

The surface species present during the reaction switch from methyl-terminated to hydroxyl-terminated. This has been proven by transmission Fourier transform infrared spectroscopy (FTIR) in which the AlO-H and AlC-H_3 stretching vibrations were monitored. In each case, the spectra showed each reaction to be self-limiting and to go to completion. As previously mentioned, the TMA/water ALD process is known to be an "ideal" ALD process. Self-termination has been proven as longer pulse and purge times do not change the amount of surface species that is adsorbed. The GPC does not increases with increased exposure time.

Although TMA is the most widely reported Al precursor, it is highly reactive which makes it difficult for doping. It is too reactive to achieve a low surface density of Al atoms. As a

consequence alternative Al precursors have been explored. Aluminium isopropoxide (AIP) has been used as an Al precursor for Al-doped ZnO. AIP is a solid at room temperature. The temperature of the precursor is controlled at the source which can then allow for control of the Al atoms present in a single dopant layer. Increasing the AIP source temperature from 115-130 °C resulted in a decrease in GPC from 1.47 to 1.27 Å/cycle attributed to a reduction in DEZn adsorption on Al_2O_3 surface[458].

Dimethylaluminium isopropoxide (DMAIP) is a bulky Al precursor which presents a compromise in terms of reactivity and volatility. Al atoms can be dispersed more widely on the surface sites due to the steric hindrance of the isopropyl ligands. Films deposited this way are found to possess higher conductivities due to the presence of higher densities of active dopant[459]. Films fabricated using DMAIP also had lower resistivity than those grown using TMA, some 3.5 mΩ cm as compared to 8 mΩ cm[460].

1.4 Properties and applications of nanolaminates of Al_2O_3, TiO_2 and ZnO

In order to make it applicable to the work in this thesis, the following section is a non-exhaustive review of the applications of nanolaminates exclusively containing Al_2O_3, TiO_2 and ZnO focusing on the application areas of electronics, mechanical fundamentals, optics and encapsulation.

Al_2O_3 is an excellent insulator with a large band gap[461]. As previously mentioned, ZnO and TiO_2 possess close band gap energies and exhibit similar photocatalytic degradation mechanisms suggesting that they may be suitable materials to be coupled together[462, 463].

Over the period 2014 to 2020 there has been a surge of interest in nanolaminates based on the materials in question leading to a myriad of potential applications. In terms of innovative devices, nanolaminate structures are increasingly important. An extensive and notable review exists on the topic of nanolaminate composite materials by Azadmanjiri and Berndt[27, 29]. This review highlights the unique properties of these materials including chemical, electrical, mechanical and physical properties. The following section builds on the information presented in the review by Azadmanjiri and Berndt and includes the most recent developments in terms of applications of the nanolaminates in question.

1.4.1 Electronic applications of nanolaminates of Al_2O_3, TiO_2 and ZnO

Metal oxide nanolayers of Al_2O_3, TiO_2 and ZnO have been deposited for use in devices such as organic field-effect transistors (OFETs) and thermoelectric devices. In particular driven by the limitations associated with the use of SiO_2 as a gate dielectric in a transistor structures, Al_2O_3 and TiO_2 have been studied extensively[464].

Baek et al.[464] demonstrated the growth of Al_2O_3/TiO_2 nanolaminate gate dielectric films for use in OFETs. Compared to a separate film of Al_2O_3 or TiO_2 not part of a laminate structure, the fabricated films had highly smooth surfaces (R_q < 0.3 nm), low leakage currents (8.6 x 10^{-9}

A/cm^2 at MV/cm) and high dielectric constants (17.8). The enhancement of the dielectric constant (2.3 times that of Al_2O_3) was due to the incorporation of the Ti^{4+} cation, which is highly polarizable. A dramatic improvement in μ_{FET} when implemented into a pentacene-based OFET was observed for 50 nm thick nanolaminate films in comparison to the use of single Al_2O_3 or TiO_2 films. A higher κ can cause attraction of mobile charge carriers into the channel and allow for traps to be filled nearby at the interface of the layers. As a result, the consensus of this study was that the nanolayered structure removes the drawbacks associated with the use of single material layers.

Al_2O_3/ZnO nanolaminate films were fabricated by Lee et al.[465] in order to investigate the thermoelectric properties of the films in which the thickness of the inserted Al_2O_3 layer differed between growths. While the overall composition remained the same (2% ZnO: Al), the nanolaminate structure was altered from deposition to deposition by changing the Al_2O_3 and ZnO ALD sequence. The Al_2O_3 thickness increased in increments from 0.13 nm to 1.23 nm. As the Al_2O_3 thickness increased, thermal conductivity decreases from 0.57 W/ mK to 0.26 W/ mK. This decrease may have been caused by the interface, whether it be interface scattering of phonons or interface confinement.

Liu et al.[466] studied the effect of annealing on the structural and optical properties of ZnO/Al_2O_3 superlattice structures grown by ALD for future practical electrical device applications. A nucleation delay was observed for ZnO and it was found that at least 6 ALD cycles (~1.10 nm) was required for growth. XRD revealed that the orientation of the ZnO crystallites was affected by altering the cycle ratios of Al_2O_3: ZnO. Changing the cycle ratio cause the orientation to switch between the c-axes lying perpendicular or parallel to the substrate. Annealing the films resulted in atomic diffusion and recrystallization. The diffusion of Zn atoms in the amorphous Al_2O_3 layers was found to be much faster than that of Al atoms in the ZnO crystallites at higher temperatures. This resulted in complete dissociation of ZnO in the films with thicker Al_2O_3

layers. This was evident due to the disappearance of its absorption bands in optical measurements.

Cao et al.[467] demonstrated the growth of ZnO/TiO_2 nanolaminates for use as ultra-long-life anode material for lithium-ion batteries (LIBs). ZnO/TiO_2 nanolaminates were fabricated that were more stable than pristine ZnO films when subjected to an electrochemical cycling process. The reversible capacity and the rate performance of ZnO films were found to be greatly enhanced after the insertion of TiO_2 layer into the ZnO film. Notably, the ZnO/TiO_2 nanolaminates fabricated exhibited excellent ultra-long-life performance which were capable of retaining a reversible capacity of ~667 mAh g^{-1} in a potential range of 0.05–2.5 V. Almost no decay was observed after 1200 cycles of charge-discharge at 500 mA g^{-1}. Electrochemical impedance spectroscopy (EIS) measurements indicated that the formation of a nanolaminate structure decreased the solid electrolyte interface (SEI) resistance and charge-transfer resistance, in addition to improving the solid state Li^+ ion diffusion in the bulk electrode. The results of this study imply that constructing layered nanolaminates structures by ALD might open up new windows for the improvement of the performance of anode materials in LIBs.

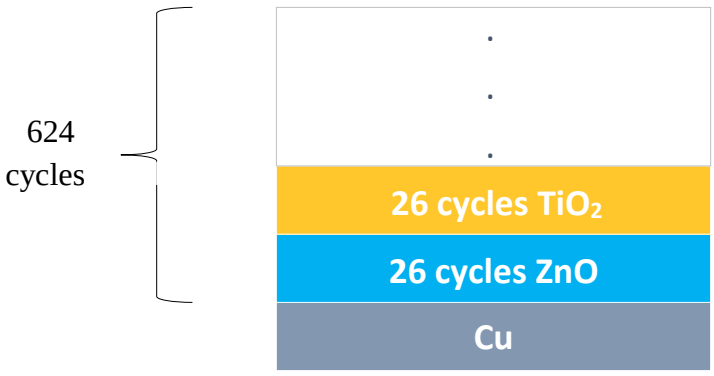

Figure 1.15: ZnO/TiO_2 nanolaminates for use as ultra-long-life anode material for lithium-ion batteries adapted from Cao et al.[467]

1.4.2 Mechanical properties of nanolaminates of Al_2O_3, TiO_2 and ZnO

Berdova et al.[468] studied the micromechanical properties of suspended ALD Al_2O_3, mixed oxide ($Al_xTi_yO_z$) and Al_2O_3/TiO_2 nanolaminate films. Bulge and MEMS shaft-loading methods were applied. Table 1.4 presents the results of the tests. As TiO_2 is incorporated, the strength of materials decreases with incorporating TiO_2 layers, which might be explained by the fact that TiO_2 has lower fracture toughness than Al_2O_3 and as a result, lower strength. This work highlighted the potential use of nanolaminates for micro- and nanosystem applications ranging from IR detectors, micro hot plate sensors, X-ray windows and large stroke mechanical actuators.

Thin film	**Residual stress (MPa)**	**Young's modulus (GPa)**	**Tensile strength (GPa)**
Al_2O_3	347-403	164-165	1.57-2.56
$Al_xTi_yO_z$ mixed oxide	365-389	151-154	1.17-2.09
Al_2O_3/TiO_2 nanolaminate	450-455	148-169	1.23-2.26

Table 1.4: Residual stresses, Young's modulus and tensile strength obtained by bulge and MEMS shaft-loading techniques[468]

The focus of the following work by Homola et al.[469] was to study the effects of bilayer period (λ) on the mechanical properties of the Al_2O_3/ZnO nanolaminate films. A closer look was taken at the effect of the ratio between the thicknesses of each material while λ was kept constant. As λ decreased, hardness also decreased as a result of a change in the deformation mechanism from dislocation-based to grain boundary sliding mechanism. The study reported that an Al_2O_3 thickness of 1 nm is all that is required to disrupt the growth of ZnO. The disruption lead to finer ZnO crystallite sizes as the material underwent re-nucleation.

Fundamental properties such as film thickness, chemical composition, microstructure and morphology of the TiO_2/Al_2O_3 nanolaminates were examined by Testoni et al.[470] to gauge a better understand on the influence of the particular number of Al_2O_3 partial-monolayers has on the TiO_2 crystallization mechanism. It was found that by depositing only one cycle of trimethyl aluminium-water (TMA–H_2O) in the supercycle of TMA–H_2O and TTIP–H_2O, the structure of the TiO_2 chemical composition could be precisely controlled. The morphology in the TiO_2/Al_2O_3 nanolaminate structure could also be controlled by adjusting the number of Al_2O_3 partial-monolayers. Mass spectrometry provided evidence for the poisoning effect of the TMA pulse had during the growth of the TiO_2 layer, perturbing the surface environment and leading to a reduction in GPC. The nanolaminate structure is of great interest as it allows for control over the crystal structure without needing high process temperatures. Such high temperatures can often lead to drastic changes in intrinsic properties such band gap energy. At low temperatures, TiO_2 is thermally unstable which is not desirable from a device point of view. However, incorporating it into a nanolaminate structure creates a stable amorphous structure that is of use for many microelectronic applications[470].

Coy et al.[471] deposited Al_2O_3/TiO_2 nanolaminates in order to study the wear rate of the structures for further applications. It was found that as the thickness, size of crystallite and increment of amorphous interfaces all reduced, the mechanical properties of the film were directly influenced. A certain thickness of bilayer and stack was found to be required in order to see altered behaviour due to the layered structure as below a critical value (~25 nm), nanocomposite coating behaviour was observed. In terms of mechanical properties, the maximum reduced modulus (E_r) and hardness (H) were located in the region closer to the surface of the nanocomposite[471].

1.4.3 Optical properties of nanolaminates of Al_2O_3, TiO_2 and ZnO

Nanolaminates are very attractive for the investigation of potentially interesting optical properties. Combining complementary metal oxides can lead to performance that cannot be achieved by either component alone. Optically, this could be extremely beneficial in terms of the development of new or improved devices.

Viter et al.[472] fabricated Al_2O_3/ZnO nanolaminate films for application in aerospace technologies as ultra-thin nanolaminates possess a high resistance against high energy particles and ultraviolet radiation. It was found that as the number and thickness of the bilayers decreased, the optical absorption peak decreased in intensity and underwent a blue shift. This behaviour was found to correlate with the formation of a disordered structure, as supported by a lack of peaks in the XRD pattern.

The RI and band gap behaviour of Al_2O_3/ZnO nanolaminates was studied by López et al.[473] It is important to understand the optical behaviour of thin films of Al_2O_3 and ZnO as a consequence of their use in a range of optical devices. In the case of the study by López et al., the optical properties of the bilayers studied were found to strongly depend on the bilayer thickness. As the bilayer thickness increases from 2 to 22 nm, the RI (λ = 370 nm) fluctuated between 1.63 and 2. By analysing a Tauc plot, the band gap was found to vary from 3.3 to 4.9 eV. These results demonstrate that nanolaminates provide the opportunity to fine tune the RI and band gap of a material as a function of layer thickness and composition.

Romo-Garcia et al.[474] fabricated Al_2O_3/ZnO nanolaminates by ALD to study the optoelectronic attenuation behaviour of the films. All films had a total thickness of 20 nm. The Al concentration varied from 1, 3 and 5% of the total thickness of the stack. XPS results revealed that it was possible to design nanolayered materials with individual layers with thicknesses of less than 1 nm and obtain high precision at the interface. The thickness of the bilayers also

contributed to the control of the optoelectronic attenuation. The intensity of the main emission from ZnO was increasingly quenched with increasing the thickness of Al_2O_3 layer. In this way it was possible for the ZnO emission to be attenuated from between 37% and 68%. It should be noted that despite the reduction of electronic transitions on the nanolayered film, a shift in the band-to-band emission of ZnO was not observed. Studies of this type further demonstrate the potential of using Al_2O_3/ZnO nanolaminates in the development of new or improved optoelectronic devices.

1.4.4 The use of nanolaminates of Al_2O_3, TiO_2 and ZnO for encapsulation and passivation

Interestingly, at the time of writing, encapsulation and passivation are the main nanolaminate application areas of focus and where the bulk of the publications lie in terms of the use of nanolaminates. Encapsulation involves the confinement of one material by another larger material. Passivation is a surface modification method that allows for protection of an active surface from the surrounding environment. The surface becomes "passive'' or less active via chemical means. Deposition of a thin film encapsulation layer can act as a barrier layer.

The use of an Al_2O_3 thin film as a moisture barrier layer has been reported by Jung et al.[475]. However, amorphous Al_2O_3 is susceptible to corrosion caused by water which means it is not appropriate for use in high humidity conditions. To overcome this, Abdulagatov et al.[445] have fabricated TiO_2/Al_2O_3 bilayers to encapsulate copper in order to prevent corrosion. A bilayer structure of TiO_2/Al_2O_3 was found to resist water corrosion. Although this is an innovative step forward as TiO_2 is known to provide resistance to water corrosion, it is not a long-term solution. TiO_2 is not a practical gas barrier so over time it is possible for gas molecules to diffuse into the Al_2O_3 layer.

Kim et al.[44] fabricated Al_2O_3/TiO_2 films for the purpose of encapsulation of organic thin films transistors (OTFTs). The aim was to produce films with excellent water anticorrosion and low gas permeation at a low-temperature process. The passivation of an OTFT using a 50 nm thick Al_2O_3/TiO_2 nanolaminate structure was found to have a prolonged lifetime which exceeded 52 days.

Al_2O_3/TiO_2 diffusion barriers were grown by Singh et al.[45] for organic light emitting diode (OLED) encapsulation. The fabrication involved depositing nanolaminates in which ozone was the oxygen source during the ALD growth first, followed by water based nanolaminates on top in which water was the oxygen source. This work achieved the deposition of nanolaminate diffusion barriers that enhanced the lifetime of the OLED and also did not damage the OLED during fabrication.

Arroval et al.[476] demonstrated the growth of $Ti_xAl_{1-x}O_y$ films in order to explore the passivation effect of the Ti precursor, $TiCl_4$ towards the chemisorption of Al precursors, TMA and $AlCl_3$. The deposition rate of Al_2O_3 was analysed and was found to be lower in the $TiCl_4$-TMA-H_2O and $TiCl_4$-$AlCl_3$-H_2O processes than that in the $TiCl_4$-H_2O-TMA-H_2O and $TiCl_4$-H_2O-$AlCl_3$-H_2O processes, respectively. The adsorption of $TiCl_4$ was limited by the surface intermediate species. This intermediate species only partially limited the adsorption of $AlCl_3$ and TMA. The growth rate of TiO_2 was enhanced in the $TiCl_4$-TMA-H_2O and $TiCl_4$-H_2O-TMA-H_2O processes. Additionally, the growth rate of Al_2O_3 was enhanced in the $TiCl_4$-H_2O-TMA-H_2O and $TiCl_4$-TMA-H_2O processes as the deposition temperature was >300 °C. No increase in growth rate was observed for the TMA-H_2O process which suggested that the effect was influenced by the Ti-containing surface layer on the adsorption of TMA precursor molecule.

The use of Al_2O_3/ZnO nanolaminates for thin-film encapsulation for flexible organic light-emitting diodes (FOLEDs) was studied by Jeong et al.[47] Tensile stress conditions were tested

in order to investigate potential long-term reliability. After 30 days the passivated FOLEDs had comparable performance to the initial state without the formation of any dark spots. These results showed that the encapsulation of FOLEDs was successful and nanostructured layers of Al_2O_3/ZnO act as excellent moisture barriers.

Nehm et al.[48] investigated the growth of TiO_x/AlO_x nanolaminates as moisture barriers for organic devices such as OLEDs. The organic devices display extreme degradation upon exposure to moisture. Single, stand-alone layers of metal oxides have been reported to fall short in terms of chemical and mechanical stability. By using a nanolaminate barrier, the stress on the film can be reduced and the lifetime of these organic devices can be prolonged. The study found the optimum individual layer thickness to be 1-2 nm which was then used to build nanolaminate structures up to 100 nm total thickness. Single layer thicknesses ranging from 4-8 nm lead to an unstable barrier film. The films were subjected to aging in ambient conditions to examine to longevity of the nanolaminate barrier films. Even after 2500 hours of continuous aging, the nanolaminates showed no significant degradation.

ALD Al_2O_3/TiO_2 nanolaminates were fabricated by Leppäniemi et al.[49] in order to improve the sealing properties and corrosion protection of chromium nitride (CrN) coatings deposited using physical vapour deposition (PVD) on high speed steel (HSS). The ALD nanolaminates sealed pinholes present on the CrN coating. By increasing the thickness of the Al_2O_3/TiO_2 bilayer from 50 to 100 nm, pinhole sealing and corrosion protection was further enhanced. Plasma pre-treatment prior to ALD deposition was found to also improve the corrosion protection and particularly the adhesion of the ALD layer.

The tribocorrosion behaviour of TiO_2/Al_2O_3 nanolaminates was investigated by Radi et al.[50] for orthopaedic corrosion protection. Tribocorrosion is explained as the degradation of a material as a consequence of both corrosion and wear. This research presented the idea of using

nanolaminate films for the fabrication of *in vivo* sensors to reduce the time for the detection of diseases e.g. cancer. An exemplary *in vivo* sensor should be biocompatible, non-toxic, extremely sensitive and stable, similar to a coating for orthopaedic implants. The results of the study showed that the TiO_2/Al_2O_3 nanolaminate films had a low friction coefficient and were suitable for application in orthopaedic applications.

Table 1.5 summarises the nanolaminate materials with their corresponding lifetimes.

Material	**Lifetime**	**Reference**
Al_2O_3/TiO_2	>52 days	Kim et al.[44]
Al_2O_3/TiO_2	>2100 hours	Singh et al.[45]
Al_2O_3/ZnO	>30 days	Jeong et al.[47]
TiO_x/AlO_x	>2500 hours	Nehm et al.[48]

Table 1.5: Lifetimes of nanolaminate materials for encapsulation and passivation applications

1.4.5 TiO_2/ZnO nanolaminates

In particular and in direct relation to the results presented in this thesis, this section focuses specifically on previous studies involving the deposition of TiO_2/ZnO nanolaminates and alludes to why these materials may be ideally coupled.

ZnO and TiO_2 are both active photocatalysts, chemically and thermally stable, low in cost and are widely available[477, 367]. Both ZnO and TiO_2 are wide band gap semiconductors with band gap energies in the region of 3.2 eV – 3.4 eV[462, 463]. The similar band gap energies of TiO_2 and ZnO and the similarity in photocatalytic mechanisms that these materials exploit suggest TiO_2 and ZnO as suitable materials to be coupled together. Another interesting point to observe is the interactions that occur at the interface of the layers[478]. It is possible to fabricate

multifunctional films by combining different materials that possess varying capabilities such as well-known photocatalysts mentioned above, ZnO and TiO_2. It is interesting to consider whether the functionalities will both act together and be enhanced or degraded.

Previous studies have shown an improvement in crystallinity and quality of ZnO as a direct consequence of a TiO_2 under layer[479]. In addition such studies have shown improved degradation of organic dyes[480, 481] and enhanced friction coefficients[482]. Interestingly, as the number of bilayers increased while the total thickness and composition of the films remained the same, an enhancement of the optical transmittance was observed[483, 484]. Analysis of the X-ray diffraction (XRD) spectra of these nanolaminates revealed weaker signature peaks for the same thickness nanolaminates with more bilayers, suggesting the possibility of tuning the crystallinity of nanolaminates from a crystalline to an amorphous phase. Films with the same overall thickness showed a decrease the refractive index (RI) as the number of bilayers decreased[484].

ZnO/TiO_2 laminates have been prepared previously using various deposition techniques such as electron-beam (E-beam) evaporation[485], sol-gel methods[480,481], atomic layer deposition (ALD)[482, 483, 486] and more recently spatial ALD[484].

Table 1.6 summarises previous work that has been carried out on ZnO/TiO_2 laminates, including various different methods of deposition.

Method	Precursors	Growth Temperature (°C)	Reference
E-beam evaporation, sol-gel	High purity (99.999%) ZnO & TiO_2 particles, $Zn(CH_3CO_2)_2$ & monoethanolamine	200, 250	Xu et al. 2008[485]
Sol-gel	Titanium(IV) butoxide, $Zn(CH_3CO_2)_2$	RT	Tian et al. 2009[480]
ALD	TTIP, DEZn, de-ionised H_2O	200	Gu et al. 2013[483]
ALD	TTIP, DEZn, de-ionised H_2O	200	Qian et al. 2013[486]
ALD	$TiCl_4$, DEZn, de-ionised H_2O	200	Wang et al. 2014[482]
ALD	$TiCl_4$, DEZn, de-ionised H_2O	100	Su et al. 2015[487]
ALD	$TiCl_4$, DEZn, de-ionised H_2O	120-240	Torrisi et al. 2016[488]
Spatial-ALD	$TiCl_4$, DEZn, de-ionised H_2O	150	Chen et al. 2016[484]
Sol-gel	TTIP, IPA, de-ionised H_2O $Zn(CH_3CO_2)_2 \cdot 2H_2O$, NaOH	RT	Prasannalakshmi et al. 2017[481]
ALD	$TiCl_4$, DEZn, de-ionised H_2O	130	Cao et al. 2019[467]
ALD	$TiCl_4$, DEZn, de-ionised H_2O	100	Wang et al 2020[489]

Table 1.6: Previous work on ZnO/TiO_2 laminates via E-beam evaporation, sol-gel, ALD and spatial-ALD deposition methods

Table 1.6 summarises previous work that has been carried out on ZnO/TiO2 laminates, including various different methods of deposition. From the table, it is clear that ALD is the most used deposition method for the growth of ZnO/TiO2 laminates. ALD presents many advantages over these other methods. ALD allows for the following; precise thickness control and a high degree of uniformity, both owing to the self-limiting nature of the reaction. A high

level of conformality, is achievable meaning high aspect ratio compatible growth. Growth at relatively low temperatures is possible which is suitable for applications in which a thermal restraint exists.

1.5 Doping of ZnO thin films

1.5.1 Advantages of doping by ALD

Doping of materials allows for manipulation of the composition and structure that impact properties such as the electrical and optical behaviour of the material. ZnO is frequently doped and to date, some 22 elements have been reported as dopants in ZnO by ALD[490] (figure 1.16). Many publications exist where a variety of different elements have been used as dopants. By far, Al is the most popular choice.

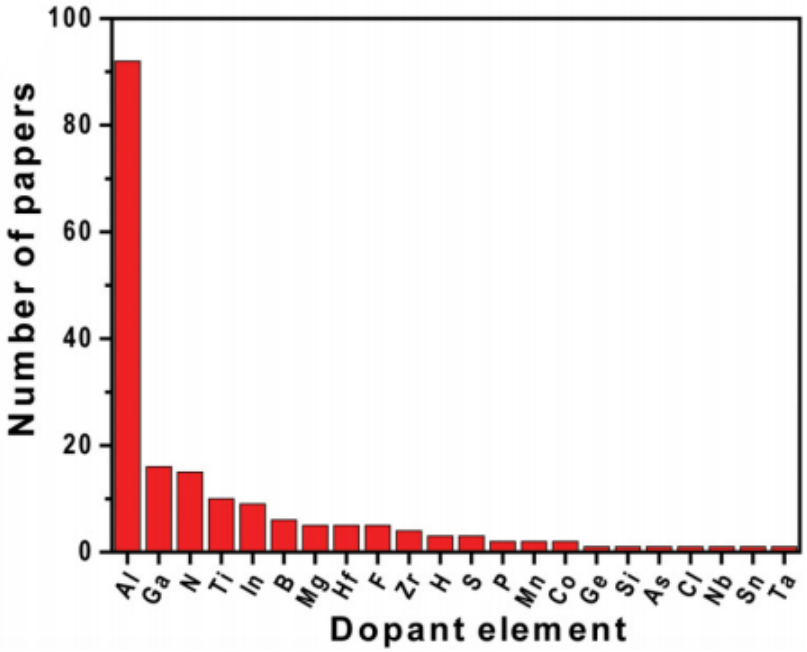

Figure 1.16: Bar chart displaying the number of papers versus the dopant element used in doping of ZnO via ALD. Al is the most frequently studied dopant followed by Ga, N, Ti, and In[490]

Doped thin films can be fabricated by many methods, all carrying both pros and cons. The most popular methods of doping have been CVD and PVD. In the case of PVD, sputtering is the most commonly used. Using these methods, Al-doped ZnO thin films have been prepared with resistivity values of 0.1 mΩ cm achieved[491].

However, in comparison, ALD presents many advantages over these methods and is a particularly suitable deposition method when the application of these thin films are considered. ALD allows for: (i) precise thickness control due to the self-limiting, cyclic manner of the reaction, (ii) a high degree of uniformity again owing to the self-limiting nature of the reaction, (iii) a high level of conformality, meaning high aspect ratio compatible growth, (iv) growth at relatively low temperatures which is suitable for applications in which a thermal restraint exists and finally, which is particularly advantageous for doping, (v) the cyclic, self-limiting manner which allows for precise thickness control can theoretically allow for accurate control over the dopant level[287, 491]. The following section describes how ALD has been used previously to dope the material of interest to this thesis- namely ZnO.

1.5.2 ALD Doping of ZnO - distribution and efficiency of the added dopant ions

In spite of the advantages of doping thin films via ALD, for ZnO doping in particular, drawbacks to the method exist and ALD doping presents its limitations. One of the main reasons for doping a material in the first place is to enhance a particular property of said material. However, this is not always as straightforward as might be expected. For example there are reports which show the etching effect dopants can have, thereby reducing the overall growth rate of the film and the efficiency of the doping process[492].

Elam et al. were the first to report the etching effect TMA has on ZnO films. This was proven by the nominal thickness being larger than the actual thickness measured[492]. This etching phenomenon has also been seen during ZnO growth when doping with trimethyl indium (TMI).

Lee et al. reported that for In-doped ZnO films, film growth rate decreased with increasing In_2O_3 ALD cycle ratio[493]. Interestingly, it has been reported that it takes approximately 6 cycles of ZnO growth via DEZn and H_2O in order to recover 63% of the original growth rate of ZnO[494]. As well as seeing decreased growth rates for doped ALD films, increased growth rates have also been observed. This is the case for ALD studies of the Ti- doping of ZnO using the titanium precursor TTIP. Adsorption of TTIP appears to accelerate the overall ZnO growth rate[495].

Wu et al.[491] have extensively studied the Al distribution in ALD-prepared ZnO: Al and the effect on doping efficiency. It was shown that the anticipated improvement in the resistivity of the resulting Al-doped ZnO was somewhat limited. Varying the Al doping level, defined as the proportion of Zn atoms that are replaced by Al, improved the resistivity from 9.8 mΩ cm to 2.2 mΩ cm. While this was a significant improvement in resistivity, the value achieved overall was still well below the level of 1.0 mΩ cm or lower that is usually required for device applications.

ZnO films utilising ALD supercycles (section 2.2.3) are perceived as flat δ-doped layers, when in reality a broadening of dopant layers may occur. The term 'δ-doping' is often oversimplified. Broadening of the Al-dopant layers may occur due intermixing effects. While diffusion of Al atoms into the ZnO is possible, it can only happen once the activation energy for diffusion has been reached. This would require annealing above 800 °C[496, 497]. As noted earlier, an etching effect is observed with the TMA precursor and the ZnO surface[492]. Effectively, Al atoms replace the Zn atoms causing a downward spreading of the Al atoms which in turn may lead to broadening of the Al-dopant layer. The influence of surface roughness due to the polycrystalline nature of ZnO and the presence of grain boundaries also play a role in the inhomogeneous distribution of Al atoms. Inactive Al atoms can act as scattering centres which in turn affect the electrical transport properties of a material such as the carrier mobility and

the carrier density. The presence of Al enrichment at the grain boundaries has been associated with the formation of Al suggests trapping centres[491].

The spacing between dopant layers has also been shown to be very important. Lee et al. have shown that an optimal spacing of 2.3 to 2.6 nm is desirable for their doped films. It was reported in this work that the Al-doping occurs predominately at the interface. An electric field is created by the Al^{3+} atoms which prevents further doping as the electric field results in Coulombic forces between Al^{3+} atoms. These repulsive forces gave rise to a decrease in doping efficiency when the electric fields overlapped as a consequence of dopant layers being too close together[498]. The relationship between each adjacent Al atom within a single dopant layer also must be considered. Studies on the lateral relationship of the Al atoms have shown that by increasing the lateral spacing between the Al atoms, the doping efficiency can be increased while also decreasing the resistivity. Wu et al. showed Al-doped ZnO to be most efficient when the lateral spacing between Al atoms was >3.8 nm[491, 499]. In order to achieve an increase in the lateral spacing, fractions of the surface functional groups were deactivated using ethanol. Another study used the bulky Al precursor, DMAIP in place of TMA to take advantage of steric hindrance to block active sites to decrease the number of Al atoms deposited per ALD cycle[459].

The solid solubility limit of Al in ZnO also plays a role in determining the doping efficiency. The solid solubility limit of Al in ZnO is low as Zn and Al exhibit different properties including ionic radii and oxidation. If the local Al density is below the solubility limit, Al atoms can be substitutionally incorporated into the Zn sites within the ZnO matrix and act as electron donors. In contrast, if the local Al density is above the solubility limit, a portion of the Al atoms may form clusters of AlO_x, $ZnAl_2O_4$ or equally segregate to the grain boundaries. As a consequence, these particular Al atoms are unlikely to behave as electron donors which in turn lowers the doping efficiency. Clusters may also form at interface when the interspacing between layers is < 3.8 nm[491, 499].

It is reported that doping efficiency at higher doping levels is reduced due to disorder-induced carrier localization. Both intrinsic and extrinsic defects can induce a defect in the crystal structure. A high local Al density will result in low doping efficiency as scattered electrons that are weakly localized are limited in their contribution to conductivity[500-502].

1.5.3 ALD growth of Al-doped ZnO

Aluminium-doped ZnO (AZO) is the most extensively studied of the metal-doped ZnO films. AZO is low cost and its constituent elements are abundant. The material has increased stability when compared to ITO, particularly in a reducing atmosphere such as the presence of a hydrogen plasma. The electrical conductivity of AZO is comparable to that of ITO[503]. AZO behaves excellently optically, with almost 100% transmittance in the visible region[504, 505]. In the IR region[505], AZO is more transparent than ITO[506]. The atomic radius of Al^{3+} is 0.53 Å which is smaller than that of Zn^{2+} (0.74 Å)[507]. This allows for Al^{3+} to easily occupy the place of Zn^{2+} causing an overall reduction in the lattice parameter. The above properties make AZO an excellent material for TCO material in solar cells[508, 509].

Equation 1.25 shows the Kröger-Vink reaction for Al_2O_3 doping of ZnO in which the two electrons generated during the reaction are donated to the conduction band. This improves the electronic conductivity of the material[490].

$$Al_2O_3 \xrightarrow{2ZnO} 2Al_{Zn}^{\bullet} + 2O_O^X + 2e^- + ½O_2 \uparrow \qquad (1.25)$$

As previously mentioned in section 1.3.6, TMA is the most widely reported Al precursor. However, due to its high reactive nature, it is difficult for doping. TMA is too reactive to achieve a low surface density of Al atoms. Aluminium isopropoxide (AIP) has been explored as an Al precursor for Al-doped ZnO.

Li et al. compared the properties of Al-doped ZnO films from different Al precursors. Both AIP and $AlCl_3$ require heating in order to generate sufficient vapour pressure. The Al dopant concentration increases gradually from TMA to AIP and finally $AlCl_3$. TMA-AZO and AIP-AZO showed the lowest resistivity values, at 3.3 and 4.0 mΩ cm respectively. $AlCl_3$-AZO showed the highest RMS which was attributed to contamination from residual Cl which may have a negative effect on the nucleation of ZnO. The XRD results showed TMA-AZO to have poor crystallinity showing only a very weak (002) peak. However, the XRD data for both the AIP-AZO and the $AlCl_3$-AZO material showed no discernible features[510]. It was suggested that the crystallisation of the ZnO may be suppressed due to thinner films with a relatively high Al doping concentration[510].

Various precursor dopant sequences have been studied in order to assess the effect that they may have. Conventionally, δ-doping is the method of doping employed during a doped ALD cycle. This results in dopants being localized within a plane that is perpendicular to the direction of growth. As noted earlier, for Al-doped ZnO, low doping efficiencies can result due to the formation of Al-O-Al clusters, the formation of insulating $ZnAl_2O_4$ or due to suppression of electron donation caused by Coulombic repulsion forces from adjacent Al atoms[498].

The most common precursor sequence used for the ALD growth of AZO consists of the use of the DEZn/H_2O process for a desired number of cycles followed by insertion of a TMA/H_2O cycle. This is then repeated a number of times until the desired thickness is obtained. This is known as the "supercycle" method. Song et al.[511] reported an alternative precursor sequence which consisted of a DEZn pulse, followed by a TMA pulse and then finally a H_2O pulse (case 1). Each precursor pulse was followed by a purge step. They have also reported a sequence of a TMA pulse, then a DEZn pulse and finally the H_2O pulse (case 2). The initial metal precursor pulse was not followed by a pulse from the oxygen source, namely water. The surface species formed in case 1 is O-Zn-$(C_2H_5)^*$. This can be replaced by Al-methyls which form Zn-methyl

species that are very volatile alongside O-Al-methyl surface groups. Case 1 produced films which showed the lowest resistivity on glass which suggested it was the most effective doping sequence. In case 2, under DEZn exposure, the O-Al-$(CH_3)^*$ surface remains stable. This is expected as the Zn-O bond is weaker than the Al-O bond. The formation of Zn-O-Al bridging units occurs as both –Zn-$(C_2H_5)^*$ and –Al-$(CH_3)^*$ surface species mix. This case favours and helps control the incorporation of the Al-dopant as the Zn surface species is present.

Films grown using the sequence in the above case 1 (DEZn/TMA/H_2O), have shown lower resistivity, smaller grain size, lower surface roughness, show (100) preferential growth and have a larger area under the (100) peak than typical Al-doped ZnO grown using the more 'usual' sequential $(DEZn/H_2O)_m$ $(TMA/H_2O)_n$ cycles [512].

Choi et al.[513] used the following sequence: DEZn pulse, TMA pulse, H_2O pulse. This sequence was employed with the aim of enhancing the distribution of Al^{3+} ions within the ZnO lattice in order to avoid deliberately forming a nanolaminates structure.

Precursor co-injection has been explored by Illiberi et al.[514] and Yuan et al.[515]. Co-injection results in homogeneous distribution of Al throughout ZnO which still allowed for accurate control over the Al: Zn ratio. The method of co-injection results in a competitive reaction between metal precursors and the surface hydroxyl species. Films fabricated this way were found to have a higher percentage of Al at the interfaces than the rest of the film. It is thought that the Al may diffuse through the ZnO and react at the surface or the reaction between the substrate and TMA precursor may be preferential.

A sequence consisting of a DEZn pulse, a TMA pulse and a combined DEZn/H_2O pulse was investigated by Pollock et al.[516]. It was thought that the addition of another DEZn step after the TMA pulse and the resulting extra purge time may allow for more DEZn molecule to bind to active sites. The DEZn is a smaller molecule compared to TMA and also is not as sterically

hindered. This precursor sequence may result in the formation of a so-called sacrificial adsorbate layer that would act to shield the ZnO from TMA etching[516].

Park et al. showed how a prolonged purge time of 120 s for the H_2O resulted in decreased chemisorption of TMA as the number of hydroxyl groups decreased due to surface dehydration[517].

Etching of ZnO is commonly reported when DEZn pulse precedes TMA pulse. The mass loss observed can be attributed to etching of surface Zn-alkyls. A similar etching reaction occurred when the TMA pulse preceded the DEZn pulse. Although this is not thermodynamically favourable, the mass loss is explained by saturation of surface hydroxyls or by passivation of surface defect sites[518].

Typically, films grow in a direction that minimizes the surface energy therefore growth occurs with the plane of lowest surface free energy parallel to the surface[519]. For undoped ZnO, the <002> direction is usually the preferential growth direction as it is the most densely packed and thermodynamically stable in the wurtzite structure[520, 521]. The ZnO (002) plane is highly polar as it consists of Zn^{2+} and O^{2-} ions[521]. It is charged either positively or negatively, depending on surface termination[494].

AZO films exhibiting a (002) plane preference have been reported[515, 522-527]. In general, as the Al concentration increases preferential growth along the <002> direction has been observed[513, 528].

Oh et al. have reported AZO films with a preference for the <100> growth direction[529]. This was explained by considering the adhesion of anions, such ethyl group fragments on the (002) polar surface of AZO causing suppression of growth of the (002) planes[353, 364]. Ahn et al. also reported the growth of AZO films with a preference for the (100) plane. It was suggested that

since the (100) plane is charge neutral and the Al^{3+} ions may cause a disturbance to the charge neutrality and cause (100) surface energy to be the most favourable[521]. With increasing Al concentration, growth preference was found in the <100> direction such that the (100) planes dominated over the (002)[460, 494, 509, 512, 527, 528, 530-538]. With further increases in %Al the intensity of the (100) reflections either decreased[527, 529, 539] or no peaks were observed at all[522, 533].

Baji et al. have studied the effects of growth temperature and have shown that the growth direction highly depends on the deposition temperature (table 1.7)[356]. Other studies have shown that at high deposition temperatures, (002) plane preferential growth prevails[516, 521, 535, 540-543].

Deposition Temperature (°)	**Intrinsic**	**Doped : 4.9at% Al**
120	Small grain size; typical orientation (100)	No pronounced orientation, (100) apparent
150	(100) dominant	No pronounced orientation, (100) apparent
180	(100) orientation even more dominant	Beside the (100) orientation (101) apparent
210	Besides (100), (002) becomes apparent	(100) and (101)
240	Better crystalline structure, (100) and (002)	No orientation, very small grains
270	(002) more dominant than (100) and (101) but all are present	No orientation, very small grains
300	(002) orientation	No orientation, very small grains

Table 1.7: Temperature study by Baji et al. showing growth directions for intrinsic ZnO and 4.9at% Al-doped ZnO[356]

Many reports cite a systematic shift of the XRD data for both the (002) and (100) reflection to higher 2θ angles indicating a decrease in the lattice constant, *d* as Al^{3+} ions substitute for Zn^{2+} ions in the ZnO lattice[460, 509, 512-514, 522, 523, 525, 526, 529, 532, 540-549]. The ionic radius of Al^{3+} (0.53 Å) is smaller than the ionic radius of Zn^{2+} (0.72 Å) which explains the decrease in the lattice constant[507].

ZnO heavily-doped with Al may lead to the formation of nano-sized metallic clusters[523], insulating Al_2O_3[399, 523, 524, 527, 529, 531, 533, 550, 551] and $ZnAl_2O_4$[552-554]. The formation of such materials may cause distortion of the ZnO crystal structure[37, 552] and lead to the creation of carrier traps[524] and scattering centres[531].

1.5.4 ALD growth of Sn-doped ZnO

Zinc tin oxide (ZTO) is a wide band gap semiconductor. The material has potential for use as a channel material in thin film transistors[555, 556]. It also presents as a promising alternative to cadmium sulfide for application in thin film solar cells[557, 558]. Previous work has shown the growth of stacks of ZnO and SnO_x deposited at low temperatures[559-561].

Hägglund et al. fabricated ZTO by ALD at 150 °C using DEZn, tetrakis-dimethylamido tin (TDMASn) and H_2O as precursors. Initially, the ZnO grew slower on SnO_x as opposed to on itself as a result of varying surface hydroxyl group densities. The variation in growth rate observed was found to result in a variation of elemental ratios as function of bilayer period, even for films with the same cycle ratio. For low bilayer numbers (<20 layers), films were characterised by ZnO inclusions such as clusters or islands within a SnO_x matrix. For larger bilayer numbers (>20 layers), more defined layers were deposited. It was found that lower growth rates resulted in island-type growth due to the number of surface nucleation sites being limited. As the islands amalgamated, growth rate reverted to the expected value. For the ZTO films deposited at 150 °C, no evidence of atomic mixing was found. For the ZTO films post-

annealed at 400 °C, a stable surface phase consisting of equal amount of Zn and Sn indicated the presence of the inverted spinel Zn_2SnO_4[562].

ZTO films have also been deposited using the same metal precursors as the case above but with ozone as the oxygen source. These films had c-axis orientation preference and a high optical transmittance (>85%) in the visible region. The band gap of the material increased from 3.26 eV to 3.54 eV as the concentration of Sn increased from 0 to 5.7 at%. Electrically, the minimum resistivity obtained was 9.5 $x10^{-4}$ Ω cm and a carrier concentration of 3.2 $x10^{20}$ cm^{-3} was measured[563].

1.5.5 ALD growth of Ti-doped ZnO

Ye et al. achieved Ti-doping of ZnO by growing alternating layers of ZnO and TiO_2[564]. DEZn, TTIP and H_2O were the precursors and co-reagent of choice. Films were deposited on Si substrates at 200 °C. The expected thickness and actual thickness of films differed which was attributed to a hampered growth mode of the ZnO layer deposited directly on TiO_2. The lowest resistivity of 8.87 $x10^{-4}$ Ω cm was recorded for a cycle ratio of 20:1 (ZnO: TiO_2). The carrier concentration increased and then decreased with increasing Ti concentration. The highest carrier concentration recorded was 4.80 $x10^{20}$ cm^{-3}. The mobility of the films was 15 cm^2 / Vs. XRD results showed the (100) peak shift towards lower diffraction angle as the concentration of Ti increased[564].

It was reported by Lee et al. that atomic-layer Ti doping by ALD resulted in films with much higher electrical conductivity and also doping efficiency than their Al counterparts. The experimental parameters used in this study were as follows; DEZn, TTIP and H_2O were used as precursors with a deposition temperature of 200 °C. A mobility of >20 cm^2/Vs was recorded which was attributed to the presence of a lower concentration of inactivated dopants which acted as scattering centres. Ti is very reactive towards oxygen and it is possible for Ti to remove

oxygen from the ZnO matrix and thus be oxidised itself. In conjunction, this action would create electron donors in the form of either oxygen vacancies ($V_O^{\cdot\cdot}$ or V_O^{2+}) or zinc interstitials ($Zn_i^{\cdot\cdot}$ or Zn_i^{2+}). The growth rate of the stack overall was found to be higher than that of the sum of the individual oxide layers. This was explained by considering enhanced absorption of either the zinc or titanium metal precursor during growth[495].

The degradation of the crystallinity of Ti-doped ZnO by ALD as the concentration of Ti increased was reported by Wan et al. in which the fabricated films were transparent and a maximum resistivity of 1.6 $x10^{-3}$ Ω cm was achieved with 6.2 at% of Ti[565].

Bergum et al. deposited Ti-doped ZnO films using DEZn, TTIP and H_2O as precursors and co-reagents. The deposition temperature for their process was 200 °C. The lowest resistivity value achieved was 1.8 $x10^{-3}$ Ω cm for a film grown with 1.7 at% Ti. An increase in mobility was observed even with minimal Ti-doping. The XRD results showed an increase in a-axis orientation with increasing Ti content alongside no obvious change in lattice parameters. Also with increasing Ti content, a Burstein-Moss shift was identified. The maximum doping efficiency was found to be at Ti 1.7at%. This high value suggested a good distribution of the Ti dopant[566]. A further study from Bergum et al. supported previous findings and also added that an increase in thickness of films resulted in an increase in a-orientation as seen by XRD. Simulations performed suggest that films grow in a hexagonal bi-pyramidal form. The electrical properties were thickness dependent below total film thicknesses of 200 nm. The optical properties in the visible region were also thickness dependent[567].

Torrisi et al. grew ZnO/TiO_2 multilayers with a nominal concentration of Ti of 2%. The films were highly transparent in the visible range (>97%). The film with the lowest resistivity of 3 $x10^{-3}$ Ω cm was deposited at 200 °C[488].

Saha et al. studied the dimensional crossover occurring in stacked ZnO/TiO_x layers. Ti-doped ZnO films were grown using DEZn, $TiCl_4$ and H_2O as precursors and co-reagents. The deposition temperature for their process was 200 °C. A smooth switch from 2D to 3D of weak localization was observed[568]. It was further reported that a decrease in the spacing of the ZnO layers resulted in an evolution of the electron transport behaviour from a metallic to a non-metallic system. Using ALD for Ti-doping was found to be beneficial as the dopants are restricted to 2D monolayers. The lower temperature of the deposition decreases the likelihood of the Ti dopant atoms migrating and diffusing from the plane of growth[569].

Chen et al. deposited ZnO/TiO_2 films via spatial-ALD (s-ALD). Linear growth was observed with respect to both the ZnO and TiO_2 growth processes. The ZnO films had a high carrier mobility. The deposited TiO_2 films possessed good optical transparency. Interestingly, as the number of number of layers in the ZnO/TiO_2 stack increased, the % transmittance increased in the visible range. Similarly, when the number of bilayers increased the intensity of the ZnO diffraction peaks decreased. The low crystallinity of the ZnO/TiO_2 nanolaminates may be explained by the individual XRD patterns of the amorphous TiO_2 interlayers and thinner ZnO with smaller crystal size. Similarly, as the number of number of layers increased, the % transmittance increased in the visible range. This work demonstrated that it should be possible to tune the RI of the films as an increase in RI was observed for films in which the thickness of each bilayer decreased[484].

1.5.6 ALD growth of Ga-doped ZnO

Doping with Ga can provide extremely stable films at elevated temperatures[570]. There is no tendency for Ga dopants to segregate at the interface[571]. This makes Ga a favourable dopant. The covalent bond lengths of Ga-O and Zn-O (1.92 Å and 1.97 Å, respectively) are very similar to each other when compared to that of Al-O (2.7 Å) and thus, the deformation of the ZnO

lattice is found to be significantly lower in GZO than in AZO even with the same dopant concentration[330]. Moreover, the ionic radii of Ga and Zn are closer in value, 0.062 nm and 0.074 nm respectively when compared to Al (atomic radius of 0.053 nm)[572]. This leads to a more uniform structure with fewer less lattice defects.

Saito et al. deposited Ga-doped ZnO films using DEZn, triethylgallium (TEG) and H_2O as precursors and co-reagents. The deposition temperature for their process was 300 °C. These films had a resistivity of 3.0 $x10^{-4}$ Ω cm. The XRD results showed an increase in the intensity of the $(10\bar{1}1)$ reflection[573].

Chang et al. found that the resistivity of Ga-Zn-O (GZO) films rose substantially after annealing in an oxygen rich environment. The resistivity values for these films on glass and sapphire were 3.9 $x10^{-4}$ Ω cm and 3.7 $x10^{-4}$ Ω cm respectively[574].

Lee et al. studied the effects of an oxygen-plasma post-treatment on Ga-doped ZnO films grown by thermal ALD. DEZn, TEG and H_2O were used as precursors. In order to remove any residual hydroxyl groups an oxygen ion bombardment process was deployed. A decrease in resistivity was recorded after the post-treatment from 6.7 $x10^{-4}$ Ω cm to 4.5 $x10^{-4}$ Ω cm. The carrier concentration increased from 9.7 $x10^{20}$ cm^{-3} to 1.2 $x10^{21}$ cm^{-3} [575].

Szabó et al. fabricated Ga-doped ZnO thin films using DEZn, hexakis(dimethylamino) gallium and H_2O as precursors. The deposition temperature was 300 °C. The optimum cycle ratio was found to be 33:1 resulting in films with a resistivity of 3.30 $x10^{-4}$ Ω cm, carrier concentration of 1.38 $x10^{21}$ cm^{-3} and a mobility of 13.0 cm^2/Vs[576].

1.5.7 ALD growth of In-doped ZnO

Indium oxide (In_2O_3) is a wide band-gap semiconductor that has been extensively researched and developed for TCO applications due to the fact it is chemically stable, possesses excellent structural stability at high temperatures, has a low resistivity value and has high transparency in the visible light region. When In is used as a dopant for ZnO, the resulting indium zinc oxide (IZO) is found to be cheaper to prepare than conventional ITO and has excellent electrical and optical properties.

Illeberi et al. investigated the effects of damp-heat tests on IZO films under the conditions of 85% humidity at 85 °C. An increase in resistivity was recorded due to a sharp increase in the carrier mobility of the material. Coinciding with this, the carrier density and the transparency partially degraded during the experiment. The increase in resistivity was attributed to this degradation of the structural properties as it lead to a high level of tensile stress within the film[577]. Illeberi et al. further reported IZO films with minimum resistivity values of 3 mΩ cm, a carrier density of 6 $x10^{20}$ cm^{-3}, a mobility of 3 cm^2/ Vs and 80% transparency[578]. Illeberi et al. have also utilised co-injection of precursors to prepare IZO films. DEZn, TMI and H_2O were the precursors and co-reagents of choice. The carrier density and resistivity values of the films were the same as previously reported with >85% transparency. The morphology of the IZO films changed from polycrystalline to amorphous as the In content increased above 15% while resistivity values of 7 Ω cm were recorded[579].

Lee et al. deposited In-doped ZnO films using DEZn, TMI and H_2O as precursors and co-reagents. The TMI precursor was heated to 50 °C in order to vapourize the (otherwise solid) precursor. The deposition temperature for their process was 200 °C. In terms of the ZnO films, the GPC achieved was 0.151 nm/cycle for ZnO and 0.048 nm/cycle for In_2O_3. The films had a resistivity of 3.9 $x10^{-4}$ Ω cm, a carrier concentration of 3.0 $x10^{20}$ cm^{-3} and a mobility of 50 cm^2/

Vs. The IZO films fabricated were amorphous, highly conductive, ultra-smooth and exhibited excellent step coverage (96% step coverage)[493].

Kim et al. fabricated IZO films using DEZn, dimethylamino- dimethyl indium (DMLDMIn) and H_2O as precursors and co-reagents. The supercycle method was employed in which the number of ZnO cycles was varied between 99, 49, 9 and 1 for every 1 In_2O_3 ALD cycle. The deposition temperature ranged from 200–400 °C. No growth was observed until a growth temperature of 250 °C was employed. The growth rate varied as deposition temperature increased as the surface reaction between the precursor and surface species was thermally activated. The GPC values for 300, 350 and 400 °C were 0.061, 0.065, 0.11 nm/cycle respectively[580].

Sheng et al. deposited IZO films using DEZn, [1, 1, 1-trimethyl-*N*-(trimethylsilyl)silanaminato]-indium (InCA-1) and H_2O_2 as precursor and co-reactants. The supercycle method was utilised featuring cycle ratios of 1 ZnO: 1 In_2O_3. The growth rate of the IZO film deviate from that of the sum of the individual growth rates of ZnO and In_2O_3 at growth temperatures of 150, 175 and 200 °C[581].

Table 1.8 summarises the cation dopants used in ALD doped ZnO along with the process parameters. The Zn precursor in all cases is diethyl zinc.

Cation	Dopant Precursor	Oxidant	Growth Temperature (°C)	Deposition rate (Å/cycle)	Reference	Other
Al^{3+}	trimethylaluminum	H_2O	200	0.97	510	511 -518, 521-524, 526-536, 538-546
	αluminium isopropoxide	H_2O	200	1.6	510	-
	aluminium trichloride	H_2O	200	1.0	510	-
Sn^{4+}	tetrakis-dimethylamido tin	H_2O	150	≈1.0	562	559-561, 563
Ti^{4+}	titanium isopropoxide	H_2O	200	0.33	565	495, 564, 566
	titanium tetrachloride	H_2O	200	0.48	488	569
Ga^{3+}	triethylgallium	H_2O	300	-	573	574-575
	hexakis(dimethylamino) gallium	H_2O	300	-	576	-
In^{3+}	trimethyl indium	H_2O		-	578	493, 577, 579
	dimethylamino- dimethyl indium	H_2O	300	0.61	580	-
	[1, 1, 1-trimethyl-*N*-(trimethylsilyl)silanaminato]-indium (InCA-1)	H_2O_2	200	0.71	581	-

Table 1.8: Listing of cation dopants used in ALD doped ZnO along with the dopant precursors, oxidants, growth temperature and deposition rate. The Zn precursor in all cases is diethyl zinc

1.5.8 Ternary/Quaternary Oxides

In recent years, there has been increasing interest in the fabrication of ternary and quaternary materials. Ternary and quaternary films have been utilised in application areas such as catalysis[582, 583], energy storage[584, 585] and photovoltaics[586-588]. An extensive review on the topic of functional multicomponent oxides has been published by Coll *et al.* which focuses on pervoskites (ABO_3), spinels (AB_2O_4), delafossites (ABO_2) and scheelites (ABO_4)[589]. In this review, the fact that the exact same metal cation can be either stable or metastable in different structures is highlighted. The work presented in this thesis focuses exclusively on ZnO-based ternary oxides. The ternaries are composed of Zn^{2+} ions combined with two other metal ions in an oxide matrix- so-called ternary oxides. Depositing ternary oxides provides more opportunities to fine-tune the composition as well as the atomic and electronic structures. Mackus et al. have published an extensive review on the growth of doped, ternary and quaternary materials by the deposition method of ALD[590]. In this review, ZnO-based ternaries studied include ZnO: Al2O_3: ZrO_2[591], ZnO: MgO: Al_2O_3[592] and ZnO: TiO_2: ZrO_2[593]. The co-reactant used in the growth of the films in this review was H_2O. In this thesis, O_2 plasma was the co-reactant of choice. The use of a more reactive co-reactant can lead to the elimination of nucleation effects such as etching by persistent ligands or memory issues associated with the persistence of H_2O in the chamber. By utilising O_2 plasma, it may also functionalize the surface of the film with more reactive sites

1.6 Summary of the contents of the thesis

The motivation behind this thesis was to explore a wide range of composite/nanolaminate materials grown by ALD. The main objective of the work was to develop an understanding of the way in which materials may be specifically engineered from the bottom up, to produce desirable properties such as electronic conductivity, electron and hole mobility, surface hydrophobicity or hydrophilicity, antimicrobial activity and transparency. In order to achieve this, ALD was the deposition method employed for materials preparation.

The central research question this thesis will ultimately aim to answer is: can we obtain a better understanding of the fundamental nature of the growth and properties of ultra-thin film hybrid/composite materials?

Chapter 1- This chapter describes the history of thin films, nanolaminates and ALD. The ALD chemistries of Al_2O_3, TiO_2 and ZnO are discussed in depth. A review of the electronic, mechanical, optical and encapsulation applications of Al_2O_3, TiO_2 and ZnO nanolaminates are presented. Doping of ZnO is discussed with a particular focus on Al, Ga, In, Sn and Ti-doped ZnO by ALD.

Chapter 2 – This chapter outlines the experimental procedures for the deposition of all films prepared during this project. It also includes a brief description of the associated methods of analysis such as electron microscopy, electrical measurements, photoactivity measurements and other analytical methods including XRD, XPS and UV/Vis spectroscopy.

Chapter 3 – This chapter presents the results of a study of the growth of nanolaminates of ZnO and TiO_2 in which the spacing and thickness of each layer has been carefully controlled. In particular we present results for nanolaminates of ZnO and TiO_2, prepared with the aim of combining the photocatalytic properties and robustness of TiO_2 with the transparent conducting behaviour of ZnO. The photocatalytic properties of the laminate layers were examined using a

simple dye test, comparing TiO_2 layers both with and without ZnO under–layers (and *vice versa*), in order to assess the magnitude and range of any possible ZnO templating influences on the photo active nature of the TiO_2. It is shown that the structure and composition of such materials play a dramatic role in terms of determining the crystallinity and photocatalytic activity while the nature of the strained interfaces that are an essential feature of such materials are highlighted.

Chapter 4 – This chapter describes a study of the deposition of ZnO onto Si and glass substrates by both thermal and remote plasma ALD. The same reactor, in this case a Picosun™ R200 ALD reactor, was used for both sets of experiments so as to minimise the influence of reactor design on the nature of the deposited materials.

Chapter 5 – This chapter describes a study of the growth of doped ZnO ALD fabricated in order to study the effects of the doping process on the structure and composition of the films. The dopants used were Al, Ga, Sn and Ti. The electrical behaviour of the various films was particularly studied via Hall Effect measurements. Similar to chapter 4, films were deposited by both thermal and plasma ALD in order to assess differences in properties as a result of growth conditions.

Chapter 6 - Building on the results obtained from chapter 5, ternaries of ZnO based films were grown. The goal here was to deposit various combinations of doped ZnO in order to find the best electrically performing film. For ternaries, the elimination of water from the list of precursors was key. These films were deposited via plasma ALD for this reason.

Chapter 7 - This chapter summarises and concludes the work presented in this thesis. Finally, some suggestions for future work are proposed.

References

1. Zeijl, H. W., Thin Film Technologies for Micro/Nano Systems; A Review. *ECS Transactions* **2014,** *61* (3), 191-206.

2. Boettger, Coating of glass, porcelain or earthenware with a thin film of lustrous metallic platinum. *Journal of the Franklin Institute* **1870,** *89* (5), 360.

3. Langley, S. P., The Bolometer and Radiant Energy. *Proceedings of the Amercian Academy of Arts and Sciences* **1880,** *16*, 342-358.

4. Stone, I., On the Electrical Resistance of Thin Films. *Phys. Rev. (Series 1)* **1898,** *6*, 1.

5. Longden, A. C., Electrical Resistance of Thin Films Deposited by Kathode Discharge. *Phys. Rev. (Series 1)* **1900,** *11* (1), 40.

6. Longden, A. C., Electrical Resistance of Thin Films Deposited by Kathode Discharge. II. *Phys. Rev. (Series 1)* **1900,** *11* (2), 84.

7. Bardeen, J. and Brattain, W. H., The Transistor, A Semiconductor Triode. *Phys. Rev.* **1948,** *74* (2), 230.

8. Riordan, M., Semiconductors: the lost history of the transistor. *IEEE Spectrum* **2004,** *41* (5), 44-49.

9. Ellis, J. N. and Osadchy V. S., The 2N3055: a case history. *IEEE Transactions on Electron Devices* **2001,** *48* (11), 2477-2484.

10. Lojek, B., *History of Semiconductor Engineering*. Springer: 2007.

11. Brock, D., *Understanding Moore's Law: four decades of innovation*. Chemical Heritage Press: Philadelphia, Pennsylvania, 2006.

12. *Nanoscale Materials in Chemistry*. 2nd ed.; John Wiley & Sons: New Jersey, 2009.

13. Piedade, A. P., Romeu, F., Branco, R. and Morais, P. V., Thin Films for Medical and Environmental Applications. In *Methods for Film Synthesis and Coating Procedures*, Nánai, L., Samantara, A., Fábián, L. and Ratha, S., Ed. IntechOpen: London, 2018.

14. Guo, Y., Porter, A. L and Huang, L., Nanotechnology-enhanced thin-film solar cells: analysis of global research activities with future prospects. *R&D Management* **20010,** *40* (2), 195-208.

15. Ngô, C. and Van de Voorde, M. H., Chapter 4 Nanomaterials: doing more with less. In *Nanotechnology in a Nutshell. From Simple to Complex Systems*, 1 ed.; Atlantis Press: 2014; p 502.

16. Gusev A. I. http://eng.thesaurus.rusnano.com/wiki/article1371. (accessed 22/03/16).

17. *Atomic Layer Deposition of Nanostructured Materials*. Wiley-VCH: Weinheim, Germany, 2012.

18. Lee, H. B., Anderson, V. R. and George, S. M., Growth and Properties of Hafnicone and HfO_2/Hafnicone Nanolaminates and Alloy Films Using Molecular Layer Deposition Techniques. *ACS Applied Materials & Interfaces* **2014,** *6*, 16880-16887.

19. Sundberg, P. and Karppinen, M., Organic and inorganic-organic thin film structures by molecular layer deposition: a review. *Beilstein Journal of Nanotechnology* **2014,** *5*, 1104-1136.

20. Radisavljevic, B., Radenovic, A., Brivio, J., Giacometti, V. and Kis, A., Single-layer MoS_2 transistors. *Nature Nanotechnology* **2011,** *6*.

21. Lopez-Sanchez, O., Lembke, D., Kayci, M., Radenovic, A. and Kis, A., Ultrasensitive photodetectors based on monolayer MoS_2. *Nat. Nanotechnol.* **2013,** *8* (7), 497–501.

22. Bertolazzi, S., Brivio, J., and Kis, A., Stretching and Breaking of Ultrathin MoS_2. *ACS Nano* **2011,** *5* (12), 9703–9709.

23. Zeng, H., Dai, J., Yao, W., Xiao, D. and Cui, X., Valley polarization in MoS_2 monolayers by optical pumping. *Nat. Nanotechnol.* **2012,** *7*, 2012.

24. Zhang, W., Chuu, C. P., Huang, J. K., Chen, C. H., Tsai, M. L., Chang, Y. H.. Liang, C. T., Chen, Y. Z., Chueh, Y. L., He, J. H., Chou, M. Y. and Li, L. J., Ultrahigh-Gain Photodetectors Based on Atomically Thin Graphene-MoS_2 Heterostructures. *Sci. Rep* **2014,** *23* (4), 3826.

25. Cong, C., Shang, J., Wu, X., Cao, B., Peimyoo, N., Qiu, C., Sun, L. and Yu, T., Synthesis and Optical Properties of Large-Area Single-Crystalline 2D Semiconductor WS_2 Monolayer from Chemical Vapor Deposition. *Adv. Optical Mater.* **2014,** *2*, 131–136.

26. Cai, Y., Lan, J., Zhang, G. and Zhang, Y. W., Lattice vibrational modes and phonon thermal conductivity of monolayer MoS_2. *Phys. Rev. B* **2014035438,** *89*.

27. Azadmanjiri, J., Berndt, C. C., Wang, J., Kapoor A. J. and Srivastavac, V. K., Nanolaminated composite materials: structure, interface role and applications. *RSC Adv.* **2016,** *6*, 109361.

28. Schmidt, D. F., Nanolaminates - Bioinspired and beyond. *Materials Letters* **2013,** *108*, 328-335.

29. Azadmanjiri, J., Berndt, C. C., Wang, J., Kapoor, A.J., Srivastavac, V. K. and Wen, C., A review on hybrid nanolaminate materials synthesized by deposition techniques for energy storage applications. *J. Mater. Chem. A* **2014,** *2*, 3695-3708.

30. Puttaswamy, M., Vehkamäki, M., Kukli, K., Dimri, M. C., Kemmel, M., Hatanpää, T., Heikkilä, M. J., Mizohata, K., Stern, R., Ritala, M. and Leskelä, M., Bismuth iron oxide thin films using atomic layer deposition of alternating bismuth oxide and iron oxide layers. *Thin Solid Films* **2016,** *611*, 78-87.

31. Zhang, G., Wu, H., Wang, X., Zhang, D., Wang, T. and Liu, C., Modulation of the dissipation factor in transparent AlZnO/ZrO_2/AlZnO capacitors. *Journal of Alloys and Compounds* **2017,** *690*, 777-782.

32. Martínez-Castelo, J. R., López, J., Domínguez, D., Murillo, E., Machorro, R., Borbón-Nuñez, H. A., Fernandez-Alvarez, I., Arias, A., Curiel, M., Nedev, N., Farías, M. H. and Tiznado, H., Structural and electrical characterization of multilayer Al_2O_3/ZnO nanolaminates grown by atomic layer deposition. *Materials Science in Semiconductor Processing* **2017,** *71*, 290-295.

33. Onaya, T., Nabatame, T., Sawada, T., Kurishima, K., Sawamoto, N., Ohi, A., Ogura, A., Improved leakage current properties of ZrO_2/(Ta/Nb)O_x -Al_2O_3/ZrO_2 nanolaminate insulating stacks for dynamic random access memory capacitors. *Thin Solid Films* **2018,** *655*, 48–53.

34. Chen, W., Ren, W., Zhang, Y., Liu, M. and Ye, Z. G., Preparation and properties of ZrO_2 and TiO_2 films and their nanolaminates by atomic layer deposition. *Ceramics International* **2015,** *41*, S278–S282.

35. Rodríguez, A., Gonzalez, M. B., Campabadal, F., Suñé, J. and Miranda, E., Electrical characterization of multiple leakage current paths in HfO_2/Al_2O_3-based nanolaminates. *Microelectronics Reliability* **2015,** *55* (9-10), 1442-1445.

36. Cho, H., Park, K. W., Park, C. H., Cho, H. J., Yeom, S. J., Hong, K., Kwak, N. J. and Ahn, J. H., Abnormally enhanced dielectric constant in ZrO_2/Ta_2O_5 multi-laminate structures by metallic Ta formation. *Materials Letters* **2015,** *154*, 148-151.

37. López, J., Martínez, J. Abundiz, N., Domínguez, D., Murillo, E., Castill, F. F., Machorro, R., Farías, M. H. and Tiznado, H., Thickness effect on the optical and morphological properties in Al_2O_3/ZnO nanolaminate thin films prepared by atomic layer deposition. *Superlattices and Microstructures* **2016,** *90*, 265-273.

38. Lo Nigro, R., Schilirò, E., Greco, G., Fiorenza, P. and Roccaforte, F., Laminated Al_2O_3–HfO_2 layers grown by atomic layer deposition for microelectronics applications. *Thin Solid Films* **2016,** *601*, 68-72.

39. Mahata, C., An, Y., Choi, S., Byun, Y. C., Kim, D. K., Lee, T., Kim, J., Cho, M. H. and Kim, H., Electrical properties of the HfO_2–Al_2O_3 nanolaminates with homogeneous and graded compositions on InP. *Current Applied Physics* **2016,** *16* (3), 294-299.

40. Zhang, J., Ding, X., Li, J. Zhang, H., Jiang, X. and Zhang, Z., Performance enhancement in InZnO thin-film transistors with compounded ZrO_2–Al_2O_3 nanolaminate as gate insulators. *Ceramics International* **2016,** *42* (7), 8115–8119.

41. Gao, J., He, G., Sun, Z., Chen, H., Zheng, C., Jin, P., Xiao, D. and Liu, M., Modification of electrical properties and carrier transportation mechanism of ALD-derived HfO_2/Si gate stacks by Al_2O_3 incorporation. *Journal of Alloys and Compounds* **2016,** *667*, 352-358.

42. Rodriguez, A., Gonzalez, M. B., Campabadal, F., Suñé, J. and Miranda, E., Breakdown time statistics of successive failure events in constant voltage-stressed Al_2O_3/HfO_2 nanolaminates. *Microelectronic Engineering* **2015,** *147*, 85-88.

43. Mahata, C., Byun, Y. C., An, C. H., Choi, S., An, Y. and Kim, H., Comparative study of atomic-layer-deposited stacked (HfO_2/Al_2O_3) and nanolaminated ($HfAlO_x$) dielectrics on $In_{0.53}Ga_{0.47}As$. *ACS Appl Mater Interfaces* **2013,** *5* (10), 4195-201.

44. Kim, L. H., Kim, K., Park, S., Jeong, Y. J., Kim, H., Chung, D. S., Kim, S. H. and Park, C. E., Al_2O_3/TiO_2 Nanolaminate Thin Film Encapsulation for Organic Thin Film Transistors via Plasma-Enhanced Atomic Layer Deposition. *ACS Applied Materials & Interfaces* **2014,** *6*, 6731−6738.

45. Singh, A., Nehm, F., Müller-Meskamp, L., Hoßbach, C., Albert, M., Schroeder, U., Leo, K. and Mikolajick, T., OLED compatible water-based nanolaminate encapsulation systems using ozone based starting layer. *Organic Electronics* **2014,** *15*, 2587–2592.

46. Oh, J., Shin, S., Park, J., Ham, G. and Jeon, H., Characteristics of Al_2O_3/ZrO_2 laminated films deposited by ozone-based atomic layer deposition for organic device encapsulation. *Thin Solid Films* **2016,** *599*, 119-124.

47. Jeong, E. G., Han, Y. C., Im, H. G., Bae, B. S. and Choi, K. C., Highly reliable hybrid nano-stratified moisture barrier for encapsulating flexible OLEDs. *Organic Electronics* **2016,** *33*, 150-155.

48. Nehm, F., Dollinger, F., Klumbies, H., Müller-Meskamp, L., Leo, K., Singh, A., Richter, C., Schroeder, U., Mikolajick, T., Hossbach, C., Albert, M. and Bartha, J. W., Atomic layer deposited TiO_x/AlO_x nanolaminates as moisture barriers for organic devices. *Organic Electronics* **2016,** *38*, 84-88.

49. Leppäniemi, J., Sippola, P., Broas, M., Aromaa, J., Lipsanen, H. & Koskinen, J., Corrosion protection of steel with multilayer coatings: Improving the sealing properties of physical vapor deposition CrN coatings with Al_2O_3/TiO_2 atomic layer deposition nanolaminates. *Thin Solid Films* **2017,** *627*, 59–68.

50. Radi, P. A., Testoni, G. E., Pessoa, R. S., Maciel, H. S., Rocha, L. A. and Vieira, L., Tribocorrosion behavior of TiO_2/Al_2O_3 nanolaminate, Al_2O_3, and TiO_2 thin films produced by atomic layer deposition. *Surface and Coatings Technology* **2018,** *349*, 1077-1082.

51. Díaz, B., Härkönen, E., S´wiatowska, J., Seyeux, A., Maurice, V., Ritala, M. and Marcus, P., Corrosion properties of steel protected by nanometre-thick oxide coatings. *Corrosion Science* **2014,** *82*, 208–217.

52. Härkönen, E., Tervakangas, S., Kolehmainen, J., Díaz, B., Swiatowska, J., Maurice, V., Seyeux, A., Marcus, P., Fenker, M., Tóth, L., Radnöczi, G. and Ritala, M., Interface control of atomic layer deposited oxide coatings by filtered cathodic arc deposited sublayers for improved corrosion protection. *Materials Chemistry and Physics* **2014,** *147*, 895-907.

53. Mohseni, H. and Scharf, T. W., Role of atomic layer deposited solid lubricants in the sliding wear reduction of carbon–carbon composites at room and higher temperatures. *Wear* **2015,** *332-333* (1303–1313).

54. López, J., Borbón-Nuñez, H. A., Lizarraga-Medina, E. G., Murillo, E., Machorro, R., Nedev, N. & Soto, G., Al_2O_3 -Y_2O_3 ultrathin multilayer stacks grown by atomic layer deposition as perspective for optical waveguides applications. *Optical Materials* **2017,** *72*, 788–794.

55. Greiner, M. T., Chai, L., Helander, M. G., Tang, W.-M., and Lu, Z.-H, Metal/Metal-Oxide Interfaces: How Metal Contacts Affect the Work Function and Band Structure of MoO3. *Adv. Func. Mat.* **2012,** *23* (2), 215–226.

56. Gerberich, W. W., Jungk, J. M. and Mook, W. M., The Bottom-Up Approach to Materials by Design. In *Nano and Microstructural Design of Advanced Materials: A Commemorative Volume on Professor G. Thomas' Seventieth Birthday*, Elsevier Inc.: 2003; pp 211-220.

57. Zobir, S., Rashid, S. A. and Tan, T., Recent Development on the Synthesis Techniques and Properties of Graphene Derivatives. In *Synthesis, Technology and Applications of Carbon Nanomaterials*, Elsevier Inc.: 2019; pp 77-107.

58. Tiwari, J. N., Tiwari, R. N. and Kim, K. S., Zero-dimensional, one-dimensional, two-dimensional and three-dimensional nanostructured materials for advanced electrochemical energy devices. *Prog. Mater. Sci* **2012,** *57*, 724-803.

59. Dahl, J. A., Maddux, B. L. S. and Hutchison, J. E., Toward Greener Nanosynthesis. *Chem. Rev.* **2007,** *107* (6), 2228-2269.

60. Carlsson. J.-O. and Martin, P. M., Handbook of Deposition Technologies for Films and Coatings 3rd Edition. Elsevier: 2010.

61. Dahmen, K.-H., Chemical Vapor Deposition. In *Encyclopedia of Physical Science and Technology*, 3rd Edition ed.; Meyers, R. A., Ed. Elsevier: 2003; Vol. 2, pp 787-808.

62. Ma, T., Effect of precursor concentration and sintering on functional properties of ZnO thin films deposited by aerosol-assisted chemical vapour deposition (AACVD). *Materials Science in Semiconductor Processing* **2021,** *121*, 105413.

63. Taylor, M., Pullar, R. C., Parkin, I. P. and Piccirillo, C., Nanostructured titanium dioxide coatings prepared by Aerosol Assisted Chemical Vapour Deposition (AACVD). *Journal of Photochemistry and Photobiology A: Chemistry* **2020,** *400*, 112727.

64. Jafer, R., Ata-ur-Rehman, Iqbal, J., Shahid. M. M. and Wageh, S., Growth of dimensionally favoured TiO2 morphologies by AACVD and their recognized performance as LIB anode. *Ceramics International* **2021,** *47* (5), 6848-6853.

65. Shaukat, S., Khaleeq-ur-Rahman, M., Dildar, I. M., Jamil, H. and Binions, R., One dimensional (1-D) signatures of nanopillars and nanowires in niobium doped zinc oxide (NZO) thin films prepared by aerosol assisted chemical vapour deposition (AACVD). *Ceramics International* **2019,** *45* (13), 16361-16368.

66. Mierczynski, P., Shtyka, O., Kozanecki, M., Filipcza, P., Maniukiewicz, W., Gromov, D. G., Dubkov, S. V., Sysa., A. V., Trifonov, A. Y., Czylkowska, A., Szynkowska, M. I. and Manieckia, T. P., Effect of the AACVD based synthesis atmosphere on the structural properties of multi-walled carbon nanotubes. *Arabian Journal of Chemistry* **2020,** *13* (1), 835-850.

67. Shaukat, S., Khaleeq-ur-Rahman, M., Dildar, I. M. and Binions, R., Aerosol assisted chemical vapor deposition (AACVD) synthesis of nanostructured cauliflower patterning in MWCNT doped tungsten oxide. *Ceramics International* **2019,** *45* (2), 1918-1927.

68. Su, X., Kim, T., Abboud, K. A. and McElwee-White, L., Synthesis of β-ketoiminate and β-iminoesterate tungsten (VI) oxo-alkoxide complexes as AACVD precursors for growth of WO_x thin films. *Polyhedron* **2019,** *157*, 548-557.

69. Sagu, J. S., Mehta, D. and Wijayantha, K. G. U., Electrocatalytic activity of $CoFe_2O_4$ thin films prepared by AACVD towards the oxygen evolution reaction in alkaline media. *Electrochemistry Communications* **2018,** *87*, 1-4.

70. Khan, M. D., Aamir, M., Sohail, M., Sher, M., Akhtar, J., Malik, M. A. and Revaprasadu, N., Novel single source precursor for synthesis of Sb_2Se_3 nanorods and deposition of thin films by AACVD: Photo-electrochemical study for water reduction catalysis. *Solar Energy* **2018,** *169*, 526-534.

71. Navarrete, E., Bittencourt, C., Noirfalise, X., Umek, P., González, E., Güell, F. and Llobet, E., WO_3 nanowires loaded with cobalt oxide nanoparticles, deposited by a two-step AACVD for gas sensing applications. *Sensors and Actuators B: Chemical* **2019,** *298*, 126868.

72. Noh, M. F. M., Soh, M. F., Teh, C. H., Lim, E. L., Yap, C. C., Ibrahim, M. A., Ludin, N. A. and Teridi, M. A. M., Effect of temperature on the properties of SnO_2 layer fabricated via AACVD and its application in photoelectrochemical cells and organic photovoltaic devices. *Solar Energy* **2017,** *158*, 474-482.

73. Monárrez-Cordero, B. E., Amézaga-Madrid, P., Fuentes-Cobas, L., Montero-Cabrera, M. E. and Miki-Yoshida, M., High and fast adsorption efficiency of simultaneous As^{+3}, As^{+5} and F^{-} by Al-doped magnetite synthesized via AACVD. *Journal of Alloys and Compounds* **2017,** *718*, 414-424.

74. Monárrez-Cordero, B. E., Amézaga-Madrid, P., Sáenz-Trevizo, A., Pizá-Ruiz, P., Antúnez-Flores, W. and Miki-Yoshida, M., Synthesis and characterization of composite Fe-Ti oxides nanoparticles with high surface area obtained via AACVD. *Ceramics International* **2018,** *44* (6), 6990-6996.

75. Boadi, N., McNaughter, P. D., Helliwell, M., Malik, M. A., Awudza, J. A. M. and O'Brien, P., The deposition of PbS and PbSe thin films from lead dichalcogenoimidophosphinates by AACVD. *Inorganica Chimica Acta* **2016,** *453*, 439-442.

76. Vilic, T. and. Llobet, E., Nickel Doped WO_3 Nanoneedles Deposited by a Single Step AACVD for Gas Sensing Applications. *Procedia Engineering* **2016,** *168*, 206-210.

77. Kevin, P., Lewis, D. J., Raftery, J., Malik, M. A. and O'Brien, P., Thin films of tin(II) sulphide (SnS) by aerosol-assisted chemical vapour deposition (AACVD) using tin(II) dithiocarbamates as single-source precursors. *Journal of Crystal Growth* **2015,** *415*, 93-99.

78. Mlowe, S., Nyamen, L. D., Ndifon, P. T., Malik, M. A., Raftery, J., O'Brien, P. and Revaprasadu, N., Aerosol assisted chemical vapor deposition (AACVD) of CdS thin films from heterocyclic cadmium(II) complexes. *Inorganica Chimica Acta* **2015,** *434*, 181-187.

79. Akhtar, M., Revaprasadu, N., Malik, M. A., and Raftery, J., Deposition of phase pure nickel sulfide thin films from bis(O-alkylxanthato)–nickel(II) complexes by the aerosol assisted chemical vapour deposition (AACVD) method. *Materials Science in Semiconductor Processing* **2015,** *30*, 368-375.

80. Elleuch, R., Salhi, R., Deschanvres, J.-L., Gucciardi, P. G. and Maalej, R., Growth rate induced high efficient light trapping/photon conversion ZnO:Nd^{3+} nanodisk shaped thin films deposited by AACVD process. *Journal of Alloys and Compounds* **2015,** *651*, 756-763.

81. Elleuch, R., Salhi, R., Maalej, N., Deschanvres, J.-L. and Maalej, R., Structural and luminescence correlation of annealed Er-ZnO/Si thin films deposited by AACVD process. *Materials Science and Engineering: B* **2013,** *178* (17), 1124-1129.

82. Kevin, P., Malik, S. N., Malik, M. A. and O'Brien, P., Growth of $Cu_2ZnSnSe_4$ and $Cu_2FeSnSe_4$ thin films by AACVD from molecular precursors. *Materials Letters* **2015,** *152*, 60-64.

83. Kevin, P., Alghamdi, Y. G., Lewis, D. J. and Malik, M .A., Morphology and band gap controlled AACVD of CdSe and CdS_xSe_{1-x} thin films using novel single source precursors:

Bis(diethyldithio/diselenocarbamato)cadmium(II). *Materials Science in Semiconductor Processing* **2015,** *40*, 848-854.

84. Hill, M. S., Johnson, A. L., Manning, T. D., Molloy, K. C. and Wickham, B. J., Single-source AACVD of composite cobalt-silicon oxide thin films. *Inorganica Chimica Acta* **2014,** *422*, 47-56.

85. Satta, A., Baklanov, M., Richard, O., Vantomme, A., Bender, H., Conard, T., Maex, K., Li, W. M., Elers, K.-E. and Haukka, S., Enhancement of ALCVD™ TiN growth on Si–O–C and α-SiC:H films by O_2-based plasma treatments. *Microelectronic Engineering* **2002,** *60* (1-2), 59-69.

86. Le Van, K., Groult, H., Mantoux, A., Perrigaud, L., Lantelme, F., Lindström, R., Badour-Hadjean, R., Zanna, S. and Lincot, D., Amorphous vanadium oxide films synthesised by ALCVD for lithium rechargeable batteries. *Journal of Power Sources* **2006,** *160* (1), 592-601.

87. Spiering, S., Hariskos, D., Powalla, M., Naghavi, N. and Lincot, D., CD-free Cu(In,Ga)Se_2 thin-film solar modules with In_2S_3 buffer layer by ALCVD. *Thin Solid Films* **2003,** *431–432*, 359-363.

88. Groult, H., Balnois, E., Mantoux, A., Le Van, K. and Lincot, D., Two-dimensional recrystallisation processes of nanometric vanadium oxide thin films grown by atomic layer chemical vapor deposition (ALCVD) evidenced by AFM. *Applied Surface Science* **2006,** *252* (16), 5917-5925.

89. Nohira, H., Tsai, W., Besling, W., Young, E., Petry, J., Conard, T., Vandervorst, W., De Gendt, S., Heyns, M., Maes, J. and Tuominen, M., Characterization of ALCVD-Al_2O_3 and

ZrO_2 layer using X-ray photoelectron spectroscopy. *Journal of Non-Crystalline Solids* **2002,** *303* (1), 83-87.

90. Besling, W. F. A., Young, E., Conard, T., Zhao, C., Carter, R., Vandervorst, W., Caymax, M., De Gendt, S., Heyns, M., Maes, J., Tuominen, M and Haukka, S., Characterisation of ALCVD Al_2O_3–ZrO_2 nanolaminates, link between electrical and structural properties. *Journal of Non-Crystalline Solids* **2002,** *303* (1), 123-133.

91. Smith, S., Li, W.-M., Elers, K.-E. and Pfeifer, K., Physical and electrical characterization of ALCVD™ TiN and WN_xC_y used as a copper diffusion barrier in dual damascene backend structures (08.2). *Microelectronic Engineering* **2002,** *64* (1-4), 247-253.

92. Spiering, S., Eicke, A., Hariskos, D., Powalla, M., Naghavi, N. and Lincot, D., Large-area Cd-free CIGS solar modules with In_2S_3 buffer layer deposited by ALCVD. *Thin Solid Films* **2004,** *451–452*, 562-566.

93. Ferrari, S., Dekadjevi, D. T., Spiga, S., Tallarida, G., Wiemer, C. and Fanciulli, M., Structural and electrical characterization of ALCVD ZrO_2 thin films on silicon. *Journal of Non-Crystalline Solids* **2002,** *303* (1), 29-34.

94. Pétry, J., Vandervorst, W. and Conard, T., The band structure of ALCVD AlZr- and AlHf-oxides as measured by XPS. *Materials Science and Engineering: B* **2004,** *109* (1-3), 56-59.

95. Cheng, H.-E. and L., W.-J., Properties of TiN films grown by atomic-layer chemical vapor deposition with a modified gaseous-pulse sequence. *Materials Chemistry and Physics* **2006,** *97* (2-3), 315-320.

96. Cheng, H.-E., Lee, W.-J. and Hsu, C.-M., The effect of deposition temperature on the properties of TiN diffusion barriers prepared by atomic layer chemical vapor deposition. *Thin Solid Films* **2005,** *485* (1-2), 59-65.

97. Puurunen, R. L., Root, A., Sarv, P., Haukka, S., IIiskola, E., Lindblad, M., Krause, A. O. I, Growth of aluminium nitride on porous silica by atomic layer chemical vapour deposition. *Applied Surface Science* **2000,** *165* (2-3), 193-202.

98. Tarre, A., Rosental, A., Sammelselg, V. and Uustare, T., Comparative study of low-temperature chloride atomic-layer chemical vapor deposition of TiO_2 and SnO_2 *Applied Surface Science* **2001,** *175-176*, 111-116.

99. Nilsen, O., Fjellvåg, H. and Kjekshus, A., Growth of calcium carbonate by the atomic layer chemical vapour deposition technique. *Thin Solid Films* **2004,** *450*, 240-247.

100. Rosental, A., Tarre, A., Gerst, A., Uustare, T. and Sammelselg, V., Atomic-layer chemical vapor deposition of SnO_2 for gas-sensing applications. *Sensors and Actuators B: Chemical* **2001,** *77* (1-2), 297-300.

101. Li, Z.-H., Cho, E.-S. and Kwon, S. J., Mg-doped ZnO thin films deposited by the atomic layer chemical vapor deposition for the buffer layer of CIGS solar cell. *Applied Surface Science* **2014,** *314*, 97-103.

102. An, J., Maurice, J.-L., Depauw, V., Roca i Cabarrocas, P. and Chen, W., Impact of PECVD-prepared interfacial Si and SiGe layers on epitaxial Si films grown by PECVD (200 °C) and APCVD (1130 °C). *Applied Surface Science* **2021,** *546*, 149056.

103. Fauzi, F. B., Ismail, E., Osman, M. N., Rosli, M. S., Ismail, A. F., Mohamed, M. A., Bakar, S. and Ani, M. H., Influence of mixed convection in atmospheric pressure chemical vapor deposition of graphene growth. *Materials Today: Proceedings* **2019,** *7*, 638-645.

104. Drosos, C. and Vernardou., D., Perspectives of energy materials grown by APCVD. *Solar Energy Materials and Solar Cells* **2015,** *140*, 1-8.

105. Shaw, G. A., Pratt, K. F. E., Parkin, I. P., and Williams, D. E., Gas sensing properties of thin film (≤3 μm) $Cr_{2-x}Ti_xO_3$ (CTO) prepared by atmospheric pressure chemical vapour deposition (APCVD), compared with that prepared by thick film screen-printing. *Sensors and Actuators B: Chemical* **2005,** *104* (1), 151-162.

106. Dagkaldiran, Ü., Gordijn, A., Finger, F., Yates, H. M., Evans, P., Sheel, D.W., Remes, Z. and Vanecek,M., Amorphous silicon solar cells made with SnO2:F TCO films deposited by atmospheric pressure CVD. *Materials Science and Engineering: B* **2009,** *159-160*, 6-9.

107. Issa, E., Nagel, H., Bartsch, J., Glatthaar,M. and Rädlein, E., Application of hydrosilane-free atmospheric pressure chemical vapor deposition of SiOx films in the manufacture of crystalline silicon solar cells. *Thin Solid Films* **2020,** *713*, 138338.

108. Beshkov, G., Lei, S., Lazarova, V., Nedev, N. and Georgiev, S. S., IR and Raman absorption spectroscopic studies of APCVD, LPCVD and PECVD thin SiN films. *Vacuum* **2002,** *69* (1–3), 301-305.

109. Naghdi, S., Nešović, K., Sánchez-Arriaga, G., Song, H.-Y., Kim, S.-W., Rhee, K.-Y., Mišković-Stanković, V., The effect of cesium dopant on APCVD graphene coating on copper. *Journal of Materials Research and Technology* **2020,** *9* (5), 9798-9812.

110. Nicolas, X., Benzaoui, A. and Xin, S., Numerical simulation of thermoconvective flows and more uniform depositions in a cold wall rectangular APCVD reactor. *Journal of Crystal Growth* **2008,** *310* (1), 174-186.

111. Vernardou, D., Paterakis, P., Drosos, H., Spanakis, E., Povey, I. M., Pemble, M. E., Koudoumas, E. and Katsarakis, N., A study of the electrochemical performance of vanadium

oxide thin films grown by atmospheric pressure chemical vapour deposition. *Solar Energy Materials and Solar Cells* **2011,** *95* (10), 2842-2847.

112. van Deelen, J., Illiberi, A., Kniknie, B., Steijvers, H., Lankhorst, A. and Simons, P., APCVD of ZnO:Al, insight and control by modeling. *Surface and Coatings Technology* **2013,** *230*, 239-244.

113. Hocine, D., Belkaid, M. S., Pasquinelli, M., Escoubas, L., Simon, J. J., Rivière, G. A. and Moussi, A., Improved efficiency of multicrystalline silicon solar cells by TiO_2 antireflection coatings derived by APCVD process. *Materials Science in Semiconductor Processing* **2013,** *16* (1), 113-117.

114. Meng, L., Hu, S., Yan, W., Feng, J., Li, H. and Yan, X., Controlled synthesis of large scale continuous monolayer WS_2 film by atmospheric pressure chemical vapor deposition. *Chemical Physics Letters* **2020,** *739*, 136945.

115. Ahmadi, S. and Afzalzadeh, R., Few-layer graphene growth from polystyrene as solid carbon source utilizing simple APCVD method. *Physica E: Low-dimensional Systems and Nanostructures* **2016,** *81*, 302-307.

116. Otani, T. and Hirata, M., High rate deposition of silicon nitride films by APCVD. *Thin Solid Films* **2003,** *442* (1-2), 44-47.

117. Vernardou, D., Louloudakis, D., Spanakis, E., Katsarakis, N. and Koudoumas, E., Thermochromic amorphous VO_2 coatings grown by APCVD using a single-precursor. *Solar Energy Materials and Solar Cells* **2014,** *128*, 36-40.

118. Agrawal, A. K., Sarkar, P. S., Singh, B., Kashyap, Y. S., Rao, P. T. and Sinha, A., Application of X-ray micro-CT for micro-structural characterization of APCVD deposited SiC coatings on graphite conduit. *Applied Radiation and Isotopes* **2016,** *108*, 133-142.

119. Remes, Z., Vanecek, M., Yates, H. M., Evans, P. and Sheel, D. W., Optical properties of SnO_2:F films deposited by atmospheric pressure CVD. *Thin Solid Films* **2009,** *517* (23), 6287-6289.

120. Kuo, D.-H. and Liao., W.-C., Ti–N, Ti–C–N, Ti–Si–N coatings obtained by APCVD at 650–800 °C. *Applied Surface Science* **2002,** *199* (1-4), 278-286.

121. Martin, P. A., Holdsworth, R. J., Sheel, D. W. and Schlatmann, R., NIR diode laser spectroscopy of HF and HCl at multiple points in the atmospheric pressure CVD of tin oxide films. **2007,** *201* (22–23), 9030-9034.

122. Lagha, K., Belkaid, M. S., Escoubas, L. and Pasquinelli, M., Elaboration of heterojunction solar cells by the deposit of tin oxide thin films on silicon by APCVD. *Thin Solid Films* **2009,** *518* (4), 1218-1221.

123. Louloudakis, D., Vernardou, D., Spanakis, E., Katsarakis, N. and Koudoumas, E., Thermochromic Vanadium Oxide Coatings Grown by APCVD at Low Temperatures. *Physics Procedia* **2013,** *46*, 137-141.

124. Karslıoğlu, R., Uysal, M. and Akbulut, H., The effect of substrate temperature on the electrical and optic properties of nanocrystalline tin oxide coatings produced by APCVD. *Journal of Crystal Growth* **2011,** *327* (1), 22-26.

125. Rao, P. T., Jain, U., Mollick, P. K., Agarwal, A., Chakravartty, J. K. and Kumar, S., Application of atmospheric CVD for internal surface coating of graphite conduit by silicon carbide. *Journal of Nuclear Materials* **2015,** *456*, 200-205.

126. Morales, C., Juarez, H., Diaz, T., Matsumoto, Y., Rosendo, E., Garcia, G., Rubin, M., Mora, F., Pacio, M. and García, A., Low temperature SnO_2 films deposited by APCVD. *586-588* **2008,** *39* (3-4), 586-588.

127. Shi, B., Liu, X.-C., Zhu, M.-X., Yang, J.-H. and Shi, E. W., Effect of propane/silane ratio on the growth of 3C-SiC thin films on Si(1 0 0) substrates by APCVD. *Applied Surface Science* **2012,** *259*, 685-690.

128. Yates, H. M., Gaskell, J. M., Thomson, M. E., Sheel, D. W., Delaup, B. and Morales-Masis, M., APCVD of dual layer transparent conductive oxides for photovoltaic applications. *Thin Solid Films* **2015,** *590*, 260-265

129. Quiñonez, C., Vallejo, W. and Gordillo, G., Structural, optical and electrochemical properties of TiO_2 thin films grown by APCVD method. *Applied Surface Science* **2010,** *256* (13), 4065-4071.

130. Black, L. E., Allen, T., McIntosh, K. R. and Cuévas, A., Improved Silicon Surface Passivation of APCVD Al_2O_3 by Rapid Thermal Annealing. **2016,** *92*, 317-325.

131. Lee, K. H., Yoo, J. H., Moon, B. Y., Jung, J. H., Jang, J., Pietruszko, S. M., Han, M. K. and Park, H. R., Low temperature fabrication of APCVD a-Si thin film transistors with ion doped layer. *Journal of Non-Crystalline Solids* **1996,** *198–200*, 1141-1145.

132. Bodurov, G., Ivanova, T., Abrashev, M., Nenova, Z. and Gesheva, K., Thin Film Optical Coatings of Vanadium Oxide and Mixed Tungsten/Vanadium Oxide Deposited by APCVD Employing Precursors of Vanadyl Acetylacetonate and a Mixture with Tungsten Hexacarbonyl. *Physics Procedia* **2013,** *46*, 127-136.

133. Hodgkinson, J. L., Massey, D. and Sheel, D. W., The deposition of copper-based thin films via atmospheric pressure plasma-enhanced CVD. *Surface and Coatings Technology* **2013,** *230*, 260-265.

134. Louloudakis, D., Vernardou, D., Spanakis, E., Katsarakis, N. and Koudoumas, E., Electrochemical properties of vanadium oxide coatings grown by APCVD on glass substrates. *Surface and Coatings Technology* **2013,** *230*, 186-189.

135. Ivanova, T., Gesheva, K. A., Sharlandjiev, P. and Koserkova-Georgieva, A., Technology and optoelectronic properties of APCVD Cr_2O_3 and Mo–Cr mixed oxide thin films. *Surface and Coatings Technology* **2007,** *201* (22–23), 9313-9318.

136. Pacio, M., Juárez, H., Escalante, G., García, G., Díaz, T. and Rosendo, E., Study of (1 0 0) orientated ZnO films by APCVD system. *Materials Science and Engineering: B* **2010,** *174* (1-3), 38-41.

137. Kambe, M., Fukawa, M., Taneda, N. and Sato, K., Improvement of a-Si solar cell properties by using SnO_2:F TCO films coated with an ultra-thin TiO_2 layer prepared by APCVD. *Solar Energy Materials and Solar Cells* **2006,** *90* (18–19), 3014-3020.

138. Milenkovic, N., Rachow, T., Janz, S. and Reber, S., Epitaxial Growth of High Quality n-type Silicon Foils in a Quasi-inline APCVD Reactor. *Energy Procedia* **2015,** *77*, 613-618.

139. Hatem, D. and Belkaid, M. S., Titanium dioxide prepared by APCVD for using as an interfacial layer in polymer solar cells. *Journal of Alloys and Compounds* **2014,** *615*, S340-S343.

140. Thomson, M., Hodgkinson J. L. and Sheel, D. W., Control of zinc oxide surface structure using combined atmospheric pressure-based CVD growth and plasma etching. *Surface and Coatings Technology* **2013,** *230*, 190-195.

141. Sahoo, R. K. and Jacob, C., Iridium catalyzed growth of vertically aligned CNTs by APCVD. *Materials Science and Engineering: B* **2014,** *185*, 99-104.

142. Wang, Y., Wua, Y., Qin, Y., Zhang, Z., Shi, C., Zhang, Q., Li, C., Xia, X., Sun, S. and Chen, L., Large-area SnO_2: F thin films by offline APCVD. *Materials Research Bulletin* **2011,** *46* (8), 1262-1265.

143. Augusto, A., Serra, F., Alves, J. M., Vallêra, A. M. and Serra, J. M., Inline Optical CVD for Silicon Deposition at Low Temperature and Atmospheric Pressure. *Energy Procedia* **2015,** *77*, 551-557.

144. Shin, Y. C. and Kong, J., Hydrogen-excluded graphene synthesis via atmospheric pressure chemical vapor deposition. *Carbon* **2013,** *59*, 439-447.

145. Hodgkinson, J. L. and Sheel, D. W., Advances in atmospheric pressure PECVD: The influence of plasma parameters on film morphology. *Surface and Coatings Technology* **2013,** *230*, 73-76.

146. Zhang, J.-I., Li, J., Luo, L. and Wo, Y., Microstructure and morphology of SiO_x film deposited by APCVD. *Journal of Alloys and Compounds* **2009,** *469* (1-2), 535-538.

147. Chai, C. C., Peng, J. and Yan, B. P., Characterization of α-Fe_2O_3 thin films deposited by atmospheric pressure CVD onto alumina substrates. *Sensors and Actuators B: Chemical* **1996,** *34* (1-3), 412-416.

148. Manole, C. C., Maury, F. and Demetrescu, I., Patterned PPy Polymer and PPy/Ag Nanocomposites Thin Films by Photo-DLICVD. *Physics Procedia* **2013,** *46*, 46-55.

149. Mungkalasiri, J., Bedel, L., Emieux, F., Vettese-DiCara, A., Freney, J., Maury, F. and Renaud, F. N. R., Antibacterial properties of TiO_2–Cu composite thin films grown by a one-step DLICVD process. *Surface and Coatings Technology* **2014,** *242*, 187-194.

150. Kumar, U. and Yadav, B. C., Synthesis of carbon nanotubes by direct liquid injection chemical vapor deposition method and its relevance for developing an ultra-sensitive room temperature based CO_2 sensor. *Journal of the Taiwan Institute of Chemical Engineers* **2019,** *96*, 652-663.

151. Boisselier, G., Maury, F. and Schuster, F., SiC coatings grown by liquid injection chemical vapor deposition using single source metal-organic precursors. *Surface and Coatings Technology* **2013,** *215*, 152-160.

152. Popa, P. L., Crêpellière, J., Leturcq, R. and Lenoble, D., Electrical and optical properties of Cu–Cr–O thin films fabricated by chemical vapour deposition. *Thin Solid Films* **2016,** *612*, 194-201.

153. Archana, P. S., Shan, Z., Pan, S. and Gupta, A., Photocatalytic water oxidation at bismuth vanadate thin film electrodes grown by direct liquid injection chemical vapor deposition method. *International Journal of Hydrogen Energy* **2017,** *42* (12), 8475-8485.

154. Guo, Z., Cai, X., Yang, C., Ruirui, N., Liao, X., Chen, Y., Zhang, Y., Luo, W., Huang, Z., Feng, Q. and Gan, Z., The preparation of cylindrical MgB_2 films on stainless steel by HPCVD for magnetic shielding. *Physica C: Superconductivity and its Applications* **2018,** *551*, 28-32.

155. Guo, X., Ni, Z., Chen, L., Hu, H., Yang, C. Feng, Q. and Liu, K., Using helium as background gas to avoid hydrogen brittleness for MgB_2 film fabrication on niobium substrate by HPCVD. *Physica C: Superconductivity and its Applications* **2016,** *524*, 13-17.

156. Yang, J., Wang, S., Yang, F. S., Zhang, Z. P., Ding, Z. and Fu, X. H., In-situ growth of superconducting MgB_2 thin films by HPCVD method at low temperature. *Physica C: Superconductivity and its Applications* **2007,** *467* (1–2), 1-3.

157. Lee, H. H., A dimensionless number for CVD processes: LPCVD versus HPCVD. *Journal of Crystal Growth* **1984,** *68* (3), 698-704.

158. Xi, X. X., Pogrebnyakov, A. V., Xu, S. Y., Chen, K., Cui, Y., Maertz, E. C., Zhuang, C. G., Li, Q., Lamborn, D. R., Redwing, J. M., Liu, Z. K., Soukiassian, A., Schlom, D. G., Weng, X. J., Dickey, E. C., Chen, Y. B., Tian, W., Pan, X. Q., Sybart, S. A. and Dynes, R. C., MgB_2 thin films by hybrid physical–chemical vapor deposition. *Physica C: Superconductivity* **2007,** *456* (1-2), 22-37.

159. Lee, T. G., Park, S. W., Seong, W. K., Huh, J. Y., Jung, S.-G., Lee, B. K., An, K.-S. and Kang, W. N., Growth of MgB_2 thin films on alumina-buffered Si substrates by using hybrid physical–chemical vapor deposition method. *Physica C: Superconductivity* **2008,** *468* (15–20), 1888-1891.

160. Ranot M. and Kang, W. N., MgB_2 coated superconducting tapes with high critical current densities fabricated by hybrid physical–chemical vapor deposition. *Current Applied Physics* **2012,** *12* (2), 353-363.

161. Chen, Y., Yang, C, Chunyan, J., Feng, Q. and Gan, Z., Thickness dependence of Jc (0) in MgB_2 films. *Physica C: Superconductivity and its Applications* **2016,** *525–526*, 56-60.

162. Hu, H., Feng, Q., Wang, Y. and Zhang, Y., The study of MgB2/BN/MgB2 trilayer films. *Physica C: Superconductivity and its Applications* **2015,** *519*, 85-88.

163. Seong, W. K. and Kang, W. N., Superconductivity of epitaxial MgB_2 thick films and MgB_2 nanowires grown by hybrid physical–chemical vapor deposition. *Physica C: Superconductivity* **2008,** *468* (15-20), 1884-1887.

164. Ranot, M., Jung, S.-G., Seong, W. K., Lee, N. H., Kang, W. N., Joo, J., Kim, C.-J., Jun, B.-H. and Oh, S., Fabrication of SiC-doped MgB_2 coated conductors by a simple process. *Physica C: Superconductivity and its Applications* **2010,** *470*, S1000-S1002.

165. Guélou, G., Martirossyan, M., Ogata, K., Ohkubo, I., Kakefuda, Y., Kawamoto, N., Kitagawa, Y., Ueda, J., Tanabe, S., Maeda, K., Nakamura, K., Aizawa, T. and Mori, T., Rapid deposition and thermoelectric properties of ytterbium boride thin films using hybrid physical chemical vapor deposition. *Materialia* **2018,** *1*, 244-248.

166. Linghu, K., Song, Q., Zhang, H., Yang, Q. Q., Zhang, J., Wu, Q., Nie, R., Dai, L., Feng, Q. and Wang, F., MgB_2 thin films grown on graphene/Ni–Mo alloy system. *Physica C: Superconductivity and its Applications* **2015,** *516*, 27-30.

167. Pham, D., Van Ngoc, H., Jung, S.-G., Kang, D. J. and Kang, W. N., Enhanced critical current density of MgB_2 thin films deposited at low temperatures by ZnO seed impurity. *Current Applied Physics* **2018,** *18* (6), 762-766.

168. Seong, W. K., Kang, W. N., Oh, S. J., Jung, J. K., Kim, C. J. and Joo, J., Superconducting property of single-crystal like MgB_2 thin film. *Physica C: Superconductivity and its Applications* **2010,** *470* (20), 1465-1467.

169. Brom, J. E., Weiss, L. Choudhury, T. H. and Redwing, J. M., Hybrid physical–chemical vapor deposition of Bi_2Se_3 films. *Journal of Crystal Growth* **2016,** *452*, 230-234.

170. Maruyama, J., Shinagawa, T., Siroma, Z. and Mineshige, A., One-pot hybrid physical–chemical vapor deposition for formation of carbonaceous thin film with catalytic activity for oxygen reduction. *Electrochemistry Communications* **2011,** *13* (12), 1451-1454.

171. Sittinger, V., Höfer, M., Harig, T., Justianto, M., Thiem, H., Vergöhl, M. and Schäfer, L., Optical grade SiO_2 films prepared by HWCVD. *Surface and Coatings Technology* **2018,** *336*, 61-66.

172. Agarwal, M., Pawar, A., Wadibhasme, N. and Dusane, R., Controlling the c-Si/a-Si:H interface in silicon heterojunction solar cells fabricated by HWCVD. *Solar Energy* **2017,** *144*, 417-423.

173. Soni. S. K., Anup Phatak and Dusane, R. O., High deposition rate device quality a-Si:H films at low substrate temperature by HWCVD technique. *Solar Energy Materials and Solar Cells* **2010,** *94* (9), 1512-1515.

174. Chaudhari, P., Meshram, N., Singh, A., Topkar, A. and Dusane, R., Hot wire chemical vapour deposition (HWCVD) of boron carbide thin films from ortho-carborane for neutron detection application. *Thin Solid Films* **2011,** *519* (14), 4561-4564.

175. Swain, B. P. and Dusane, R., Effect of substrate temperature on HWCVD deposited a-SiC:H film. *Materials Letters* **2007,** *61* (25), 4731-4734.

176. Goh, B. T. and Rahman, S. A., Synthesis of nickel catalyzed Si/SiC core–shell nanowires by HWCVD. *Journal of Crystal Growth* **2014,** *407*, 25-30.

177. Lau, K. K. S., Mao, Y., Pryce Lewis, H. G., Murthy, S. K., Olsen, B. D., Loo, L. S. and Gleason, K. K., Polymeric nanocoatings by hot-wire chemical vapor deposition (HWCVD). *Thin Solid Films* **2006,** *501* (1-2), 211-215.

178. Nazarudin, B. N. F. F., Noor, N. J. B. M., Rahman, S. A. and Goh, B. T., Photoluminescence and structural properties of Si/SiC core–shell nanowires growth by HWCVD. *Journal of Luminescence* **2015,** *157*, 149-157.

179. Gogoi, P., Jha, H. S. and Agarwal, P., Effect of Silane flow rate on microstructure of Silicon films deposited by HWCVD. *Journal of Non-Crystalline Solids* **2012,** *358* (17), 1990-1994.

180. Swain, B. P., Swain, B. S. and Hwang, N. M., Investigation of local order of a-SiN:H films deposited by hot wire chemical vapour deposition (HWCVD). *Applied Surface Science* **2008,** *255* (5), 2557-2560.

181. Mai, Y., Klein, S., Geng, X., Hülsbeck, M., Cariusa, R. and Finger, F., Differences in the structure composition of microcrystalline silicon solar cells deposited by HWCVD and PECVD: Influence on open circuit voltage. *Thin Solid Films* **2006,** *501* (1-2), 272-275.

182. Tehrani, F. S., Badaruddin, M. R., Rahbari, R. G., Muhamad, M. R. and Rahman, S. A., Low-pressure synthesis and characterization of multiphase SiC by HWCVD using CH_4/SiH_4. *Vacuum* **2012,** *86* (8), 1150-1154.

183. Dillon, A. C., Riley L. A., Jung, Y .S., Ban, C., Molina, D., Mahan, A. H., Cavanagh, A. S., George, S. M. and Lee, S.-H., HWCVD MoO_3 nanoparticles and a-Si for next generation Li-ion anodes. *Thin Solid Films* **2011,** *519* (14), 4495-4497.

184. Hope, D. A. O., Pickering, C., Carline, R. T., Leong, W. Y. and Robbins, D. J., Real-time control of layer thickness in LPCVD $Si/Si_{.88}Ge_{.12}$ HBT structures. *Thin Solid Films* **1997,** *294* (1-2), 18-21.

185. Vescan, L., Strained SiGe/Si quantum well dots and wires selectively grown by LPCVD and their optical properties. *Thin Solid Films* **1997,** *294* (1-2), 284-290.

186. Mazel, A., Marti, P., Henry, F., Armas, B., Bonnet, R. and Loubradou, M., Nanostructure and local chemical composition of $AlNSi_3N_4$ layers grown by LPCVD. *Thin Solid Films* **1997,** *304* (1-2), 256-266.

187. Bourhila, N., Torres, J., Palleau, J., Bernard, C. and Madar, R., Copper LPCVD for advanced technology. *Microelectronic Engineering* **1997,** *33* (1-4), 25-30.

188. Yan, X., Suhaimi, F. B., Xu, M., Yang, J., Zhang, X., Wang, Q., Jin, H., Shanmugam, V. and Duttagupta, S., Development of ultra-thin doped poly-Si via LPCVD and ex-situ tube diffusion for passivated contact solar cell applications. *Solar Energy Materials and Solar Cells* **2020,** *209*, 110458.

189. Calvo, J., Drescher, M., Kühnel, K., Sauer, B., Müller, M., Schmidt, C., Boui, F., Völklein, F. and Wagner-Reetz, M., LPCVD in-situ doped silicon for thermoelectric applications. *Materials Today: Proceedings* **2018,** *5* (4), 10249-10256.

190. Padhamnath, P., Nandakumar, N., Kitz, B. J., Balaji, N., Naval, M.-J., Shanmugam, V. and Duttagupta,S., High-Quality Doped Polycrystalline Silicon Using Low-Pressure Chemical Vapor Deposition (LPCVD). *Energy Procedia* **2018,** *150*, 9-14.

191. Uny, F., Achache, S., Lamri, S., Ghanbaja, J., Fischer, E., Pons, M., Blanquet, E., Schuster, F. and Sanchette, F., Deposition and characterization of (Ti, Al)N coatings deposited by thermal LPCVD in an industrial reactor. *Surface and Coatings Technology* **2019,** *358*, 923-933.

192. Faÿ, S., Steinhauser, J., Nicolay, S. and Ballif, C., Polycrystalline ZnO: B grown by LPCVD as TCO for thin film silicon solar cells. *Thin Solid Films* **2010,** *518* (11), 2961-2966.

193. Zhu, H., Jia, H., Liu, D., Feng, Y., Zhang, L., Lai, B., He, T., Ma, Y., Wang, Y., Yin, J., Huang, Y. and Mai, Y., Study of thermal stability of ZnO:B films grown by LPCVD technique. *Applied Surface Science* **2012,** *258* (16), 6018-6023.

194. Cecchini, R., Martella, C., Wiemer, C., Lamperti, A., Debernardi, A., Nasi, L., Lazzarini, L., Molle, A. and Longo, M., Vapor phase epitaxy of antimonene-like nanocrystals on germanium by an MOCVD process. *Applied Surface Science* **2021,** *535*, 147729.

195. Shimizu, M., Fujisawa, H. and Shiosaki, T., MOCVD of Pb-based ferroelectric oxide thin films. *Journal of Crystal Growth* **1997,** *174* (1-4), 464-472.

196. Kartopu, G., Fan, Q., Oklobia, O. and Irvine, S. J. C., Combinatorial study of the structural, optical, and electrical properties of low temperature deposited $Cd_{1-x}Zn_xTe$ ($0 \leq x \leq 1$) thin films by MOCVD. *Applied Surface Science* **2021,** *540*, 148452.

197. Yusof, A. S., Hassan, Z., Ng, S. S., Ahmad, M. A., Md Sahar, M. A. A. Z., Hamady, S. O. S. and Chevallier, C., The dependence of indium incorporation on specified temperatures in growing InGaN/GaN heterostructure using MOCVD technique. *Materials Research Bulletin* **2021,** *137*, 111176.

198. He, Z., Wang, H., Wang, Q., Fan, J., Zou, Y. and Ma, X., The effect of unintentional carbon incorporation on the electrical properties of AlGaAs grown by MOCVD. *Optical Materials* **2020,** *108*, 110227.

199. Sang, B., Nagoya, Y., Kushiy, K. and Yamase, O., MOCVD-ZnO windows for 30 cm×30 cm CIGS-based modules. *Solar Energy Materials and Solar Cells* **2003,** *75* (1-2), 179-184.

200. Endo, K., Badica, P. and Itoh, J., $(Ca,Ba)CuO_2$ films grown by MOCVD: surface morphology and structural studies. *Physica C: Superconductivity* **2003,** *386*, 318-322.

201. Ko, Y. K., Park, D. S., Seo, B. S., Yang, H. J., Shin, H. J., Kim, J. Y., Lee, J. H., Lee, W. H., Reucroft, P. J. and Lee, J. G., Studies of cobalt thin films deposited by sputtering and MOCVD. *Materials Chemistry and Physics* **2003,** *80* (2), 560-564.

202. Gorbenko, O. Y., Kaul, A. R., Molodyk, A. A., Fuflyigin, V. N., Novozhilov, M. A., Bosak, A. A., Krause, U. and Wahl, G., MOCVD of perovskites with metallic conductivity. *Journal of Alloys and Compounds* **1997,** *251* (1-2), 337-341.

203. Irvine, S. J. C., Barrioz, V., Lamb, D., Jones, E. W. and Rowlands-Jones, R. L., MOCVD of thin film photovoltaic solar cells—Next-generation production technology? *Journal of Crystal Growth* **2008,** *310* (23), 5198-5203.

204. Yang, C., Wang, X., Xiao, H., Zhang, X., Hu, G., Ran, J., Wang, C., Li, J., Li, J. and Wang, Z., Growth temperature dependences of InN films grown by MOCVD. *Applied Surface Science* **2008,** *255* (5), 3149-3152.

205. Jia, C., Chen, Y., Liu, G., Liu, X., Yang, S. and Wang, Z., Growth of c-oriented ZnO films on (0 0 1) $SrTiO_3$ substrates by MOCVD. *Journal of Crystal Growth* **2008,** *311* (1), 200-204.

206. Thürer, K.-H., Schreck, M., Stritzker, B., Fuchs, N. and Pongratz, P., Growth and defects of diamond facets under negative biasing conditions in a microwave plasma CVD process. *Diamond and Related Materials* **1997,** *6* (8), 1010-1014.

207. Pereira, L., Pereira, E. and Gomes, H., Photoconductivity and electrical properties of diamond films grown by MPCVD. *Diamond and Related Materials* **1998,** *7* (6), 892-898.

208. Zhang, Y. P., Gu, Y. S., Chang, X. R., Tian, Z. Z., Shi, D. X. and Zhang, X. F., Characterization of carbon nitride thin films deposited by microwave plasma chemical vapor deposition. *Surface and Coatings Technology* **2000,** *127* (2-3), 259-264.

209. Hsu, C. M., Lin, C. H., Lai, H. J., Kuo, C. T., Root growth of multi-wall carbon nanotubes by MPCVD. *Thin Solid Films* **2005,** *471* (1-2), 140-144.

210. Zhu, F., Yang, Z. X., Zhou, W. M. and Zhang, Y. F., Synthesis of beta-gallium oxide nanobelts through microwave plasma chemical vapor deposition. *Physica E: Low-dimensional Systems and Nanostructures* **2005,** *30* (1-2), 155-158.

211. Gautama, P., Toyota, H., Iwamoto, Y., Zhu, X., Nomura, S. and Mukasa, S., Synthesizing diamond film on Cu, Fe and Si substrate by in-liquid microwave plasma CVD. *Precision Engineering* **2017,** *49*, 412-420.

212. Wu, A.-M., Feng, C.-C. Huang, H., Camacho, R. A. P., Gao, S., Lei, M.-K. and Cao, G.-Z., Microwave plasma-assisted chemical vapor deposition of porous carbon film as supercapacitive electrodes. *Applied Surface Science* **2017,** *409*, 261-269.

213. Liu, X., Wang, W., Zhang, H., Wang, Y., Ren, Y., Tan, X., Sun, S. and Jia, H., La-doped diamond films prepared through microwave plasma chemical vapor deposition. *Thin Solid Films* **2019,** *692*, 137620.

214. Zheng, Y., Liu, J., Wei, J., Chen, L., Li, Z., Hao, H., Li, F., Ye, H. and Li, C., Ultra-smooth and hydrophobic nitrogen-incorporated ultranano-crystalline diamond film growth in C-H-O-N gas phase system via microwave plasma CVD. *Surface and Coatings Technology* **2019,** *374*, 409-417.

215. Zhao, X. a. G., L., Comparative analysis of graphene grown on copper and nickel sheet by microwave plasma chemical vapor deposition. *Vacuum* **2018,** *153*, 48-52.

216. Rölver, R., Winkler, O, Först, M., Spangenberg, B. and Kurz, H., Light emission from Si/SiO2 superlattices fabricated by RPECVD. *Microelectronics Reliability* **2005,** *45* (5-6), 915-918.

217. Essakhi, A., Löfberg, A., Supiot, P., Mutel, B., Paul, S., Le Courtois, V. and Bordes-Richard, E., Coating metallic foams and structured reactors by VO_x/TiO_2 oxidation catalyst: Application of RPECVD. *Studies in Surface Science and Catalysis* **2010**.

218. Fainer, N. I., Rumyantsev, Yu. M., Kosinova, M. L., Yurjev, G. S., Maximovskii, E. A. and Kuznetsov, F. A., The investigation of properties of silicon nitride films obtained by RPECVD from hexamethyldisilazane. *Applied Surface Science* **1997,** *113-114*, 614-617.

219. Parsons, G. N., Tsu, D. V. and Lucovsky, G., Optical and electrical properties of a-Si:H films grown by remote plasma enhanced chemical vapor deposition (RPECVD). *Journal of Non-Crystalline Solids* **1987,** *97-98*, 1375-1378.

220. Tsu, D. V. and Lucovsky, G., Properties of the Si:H bond-stretching absorption band in a-Si:H grown by remote plasma enhanced CVD (RPECVD). *Journal of Non-Crystalline Solids* **1987,** *97-98*, 839-842.

221. Belmonte, T., Czerwiec, T., Gavillet, J. and Michel, H., Synthesis of zirconia thin films by RPECVD: Modeling of $Ar–O_2$ post-discharge and comparison between $Ar–O_2$ and $Ar–O_2–H_2$ post-discharges processes. *Surface and Coatings Technology* **1997,** *97* (1-3), 642-648.

222. Bae, C., Rayner, G. B. and Lucovsky, G., Device-quality GaN–dielectric interfaces by 300 °C remote plasma processing. *Applied Surface Science* **2003,** *216* (1-4), 119-123.

223. Kulisch, W., Remote plasma-enhanced chemical vapour deposition with metal organic source gases: principles and applications. *Surface and Coatings Technology* **1993,** *59* (1-3), 193-201.

224. Lenkeit, B., Steckemetz, S., Artuso, F. and Hezel, R., Excellent thermal stability of remote plasma-enhanced chemical vapour deposited silicon nitride films for the rear of screen-

printed bifacial silicon solar cells. *Solar Energy Materials and Solar Cells* **2001,** *65* (1-4), 317-323.

225. Pierson, J. F., Belmonte, T., Czerwiec, T., Hertz, D. and Michel, H., Low temperature ZrB_2 remote plasma enhanced chemical vapor deposition. *Thin Solid Films* **2000,** *359* (1), 68-76.

226. Choi, S. S., Kim, D. W., Joe, J. W., Moon, J. H., Park, K. C. and Jang, J., Deposition of diamondlike carbon films by plasma enhanced chemical vapour deposition. *Materials Science and Engineering: B* **1997,** *46* (1-3).

227. Berger, S., Microstructure evolution of nanometer-sized hemispherical-grained Si deposited by RTCVD. *Materials Science and Engineering: C* **2001,** *15* (1-2), 303-305.

228. Warren, P., Dutoit, M., Boucaud, P., Lourtioz, J.-M. and Julien, F. H., RTCVD growth and characterization of SiGeC multi-quantum wells. *Thin Solid Films* **1997,** *294* (1-2), 125-128.

229. Grozdanić, D., Milat, O., Rakvin, B., Pivac, B., Slaoui, A. and Monna, R., Grain boundary defects in RTCVD polycrystalline silicon for solar cells. *Vacuum* **2001,** *61* (2-4), 257-262.

230. Möller, H., Böbel, F. G., Hertel, B., Lindenberg, T. and Ritter, G., In situ real-time temperature and thickness measurement for SiSiGe growth on MBE and RTCVD systems. *Journal of Crystal Growth* **1995,** *157* (1-4), 327-332.

231. Aubry, V., Meyer, F., Laval, R., Clerc, C., Warren, P. and Dutartre, D., Thermal stability of W on RTCVD $Si_{1-x}Ge_x$ films. *Applied Surface Science* **1993,** *73*, 285-289.

232. Guedj, C., Portier, X., Hairie, A., Bouchier, D., Calvarin, G. and Pirioue, B., Carbon and germanium distributions in $Si_{1-x-y}Ge_xC_y$ layers epitaxially grown on Si(001) by RTCVD. *Thin Solid Films* **1997,** *294* (1-2), 129-132.

233. Ribot, P. and Dutartre, D., Low-temperature selective epitaxy of silicon with chlorinated chemistry by RTCVD. *Materials Science and Engineering: B* **2002,** *89* (1-3), 306-309.

234. Warren, P., Sagnes, I., Dutartre, D., Badoz, P. A., Berroir, J. M., Guldner, Y., Vieren, J.P. and Voos, M., Charge transfer in p^+-Si / $Si_{1-x}Ge_x$ modulation doped heterostructures grown by RTCVD. *Microelectronic Engineering* **1994,** *25* (2-4), 171-176.

235. Sidiki, T., Christiansen, S. H., Chabert, S., de Boer, W. B., Ferrari, C., Strunk, H. P. and Sotomayor Torres, C. M., Optical and structural characterization of Si/SiGe heterostructures grown by RTCVD. *Thin Solid Films* **2000,** *369* (1-2).

236. Jansson, U., Ultra-high vacuum CVD of W and WSi_2 films by Si reduction of WF_6. *Applied Surface Science* **1993,** *73*, 51-57.

237. Alharthi, B., Dou, W., Grant, P. C., Grant, J. M., Morgan, T., Mosleh, A., Du, W., Li, B., Mortazavi, M., Naseem, H. and Yu, S.-Q., Low temperature epitaxy of high-quality Ge buffer using plasma enhancement via UHV-CVD system for photonic device applications. *Applied Surface Science* **2019,** *481*, 246-254.

238. Mueller, N. S., Morfa, A. J., Abou-Ras, D., Oddone, V., Ciuk, T. and Giersig, M., Growing graphene on polycrystalline copper foils by ultra-high vacuum chemical vapor deposition. *Carbon* **2014,** *78*, 347-355.

239. Wang, J., Shen, L., Lin, G., Wang, J., Xu, J., Chen, S., Xiang, G. and Li, C., Homoepitaxy of Ge on ozone-treated Ge (1 0 0) substrate by ultra-high vacuum chemical vapor deposition. *Journal of Crystal Growth* **2019,** *507*, 113-117.

240. Wang, B., Fang, Z.-Q., Claflin, B., Look, D., Kouvetakis, J. and Yeo, Y. K., Electrical characterization and deep-level transient spectroscopy of $Ge_{0.873}Si_{0.104}Sn_{0.023}$ photodiode grown on Ge platform by ultra-high vacuum chemical vapor deposition. *Thin Solid Films* **2018,** *654*, 77-84.

241. Lee, S. W., Chen, P. S., Cheng, S. L., Lee, M. H., Chang, H. T., Lee, C.-H. and Liu, C. W., Modified growth of Ge quantum dots using C_2H_4 mediation by ultra-high vacuum chemical vapor deposition. *Applied Surface Science* **2008,** *254* (19), 6261-6264.

242. Hazbun, R., Hart, J., Hickey, R., Ghosh, A., Fernando, N., Zollner, S., Adam, T. N. and Kolodzey, J., Silicon epitaxy using tetrasilane at low temperatures in ultra-high vacuum chemical vapor deposition. *Journal of Crystal Growth* **2016,** *444*, 21-27.

243. Carlsson, J.-O. and Martin. P. M., Chemical Vapour Deposition. In *Handbook of Deposition Technologies for Films and Coatings (Third Edition)*, 2010.

244. *Fundamentals of Electrochemistry*. 2nd Edition ed.; John Wiley & Sons, Inc.: 2005.

245. Rodriguez, C. A. D. and. Tremiliosi-Filho, G., Electrochemical Deposition. In *Encyclopedia of Tribology*, Ed. Springer, Boston, MA: 2013.

246. Abdel-Karim, R., Electrochemical Fabrication of Nanostructures. In *Handbook of Nanoelectrochemistry*, Ed. Springer, Cham: 2015; pp 1-20.

247. Rao, C. R. K. and Trivedi., D. C., Chemical and electrochemical depositions of platinum group metals and their applications. *Coordination Chemistry Reviews* **2005,** (249), 613–631.

248. Shanshan, H., S., Li, W., Finklea, H. and Liu, X., A review of electrophoretic deposition of metal oxides and its application in solid oxide fuel cells. *Advances in Colloid and Interface Science* **2020,** *276,* 102102

249. Love, J. C., Estroff, L. A., Kriebel, J. K., Nuzzo, R. G. and Whitesides, G. M., Self-assembled monolayers of thiolates on metals as a form of nanotechnology. *Chem. Rev.* **2005,** *105* (4), 1103-1169.

250. Borges, J. and Mano., J. F., Molecular Interactions Driving the Layer-by-Layer Assembly of Multilayers. *Chem. Rev.* **2014,** *114* (18), 8883-8942.

251. Bobb-Semple, D., Nardi, K. L., Draeger, N., Hausmann, D. N. and Bent, S. F., Area-Selective Atomic Layer Deposition Assisted by Self-Assembled Monolayers: A Comparison of Cu, Co, W, and Ru. *Chem. Mater.* **2019,** *31* (5), 1635–1645.

252. de Paula, C. B.-S., D. and Bent, S. F., Increased selectivity in area-selective ALD by combining nucleation enhancement and SAM-based inhibition. *Journal of Materials Research* **2021**.

253. Ariga, K., Nakanishi, T. and Michinobu, T., Immobilization of Biomaterials to Nano-Assembled Films (Self-Assembled Monolayers, Langmuir-Blodgett Films, and Layer-by-Layer Assemblies) and Their Related Functions. *J. Nanosci. Nanotechnol.* **2006,** *6*, 2278–2301.

254. Zasadzinski, J. A., Viswanathan, R., Madsen, L., Garnaes, J. and Schwartz, D. K., Langmuir-Blodgett films. *Science* **1994,** *263* (5154), 1726-1733.

255. Singhal, R., Chaubey, A., Kaneto, K., Takashima, W. and Malhotra, B. D., Poly-3-hexyl thiophene Langmuir-Blodgett films for application to glucose biosensor. *Biotechnology and Bioengineering* **2003,** *85* (3), 277-282.

256. Faye, N. R., Gammoudi, I., Moroté, F., Grauby-Heywang, C. and Cohen-Bouhacina, T., Phase Behavior and Structure Properties of Supported Lipid Monolayers and Bilayers in Interaction with Silica Nanoparticles. *International Scholarly and Scientific Research & Innovation* **2013,** *7* (6), 441-448.

257. Bellanger, H., Casdorff, K., Muff, L. F., Ammann, R., Burgert, I., and Michen, B., Layer-by-layer deposition on a heterogeneous surface: Effect of sorption kinetics on the growth of polyelectrolyte multilayers. *Journal of Colloid and Interface Science* **2017,** (500), 133–141.

258. Kolasinska, M., Krastev, R., Gutberlet, T. and Warszynski, P., Layer-by-Layer Deposition of Polyelectrolytes. Dipping versus Spraying. *Langmuir* **2009,** *25* (2).

259. Chiarelli, P. A., Johal, M. S., Casson, J. L., Roberts, J. B., Robinson, J. B. and Wang, H.-L., Controlled Fabrication of Polyelectrolyte Multilayer Thin Films Using Spin-Assembly. *Advanced Materials* **2001,** *13* (15), 1167-1171.

260. Li, Y., Wang, X. and Sun, J., Layer-by-layer assembly for rapid fabrication of thick polymeric films. *Chem. Soc. Rev.* **2012,** *41* (18).

261. Michel, M., Izquierdo, A., Decher, G., Voegel, J.-C., Schaaf, P. and Ball, V., Layer by Layer Self-Assembled Polyelectrolyte Multilayers with Embedded Phospholipid Vesicles Obtained by Spraying: Integrity of the Vesicles. *Langmuir* **2005,** *21* (17), 7854-7859.

262. Lee, T., Min, S. H., Gu, M., Jung, Y. K., Lee, W., Lee, J. U., Seong, D. G. and Kim, B.-S., Layer-by-Layer Assembly for Graphene-Based Multilayer Nanocomposites: Synthesis and Applications. *Chemistry of Materials* **2015,** *27* (11), 3785-3796.

263. Chapter 1 - Deposition Technologies: An Overview. In *Handbook of Deposition Technologies for Films and Coatings. Science, Applications and Technology*, Third Edition ed.; Martin, P. M., Ed. William Andrew: 2010; pp 1-31.

264. Braun, M., Magnetron Sputtering Technique. In *Handbook of Manufacturing Engineering and Technology*, Nee, A. Y. C., Ed. Springer-Verlag London: 2015; Vol. 5, pp 2929-2957.

265. Wasa, K., Kitabatake, M. and Adachi, H., *Thin Films Material Technology. Sputtering of Compound Materials*. 1 ed.; Springer-Verlag Berlin Heidelberg: 2004; p 518.

266. Thin film growth for thermally unstable noble-metal nitrides by reactive magnetron sputtering. In *Woodhead Publishing Series in Electronic and Optical Materials*, Cao, Z., Ed. Woodhead Publishing: 2011; Vol. Thin Film Growth. Physics, Materials Science and Applications, pp 185-210.

267. Bouras, K., Schmerber, G., Rinnert, H., Aureau, D., Park, H., Ferblantier, G., Colis, S., Fix, T., Park, C., Kim, K., Dinia, A. and Slaoui, A., Structural, Optical and Electrical properties of Nd-doped SnO_2 thin films fabricated by reactive magnetron sputtering for solar cell devices. *Solar Energy Materials and Solar Cells* **2015,** *145*, 134-141.

268. Taton, G., Lagrange, D., Conedera, V.,Renaud, L. and Rossi, C., Micro-chip initiator realized by integrating Al/CuO multilayer nanothermite on polymeric membrane. *J. Micromech. Microeng.* **2013,** *23* (105009).

269. Shaat, M., Effects of processing force on performance of nano-resonators produced by magnetron sputtering deposition. *Physica E: Low-Dimensional Systems and Nanostructures* **2018,** *104*, 42-48.

270. Dijkkamp, D. and Venkatesan, T., Preparation of Y-Ba-Cu oxide superconductor thin films using pulsed laser evaporation from high T_c bulk material. *Appl. Phys. Lett.* **1987,** *51* (8), 619.

271. Boyd, I. W., Thin film growth by pulsed laser deposition. *Ceramics International* **1996,** *22* (5), 429-434.

272. Liu, Z., 4.09 - Laser Applied Coatings. In *Shreir's Corrosion*, 2010; Vol. 4, pp 2622-2635.

273. Bozovic, I. and Schlom, D. G., Superconducting Thin Films: Materials, Preparation, and Properties. In *Encyclopedia of Materials: Science and Technology*, 1st Edition ed.; Buschow, K. H. J., Ed. Pergamon: 2001; pp 8955-8964.

274. Krebs, H. U., Weisheit, W., Faupel, J., Süske, E., Scharf, T., Fuhse, C., Störmer, M., Sturm, K., Seibt, M., Kijewski, H., Nelke, D., Panchenko, E. and Buback, M., Pulsed Laser Deposition (PLD) -- A Versatile Thin Film Technique. In *Advances in Solid State Physics*, Kramer, B., Ed. Springer, Berlin, Heidelberg: 2003; Vol. 43, pp 505-518.

275. Bellardita, M., Di Paola, A., Yurdakal, S., and Palmisano, L., Preparation of Catalysts and Photocatalysts Used for Similar Processes. In *Heterogeneous Photocatalysis*, Schiavello, M., Ed. John Wiley and Sons: 2019; pp 25-56.

276. Biswas, A., Sengupta, A., Rajput, U., Singh, S. K., Antad, V., Hossain, S. K., Parmar, S., Rout, D., Deshpande, A., Nair, S. and Ogale, S., Growth, Properties, and Applications of Pulsed Laser Deposited Nanolaminate Ti_3AlC_2 Thin Films. *Phys. Rev. Applied* **2020,** *13*, 044075.

277. Benetti, D., Nouar, R., Nechache, R., Pepin, H, Sarkissian, A., Rosei, F. and MacLeod, J. M., Combined magnetron sputtering and pulsed laser deposition of TiO_2 and BFCO thin films. *Sci. Rep.* **2017,** *7*, 2503.

278. Faraday, M., The Bakerian Lecture: Experimental Relations of Gold (and Other Metals) to Light. *Philosophical Transactions of the Royal Society of London* **1857,** *147*, 145-181.

279. Levy, F., Film Growth and Epitaxy: Methods. In *Encyclopedia of Condensed Matter Physics*, Elsevier Inc.: 2016; pp 210-222.

280. Mattox, D. M., Thermal Evaporation and Deposition in Vacuum. In *The Foundations of Vacuum Coating Technology2nd Edition*, William Andrew: 2018; p 378.

281. Martín-Palma, R. J. and Lakhtakia, A., Chapter 15 - Vapor-Deposition Techniques. In *Engineered Biomimicry*, Elsevier: 2013; pp 383-398.

282. Johnson, R. W., Hultqvist, A. and Bent, S. F., A brief review of atomic layer deposition: from fundamentals to applications. *Materials Today* **2014,** *17* (5), 236-246.

283. Malygin, A. A., Drozd, V. E., Malkov, A. A. and Smirnov, V. M., From V. B. Aleskovskii's "Framework" Hypothesis to the Method of Molecular Layering/Atomic Layer Deposition. *Chemical Vapour Deposition* **2015,** *21* (10-11-12), 216-240.

284. Suntola, T., Atomic Layer Epitaxy. In *Handbook of Crystal Growth*, Hurle, D. T. J., Ed. Elsevier Science Publishers B.V.: Amsterdam, 1994; Vol. 3.

285. Suntola, T. and Antson., J. International patent, FIN 52359, US 4 058 430, priority. Nov 29, 1974.

286. Ahonen, M., Pessa, M. and Suntola, T., A study of ZnTe films grown on glass substrates using an atomic layer evaporation method. *Thin Solid Films* **1980,** *65*, 301-307.

287. George, S. M., Atomic Layer Depostion: An Overview. *Chem. Rev.* **2010,** *110*, 111-131.

288. Ritala, M. and Leskela., M., Chapter 2 – Atomic layer deposition. In *Handbook of Thin Films*, Nalwa, H. S., Ed. Academic Press: San Diego, CA, 2002; Vol. Volume 1: Deposition and processing of thin films.

289. Barron, A. R. http://cnx.org/contents/rimBK1xx@2/Atomic-Layer-Deposition#id5094678. (accessed 23/03/16).

290. Puurunen, R. K., Growth Per Cycle in Atomic Layer Deposition: A Theoretical Model. *Chem. Vap. Deposition* **2003,** *9* (5), 249-257.

291. Puurunen, R. K., Surface chemistry of atomic layer deposition: A case study for the trimethylaluminum/water process. *Journal of Applied Physics* **2005,** *97* (121301).

292. Jones, A. C. and Hitchman, M. L., *Chemical Vapour Deposition: Precursors, Processes and Applications*. RSC Publishing: Royal Society of Chemistry, 2009.

293. Langereis, E., Heil, S. B. S., Knoops, H. C. M., Keuning, W., van de Sanden, M. C. M. and Kessels, W. M. M., In situ spectroscopic ellipsometry as a versatile tool for studying atomic layer deposition,. *J. of Physics D: Applied Physics* **2009,** *42*, 073001.

294. *Atomic Layer Deposition Applications 6*. 2 ed.; The Electrochemical Society: Pennington, NJ, USA, 2010; Vol. 33.

295. Sarkar, A., Potts, S. E., Rushworth, S. A., Roozeboom, F., van de Sanden, M. C. M., Kessels, W. M. M., Plasma-Enhanced ALD of TiO_2 using a Novel Cyclopentadienyl Alkylamido Precursor [$Ti(CpMe)(NMe_2)_3$] and O_2 plasma. *Electrochemical Society Transactions* **2010,** *33* (2).

296. Profijt, H. B., Potts, S. E., van de Sanden, M. C. M. and Kessels, W. M. M., Plasma-Assisted Atomic Layer Deposition: Basics, Opportunities and Challenges. *J. Vac. Sci. Technol. A* **2011,** *29* (5).

297. Potts, S. E., van den Elzen, L. R. J., Dingemans, G., Langereis, E., Keuning, W., van de Sanden, M. C. W., Kessels, W. M. M., Low Temperature Plasma-Enhanced Atomic Layer Deposition of Metal Oxide Thin Films. *Electrochemical Society Transactions* **2009,** *25* (4).

298. Tynell, T. and Karppinen, M., Atomic layer deposition of ZnO: a review. *Semicond. Sci. Technol.* **2014,** *29* (043001).

299. Kwon, S., Bang, S., Lee, S., Jeon, S., Jeong, W., Kim, H., Gong, S. C., Chang, H. J., Park, H.-H. and Jeon, H., Characteristics of the ZnO thin film transistor by atomic layer deposition at various temperatures. *Semiconductor Science and Technology* **2009,** *24* (3), 035015.

300. Bang, S., Lee, S., Jeon, S., Kwon, S., Jeong, W., Kim, H., Shin, I., Chang, H. J., Park, H.-H, and Jeon, H., Al_2O_3 buffer in a ZnO thin film transistor with poly-4-vinylphenol dielectric. *Semicond. Sci. Technol.* **2008,** *24* (2), 025008.

301. Choi, W.-S., ALD-Grown ZnO Thin-Film Transistor with a Polymeric Dielectric. *J. Korean Phy. Soc.* **2009,** *54* (2), 678-681.

302. Bang, S., Lee, S., Park, J., Park, S., Jeong, W. and Jeon, H., Investigation of the effects of interface carrier concentration on ZnO thin film transistors fabricated by atomic layer deposition. *Journal of Physics D: Applied Physics* **2009,** *42* (23).

303. Kawamura, Y., Horita, M. and Uraoka, Y., Effect of Post-Thermal Annealing of Thin-Film Transistors with ZnO Channel Layer Fabricated by Atomic Layer Deposition. *Japanese Journal of Applied Physics* **2010,** *49* (04DF19).

304. Zhao, D., Mourey, D. A. and Jackson, T. N., Fast Flexible Plastic Substrate ZnO Circuits. *IEEE Electron Device Letters* **2010,** *31* (4), 323-325.

305. Lee, S., Bang, S., Park, J., Park, S., Jeong, W. and Jeon, H., The effect of oxygen remote plasma treatment on ZnO TFTs fabricated by atomic layer deposition. *Phys. Status Solidi a* **2010,** *207* (8), 1845-1849.

306. Choi, K. M., Hyung, G. W., Yang, J. W., Koo, J. R., Kim, Y. K., Kwon, S. J. and Cho, E. S., Fabrication of Atomic Layer Deposited Zinc Oxide Thin Film Transistors with Organic Gate Insulator on Flexible Substrate. *Mol. Cryst. Liq. Cryst.* **2010,** *529* (1), 131-136.

307. Yang, J., Park, J. K., Kim, S., Choi, W., Lee, S. and Kim, H., Atomic-layer-deposited ZnO thin-film transistors with various gate dielectrics. *Phys. Status Solidi a* **2012,** *209* (10), 2087-2090.

308. Mourey, D. A., Zhao, D. A., Sun, J. and Jackson, T. N., Fast PEALD ZnO Thin-Film Transistor Circuits. *IEEE Transactions on Electron Devices* **2010,** *57* (2), 530 - 534.

309. Lim, S. J., Kim, J.-M., Kim, D., Lee, C., Park, J.-S. and Kim, H., The Effects of UV Exposure on Plasma-Enhanced Atomic Layer Deposition ZnO Thin Film Transistor. *Electrochem. Solid-State Lett.* **2010,** *13* (5), H151.

310. Zhu, C., Smith, D. J. and Nemanich, R. J., Band alignment of zinc oxide as a channel layer in a gate stack structure grown by plasma enhanced atomic layer deposition. *J. Vac. Sci. Technol. B* **2012,** *30* (5), 051807.

311. Kawamura, Y., Tani, M., Hattori, N., Miyatake, N., Horita, M., Ishikawa, Y. and Uraoka, Y., Low-Temperature-Processed Zinc Oxide Thin-Film Transistors Fabricated by Plasma-Assisted Atomic Layer Deposition. *Japan. J. Appl. Phys.* **2012,** *51* (25), 02BF04.

312. Chaisitsak, S., Sugiyama, T., Yamada, A. and Konagai, M., Cu(InGa)Se_2 Thin-film Solar Cells with High Resistivity ZnO Buffer Layers Deposited by Atomic Layer Deposition. *Japan. J. Appl. Phys.* **1999,** *38*, 4989.

313. Canava, B., Guillemoles, J.-F., Yousfi, E.-B., Cowache, P., Kerber, H., Loeffl, A., Schock, H.-W., Powalla, M., Hariskos, D. and Lincot, D., Wet treatment based interface engineering for high efficiency Cu(In,Ga)Se_2 solar cells. *Thin Solid Films* **2000,** *361-362*, 187-192.

314. Chaisitsak, S., Yamada, A., Konagai, M. and Saito, K., Improvement in Performances of ZnO:B/i-ZnO/Cu(InGa)Se_2 Solar Cells by Surface Treatments for Cu(InGa)Se_2. *Japan. J. Appl. Phys.* **2000,** *39*, 1660.

315. Shimizu, A., Chaisitsak, S., Sugiyama, T., Yamada, A. and Konagai, M., Zinc-based buffer layer in the Cu(InGa)Se_2 thin film solar cells. *Thin Solid Films* **2000,** *361-362*, 193-197.

316. Malm, U., Malmstrom, J., Platzer-Bjorkman, C. and Stolt, L., Determination of dominant recombination paths in Cu(In,Ga)Se_2 thin-film solar cells with ALD–ZnO buffer layers. *Thin Solid Films* **2005,** *480-481*, 208-212.

317. Platzer-Bjorkman, C., Torndahl, T., Abou-Ras, D., Malmstrom, J., Kessler, J. and Stolt, L. , Zn(O,S) buffer layers by atomic layer deposition in Cu(In,Ga)Se_2 based thin film solar cells: Band alignment and sulfur gradient. *Journal of Applied Physics* **2006,** *100* (4), 044506.

318. Wang, J.-C., Weng, W.-T., Tsai, M.-Y., Lee, M.-K., Horng, S.-F., Perng, T.-P., Kei, C.-C., Yu, C.-C. and Meng, H.-F., Highly efficient flexible inverted organic solar cells using atomic layer deposited ZnO as electron selective layer. *J. Mater. Chem.* **2010,** *20* (5), 862-866.

319. Stakhira, P. I., Pakhomov, G. L., Cherpak, V. V., Volynyuk, D., Luka, G., Godlewski, M., Guziewicz, E. and Hotra, Z. Y., Photovoltaic cells based on nickel phthalocyanine and zinc oxide formed by atomic layer deposition. *Cent. Eur. J. Phys.* **2010,** *8*, 798–803.

320. Stakhira, P. Y., Grygorchak, I. I., Cherpak, V. V., Ivastchyshyn, F. O., Volynyuk, D. Y., Luka, G., Godlewski, M., Guziewicz, E., Pakhomov, G. L. and Hotra, Z. Y., Long time stability of ITO/NiPc/ZnO/Al devices with ZnO buffer layer formed by atomic layer deposition technique–impedance spectroscopy analysis. *Mater. Sci. Eng. B* **2010,** *172* (3), 272-275.

321. Cheun, H., Fuentes-Hernandez, C., Zhou, Y., Potscavage, W. J. Jr., Kim, S.-J., Shim, J., Dindar, A. and Kippelen, B., Electrical and Optical Properties of ZnO Processed by Atomic Layer Deposition in Inverted Polymer Solar Cells. *J. Phys. Chem. Commun.* **2010,** *114* (48), 20713–20718.

322. Park, S.-Y., Seo, H. O., Kim, K.-D., Lee, J. E., Kwon, J.-D., Kim, Y. D. and Lim, D. C., Organic photovoltaics with high stability sustained for 100 days without encapsulation fabricated using atomic layer deposition. *Phys. Status Solidi RRL* **2012,** *6* (5), 196-198.

323. Lim, D. C., Kim, K.-D., Park, S.-Y., Hong, E. M., Seo, H.O., Lim, J. H., Lee, K. H., Jeong, Y., Song, C., Lee, E., Kim, Y. D. and Cho, S., Towards fabrication of high-performing organic photovoltaics: new donor-polymer, atomic layer deposited thin buffer layer and plasmonic effects. *Energy Environ. Sci.* **2012,** *5* (12), 9803-9807.

324. Kang, Y.-J., Kim, C. S., Kwack, W.-S., Ryu, S. Y., Song, M., Kim, D.-H., Hong, S. W., Jo, S., Kwon, S.-H. and Kang, J.-W., Air-Stable Inverted Organic Solar Cells with an Ultrathin Electron-Transport Layer Made by Atomic Layer Deposition. *ECS Solid State Lett.* **2012,** *1*.

325. Tetreault, N., Heiniger, L.-P., Stefik, M., Labouchere P. P., Arsenault, É., Nazeeruddin, N. K., Ozin, G. A. and Gratzel, M., (Invited) Atomic Layer Deposition for Novel Dye-Sensitized Solar Cells. *ECS Trans.* **2011,** *41*.

326. Williams, V. O., Jeong, N. C., Prasittichai, C., Farha, O. K., Pellin, M. J. and Hupp, J. T., Fast Transporting ZnO–TiO_2 Coaxial Photoanodes for Dye-Sensitized Solar Cells Based on ALD-Modified SiO2 Aerogel Frameworks. *ACS Nano* **2012,** *6* (7), 6185–6196.

327. Ding, J., Li, Y., Hu, H., Bai, L., Zhang, S. and Yuan, N., The influence of anatase-rutile mixed phase and ZnO blocking layer on dye-sensitized solar cells based on TiO_2 nanofiberphotoanodes. *Nanoscale Res. Lett.* **2013,** *8* (9).

328. Wu, M. K., Shih, Y. T., Li, W. C., Chen, H. C., Chen, M. J., Kuan, H., Yang, J. R. and Shiojiri, M., Ultraviolet Electroluminescence From n-ZnO–SiO_2–ZnO Nanocomposite/p-GaN Heterojunction Light-Emitting Diodes at Forward and Reverse Bias. *IEEE Photonics Technol. Lett.* **2008,** *20* (21), 1772 - 1774.

329. Shih, Y. T., Wu, M. K., Li, W. C., Kuan, H., Yang, J. R., Shiojiri, M. and Chen, M. J., Amplified spontaneous emission from ZnO in n-ZnO/ZnO nanodots–SiO_2 composite/p-AlGaN heterojunction light-emitting diodes. *Nanotechnology* **2009,** *20,* 165201.

330. Chen, H.-C., Chen, M.-J., Wu, M.-K., Li, W.-C., Tsai, H.-L., Yang, J.-R., Kuan, H. and Shiojiri, M., UV Electroluminescence and Structure of n-ZnO/p-GaN Heterojunction LEDs Grown by Atomic Layer Deposition. *IEEE J. Quantum Electron.* **2010,** *46* (2), 265 - 271.

331. Chen, H. C., Chen, M. J., Huang, Y. H., Sun, W. C., Li, W. C.,Yang, J. R., Kuan, H. and Shiojiri, M., White-Light Electroluminescence From n-ZnO/p-GaN Heterojunction Light-Emitting Diodes at Reverse Breakdown Bias. *IEEE Trans. Electron Devices* **2011,** *58* (11), 3970 - 3975.

332. Chen, M.-J., Yang, J.-R. and Shiojiri, M. , ZnO-based ultra-violet light emitting diodes and nanostructures fabricated by atomic layer deposition. *Semicond. Sci. Technol.* **2012,** *27* (7), 074005.

333. Wang, T., Wu, H., Wang, Z., Chen, C. and Liu, C., Improvement of optical performance of ZnO/GaN p-n junctions with an InGaN interlayer. *Appl. Phys. Lett.* **2012,** *101*, 161905.

334. Wang, T., Wu, H., Wang, Z., Chen, C. and Liu, C., Blue light emission from the heterostructured ZnO/InGaN/GaN. *Nanoscale Res. Lett.* **2013,** *8* (99).

335. Chien, J.-F., Liao, H.-Y., Yu, S.-F., Lin, R.-M., Shiojiri, M., Shyue, J.-J. and Chen, M.-J., Ultraviolet Electroluminescence from Nitrogen-Doped ZnO-Based Heterojuntion Light-Emitting Diodes Prepared by Remote Plasma in situ Atomic Layer-Doping Technique. *ACS Appl. Mater. Interfaces* **2013,** *5* (2), 227-232.

336. Wang, T., Wu, H., Zheng, H., Wang, J. B., Wang, Z., Chen, C., Xu, Y. and Liu, C., Nonpolar light emitting diodes of m-plane ZnO on c-plane GaN with the Al_2O_3 interlayer. *Appl. Phys. Lett.* **2013,** *102*, 141912.

337. Kohan, A. F., Ceder, G., Morgan, D. and Van de Walle, C. G., First-principles study of native point defects in ZnO. *Phys. Rev. B* **2000,** *61* (15019).

338. Van de Walle, C. G., Defect analysis and engineering in ZnO. *Physica B: Condensed Matter* **2001,** *308-310*, 899-903.

339. Janotti, A. and Van de Walle, C. G., New insights into the role of native point defects in ZnO. *Journal of Crystal Growth* **2006,** *287* (1), 58-65.

340. Cho, S., Kim, D.-H., Lee, B.-S., Jung, J., Yu, W.-R., Hong, S.-H. and Lee, S. , Ethanol sensors based on ZnO nanotubes with controllable wall thickness via atomic layer deposition, an O_2 plasma process and an annealing process. *Sensors Actuators B* **2012,** *162* (1), 300-306.

341. Choi, S.-W., Park, J. Y. and Kim, S. S., Synthesis of SnO_2–ZnO core–shell nanofibers via a novel two-step process and their gas sensing properties. *Nanotechnology* **2009,** *20* (46), 465603.

342. Park, J. Y., Choi, S.-W. and Kim, S. S. , A model for the enhancement of gas sensing properties in SnO_2–ZnO core–shell nanofibres. *J. Phys. D: Appl. Phys.* **2011,** *44*, 205403.

343. Singh, U., Lee, H. A., Byun, Y.-C., Kumar, A., Seal, S., Kim, H. and Cho, H. J., ZnO Modified High Aspect Ratio Carbon Electrodes for Hydrogen Sensing Applications. *Procedia Eng.* **2011,** *25*, 1669-1672.

344. Güder, F., Yang. Y., Menzel, A., Wang, C., Danhof, J., Subannajui, K., Hartel, H., Hiller, D., Kozhummal, R., Ramgir, N. S., Cimalla, V., Schwarz, U. T., Zacharias, M., Superior Functionality by Design: Selective Ozone Sensing Realized by Rationally Constructed High-Index ZnO Surfaces. *Small* **2012,** *8* (21), 3307-3314.

345. Coleman, V. A. and Jagadish, C., Chapter 1 - Basic Properties and Applications of ZnO. In *Zinc Oxide Bulk, Thin Films and Nanostructures. Processing, Properties and Applications*, Pearton, C. J. a. S., Ed. 2016; pp 1-20.

346. Dixon, S. C., Scanlon, D. O., Carmalt, C. J. and Parkin, I. P., n-Type doped transparent conducting binary oxides: an overview. *J. Mater. Chem. C* **2016,** *4* (29), 6946-6961.

347. Ellmer, K., Klein, A. and Rech, B., Transparent Conductive Zinc Oxide Basics and Applications in Thin Film Solar Cells Springer, Heidelberg: 2008; Vol. 104.

348. Minami, T., Transparent Conducting Oxide Semiconductors for Transparent Electrodes. *Semicond. Sci. Technol.* **2005,** *20* (4), S35-S44.

349. Malm, J., Sahramo, E., Perala, J., Sajavaara, T. and Karppinen, M., Low-temperature atomic layer deposition of ZnO thin films: Control of crystallinity and orientation. *Thin Solid Films* **2011,** *519* (16), 5319-5322.

350. Yuan, N. Y., Wang, S. Y., Tan, C. B., Wang, X. Q., Chen, G. G. and Ding, J. N., The influence of deposition temperature on growth mode, optical and mechanical properties of ZnO films prepared by the ALD method. *J. Cryst. Growth* **2013,** *366*, 43-46.

351. Yousfi, E. B., Fouache, J. and Lincot, D., Study of atomic layer epitaxy of zinc oxide by in-situ quartz crystal microgravimetry. *Appl. Surf. Sci.* **2000,** *153* (4), 223-234.

352. Jeon, S., Bang, S., Lee, S., Kwon, S., Jeong, W., Jeon, H., Chang, H. J. and Park, H.-H., Structural and Electrical Properties of ZnO Thin Films Deposited by Atomic Layer Deposition at Low Temperatures. *J. Electrochem. Soc.* **2008,** *155* (10), H738.

353. Pung, S.-Y., Choy, K.-L., Hou, X. and Shan, C., Preferential growth of ZnO thin films by the atomic layer deposition technique. *Nanotechnology* **2008,** *19* (43), 435609.

354. Makino, H., Miyake, A., Yamada, T., Yamamoto, N. and Yamamoto, T., Influence of substrate temperature and Zn-precursors on atomic layer deposition of polycrystalline ZnO films on glass. *Thin Solid Films* **2009,** *517* (10), 3138-3142.

355. Guziewicz, E., Kowalik, I. A., Godlewski, M., Kopalko, K., Osinniy, V., Wojcik, A., Yatsunenko, S., Łusakowska, E., Paszkowicz, W. and Guziewicz, M., Extremely low temperature growth of ZnO by atomic layer deposition. *J. Appl. Phys.* **2008,** *103* (3), 033515.

356. Baji, Z., Lábadi, Z., Horváth, Z. E., Fried, M., Szentpáli, B. and Bársony, I., Temperature dependent in situ doping of ALD ZnO. *J. Therm. Anal. Calorim.* **2011,** *105*, 93–99.

357. Park, S.-H. K. and Lee, Y. E., Controlling preferred orientation of ZnO thin films by atomic layer deposition. *J. Mater. Sci.* **2004,** *39*, 2195–2197.

358. Thomas, M. A. and Cui, J. B., Highly Tunable Electrical Properties in Undoped ZnO Grown by Plasma Enhanced Thermal-Atomic Layer Deposition. *ACS Appl. Mater. Interfaces* **2012,** *4* (6), 3122–3128.

359. Tammenmaa, M., Koskinen, T. Hiltunen, L., Niinisto, L. and Leskala, M. , Zinc chalcogenide thin films grown by the atomic layer epitaxy technique using zinc acetate as source material. *Thin Solid Films* **1985,** *124* (2), 125-128.

360. Guziewicz, E., Godlewski, M., Krajewski, T., Wachnicki, L., Szczepanik, A., Kopalko, K., Wójcik-Głodowska, A., Przeździecka, E., Paszkowicz, W., Łusakowska, E., Kruszewski, P., Huby, N., Tallarida, G. and Ferrari, S., ZnO grown by atomic layer deposition: A material for transparent electronics and organic heterojunctions. *J. Appl. Phys.* **2009,** *105* (122413).

361. Wojcik, A., Godlewski, M., Guziewicz, E., Minikayev, R. and Paszkowicz, W., Controlling of preferential growth mode of ZnO thin films grown by atomic layer deposition. *J. Cryst. Growth* **2008,** *310* (2), 284-289.

362. Lujala, V., Skarp, J., Tammenmaa, M. and Suntola, T., Atomic layer epitaxy growth of doped zinc oxide thin films from organometals. *Appl. Surf. Sci.* **1994,** *82-83*, 34-40.

363. Kim, L. H., Kim, K., Park, S., Jeong, Y. J., Kim, H., Chung, D. S., Kim, S. H. and Park, C. E., Al_2O_3/TiO_2 nanolaminate thin film encapsulation for organic thin film transistors via plasma-enhanced atomic layer deposition. *ACS Appl Mater Interfaces* **2014,** *6* (9), 6731-8.

364. Yamada, A., Sang, B. and Konagai, M., Atomic layer deposition of ZnO transparent conducting oxides. *Appl. Surf. Sci.* **1997,** *112*, 216-222.

365. Saito, K., Watanabe, Y., Takahashi, K., Matsuzawa, T., Sang, B. and Konagai, M., Photo atomic layer deposition of transparent conductive ZnO films. *Sol. Energy Mater. Sol. Cells* **1997,** *49* (1-4), 187-193.

366. Ott, A. W. and Chang, R. P. H., Atomic layer-controlled growth of transparent conducting ZnO on plastic substrates. *Mater. Chem. Phys* **1999,** *58* (2), 132-138.

367. Elam, J. W., Sechrist, Z. A. and George, S. M., ZnO/Al_2O_3 nanolaminates fabricated by atomic layer deposition: growth and surface roughness measurements. *Thin Solid Films* **2002,** *414*, 43-55.

368. Park, S.-H. K. and Lee, Y. E., Controlling preferred orientation of ZnO thin films by atomic layer deposition. *J. Mater. Sci.* **2004,** *39*, 2195-2197.

369. Lim, J. and Lee, C., Effects of substrate temperature on the microstructure and photoluminescence properties of ZnO thin films prepared by atomic layer deposition. *Thin Solid Films* **2007,** *515* (7-8), 3335-3338.

370. Makino, H., Kishimoto, S., Yamada, T., Miyake, A., Yamamoto, N. and Yamamoto, T., Effects of surface pretreatment on growth of ZnO on glass substrate. *Phys. Status Solidi a* **2008,** *205* (8), 1971-1974.

371. Krajewski, T., Guziewicz, E., Godlewski, M., Wachnicki, L., Kowalik, I. A., Wojcik-Glodowska, A., Lukasiewicz, M., Kopalko, K., Osinniy, V. and Guziewicz, M., The influence of growth temperature and precursors' doses on electrical parameters of ZnO thin films grown by atomic layer deposition technique. *Microelectron. J.* **2009,** *40* (2), 293-295.

372. Rowlette, P. C., Allen, C. G., Bromley, O. B., Dubetz, A. E. and Wolden, C. A., Plasma-Enhanced Atomic Layer Deposition of Semiconductor Grade ZnO Using Dimethyl Zinc. *9 Chem. Vapor Depos.* **2009,** *15* (1-3), 15-20.

373. Luka, G., Krajewski, T., Wachnicki, L., Witkowski, B., Lusakowska, E., Paszkowicz, W., Guziewicz, E. and Godlewski, M., Transparent and conductive undoped zinc oxide thin films grown by atomic layer deposition. *Phys. Status Solidi a* **2010,** *207* (7), 1568-1571.

374. Guziewicz, E., Godlewski, M., Krajewski, T. A., Wachnicki, L., Łuka, G., Domagała, J. Z., Paszkowicz, W., Kowalski, B. J., Witkowski, B. S., Dużyńska, A., and Suchocki, A., Zinc oxide grown by atomic layer deposition – a material for novel 3D electronics. *Phys. Status Solidi b* **2010,** *247* (7), 1611-1615.

375. Gong, S. C., Bang, S., Jeon, H., Park, H.-H., Chang, Y.-C. and Chang, H. J., Effects of atomic layer deposition temperatures on structural and electrical properties of ZnO films and its thin film transistors. *Met. Mater. Int* **2010,** *16*, 953–958.

376. Kim, J.-E., Bae, S.-M., Yang, H. and Hwang, J.-H. , Electrical and Optical Properties of Zinc Oxide Thin Films Deposited Using Atomic Layer Deposition. *J. Korean Ceram. Soc.* **2010,** *47* (4), 353.

377. Min Y.-S., An, C.-J., Kim, S.-K., Song, J.-W. and Hwang, C.-S., Growth and Characterization of Conducting ZnO Thin Films by Atomic Layer Deposition. *Bull. Korean Chem. Soc.* **2010,** *31* (9), 2503-2508.

378. Chiang, T.-Y., Dai, C.-L. and Lian, D.-M., Influence of growth temperature on the optical and structural properties of ultrathin ZnO films. *J. Alloys Compounds* **2011,** *509* (18), 5623-5626.

379. Cheng, Y.-C., Kuo, Y.-S., Li, Y.-H., Shyue, J.-J. and Chen, M.-J., Stable p-type ZnO films grown by atomic layer deposition on GaAs substrates and treated by post-deposition rapid thermal annealing. *Thin Solid Films* **2011,** *519* (16), 5558-5561.

380. Kudrawiec, R., Misiewicz, J., Wachnicki, Ł., Guziewicz, E. and Godlewski, M., Contactless electroreflectance of ZnO layers grown by atomic layer deposition at low temperature. *Semicond. Sci. Technol.* **2011,** *26* (7), 075012.

381. Janocha, E. and Pettenkofer, C., ALD of ZnO using diethylzinc as metal-precursor and oxygen as oxidizing agent. *Appl. Surf. Sci.* **2011,** *257* (13), 10031-10035.

382. Tapily, K., Gu, D., Baumgart, H., Namkoong, G., Stegall, D. and Elmustafa, A. A., Mechanical and structural characterization of atomic layer deposition-based ZnO films. *Semicond. Sci. Technol.* **2011,** *26*, 115005.

383. Lin, M.-C., Wu, M.-K., Yuan, K.-Y., Chen, M.-J., Yang, J.-R. and Shiojiri, M., Structural and Photoluminescence Properties of ZnO Films Grown on 6H-SiC Substrates by Low-Temperature Atomic Layer Deposition. *J. Electrochem. Soc.* **2011,** *158* (H1213).

384. Pradhan, K. and Lyman., P. F., Study of Atomic Layer Deposition of ZnO on a Polar Oxide Substrate by In Situ Quartz Crystal Microbalance. *ECS Trans.* **2011,** *41* (2), 247.

385. Wang, T., Wu, H., Chen, C. and Liu, C., Growth, optical, and electrical properties of nonpolar m-plane ZnO on p-Si substrates with Al_2O_3 buffer layers. *Appl. Phys. Lett.* **2012,** *100* (1), 011901.

386. Illiberi, A., Roozeboom, F. and Poodt, P., Spatial Atomic Layer Deposition of Zinc Oxide Thin Films. *ACS Appl. Mater. Interfaces* **2012,** *4* (1), 268-272.

387. Mousa, M. B. M., Oldham, C. J., Jur, J. S. and Parsons, G. N., Effect of temperature and gas velocity on growth per cycle during Al_2O_3 and ZnO atomic layer deposition at atmospheric pressure. *J. Vac. Sci. Technol. A* **2012,** *30* (1), 01A155.

388. Zhimin, C., Xinchun, L. and Dannong, H., Atomic layer deposition of zinc oxide films: Effects of nanocrystalline characteristics on tribological performance. *Surf. Coat. Technol.* **2012,** *207*, 361-366.

389. Baji, Z., Labadi, Z., Horváth, Z. E., Molnár, G., Volk, J., Bársony, I. and Barna, P., Nucleation and Growth Modes of ALD ZnO. *Cryst. Growth Des* **2012,** *12* (11), 5615–5620.

390. Lee, W.-J., Bera, S., Wan, Z., Dai, W., Bae, J.-S., Hong, T. E., Kim, K.-H., Ahn, J.-H. and Kwon, S. H., Comparative study of the electrical characteristics of ALD-ZnO thin films using H_2O and H_2O_2 as the oxidants. *Journal of the American Ceramic Society* **2019,** *102* (10), 5881-5889.

391. Lee, S., Im, Y. H., Kim, S. H. and Hahn, Y. B., Structural and optical properties of high quality ZnO films on Si grown by atomic layer deposition at low temperatures. *Superlattice Microstruct.* **2006,** *39* (1-4), 24-32.

392. Kim, D., Kang, H., Kim, J.-M. and Kim, H., The properties of plasma-enhanced atomic layer deposition (ALD) ZnO thin films and comparison with thermal ALD. *Appl. Surf. Sci.* **2011,** *257* (8), 3776-3779.

393. Park, S.-H. K., Hwang, C.-S., Kwack, H.-S., Lee, J.-H. and Chu, H. Y., Characteristics of ZnO Thin Films by Means of Plasma-Enhanced Atomic Layer Deposition. *Electrochem. Solid State* **2006,** *9* (10), G299.

394. Kim, C. R., Lee, J. Y., Shin, C. M., Leem, J. Y., Ryu, H., Chang, J. H., Lee, H. C., Son, C. S., Lee, W. J., Jung, W. G., Tan, S. T., Zhao, J. L. and Sun, X. W., Effects of annealing

temperature of buffer layer on structural and optical properties of ZnO thin film grown by atomic layer deposition. *Solid State Commun.* **2008,** *148* (9-10), 395-398.

395. Kawamura, Y., Hattori, N., Miyatake, N., Horita, M. and Uraoka, Y., ZnO Thin Films Fabricated by Plasma-Assisted Atomic Layer Deposition. *Japan. J. Appl. Phys.* **2011,** *50*, 04DF05.

396. Kawamura, Y., Hattori, N., Miyatake, N. and Uraoka, Y., Comparison between ZnO films grown by plasma-assisted atomic layer deposition using H_2O plasma and O_2 plasma as oxidant. *J. Vac. Sci. Technol. A* **2013,** *31* (1).

397. Sultan, S. M., Clark, O. D., Masaud, T. B., Fang, Q., Gunn, R., Hakim, M. M. A., Sun, K., Ashburn, P. and Chong, H. M. H., Remote plasma enhanced atomic layer deposition of ZnO for thin film electronic applications. *Microelectron. Eng.* **2012,** *97*, 162-165.

398. Kim, S. K., Hwang, C. S., Park, S.-H. K. and Yun, S. J., Comparison between ZnO films grown by atomic layer deposition using H_2O or O_3 as oxidant. *Thin*

Solid Films **2005,** *478* (1-2), 103-108.

399. Park, J., Jung, T. H., Lee, J. H., Kim, H. S. and Park, J. S., The growth behavior and properties of atomic layer deposited zinc oxide films using hydrogen peroxide (H_2O_2) and ozone (O_3) oxidants. *Ceramics International* **2015,** *41* (1), 1839-1845.

400. Lin, P.-Y., Gong, J.-R., Li, P.-C., Lin, T.-Y., Lyu, D.-Y., Lin, D.-Y., Lin, H.-J., Li, T.-C., Chang, K.-J. and Lin, W.-J., Optical and structural characteristics of ZnO films grown on (0 0 0 1) sapphire substrates by ALD using DEZn and N_2O. *J. Cryst. Growth* **2008,** *310* (12), 3024-3028.

401. Lin, Y.-T., Chung, P.-H., Lai, H.-W., Su, H.-L., Lyu, D.-Y., Yen, K.-Y., Lin, T.-Y., Kung, C.-Y. and Gong, J.-R., Self-limiting growth of ZnO films on (0 0 0 1) sapphire substrates by atomic layer deposition at low temperatures using diethyl-zinc and nitrous oxide. *Appl. Surf. Sci.* **2009,** *256* (3), 819-822.

402. Chung, P.-H., Lai, H.-W., Lin, Y.-T., Yen, K.-Y., Kung, C.-Y. and Gong, J.-R., Observation of Self-limiting Regime in the Atomic Layer Deposition of ZnO Films using Nitrous Oxide as the Oxygen Supply. *ECS Trans.* **2009,** *19* (3), 167.

403. Yen, K.-Y., Liu, K.-P., Lin, Y.-T., Gong, J.-R., Tsai, K.-Y., Lyu, D.-Y., Lin, T.-Y., Liang, S.-C., Ni, G.-Y. and Jih, F.-W., On the Characteristics of Zinc Oxide Films Grown on (11-20) Sapphire Substrates by Atomic Layer Deposition Using Diethylzinc and Nitrous Oxide. *ECS Trans.* **2009,** *19* (2), 843.

404. Kwon, S.-K., Kim, D.-W., Jung, Y.-H. and Lee, B.-J., Effect of Process Parameters on Remote PEALD for HighlyTransparent ZnO Film Growth. *J. Korean Phys. Soc.* **2009,** *55* (3), 999-1004.

405. Huang, H.-W., Chang, W.-C., Lin, S.-J. and Chueh, Y.-L., Growth of controllable ZnO film by atomic layer deposition technique via inductively coupled plasma treatment. **2011,** *112*, 124102.

406. Wang, Y., Kang, K. M., Kim, M. and Park, H. H., Effective oxygen-defect passivation in zno thin films prepared by atomic layer deposition using hydrogen peroxide. *Journal of the Korean Ceramic Society* **2019,** *56* (3), 302-307.

407. Nam, T., Kim, J.-M., Kim, M.-K., Kim, H. and Kim, W.-H. , Low-temperature Atomic Layer Deposition of TiO_2, Al_2O_3, and ZnO Thin Films. *J. Korean Phys. Soc.* **2011,** *59* (2), 452-457.

408. Tanskanen, J. T., Bakke, J. R., Pakkanen, T. A. and Bent, S. F., Influence of organozinc ligand design on growth and material properties of ZnS and ZnO deposited by atomic layer deposition. *J. Vac. Sci. Technol. A* **2011,** *29* (3), 031507.

409. Kopalko, K., Wojcik, A., Godlewski, M., Łusakowska, E., Paszkowicz, W., Domagała, J. Z., Godlewski, M. M., Szczerbakow, A., Swiatek, K. and Dybko, K., Growth by atomic layer epitaxy and characterization of thin films of ZnO. *Phys. Status Solidi* **2005,** *2* (3), 1125-1130.

410. Kopalko, K., Godlewski, M., Domagala, J. Z., Lusakowska, E., Minikayev, R., Paszkowicz, W. and Szczerbakow, A., Monocrystalline ZnO Films on GaN/Al_2O_3 by Atomic Layer Epitaxy in Gas Flow. *Chem. Mater.* **2004,** *16* (8), 1447-1450.

411. Kopalko, K., Godlewski, M., Guziewicz, E., Łusakowska, E., Paszkowicz, W., Domagała, J., Dynowska, E., Szczerbakow, A., Wójcik, A. and Phillips, M. R., Monocrystalline thin films of ZnSe and ZnO grown by atomic layer epitaxy. *Vacuum* **2004,** *74* (2), 269-272.

412. An, K.-S., Cho, W., Lee, B. K., Lee, S. S. and Kim, C. G., Atomic Layer Deposition of Undoped and Al-Doped ZnO Thin Films Usingthe Zn Alkoxide Precursor Methylzinc Isopropoxide. *J. Nanosci. Nanotechnol.* **2008,** *8* (9), 4856-4859.

413. Thampaphat, K., Limsuwan, P.; Ngotawornchai, B., Phase Characterization of TiO_2 Powder by XRD and TEM. *Nat. Sci.* **2008,** *42*, 357-361.

414. Luttrell, T., Halpegamage, S., Tao, J.; Kramer, A., Sutter, E.; Batzill, M., Why is anatse a better photocatalyst than rutile? – Model studies on epitaxial films. *Scientific Reports* **2014,** *4* (4043).

415. Guo, J., Van Bui, H., Valdesueiro, D., Yuan, S., Liang, B., and van Ommen, J. R., Suppressing the Photocatalytic Activity of TiO_2 Nanoparticles by Extremely Thin Al_2O_3 Films

Grown by Gas-Phase Deposition at Ambient Conditions. *Nanomaterials (Basel)* **2018,** *8* (2), 61.

416. Suntola, T. and Hyvarinen., J., Atomic Layer Epitaxy. *Ann. Rev. Mater. Sci.* **1985,** *15*, 177-195.

417. Lakomaa, E. L., Haukka, S. and Suntola, T., Atomic layer growth of TiO2 on silica. *Applied Surface Science* **1992,** *60*, 742–748.

418. Ritala, M., Leskela, M., Nykanen, E., Soininen, P. and Niinisto, L., Growth of titanium dioxide thin films by atomic layer epitaxy. *Thin Solid Films* **1993,** *225*, 288–295.

419. Kukli, K., Ritala, M., Schuisky, M., Leskela, M., Sajavaara, T., Keinonen, J., Uustare, T. and Harsta, A., Atomic Layer Deposition of Titanium Oxide from TiI_4 and H_2O_2. *Chemical Vapor Deposition* **2000,** *6*, 303–310.

420. Schuisky, M., Harsta, A., Aidla, A., Kukli, K., Kiisler, A.-A. and Aarik, J., Atomic Layer Chemical Vapor Deposition of TiO_2 Low Temperature Epitaxy of Rutile and Anatase. *J. Electrochem. Society* **2000,** *147* (9), 3319–3325.

421. Kukli, K., Aidla, A., Aarik, J., Schuisky, M., Harsta, A., Ritala, M. and Leskela, M., Real-Time Monitoring in Atomic Layer Deposition of TiO_2 from TiI_4 and H_2O−H_2O_2. *Langmuir* **2000,** *16*, 8122–8128.

422. Schuisky, M., Aarik, J., Kukli, K., Aidla, A. and Harsta, A., Atomic Layer Deposition of Thin Films Using O_2 as Oxygen Source. *Langmuir* **2001,** *17*, 5508–5512.

423. Schuisky, M., Kukli, K., Aarik, J., Lu, J. and Harsta, A., Epitaxial growth of TiO_2 films in a hydroxyl-free atomic layer deposition process. *J. Crystal Growth,* **2002,** *235*, 293–299.

424. Hu, Z. and Turner, C. H., Atomic Layer Deposition of TiO_2 from TiI_4 and H_2O onto SiO_2 Surfaces: Ab Initio Calculations of the Initial Reaction Mechanisms. *J. Am. Chem. Soc.* **2007,** *129* (13), 3863–3878.

425. Aarik, J., Aidla, A., Uustare, T., Kukli, K., Sammelselg, V., Ritala, M. and Leskela, M., Atomic layer deposition of TiO_2 thin films from TiI_4 and H_2O. *Appl. Surf. Sci.* **2002,** *193*, 277–286.

426. Pore, V., Rahtu, A., Leskela, M., Ritala, M., Sajavaara, T. and Keinonen, J., Atomic Layer Deposition of Photocatalytic TiO_2 Thin Films from Titanium Tetramethoxide and Water. *Chem. Vap. Deposition* **2004,** *10*, 143–148.

427. Niskanen, A., Arstila, K., Leskelä, M. and Ritala, M., Radical Enhanced Atomic Layer Deposition of Titanium Dioxide. *Chem. Vap. Deposition* **2007,** *13*, 152-157.

428. Alekhin, A. P., Gudkova, S. A., Markeev, A. M., Mitiaev, A. S. Sigarev, A. A. and Toknova, V. F., Structural properties of the titanium dioxide thin films grown by atomic layer deposition at various numbers of reaction cycles. *Appl. Surf. Sci.* **2010,** *257* (1), 186-191.

429. Ritala, M., Leskela, M. and Rauhala, E., Atomic layer epitaxy growth of titanium dioxide thin films from titanium ethoxide. *Chemistry of Materials* **1994,** *6*, 556–561.

430. Aarik, J., Aidla, A., Sammelselg, V., Uustare, T., Ritala, M. and Leskela, M., Characterization of titanium dioxide atomic layer growth from titanium ethoxide and water. *Thin Solid Films* **2000,** *370*, 163–172.

431. Aarik, J., Karlis, J., Mandar, H., Uustare, T. and Sammelselg, V., Influence of structure development on atomic layer deposition of TiO_2 thin films. *Appl. Surf. Sci.* **2001,** *181*, 339–348.

432. Rahtu, A., Kukli, K. and Ritala, M., In Situ Mass Spectrometry Study on Atomic Layer Deposition from Metal (Ti, Ta, and Nb) Ethoxides and Water. *Chemistry of Materials* **2001,** *13* (3), 817– 823.

433. Kim, I.-D., Tuller, H. L., Kim, H.-S. and Park, J.-S., High tunability (Ba,Sr)TiO_3 thin films grown on atomic layer deposited TiO_2 and Ta_2O_5 buffer layers. *Appl. Phys. Lett.* **2004,** *85*, 4705–4707.

434. Doring, K., Hashimoto, K., and Fujishima, A., TiO_2 Thin Films Prepared by Pulsed Beam Chemical Vapor Deposition from Titanium Tetraisopropoxide and Water. *Berichte der Bunsengesellschaft fur Physikalische Chemie* **1992,** *96*, 620–622.

435. Aarik, J., Aidla, A., Uustare, T., Ritala, M. and Leskela, M., Titanium isopropoxide as a precursor for atomic layer deposition: characterization of titanium dioxide growth process. *Appl. Surf. Sci.* **2000,** *161*, 385–395.

436. Rahtu, A. a. R., M., Reaction Mechanism Studies on Titanium Isopropoxide–Water Atomic Layer Deposition Process. *Chem. Vap. Dep.* **2002,** *8*, 21–28.

437. Shin, H., Jeong, D.-K., Lee, J., Sung, M. M. and Kim, J., Formation of TiO_2 and ZrO_2 Nanotubes Using Atomic Layer Deposition with Ultraprecise Control of the Wall Thickness. *Advanced Materials* **2004,** *16*, 1197–1200.

438. Jeong, D. K., Park, N., Jung, S.-H., Jung, W. G, Shin, H., Lee, J. and Kim, J., Fabrication of Oxide/Semiconducting Coaxial Nanotubular Materials Using Atomic Layer Deposition. *Materials Science Forum* **2004,** *449*, 1165–1168.

439. Jeong, D. K., Lee, J. Shin, H. Lee, J. Kim, J. and Sung, M., Synthesis of Metal Oxide Nanotubular Structure Using Atomic Layer Deposition on Nanotemplates. *J. Korean Phy. Soc.* **2004,** *45* (5), 1249–1252.

440. Lim, J. W., Yun, S. J. and Lee, J. H., Characteristics of TiO_2 Films Prepared by ALD With and Without Plasma. *Electrochem. Solid-State Lett.* **2004,** *7*, F73–F76.

441. Maeng, W. J and Kim, H., Thermal and Plasma-Enhanced ALD of Ta and Ti Oxide Thin Films from Alkylamide Precursors. *Electrochem. Solid-State Lett.* **2006,** *9*, G191–G194.

442. Pheamhom, R. S., C., and Kim, D.-H., Characteristics of atomic layer deposited TiO_2 films and their photocatalytic activity. *J. Vacuum Science and Technology A: Vacuum, Surfaces and Films* **2006,** *24*, 1535-1539.

443. Xie, Q., Jiang, Y.-L., Detavernier, C., Deduytsche, D., Van Meirhaeghe, R. L., Ru, G.-P., Li, B.-Z., and Qu, X.-P., Atomic layer deposition of TiO_2 from tetrakis-dimethylamido titanium or Ti isopropoxide precursors and H_2O. *J. Appl. Phys.* **2007,** *102* (8).

444. Xie, Q., Musschoot, J., Deduytsche, D., Van Meirhaeghe, R., Detavernier, C., Van; Den Berghe, S., Jiang, Y.-L., Ru, G.-P., Li, B.-Z. and Qu, X.-P., Growth Kinetics and Crystallization Behavior of TiO_2 Films Prepared by Plasma Enhanced Atomic Layer Deposition. *J. Electrochem. Soc.* **2008,** *155* (9), H688-H692.

445. Abdulagatov, A. I., Yan, Y., Cooper, J. R., Zhang, Y., Gibbs, Z. M., Cavanagh, A. S., Yang, R. G., Lee, Y. C. George, S. M., Al_2O_3 and TiO_2 Atomic Layer Deposition on Copper for Water Corrosion Resistance. *ACS Applied Materials & Interfaces* **2011,** *3* (12), 4593-4601.

446. Reiners, M., Xu, K., Aslam, N., Devi, A., Waser, R. and Hoffmann-Eifert, S., Growth and Crystallization of TiO_2 Thin Films by Atomic Layer Deposition Using a Novel Amido Guanidinate Titanium Source and Tetrakis-dimethylamido-titanium. *Chem. Mat.* **2013,** *25*, 2934–2943.

447. Yun, J. Y., Park, M. Y. and Rhee, S. W., Comparison of Tetrakis(dimethylamido)titanium and Tetrakis(diethylamido)titanium as Precursors for

Metallorganic Chemical Vapor Deposition of Titanium Nitride. *J. Electrochem. Soc.* **1999,** *146* (5), 1804-1808.

448. Cho, G. and Rhee, S.-W., Effect of the amido Ti precursors on the atomic layer deposition of TiN with NH_3. *J. Vac. Sci. Tech. A,* **2013,** *31* (1).

449. Ritala, M., Leskela, M., Niinisto, L. and Haussalo, P., Titanium isopropoxide as a precursor in atomic layer epitaxy of titanium dioxide thin films. *Chem. Mater.* **1993,** *5* (8), 1174-1181.

450. Matero, R., Rahtu, A., Ritala, M., Leskelä, M. and Sajavaara, T., Effect of water dose on the atomic layer deposition rate of oxide thin films. *Thin Solid Films* **2000,** *368*, 1-7.

451. Jin, C., Liu, B., Lei, Z. and Sun, J., Structure and photoluminescence of the TiO_2 films grown by atomic layer deposition using tetrakis-dimethylamino titanium and ozone. *Nanoscale Research Letters* **2015,** *10* (95).

452. Primet, M., Pichat, P. and Mathieu, M.-V., Infrared study of the surface of titanium dioxides. I. Hydroxyl groups. *J. Phys. Chem.* **1971,** *75* (9), 1216-1220.

453. Parfitt, G. D., The surface of titanium dioxide. *Progr. Surf. Membrane Sci.* **1976,** *11*, 181-226.

454. Kimney, J. B. and Staley, R. H., Reactions of titanium tetrachloride and trimethylaluminum at silica surfaces studied by using infrared photoacoustic spectroscopy. *J. Phys. Chem.* **1983,** *87*, 3735-3740.

455. Parfitt, G. D., Ramsbotham, J. and Rochester, C. H., Infra-red study of ammonia adsorption on rutile surfaces. *Trans. Faraday Soc* **1971,** *67*, 841-847.

456. Ponraj, J., Attolini, G. and Bosi, M., Review on Atomic Layer Deposition and Applications of Oxide Thin Films. *Critical Reviews in Solid State and Material Sciences* **2013,** *38* (3), 203–233.

457. Ruys, A., *Alumina Ceramics, Biomedical and Clinical Applications*. 1st Edition ed.; 2018.

458. Qian, X., Cao, Y., Guo, B., Zhai, H. and Li, A., Atomic Layer Deposition of Al-doped ZnO Films Using Aluminum Isopropoxide as the Al Precursor. *Chem. Vap. Deposition* **2013,** *19* (4-6), 180-185.

459. Wu, Y., Potts, S. E., Hermkens, P. M., Knoops, H. C. M.,	Roozeboom, F. and Kessels, W. M. M.	, Enhanced Doping Efficiency of Al-Doped ZnO by Atomic Layer Deposition Using Dimethylaluminum Isopropoxide as an Alternative Aluminum Precursor. *Chem. Mater.* **2013,** *25*, 4619-4622.

460. Garcia-Alonso, D., Potts, S. E., van Helvoirt, C. A., Verheijen, M. A. and Kessels, W. M. M., Atomic layer deposition of B-doped ZnO using triisopropyl borate as the boron precursor and comparison with Al-doped ZnO. *J. Mater. Chem. C* **2015,** *3* (13), 3095-3107.

461. Klimm, D., Electronic materials with a wide band gap: recent developments. *IUCrJ* **2014,** *1* (5), 281-290.

462. Janotti, A. and Van de Walle, C. G., Fundamentals of zinc oxide as a semiconductor. *Rep. Prog. Phys.* **2009,** *72*.

463. Reyes-Coronado, D., Rodríguez-Gattorno, G., Espinosa-Pesqueira, M. E., Cab, C., de Coss R. and Oskam, G., Phase-pure TiO_2 nanoparticles: anatase, brookite and rutile. *Nanotechnology* **2008,** *19* (145605).

464. Baek, Y., Lim, S., Kim, L. H., Park, S., Lee, S. W., Oh, T. H., Kim, S. H. and Park, C. E., Al_2O_3/TiO_2 nanolaminate gate dielectric films with enhanced electrical performances for organic field-effect transistors. *Organic Electronics* **2016,** *28*, 139-146.

465. Lee, J.-H., Park, T.-H., Lee, S.-H., Park, N.-W., Lee, W.-Y., Lim, J.-H., Lee. S.-K. and Park, J.-S., Enhancing the thermoelectric properties of super-lattice Al_2O_3/ZnO atomic film via interface confinement. *Ceramics International* **2016,** *42*, 14411–14415.

466. Liu, H., Yang, R. B., Guo, S., Lee, C. J. J. and Yakovlev, N. L., Effect of annealing on structural and optical properties of ZnO/Al_2O_3 superlattice structures grown by atomic layer deposition at 150 °C. *Journal of Alloys and Compounds* **2017,** *703*, 225-231.

467. Cao, Y. Q., Wang, S.-S., Liu, C., Wu, D. and Li, A.-D., Atomic layer deposition of ZnO/TiO_2 nanolaminates as ultra-long life anode material for lithium-ion batteries. *Sci Rep* **2019,** *9* (11526).

468. Berdova, M., Ylitalo, T., Kassamakov, I., Heino, J., Törmä, P. T., Kilpi, L., Ronkainen, H., Koskinen, J., Hæggström, E. and Franssila, S., Mechanical assessment of suspended ALD thin films by bulge and shaft-loading techniques. *Acta Materialia* **2014,** *66*, 370-377.

469. Homola, T., Buršíková, V., Ivanova, T. V., Souček, P., Maydannik, P. S., Cameron, D. C. and Lackner, J. M., Mechanical properties of atomic layer deposited Al_2O_3/ZnO nanolaminates. *Surface and Coatings Technology* **2015,** *284*, 198-205.

470. Testoni, G. E., Chiappim, W., Pessoa, R. S., Fraga, M. A., Miyakawa, W., Sakane, K. K., Galvão, N. K. A. M., Vieira, L. and Maciel, H. S., Influence of the Al_2O_3 partial-monolayer number on the crystallization mechanism of TiO_2 in ALD TiO_2/Al_2O_3 nanolaminates and its impact on the material properties. *J. Phys. D: Appl. Phys.* **2016,** *49*.

471. Coy, E., Yate, L., Kabacińska, Z., Jancelewicz, M., Jurga, S. and Iatsunskyi, I., Topographic reconstruction and mechanical analysis of atomic layer deposited Al_2O_3/TiO_2 nanolaminates by nanoindentation. *Materials and Design* **2016,** (111), 584–591.

472. Viter, R., Baleviciute, I., Abou Chaaya, A., Mikoliunaite, L., Balevicius, Z., Ramanavicius, A., Zalesska, A., Vataman, V., Smyntyna, V., Gertnere, Z., Erts, D., Miele, P. and Bechelany, M., Optical properties of ultrathin Al_2O_3/ZnO nanolaminates. *Thin Solid Films* **2015,** *594*, 96-100.

473. López, J., Solorio, E., Borbón-Nunez, H. A., Castillón, F. F., Machorro, R., Nedev, N., Farías, M. H. and Tiznado, H., Refractive index and bandgap variation in Al_2O_3-ZnO ultrathin multilayers prepared by atomic layer deposition. *Journal of Alloys and Compounds* **2017,** *691*, 308-315.

474. Romo-Garcia, F., Higuera-Valenzuela, H. J., Cabrera-German, D., Berman-Mendoza, D., Ramos-Carrazco, A., Tiznado, H., Hirata, G. A., Contreras, O. E. and Garcia-Gutierrez, R., Optoelectronic attenuation behavior of Al_2O_3/ZnO nanolaminates grown by Atomic Layer Deposition. *Thin Solid Films* **2019,** *669*, 419-424.

475. Jung, H., Choi, H., Jeon, H., Lee, S. and Jeon, H., Radio Frequency Plasma Power Dependence of the Moisture Permeation Barrier Characteristics of Al_2O_3 Films Deposited by Remote Plasma Atomic Layer Deposition. *J. Appl. Phys.* **2013,** *114* (173511).

476. Arroval, T., Aarik, L., Rammula, R. and Aarik, J., Growth of $Ti_xAl_{1-x}O_y$ films by atomic layer deposition using successive supply of metal precursors. *Thin Solid Films* **2015,** *591*, 276-284.

477. Mikhelashvili, V. and Eisenstien, G., Composition, surface morphology and electrical characteristics of Al_2O_3–TiO_2 nanolaminates and AlTiO films on silicon. *Thin Solid Films* **2006,** *515*, 346 – 352.

478. Iatsunskyi, I., Coy, E., Viter, R., Nowaczyk, G., Jancelewicz, M., Baleviciute, I., Zaleski, K. and Jurga, S., Study on Structural, Mechanical and Optical Properties of Al_2O_3-TiO_2 Nanolaminates Prepared by Atomic Layer Deposition. *Journal of Physical Chemistry* **2015,** *119*.

479. Xu, L., Shi, L. and Li, X., Effect of TiO_2 buffer layer on the structural and optical properties of ZnO thin films deposited by E-beam evaporation and sol-gel method. *Applied Surface Science* **2008,** *255*, 3230-3234.

480. Tian, J., Chen, L., Yin, Y., Wang, X., Dai, J., Zhu, Z., Liu, X. and Wu, P., Photocatalyst of TiO_2/ZnO nano composite film: Preparation, characterization, and photodegradation activity of methyl orange. *Surface & Coatings Technology* **2009,** *204*, 205-214.

481. Prasannalakshmi, P. and Shanmugam., N., Fabrication of TiO_2/ZnO nanocomposites for solar energy driven photocatalysis. *Materials Science in Semiconductor Processing* **2017,** *61*, 114-124.

482. Wang, W. K., Wen, H. C., Cheng, C. H., Hung, C. H., Chou, W. C., Yau, W. H., Yang, P. F. and Lai, Y. S., Nanotribological properties of ALD-processed bilayer TiO_2/ZnO films. *Microelectronics Reliability* **2014,** *54*, 2754–2759.

483. Gu. Y. Z., L., H. L., Geng, Y., Ye, Z. Y., Zhang, Y., Sun, Q. Q., Ding, S. J. and Zhang, D. W., Optical and microstructural properties of ZnO/TiO_2 nanolaminates. *Nanoscale Research Letters* **2013,** *8*, 107.

484. Chen, R., Lin, J. L., He, W. J., Duan, C. L., Peng, Q. and Wang, X. L., Spatial atomic layer deposition of ZnO/TiO_2 nanolaminates. *J. Vac. Sci. Technol. A* **2016,** *34* (5).

485. Xu, L., Shi, L and Li, X., Effect of TiO_2 buffer layer on the structural and optical properties of ZnO thin films deposited by E-beam evaporation and sol–gel method. *Applied Surface Science* **2008,** *255*, 3230–3234.

486. Qian, X., Gao, M. Y., Cao, Y. Q., Guo,B. L. and Li, A .D., Preparation and phase structures of Zn–Ti–O ternary compounds by atomic layer deposition. *J. Vac. Sci. Technol. A* **2013,** *31*.

487. Su, C.-Y., Wang, C.-C., Hsueh, Y.-C., Gurylev, V., Kei, C.-C. and Perng, T.-P. , Enabling high solubility of ZnO in TiO_2 by nanolamination of atomic layer deposition. *Nanoscale* **2015,** *7* (45), 19222-19230.

488. Torrisi, G., Di Mauro, A., Scuderi, M., Nicotra, G. and Impellizzeri, G., Atomic layer deposition of ZnO/TiO_2 multilayers: towards the understanding of Ti-doping in ZnO thin films. *RSC Adv.* **2016,** *6* (91), 88886-88895.

489. Wang, C.-C., Lin, J.-W., Yu, Y.-H., Lai, K.-H., Lee, S.-M., Chiu, K.-F. and Kei, C.-C., Nanolaminated ZnO–TiO_2 coated lithium-rich layered oxide cathodes by atomic layer deposition for enhanced electrochemical performances. *Journal of Alloys and Compounds* **2020,** *842*, 155845.

490. Gao, Z. and Banerjee, P., Review Article: Atomic layer deposition of doped ZnO films. *Journal of Vacuum Science & Technology A* **2019,** *37* (5), 050802.

491. Wu, Y., Devin Giddings, A., Verheijen, M. A., Macco, B., Prosa, T. J., Larson, D. J., Roozeboom, F. and Kessels, W. M. M., Dopant Distribution in Atomic Layer Deposited

ZnO:Al Films Visualized by Transmission Electron Microscopy and Atom Probe Tomography. *Chem. Mater.* **2018,** *30*, 1209-1217.

492. Elam, J. W. and George, S. M., Growth of ZnO/Al_2O_3 Alloy Films Using Atomic Layer Deposition Techniques. *Chem. Mater.* **2003,** *15* (4), 1020-1028.

493. Lee, D.-J., Kwon, J.-Y., Kim, J., Kim, K.-J., Cho, Y.-H., Cho, S.-Y., Kim, S.-H., Xu, J. and Kim, K.-B., Ultrasmooth, High Electron Mobility Amorphous In–Zn–O Films Grown by Atomic Layer Deposition. *J. Phys. Chem. C* **2014,** *118* (1), 408-415.

494. Banerjee, P., Lee, W.-J., Bae, K.-R., Lee, S. B. and Rubloff, G. W., Structural, electrical, and optical properties of atomic layer deposition Al-doped ZnO films. *J. Appl. Phys.* **2010,** *108*, 043504.

495. Lee, D.-J., Kim, K.-J., Kim, S.-H., Kwon, J.-Y., Xu, J. and Kim, K.-B. , Atomic layer deposition of Ti-doped ZnO films with enhanced electron mobility. *J. Mater. Chem. C* **2013,** *1* (31), 4761-4769.

496. Nakagawa, T., Sakaguchi, I., Matsumoto, K., Uematsu, M., Haneda, H. and Ohashi, N., Observation of Diffusion Behavior in Al-Implanted ZnO Single Crystal. *Key Eng. Mater.* **2009,** *421-422*, 197-200.

497. Johansen, K. M., Vines, L., Bjørheim, T. S., Schifano, R. and Svensson, B. G., Aluminum Migration and Intrinsic Defect Interaction in Single-Crystal Zinc Oxide. *Phys. Rev. Appl.* **2015,** *3* (2), 24003.

498. Lee, D.-J. K., H.-M. Kwon, J.-Y. Choi, H., Kim, S.-H. and Kim, K.-B., Structural and Electrical Properties of Atomic Layer Deposited Al-Doped ZnO Films. *Adv. Funct. Mater.* **2011,** *21* (3), 448-455.

499. Wu, Y., Hermkens, P. M., van de, Loo, B. W. H., Knoops, H. C. M., Potts, S. E., Verheijen, M. A., Roozeboom, F. and Kessels, W. M. M., Electrical transport and Al doping efficiency in nanoscale ZnO films prepared by atomic layer deposition. *J. Appl. Phys.* **2013,** *114*, 024308.

500. Saha, D., Das, A. K., Ajimsha, R. S., Misra, P. and Kukreja, L. M., Disorder-Driven Carrier Transport in Atomic Layer Deposited ZnO Thin Films. *arXiv Prepr.* **2013,** *arXiv: 1301.1172*.

501. Tiwari, A., Jin, C., Narayan, J. and Park, M., Electrical Transport in ZnO 1-δ Films: Transition from Band-Gap Insulator to Anderson Localized Insulator. *J. Appl. Phys.* **2004,** *96* (7), 3827−3830.

502. Bhosle, V., Tiwari, A. and Narayan, J., Electrical Properties of Transparent and Conducting Ga Doped ZnO. *J. Appl. Phys.* **2006,** *100* (3), 33713.

503. El Akkad, F., Punnoose, A. and Prabu, G., Properties of ITO films prepared by rf magnetron sputtering. *Applied Physics A* **2000,** *71*, 157-160.

504. Yang, W., Wu, Z., Liu, Z., Pang, A., Tu, Y.-L. and Feng, Z. C., Room temperature deposition of Al-doped ZnO films on quartz substrates by radio-frequency magnetron sputtering and effects of thermal annealing. *Thin Solid Films* **2010,** *519* (1), 31-36.

505. Dhakal, T., Nandur, A. S., Christian, R., Vasekar, P., Desu, S., Westgate, C., Koukis, D. I., Arenas, D. J. and Tanner, D. B., Transmittance from visible to mid infra-red in AZO films grown by atomic layer deposition system. *Sol. Energy Mater. Sol. Cells* **2012,** *86* (5), 1306-1312.

506. Guillén, C. and Herrero, J., Comparison study of ITO thin films deposited by sputtering at room temperature onto polymer and glass substrates. *Thin Solid Films* **2005,** *480–481*, 129-132.

507. Liu, Y., Li, Y. and Zeng, H., ZnO-Based Transparent Conductive Thin Films: Doping, Performance, and Processing. *Journal of Nanomaterials* **2013,** *2013*, 1-9.

508. Sinha, S., Maurya, S. K., Balasubramaniam, R. and Sarkar, S. K., Development of Al doped ZnO as TCO by Atomic Layer Deposition. In *IEEE 42nd Photovoltaic Specialist Conference (PVSC)*, New Orleans, LA, USA, 2015; pp 1-4.

509. Zhai, C.-H., Zhang, R.-J., Chen, X., Zheng, Y.-X., Wang, S.-Y., Liu, J., Dai, N. and Chen, L.-Y. , Effects of Al Doping on the Properties of ZnO Thin Films Deposited by Atomic Layer Deposition. *Nanoscale Res. Lett.* **2016,** *11* (407).

510. Li, M., Qian, X., Li, A.-D., Cao, Y.-Q., Zhai, H.-F. and Wu, D, A comparative study of growth and properties of atomic layer deposited transparent conductive oxide of Al doped ZnO films from different Al precursors. *Thin Solid Films* **2018,** *646*, 126-131.

511. Song, J., Mu, H. C., Jiang, L. X., Yin, G. L., Yu, Z. and He, D. N., The Electrical and Optical Properties of Al-Doped ZnO Thin Films Prepared by Atomic Layer Deposition. *Adv. Mater. Res.* **2011,** *306-307*, 1402-1405.

512. Li, Y., Yao, R., Wang, H., Wu, X., Wu, J.,Wu, X. and Qin, W., Enhanced Performance in Al-Doped ZnO Based Transparent Flexible Transparent Thin-Film Transistors Due to Oxygen Vacancy in ZnO Film with Zn–Al–O Interfaces Fabricated by Atomic Layer Deposition. *ACS Appl. Mater. Interfaces* **2017,** *9* (13), 11711–11720.

513. Choi, Y.-J., Gong, S. C., Johnson, D. C., Golledge, S., Yeom, G. Y. and Park, H.-H., Characteristics of the electromagnetic interference shielding effectiveness of Al-doped ZnO thin films deposited by atomic layer deposition. *Appl. Surf. Sci.* **2013,** *269* (92).

514. Illiberi, A., Scherpenborg, R., Wu, Y., Roozeboom, F. and Poodt, P., Spatial Atmospheric Atomic Layer Deposition of $Al_xZn_{1-x}O$. *ACS Appl. Mater. Interfaces* **2013,** *5* (24), 13124-13128.

515. Yuan, H., Luo, B., Yu, D., Cheng, A.-J., Campbell, S. A. and Gladfelter, W. L., Atomic layer deposition of Al-doped ZnO films using ozone as the oxygen source: A comparison of two methods to deliver aluminum. *J. Vac. Sci. & Tech. A* **2012,** *30*, 01A138.

516. Pollock, E. B. and Lad, R. J., Influence of dosing sequence and film thickness on structure and resistivity of Al-ZnO films grown by atomic layer deposition. *J. Vac. Sci. & Tech. A* **2014,** *32* (4), 041516.

517. Park, H. K. and Heo, J., Improved efficiency of aluminum doping in ZnO thin films grown by atomic layer deposition. *Appl. Surf. Sci.* **2014,** *309*, 133-137.

518. Le Tulzo, H., Schneider, N., Lincot, D., Patriarche, G. and Donsanti, F., Impact of the sequence of precursor introduction on the growth and properties of atomic layer deposited Al-doped ZnO films. *J. Vac. Sci. & Tech. A* **2018,** *36*, 041502.

519. Burton, W. K., Carberra, N. and Frank, F. C., The growth of crystals and the equilibrium structure of their surfaces. *Philos. Trans. R. Soc. London, Ser. A* **1951,** *243* (866), 299.

520. Rehana, R. T. and Raheevkumar, K., Synthesis of ZnO Nanostructures Using Domestic Microwave Oven Based Remote Plasma Deposition System. *Nanoscience and Nanotechnology* **2012,** *2* (3), 66-70.

521. Ahn, C. H., Lee, S. Y. and Cho, H. K., Influence of growth temperature on the electrical and structural characteristics of conductive Al-doped ZnO thin films grown by atomic layer deposition. *Thin Solid Films* **2013,** *545*, 106-110.

522. Luka, G., Wachnicki, L., Witkowski, B., Krajewski, T., Jakiela, R., Guziewicz, E. and Godlewski, M., The uniformity of Al distribution in aluminum-doped zinc oxide films grown by atomic layer deposition. *Mater. Sci. Eng. B* **2011,** *176* (3), 237-241.

523. Lee, J. H., Lee, J.-W., Hwang, S., Kim, S. Y., Cho, H. K., Lee, J. Y. and Park, J.-S., Effects of Al Concentration on Microstructural Characteristics and Electrical Properties of Al-Doped ZnO Thin Films on Si Substrates by Atomic Layer Deposition. *J. Nanosci. Nanotechnol.* **2012,** *12* (7), 5598-5603.

524. Maeng, W., Kim, S.-J., Park, J.-S., Chung, K.-B. and Kim, H., Low temperature atomic layer deposited Al-doped ZnO thin films and associated semiconducting properties. *J. Vac. Sci. Technol. B* **2012,** *30*, 031210.

525. Yuan, H., Luo, B., Gladfelter, W. L., and Campbell, S., (Invited) Ozone Assisted ALD of Doped ZnO as a Transparent Metal. *ECS Trans.* **2012,** *45* (3), 389.

526. Geng, Y., Guo, L., Xu, S.-S., Sun, Q.-Q., Ding, S.-J., Lu, H.-L. and Zhang, D. W., Influence of Al Doping on the Properties of ZnO Thin Films Grown by Atomic Layer Deposition. *J. Phys. Chem. C* **2011,** *115* (25), 12317–12321.

527. Jeong, J.-K., Yun, H.-J., Yang, S.-D., Eom, K.-Y., Chea, S.-W., Park, J.-H., Lee, H.-D. and Lee, G.-W., Investigation of atomic-layer-deposited Al-doped ZnO film for AZO/ZnO double-stacked active layer thin-film transistor application. *Thin Solid Films* **2017,** *638*, 89-95.

528. Gong, C., Jang, J. G., Chang, H. J. and Park, J.-S. , The characteristics of organic light emitting diodes with Al doped zinc oxide grown by atomic layer deposition as a transparent conductive anode. *Synthetic Metals* **2011,** *161* (9-10), 823-827.

529. Oh, B.-Y., Han, J.-W., Seo, D.-S., Kim, K.-Y., Baek, S.-H., Jang, H. S. and Kim, J. H., Characteristics of Al-Doped ZnO Films Grown by Atomic Layer Deposition for Silicon Nanowire Photovoltaic Device. *J. Nanosci. Nanotechnol.* **2012,** *12* (7), 5330-5335.

530. Kim, J. Y., Choi, Y.-J. and Park, H. H., Effective atomic layer deposition procedure for Al-dopant distribution in ZnO thin films. *J. Vac. Sci. & Tech. A* **2010,** *28*, 1111.

531. Steglich, M., Bingel, A., Jia, G. and Falk, F., Atomic layer deposited ZnO:Al for nanostructured silicon heterojunction solar cells. *Sol. Energy Mater. Sol. Cells* **2012,** *103*, 62-68.

532. Geng, Y., Xie, Z.-Y., Xu, S.-S., Sun, Q.-Q., Ding, S.-J., Lu, H.-L. and Zhang, D. W., Effects of Rapid Thermal Annealing on Structural, Luminescent, and Electrical Properties of Al-Doped ZnO Films Grown by Atomic Layer Deposition. *ECS J. Solid State Sci. Technol.* **2012,** *1* (3), N45.

533. Tynell, T., Yamauchi, H., Karppinen, M., Okazaki, R. and Terasaki, I., Atomic layer deposition of Al-doped ZnO thin films. *J. Vac. Sci. Technol. A* **2013,** *31* (01A109).

534. Tsai, F. T., Hou, H. T., Chao, C. K. and Chang, R. C., Depositing High-Performance Conductive Thin Films by Using Atomic Layer Deposition. *Appl. Mech. Mater.* **2015,** *764-765*, 138-142.

535. Luka, G., Witkowski, B., Wachnicki, L., Jakiela, R., Virt, I., Andrzejczuk, M., Lewandowska, M. and Godlewski, M., Electrical and mechanical stability of aluminum-doped

ZnO films grown on flexible substrates by atomic layer deposition. *Mater. Sci. Eng. B* **2014,** *186*, 15-20.

536. Blagoev, B. S., Dimitrov, D. Z., Mehandzhiev, V. B., Kovacheva, D., Terziyska, P., Pavlic, J., Lovchinov, K., Mateev, E., Leclercq, J. and Sveshtarov, P., Electron transport in Al-doped ZnO nanolayers obtained by atomic layer deposition. *J. Phys. Conf. Ser.* **2016,** *700* (012040).

537. Romanyuk, V., Dmitruk, N., Karpyna, V., Lashkarev, G., Popovych, V., Dranchuk, M., Pietruszka, R., Godlewski, M., Dovbeshko, G., Timofeeva, I., Kondratenko, O., Taborska, M. and Ievtushenko, A., Optical and Electrical Properties of Highly Doped ZnO:Al Films Deposited by Atomic Layer Deposition on Si Substrates in Visible and Near Infrared Region. *Acta Phys. Pol. A* **2016,** *129* (A36).

538. Kim, E.-J., Lee, W.-H., and Yoon, S.-M., Threshold voltage control of a thin-film transistor using an Al–Zn–O channel prepared using atomic layer deposition by controlling the Al dopant positions. *RSC Adv.* **2016,** *6* (92534).

539. Panigrahi, J., Vandana, Singh, R., Rauthan, C. M. S. and Singh, P. K., Crystalline silicon surface passivation by thermal ALD deposited Al doped ZnO thin films. *AIP Adv.* **2017,** *7* (035219).

540. Oh, B.-Y., Kim, J.-H., Han, J.-W., Seo, D.-S., Jang, H. S., Choi, H.-J., Baek, S.-H., Kim, J. H., Heo, G.-S., Kim, T.-W. and Kim, K.-Y., Transparent conductive ZnO:Al films grown by atomic layer deposition for Si-wire-based solar cells. *Curr. Appl. Phys.* **2012,** *12* (1), 273-279.

541. Gong, S. C., Choi, Y.-J., Kim, H., Park, C.-S., Park, H.-H., Jang, J. G., Chang, H. J. and Yeom, G. Y. , Aluminum-doped zinc oxide formed by atomic layer deposition for use as anodes in organic light emitting diodes. *J. Vac. Sci. Technol. A* **2013,** *31* (01A101).

542. Choi, N.-J., Kim, K.-W., Son, H.-S. and Lee, S.-N., Optical and electrical characterization of AZO films grown on c-plane sapphire substrates by atomic layer deposition. *Electron. Mater. Lett.* **2014,** *10*, 259–262.

543. Lin, M.-L., Huang, J.-M., Ku, C.-S., Lin, C.-M., Lee, H.-Y. and Juang, J.-Y., High mobility transparent conductive Al-doped ZnO thin films by atomic layer deposition. *J. Alloys Compd* **2017,** *727*, 565-571.

544. Hou, Q., Meng, F. and Sun, J., Electrical and optical properties of Al-doped ZnO and $ZnAl_2O_4$ films prepared by atomic layer deposition. *Nanoscale Res. Lett.* **2013,** *8* (144).

545. Mundle, R. M., Terry, H. S., Santiago, K., Shaw, D., Bahoura, M., Pradhan, A. K., Dasari, K. and Palai, R., Electrical conductivity and photoresistance of atomic layer deposited Al-doped ZnO films. *J. Vac. Sci. Technol. A* **2013,** *31* (01A146).

546. Ko, B.-S., Lee, S.-J., Kim, D.-H. and Hwang, D.-K., Effects of a Pretreatment on Al-Doped ZnO Thin Films Grown by Atomic Layer Deposition. *J. Nanosci. Nanotechnol.* **2015,** *15* (3), 2432-2435.

547. Nayak, P. K., Wang, Z. and Alshareef, H. N., Indium-Free Fully Transparent Electronics Deposited Entirely by Atomic Layer Deposition. *Adv. Mater.* **2016,** *28* (35), 7736-7744.

548. Nguyen, V. H., Resende, J., Jiménez, C., Deschanvres, J.-L., Carroy, P., Muñoz, D. Bellet, D. and Muñoz-Rojas, D., Deposition of ZnO based thin films by atmospheric pressure

spatial atomic layer deposition for application in solar cells. *J. Renew. Sustain. Energy* **2017,** *9* (021203).

549. Liu, W.-J., Wang, Y.-H., Zheng, L.-L., Lu, H.-L. and Ding, S.-J., Stability enhancement of low temperature thin-film transistors with atomic-layer-deposited ZnO:Al channels. *Microelectron. Eng.* **2017,** *167*, 105-109.

550. Kong, B. H., Cho, H. K., Kim, M. Y., Choi, R. J. and Kim, B. K., InGaN/GaN blue light emitting diodes using Al-doped ZnO grown by atomic layer deposition as a current spreading layer. *J. Cryst. Growth* **2011,** *326* (1), 147-151.

551. Maeng, W., Lee, J.-W., Lee, J. H., Chung, K.-B. and Park, J.-S., Studies on optical, structural and electrical properties of atomic layer deposited Al-doped ZnO thin films with various Al concentrations and deposition temperatures. *J. Phys. D Appl. Phys. Lett.* **2011,** *44* (445305).

552. Čeh, M., Chen, H.-C., Chen, M.-J., Yang, J.-R. and Shiojiri, M., Structure and Electro-Optical Properties of Thin Films Grown by Alternate Atomic Layer Deposition of ZnO and Al_2O_3 on the Sapphire Substrate. *Mater. Trans.* **2010,** *51* (2), 219-226.

553. Cheng, Y.-C., Effects of post-deposition rapid thermal annealing on aluminum-doped ZnO thin films grown by atomic layer deposition. *Appl. Surf. Sci.* **2011,** *258* (1), 604-607.

554. Na, J.-S., Peng, Q., Scarel, G. and Parsons, G. N., Role of Gas Doping Sequence in Surface Reactions and Dopant Incorporation during Atomic Layer Deposition of Al-Doped ZnO. *Chem. Mater.* **2009,** *21* (23), 5585–5593.

555. Heo, J., Bok Kim, S. and Gordon, R. G., Atomic layer deposited zinc tin oxide channel for amorphous oxide thin film transistors. *Appl. Phys. Lett.* **2012,** *101* (113507).

556. Chiang, H. Q., Wager, J. F., Hoffman, R. L., Jeong, J. and Keszler, D. A., High mobility transparent thin-film transistors with amorphous zinc tin oxide channel layer. *Appl. Phys. Lett.* **2005,** *86* (013503).

557. Hultqvist, A., Edoff, M. and Torndahl, T., Evaluation of Zn□Sn□O buffer layers for $CuIn_{0.5}Ga_{0.5}Se_2$ solar cells. *Prog. Photovoltaics Res. Appl.* **2011,** *19* (4), 478-481.

558. Wu, X., High-efficiency polycrystalline CdTe thin-film solar cells. *Sol. Energy* **2004,** *77* (6), 803-814.

559. Mullings, M. N., Hägglund, C., Tanskanen, J. T., Yee, Y., Geyer, S. and Bent, S. F., Thin film characterization of zinc tin oxide deposited by thermal atomic layer deposition. *Thin Solid Films* **2014,** *556*, 186-194.

560. Hultqvist, A., Platzer-Björkman, C., Zimmermann, U., Edoff, M. and Törndahl, T., Growth kinetics, properties, performance, and stability of atomic layer deposition Zn–Sn–O buffer layers for $Cu(In,Ga)Se_2$ solar cells. *Prog. Photovoltaics Res. Appl.* **2012,** *20* (7), 883-891.

561. Lindahl, J., Hagglund, C., Watjen, J. T., Edoff, M and Torndahl, T., The effect of substrate temperature on atomic layer deposited zinc tin oxide. *Thin Solid Films* **2015,** *586*, 82-87.

562. Hagglund, C., Grehl, T., Tanskanen, J. T., Yee, Y. S., Mullings, M. N., Mackus, A. J. M., MacIsaac, C., Clemens, B. M., Brongersma, H. H. and Bent, S. F., Growth, intermixing, and surface phase formation for zinc tin oxide nanolaminates produced by atomic layer deposition. *J. Vac. Sci. & Tech. A* **2016,** *34* (2).

563. Yuan, H. and Lee, Z.-T., Structural, electrical and optical properties of Sn doped ZnO films deposited by atomic layer deposition. *Rengong Jingti Xuebao/Journal of Synthetic Crystals* **2013,** *42* (2), 240-245.

564. Ye, Z.-Y., Lu, H.-L., Geng, Y., Gu, Y.-Z., Xie, Z.-Y., Zhang, Y., Sun, Q.-Q., Ding, S.-J. and Zhang, D. W., Structural, electrical, and optical properties of Ti-doped ZnO films fabricated by atomic layer deposition. *Nanoscale Res. Lett.* **2013,** *8* (108).

565. Wan, Z., Kwack, W.-S., Lee, W.-J., Jang, S.-I., Kim, H.-R., Kim, J.-W., Jung, K.-W. Min, W.-J., Yu, K.-S., Park, S.-H., Yun, E.-Y., Kim, J.-H. and Kwon, S.-H., Electrical and optical properties of Ti doped ZnO films grown on glass substrate by atomic layer deposition. *Mater. Res. Bull.* **2014,** *57*, 23-28.

566. Bergum, K., Hansen, P.-A., Fjellvåg, H. and Nilsen, O., Structural, electrical and optical characterization of Ti-doped ZnO films grown by atomic layer deposition. *J. Alloys Compounds* **2014,** *616*, 618-624.

567. Bergum, K., Fjellvåg, H. and Nilsen, O., Thickness dependent structural, optical and electrical properties of Ti-doped ZnO films prepared by atomic layer deposition. *Appl. Surf. Sci.* **2015,** *332*, 494-499.

568. Saha, D. M., P., Bhartiya, S., Gupta, M. Joshi, M. and Kukreja, L, Dimensional crossover of electron weak localization in ZnO/TiO_x stacked layers grown by atomic layer deposition. *Appl. Phys. Lett.* **2016,** *108*, 042109.

569. Saha, D., Misra, P., Das, G., Joshi, M. and Kukreja, L., Observation of dopant-profile independent electron transport in sub-monolayer TiO_x stacked ZnO thin films grown by atomic layer deposition. *Appl. Phys. Lett.* **2016,** *108*, 032101.

570. Asvarov, A., Abduev, A., Akhmedov, A. and Abdullaev, A., Effects of a high humidity environment and air anneal treatments on the electrical resistivity of transparent conducting ZnO-based thin films. *Phys. Status Solidi* **2010,** *7*, 1553–1555.

571. Kvit, A. V., Yankovich, A. B., Avrutin, V., Liu, H., Izyumskaya, N., Ozgür, Ü., Morkoç, H. and Voyles, P. M., Impurity distribution and microstructure of Ga-doped ZnO films grown by molecular beam epitaxy. *J. Appl. Phys.* **2012,** *112*, 123527.

572. Wiglusz, R. J., Watras, A., Malecka, M., Deren, P. J. and Pazik, R., Structure Evolution and Up-Conversion Studies of ZnX2O4:Er3+/Yb3+ (X=Al3+. Ga3+, In3+) Nanoparticles. *European Journal of Inorganic Chemistry* **2014,** *2014* (6), 1090-1101.

573. Saito, K., Hiratsuka, Y., Omata, A., Makino, H., Kishimoto, S., Yamamoto, T., Horiuchi, N. and Hirayama, H., Atomic layer deposition and characterization of Ga-doped ZnO thin films. *Superlattices Microstruct.* **2007,** *42* (1-6), 172-175.

574. Chang, Y.-F., Liao, C.-L., Ho, C.-L., Liu, A.-S. and Wu, M.-C., Effects of Passivation Layer and Post-Annealing on Ga-Doped ZnO Films Grown by ALD. *ECS J. Solid State Sci. Technol.* **2013,** *2* (6), N140.

575. Lee, Y.-L., Chen, S.-F., Ho, C.-L. and Wu, M.-C., Effects of Oxygen Plasma Post-Treatment on Ga-Doped ZnO Films Grown by Thermal-Mode ALD. *ECS J. Solid State Sci. Technol.* **2013,** *2* (7), P316.

576. Szabó, Z. B., Z., Basa, P., Czigány, Z., Bársony, I., Wang, H.-Y. and Volk, J., Homogeneous transparent conductive ZnO:Ga by ALD for large LED wafers. *Appl. Surf. Sci.* **2016,** *379*, 304-308.

577. Illiberi, A., Scherpenborg, R., Theelen, M., Poodt, P. and Roozeboom, F., On the environmental stability of ZnO thin films by spatial atomic layer deposition. *J. Vac. Sci. Tech. A.* **2013,** *31*, 061504.

578. Illiberi, A., Scherpenborg, R., Poodt, P. and Roozeboom, F., (Invited) Spatial Atomic Layer Deposition of Transparent Conductive Oxides. *ECS Trans.* **2013,** *58*, 105.

579. Illiberi, A., Scherpenborg, R., Roozeboom, F. and Poodt, P., Atmospheric Spatial Atomic Layer Deposition of In-Doped ZnO. *ECS J. Solid State Sci. Technol.* **2014,** *3* (5), P111.

580. Kim, D., Nam, T., Park, J., Gatineau, J. and Kim, H., Growth characteristics and properties of indium oxide and indium-doped zinc oxide by atomic layer deposition. *Thin Solid Films* **2015,** *587*, 83-87.

581. Sheng, J., Lee, H.-J., Oh, S. and Park, J.-S., Flexible and High-Performance Amorphous Indium Zinc Oxide Thin-Film Transistor Using Low-Temperature Atomic Layer Deposition. *ACS Appl Mater Interfaces* **2016,** *8* (49), 33821-33828.

582. O'Neill, B. J., Jackson, D. H. K., Lee, J., Canlas, C., Stair, P. C., Marshall, C. L., Elam, J. W., Kuech, T. F., Dumesic, J. A. and Huber, G. W. Catalyst Design with Atomic Layer Deposition. *ACS Catal.* **2015**, *5* (3), 1804–1825.

583. Singh, J. A., Yang, N. and Bent, S. F. Nanoengineering Heterogeneous Catalysts by Atomic Layer Deposition. *Annu. Rev. Chem. Biomol. Eng.* **2017**, *8* (1), 41–62.

584. Meng, X., Yang, X.-Q. and Sun, X. Emerging Applications of Atomic Layer Deposition for Lithium Ion Battery Studies. *Adv. Mater.* **2012**, *24*, 3589–3615.

585. Peng, Q., Lewis, J. S., Hoertz, P. G., Glass, J. T. and Parsons, G. N. Atomic Layer Deposition for Electrochemical Energy Generation and Storage Systems. *J. Vac. Sci. Technol. A* **2012**, *30* (1), 010803-010801–010814.

586. Bakke, J. R., Pickrahn, K. L., Brennan, T. P. and Bent, S. F. Nanoengineering and Interfacial Engineering of Photovoltaics by Atomic Layer Deposition *Nanoscale* **2011**, *3*, 3482–3508. 335

587. van Delft, J. A., Garcia-Alonso, D. and Kessels, W. M. M. Atomic Layer Deposition for Photovoltaics: Applications and Prospects for Solar Cell Manufacturing. *Semicond. Sci. Technol.* **2012**, *27* (7), 074002.

588. Palmstrom, A. F., Santra, P. K. and Bent, S. F. Atomic Layer Deposition in Nanostructured Photovoltaics: Tuning Optical, Electronic and Surface Properties *Nanoscale* **2015**, *7* (29), 12266– 12283.

589. Coll, M. and Napari, M. Atomic layer deposition of functional multicomponent oxides. *APL Materials* **2019**, *7*, 110901.

590. Mackus, A. J. M., Schneider, J. R., MacIsaac, C., Baker, J. G. and Bent, S. F. Synthesis of Doped, Ternary, and Quaternary Materials by Atomic Layer Deposition: A Review. *Chem. Mater.* **2019**, *31*, 1142−1183.

591. Mohseni; H. and Scharf, T. W. Atomic layer deposition of ZnO/Al2O3/ZrO2 nanolaminates for improved thermal and wear resistance in carbon-carbon composites. *J. Vac. Sci. Technol. A* **2012**, *30* (1), 01A149.

592. Luka; G., G., M., Guziewicz, E., Stakhira, P., Cherpak, V. and Volynyuk, D. ZnO Films Grown by Atomic Layer Deposition for Organic Electronics. *Semicond. Sci. Technol.* **2012**, *27* (7), 07400.

593. Ageh, V., Choudhuri, D. and Scharf, T. W. High Frequency Reciprocating Sliding Wear Behavior and Mechanisms of Quaternary Metal Oxide Coatings. *Wear* **2015**, *330−331*, 390−399.

Chapter 2: Experimental Methods

2.1 Substrate cleaning

Prior to all depositions, glass substrates were cleaned by ultrasonication in Decon 90 (5% solution in deionised water) acetone, and isopropyl alcohol (IPA) successively for 15 minutes each. The substrates were thoroughly dried after each step using an in-house supply of dry nitrogen gas produced by boil-off from a liquid nitrogen supply. Si (100) wafers (SI-MAT) were cleaned using ozone followed by treatment in hydrogen fluoride (HF) to remove any oxide from the surface of the wafer. Immediately before being placed in reactor, dry N_2 gas was again used to clean the substrates.

2.2 ALD growths

2.2.1 Preparations of TiO_2/ZnO composites

TiO_2/ZnO bilayer laminate films were deposited on Corning© glass and Si (100) substrates using a Cambridge Nanotech Fiji 200 ALD system (figure 2.1). All substrates were loaded in to the reactor together to avoid run-by-run variations. Diethyl zinc (DEZn) (min. 95% Strem Chemicals), tetrakis(dimethylamido)titanium(IV) (TDMAT) (99% Strem Chemicals) and water were used as precursors under a growth temperature of 200 °C. Argon was used a carrier gas to transport the precursor molecules into the chamber. During the deposition process, DEZn and water were sustained at room temperature while the titanium precursor; TDMAT was heated to a temperature of 80 °C to ensure sufficient vapour pressure was generated. Pulse times were 0.4 s, 0.2 s and 0.1 s for TDMAT, DEZn and water respectively accompanied with a 10 s Argon purge between precursor pulses to remove redundant ligands and any excess precursor. The deposition rate was controlled at 2 Å/cycle for ZnO layers and 0.5 Å/cycle for

TiO_2 layers. The thickness of both the ZnO and TiO_2 layers was set to 40 nm (200 cycles for ZnO and 670 cycles for TiO_2). Films were produced with ZnO layer (40 nm) followed by TiO_2 layer (40 nm) and vice versa. For comparison, TiO_2 and ZnO films were grown with a thickness of 40 nm using the same precursors already mentioned. A laminate consisting of ZnO and TiO_2 multilayers, (4 nm ZnO + 4 nm TiO_2) x5 was grown. A deliberately mixed ZnO/TiO_2 1:1 film was also grown by alternating very short pulses (0.05 s) of each metal precursor followed by water. This was repeated until the desired thickness of 40 nm was reached (as mentioned above, 200 cycles for ZnO and 670 cycles for TiO_2).

Figure 2.1: The Cambridge Nanotech Fiji 200 ALD deposition system at the Tyndall National Institute

Figure 2.2 (a) – (f) below shows schematics of the samples prepared.

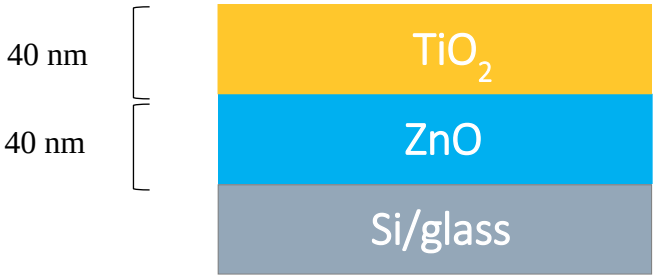

(a) ZnO and TiO_2 bilayer laminate

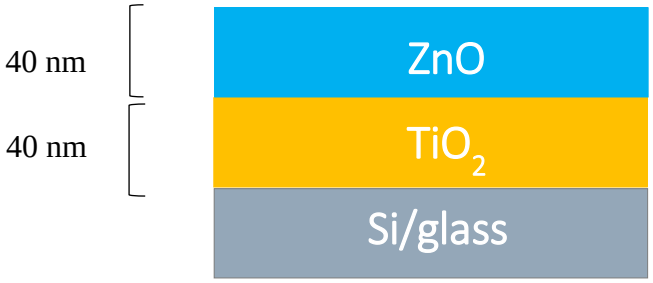

(b) TiO_2 and ZnO bilayer laminate

(c) TiO_2

(d) ZnO

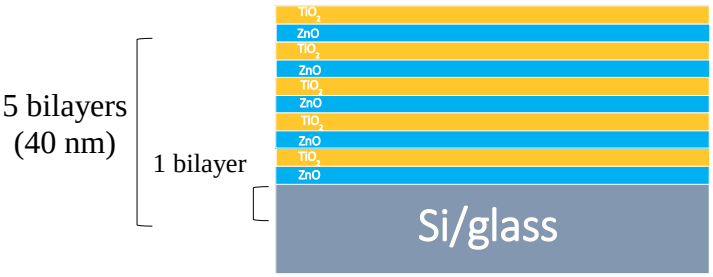

(e) ZnO and TiO_2 multilayers laminate

(4 nm ZnO + 4 nm TiO_2) x5

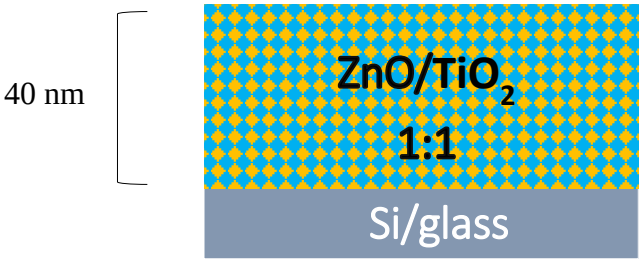

(f) Standard ZnO/TiO_2 1:1 laminate

2.2.2 Preparation of ZnO thin films

ZnO films were deposited on Corning© glass and Si (100) substrates using both thermal and plasma processes on a 200 mm Picosun™ R200 ALD reactor (figure 2.3).

It must be noted that films deposited using different ALD reactors cannot be directly compared as reactors vary substantially in terms of chamber size, pumps, flow rates and heating of precursors. A clear example of this is seen in this work when using the Ti precursor, TDMAT. For the Cambridge Nanotech Fiji reactor, the TDMAT container was heated to 75 °C while on the Picosun™ R200 reactor, a boost function is used and it was found that optimum transfer was obtained when the precursor container was heated to 65 °C.

Figure 2.3: The Picosun™ R200 ALD deposition system at the Tyndall National Institute

All substrates were loaded in to the reactor together to avoid run-by-run variations. DEZn (min. 95% Strem Chemicals) was used as a metal precursor. The substrate temperatures for both the thermal and plasma ALD-grown ZnO films were 100, 150 and 200 °C. Nitrogen (N_2) was used a carrier gas to transport the precursor molecules into the chamber. During the deposition process, DEZn and water were sustained at RT in which adequate vapour pressure was achieved. Pulse times were 0.05 s and 0.1 s for DEZn and water respectively accompanied with a 6.0 s Ar purge between precursor pulses to remove redundant ligands. The PE-ALD ZnO growth consisted of 0.05 s of DEZn exposure, 6 s Ar purge, 28.0 s of oxygen plasma exposure with RF power of 2800 and 3000 W, followed by 6.0 s of Ar purge. The flow rate of the oxygen was 80 sccm. Further details regarding plasma growth are given in table 2.1. Prior to deposition, the substrates were subjected to a stabilisation time of 30 minutes in the chamber due to the indirect heating of the substrate which is a feature of the Picosun™ reactor.

RF power	2800/3000 W
MFC700 (Ar carrier)	80 sccm
Plasma gas	150 sccm
t_1, flow stabilisation	1.4
t_2, RF power on	20.0

Table 2.1: Plasma growth process details using Litmas® RPS 3001 by Advanced Energy™

A study was carried out to determine the time required for plasma exposure. The plasma exposure times tested at 2800 W radio frequency (RF) power were 14.0, 20.0, 21.0, 22.0, 23.0, 24.0, 25.0, 26.0, 27.0, and 28.0 s. It was found that the plasma cut out at 14.0, 20.0 and 21.0 s

exposure time as the plasma was not stable. A study was also completed in which the RF plasma power was reduced to 2500 W. Films were successfully deposited using this RF plasma power however, based on a manufacturer suggestion, 2800 W was selected as the RF plasma power to use for the study presented here.

2.2.3 Preparation of doped ZnO thin films

ZnO thin films were doped with Al (AZO), Ga (GZO), Sn (SZO) and Ti (TZO). Growth of all doped films were carried out using a Picosun™ R200 system following the supercycle method seen in figure 2.4 below in which X = Al, Ga, In, Ti and Sn. Dopant ratios of 9:1 and 19:1 were used. Films were deposited at 150 °C. Variations in different dopant precursors pulse and purge times are displayed in table 2.2.

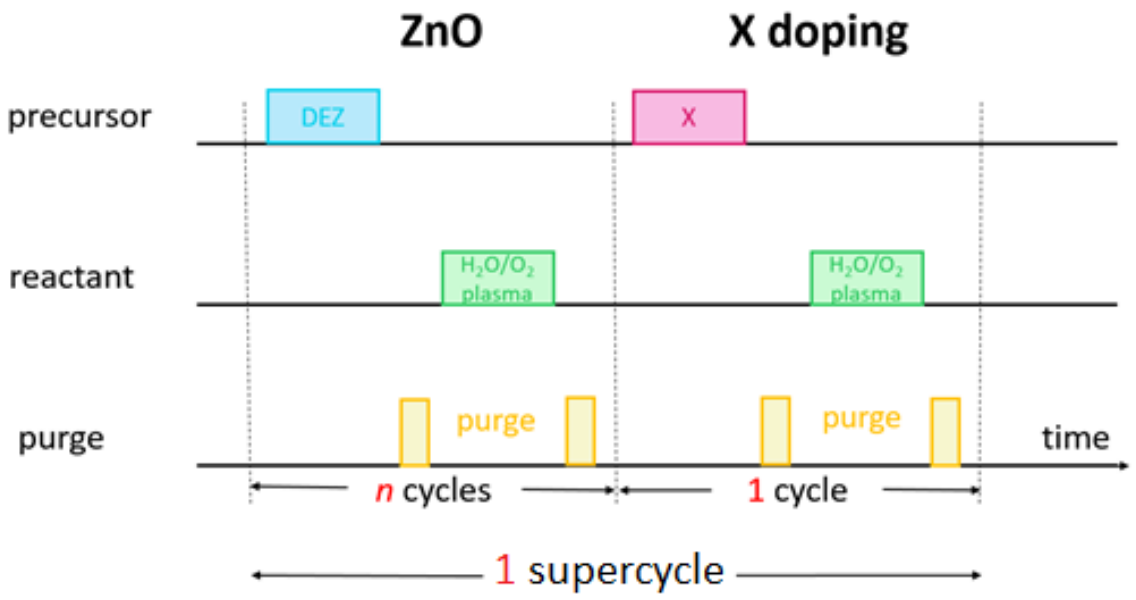

Figure 2.4: Supercycle method schematic for doped ZnO thin films in which X = Al, Ga, In, Ti and Sn

Dopant	Precursor	Carrier gas flow rate (sccm)	Pulse time (s)	Purge time (s)	T (°C)	
					bottle	neck
Al	Trimethylaluminium (TMA)	150	0.1	6.0	20	60
Ga	Trimethylgallium (TMG)	150	0.03	10.0	20	60
Sn	Tetrakis(dimethylamino)tin(IV) (TDMASn)	80	1.6	8.0	65	80
Ti	Tetrakis(dimethylamino)titanium(IV) (TDMAT)	80	1.8	8.0	65	80

Table 2.2: Carrier gas flow rate, precursor pulse, purge times and temperatures for TMA, TMG, TDMASn and TDMAT

A typical supercycle recipe used for the growth of ZnO: Al with a 19:1 dopant ratio was as follows: firstly the zinc precursor; DEZn was introduced to the chamber for a pulse time of 0.05 s followed by a 6 s purge. Next, a 28.0 s pulse of O_2 plasma was introduced (0.1 s pulse of H_2O for thermal ALD process). These two steps were then repeated a further 18 times giving a total of 19 ZnO growth cycles. The dopant was then introduced into the chamber. In the case of aluminium dopant, a 0.1 s pulse of TMA was employed followed by a 28.0 s pulse of O_2 plasma. This supercycle was repeated until the desired number of cycles is completed, 900 cycles in this case. Similar recipes were used for 9:1 dopant ratio films. This recipe presents a supercycle which has been altered in order to ensure growth does not cease on a dopant layer.

The Picosun™ R200 system offers a boost option which is particularly suitable for solid precursors with a low vapour pressure. The boost function works by flowing the carrier gas (N_2) through the precursor vessel when the pulsing valves are active. This is made possible as the precursor vessels were equipped with a second valve which the carrier gas could flow through. The boost function allows for more efficient transport of the precursor to the chamber. This function was utilized in the case of the TDMASn and TDMAT precursors.

2.2.4 Preparation of ZnO-based ternary thin films

The growth of ZnO-based ternary thin films also followed the supercycle method which is shown in figures 2.5, 2.6 and 2.7. In all cases, an additional 10 cycles of ZnO was grown at the end so as to not terminate the growth on a dopant layer. For each ternary with dopant 1 and 2, three combinations of dopant ratios were used (table 2.3). Ternary films that have been grown include; ZnO: TiO_2: Al_2O_3, ZnO: SnO_2: Al_2O_3 and ZnO: Ga_2O_3: Al_2O_3. All ternary films were deposited at 150 °C.

Case	Dopant 1 ratio	Dopant 2 ratio
1	9:1	19:1
2	19:1	9:1
3	19:1	19:1

Table 2.3: Dopant ratios used for the growth of ternary films

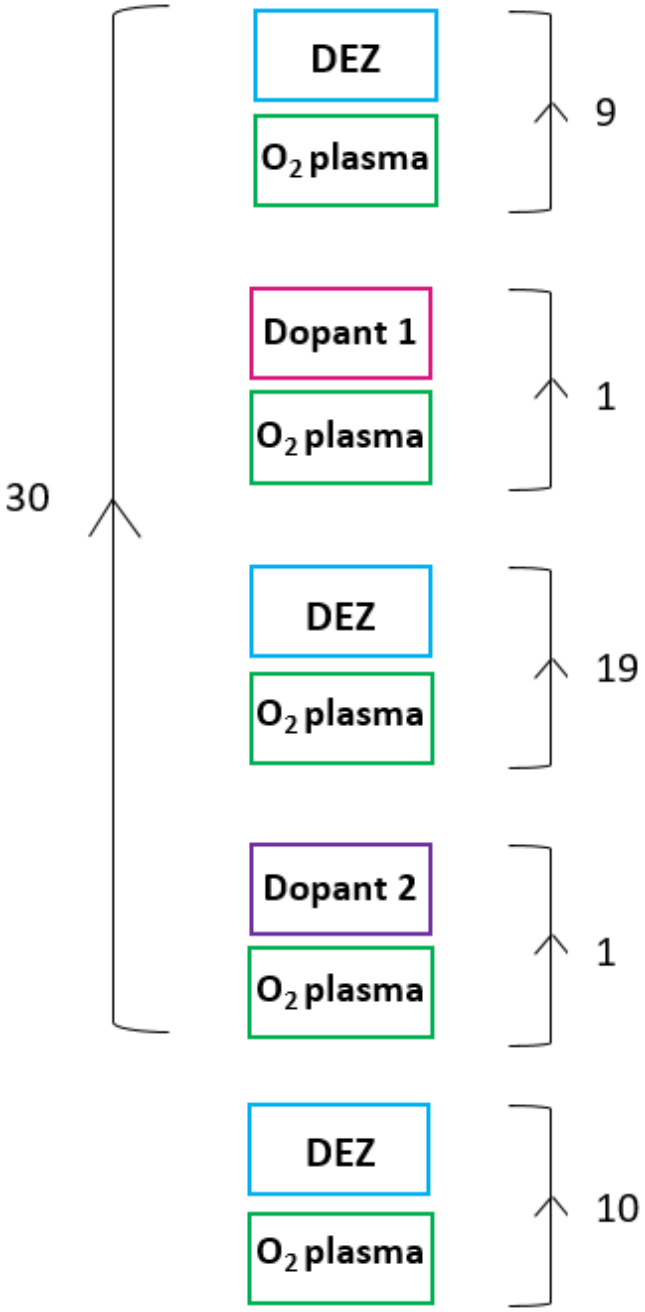

Figure 2.5: Supercycle recipe for the deposition of PE-ALD ZnO-based quaternary with 9:1 dopant 1 and 19:1 dopant 2 ratios using the Picosun™ R200

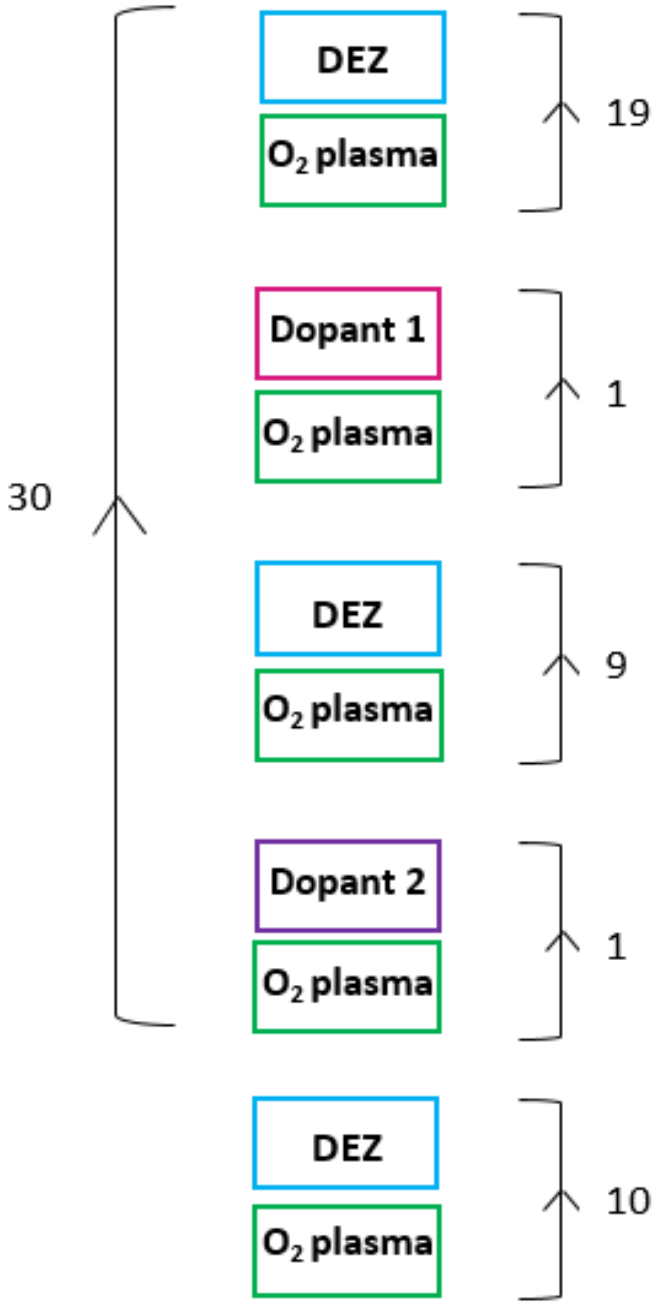

Figure 2.6: Supercycle recipe for the deposition of PE-ALD ZnO-based quaternary with 19:1 dopant 1 and 9:1 dopant 2 ratios using the Picosun™ R200

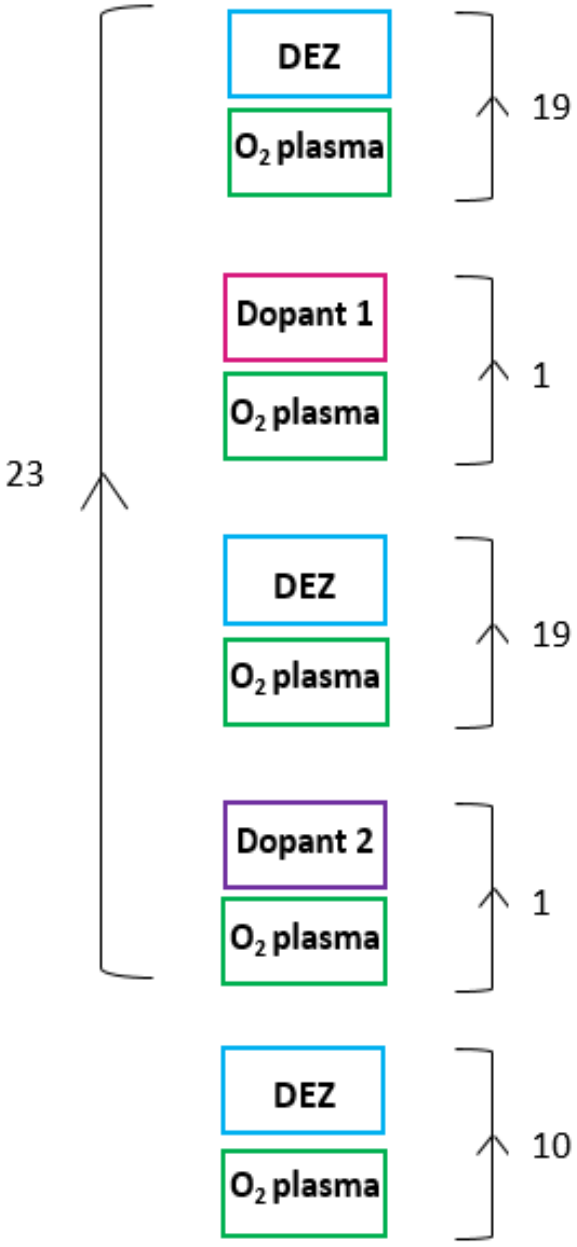

Figure 2.7: Supercycle recipe for the deposition of PE-ALD ZnO-based quaternary with 19:1 dopant 1 and 19:1 dopant 2 ratios using the Picosun™ R200

2.3 Methods of Analysis

2.3.1 Scanning Electron Microscopy

Scanning Electron Microscopy (SEM) is a microscopy technique that focuses a beam of electrons on a material in order to produce an image[1]. SEM is capable of achieving a resolution of less than 1 nm. The maximum resolution possible depends on a combination of the electron spot size and the interaction volume of electron beam occurring with the sample[2-4]. Prior to analysis, samples may be low vacuum sputter- coated with gold. Non-conductive samples or those deposited on insulating glass substrates tend to become charged under the electron beam and a gold coating is required in order to reduce charging effects so as to obtain a better quality image[2]. The sample is mounted on to a holder/stage and placed in a chamber. The high pressure region around the sample neutralizes any build-up of charge and allows for amplification of secondary electron (SE) signal. The optical column is pumped down in order to keep a low vacuum at the electron gun. Once sample preparation has been completed, primary electrons are released. There are three types of commonly used electron sources; tungsten filament, solid state crystal (CeB_6 or LaB_6) and field emission gun (FEG). The electron beam passes through a series of condenser lenses in which the beam is focused to a spot size of 0.4 and 0.5 nm in diameter. The electron beam then passes through a coiled Cu wire in which an electromagnetic field causes convergence of the beam. This focused, fine beam of electrons scans the sample surface using scanning coils in a raster pattern. The detector counts the number of SEs emitted from each point of the sample and the cathode ray tube scans to create an image. The higher the number of electrons detected, the brighter the spot on the image appears. The sample may be mounted and tilted at a certain angle in order to obtain a higher quality image. The tilt angle allows for the incident beam to move greater distances in the surface region meaning more SEs can be produced in this area than those that are normal to the electron beam[5].

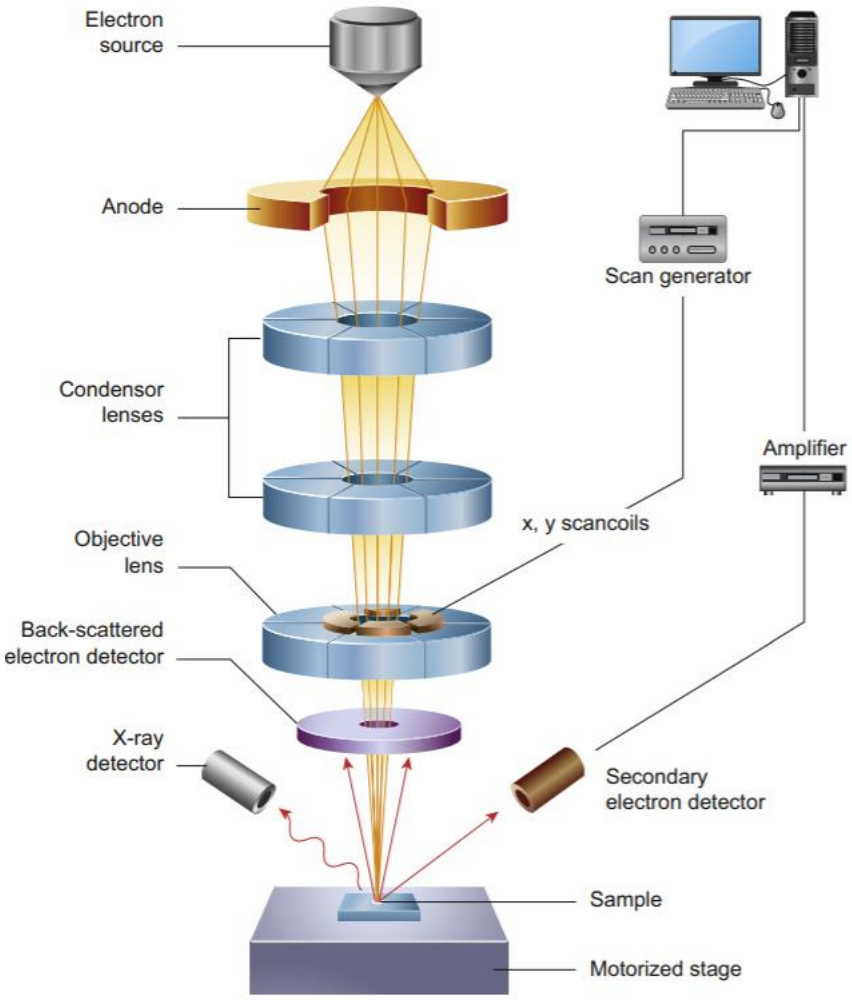

Figure 2.8: Schematic of components of a Scanning Electron Microscope[6]

SEM was undertaken using the FEI Quanta 650 FEG High Resolution Scanning Electron Microscope in order to view the surface of the films prepared. The followings conditions were applied; high vacuum, spot 2.0 – 3.0 and HV 15-20 kV. Prior to analysis, samples deposited on glass substrates were low vacuum sputter- coated with gold. SEM analysis was performed by Vince Lodge and Dr Michael Schmidt, Tyndall National Institute.

2.3.2 Transmission Electron Microscopy

Transmission Electron Microscopy (TEM) is a microscopy technique that produces highly detailed and magnified images. It allows for the analysis of internal microstructures. TEM sample preparation is more specialized than that for SEM analysis. Sample are cut thinly using a focused ion beam system (FIB) and often protective layers are deposited on top. The system operates by firstly heating of an emission source, typically a tungsten wire, and electrons are emitted by thermionic emission into a vacuum. For field emission, a field emission electron gun is used which uses a strong electric field to extract electrons from a metal filament. The electrons are accelerated towards the specimen through a series of electrostatic plates and a columnar aperture to the anode at high voltage. The electron beam then passes through a system of condenser lenses which focuses it on the specimen. The electrons are focused by an objective lens in which a diffraction pattern is formed, followed by an image. Projector lenses are then utilized to magnify the image/diffraction pattern onto the detection system. In order to create a sharper image, it is possible to decrease the number of electrons lost by controlling the size of the beam to be larger than that of the field of view[7, 8].

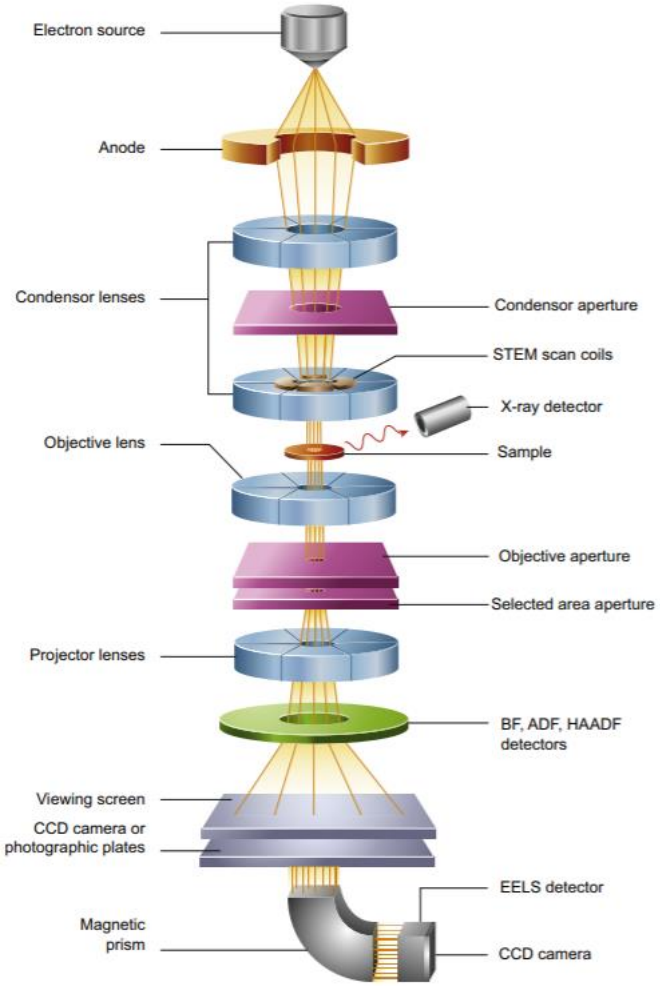

Figure 2.9: Schematic of components of a Transmission Electron Microscope[6]

In this work, cross sections of samples were prepared using a DualBeam FIB FEI Helios NanoLab 600i. Protective layers consisting of 50 nm C layer and 300 nm Pt layer were deposited within the DualBeam FIB by electron beam induced deposition and 2 um thick Pt layer with ion beam induced deposition. These layers were grown to protect the sample before the milling process. The lamellas were prepared and thinned down for the TEM analysis. The thinning at 30 kV was followed by polishing at 5 kV in order to reduce the ion-beam induced damage to a less than 2 nm thin layer on both sides. TEM analysis was performed using a JEOL JEM-2100 at 200kV operating in bright field mode (chapter 3). Cross sections of samples were

prepared by Dr Micheal Schmidt, Tyndall National Institute. TEM analysis for the work presented in chapter 3 was performed by Dr Micheal Schmidt. The Scanning electron transmission microscopy (STEM) analysis in chapter 5 was performed by Dr Michele Conroy at the Bernal Institute, University of Limerick using a Thermo-Fisher Scientific double tilt STEM holder in the Thermo-Fisher Scientific FEI double aberration-corrected monochromated Titan Themis Z. The microscope was operated at 300 kV. The imaging mode used was STEM at 146 mm camera length with a 50-µm C2 aperture. EDS mapping was done using a Bruker Super X detector. All Titan STEM and EDS data processing was done using Thermo-Fisher Scientific Velox Software.

2.3.3 X-ray Diffraction

X-ray diffraction (XRD) is an analytical technique which determines the crystallinity and allows for the phase identification of materials. A metal target, typically Cu, Cr or Mo is bombarded with electrons generated from the heating of a metal filament. This bombardment of a target causes the production of X-rays (electromagnetic radiation of wavelength ranging from 10 picometres to 10 nanometres). The X-rays produced are directed towards the thin film to be analysed. For a crystalline film, X-rays will be diffracted at different angles from the various crystal planes within the thin film. The nature of the planes is revealed from the analysis of the various diffracted beams and hence the crystalline type can then be determined.

XRD ideally requires a monochromatic X-ray source. The X-rays may interact constructively or destructively with the atoms and are used to measure the interatomic distances between atoms. Constructive interference occurs in crystalline materials due to in-phase waves combining which results in the reflection of X-rays in specific directions. Destructive

interference occurs when no reflected energy is emitted as waves that could combine are out of phase[9].

Bragg's Law presents the conditions necessary for constructive interference. Braggs Law (equation 2.1) is as follows[10];

$$n\lambda = 2d\sin\theta \qquad (2.1)$$

Where:

n is the order of diffraction

λ is the wavelength of light that is diffracted (nm)

d is the interatomic spacing (nm)

θ is the angle between the normal plane and incident X-rays

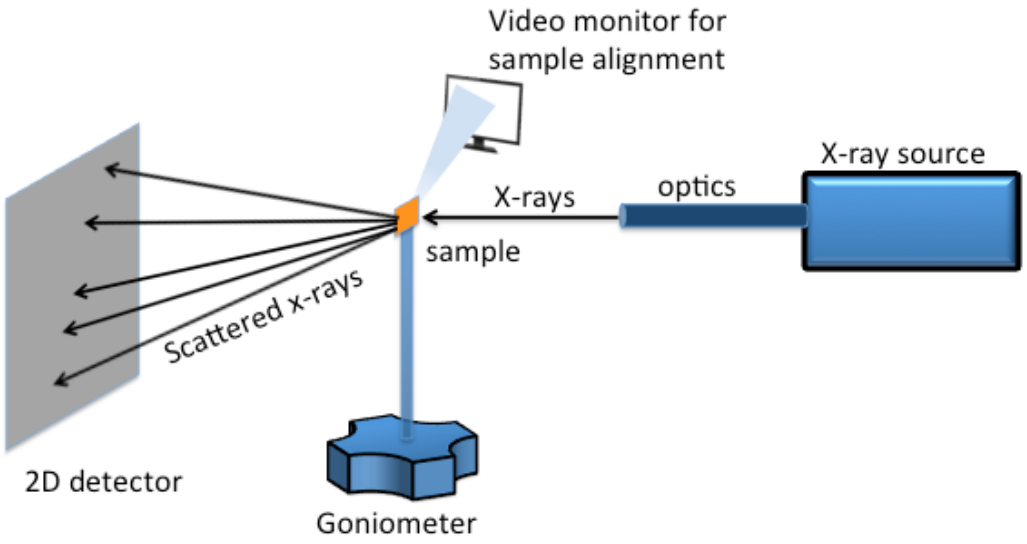

Figure 2.10: X-ray diffraction schematic. Adapted from He et al.[11]

All films in this work were analysed using a Phillips (PW3719) X'pert Materials Research X-ray diffractometer with a Cu Kα radiation (λ = 0.154056 nm) and a Panalytical X`Pert MRD

X-Ray diffractometer (Cu Kα radiation λ = 0.1541874 nm), 10 to 70° at a step size of 0.02° under 45 kV and 30 mA. The XRD analysis presented in chapters 5 and 6 was performed by Jennifer Halpin, Tyndall National Institute.

2.3.4 X-ray Photoelectron Spectroscopy

X-ray photoelectron spectroscopy (XPS) is a surface-sensitive spectroscopic technique that quantitatively identifies the elemental composition of materials. The technique can be used to generate empirical formula for materials. Detection limits of 0.1-1.0% are possible. During the analysis, a sample is irradiated by a beam of X-rays. The electron binding energy of each of the emitted electrons can be obtained using the equation for the photoelectron effect (equation 2.2)

$$E_{binding} = E_{photon} - (E_{kinetic} + \emptyset) \quad (2.2)$$

Where:

$E_{binding}$ - binding energy of electron measured in relation to the Fermi level of the material

E_{photon} - energy of X-ray photon

$E_{kinetic}$ - kinetic energy of electron measured by instrument

$\emptyset$ - work function of surface of the spectrometer

Each element produces a characteristic XPS peak and each peak corresponds to an electron configuration within an atom. The number of corresponding electrons in each peak that are detected directly relate to the amount of that element that is present in the sample being analysed. Variations in peaks may arise due to the following factors; different chemical environments may cause a shift in energy for materials with the same core levels. This effect

can be seen when a change in oxidation state can shift the position of an XPS peak by 1 eV. Differences in the hybridisation of orbitals can increases the binding energy and result in a shift in the XPS peak position. For carbon, different hybridisations resulted in a varying energies required to remove an electron such as carbon-carbon single bond 284.8 eV, carbon-oxygen single bond 286 eV and oxygen=carbon-oxygen both single and double bond to oxygen 288 eV[12, 13]. The position of a peak can be effected by spin-orbital coupling influences[14]. Doublet and triplet peaks can be obtained, particularly for p, d and f orbitals. The Ti 2p peak is observed as a doublet due to two spin-coupling modes; Ti 2p ½ and Ti 2p $^{3}/_{2}$. The atomic percentages of constituent atoms may be calculated. The XPS spectrum produced is a plot of the number of detected electrons at specific binding energies. The presence of H or He are not detected by XPS analysis[15].

The composition and binding energies of the films were investigated by XPS using a Kratos AXIS_ULTRA spectrometer with the following parameters; sample temperature: 20-30 °C and X-ray gun: mono Al K_{α} 1486.58 eV; 150 W, 10 mA, 15kV (300 W, 20 mA, 15 kV for doped ZnO). Samples were sputtered with Argon Gas Cluster source (10keV, Ar1000+ clusters) for 2-3 seconds in order to remove the carbon over layer. Analysis was completed by Dr Fathima Laffir and Dr Karrina McNamara at the Bernal Institute, University of Limerick.

2.3.5 UV/Visible Spectroscopy

UV/Visible spectroscopy is an optical technique in which light interacts with matter and causes electronic transitions to occur. Incident light interacting with a sample can undergo the following processes; absorption, transmission and reflection. Scattering of light is also possible but tends to be negligible for samples that are particularly transparent[16, 17]. Table 2.4 shows the characteristic wavelength ranges for UV, visible and IR.

Region	Wavelength range (nm)
UV	190-380
Visible	380-750
IR	750-2000

Table 2.4: Characteristic wavelength ranges for UV, Visible and IR regions

The principle of UV/Visible spectroscopy is based on the so-called Beer-Lambert Law which is given in equation 2.3[18].

$$A = \log_{10}\left(\frac{I_0}{I}\right) = \varepsilon c l \qquad (2.3)$$

The Beer-Lambert law describes the exponential relationship that exists between the light intensity before (I_0) and after (I) interaction with a sample and relates to the molar absorptivity (ε) ($M^{-1}cm^{-1}$), concentration (c) (M) and optical pathway length (l) (cm).

Equation 2.3 shows the relationship between The Beer-Lambert law and absorbance (A). The transmittance (T) and percentage transmittance (%T) are given by;

$$\frac{I_0}{I} = T \qquad (2.4)$$

$$\frac{I_0}{I}\ x\ 100 = \%T \qquad (2.5)$$

The experimental set up of a UV/Visible spectrometer is shown in figure 2.11. The light source for UV is provided by a deuterium arc lamp and for visible and IR, a tungsten-halogen lamp is

used. Prior to the analysis of a sample, a background scan using a blank substrate reference should be carried out. Light emitted from the suitable source lamp passes through a diffraction grating/prism in which it is dispersed into different wavelengths. It then passes through a monochromator which selects a single wavelength that is sent in the direction of the sample to be measured. Monochromators may be single or double beam, the latter creates two beam paths which allows for better quality spectra as the amount of scattered light is reduced. A lens is then used to focus the beam onto a detector. The detector measures the intensity of light that has been transmitted thought the sample. A spectrum is produced that plots %A or %T as a function of wavelength. A Perkin Elmer 950 Spectrometer was used to analyse the %T of all films in this work. The analysis presented in chapters 5 and 6 was performed by Dr Mircea Modreanu, Tyndall National Institute.

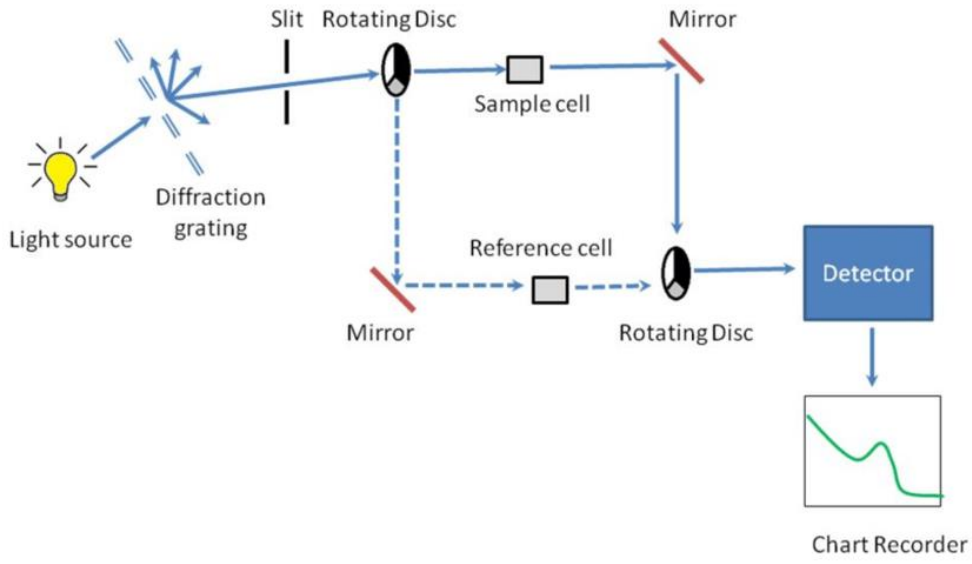

Figure 2.11: Schematic of the components of a UV/Visible Spectrometer[19]

2.3.6 Contact Angle Measurement

When a liquid comes in contact with a solid surface, the angle created between the two media is referred to as the contact angle (CA). It is determined by the properties of the liquid and solid and is influenced by the intermolecular forces that occur between them. Both cohesive and adhesive forces explain the interactions that occur[20, 21]. Young's equation is used to study the wettability of a surface. According to Young's equation[22];

$$\gamma_{SG} - \gamma_{LS} - \gamma_{LG}\mathrm{Cos}\theta_c = 0 \quad (2.6)$$

Where:

γ_{SG} - solid-gas surface tension

γ_{LS} - liquid-solid surface tension

γ_{LG} - liquid-gas surface tension

θ_c - contact angle (°)

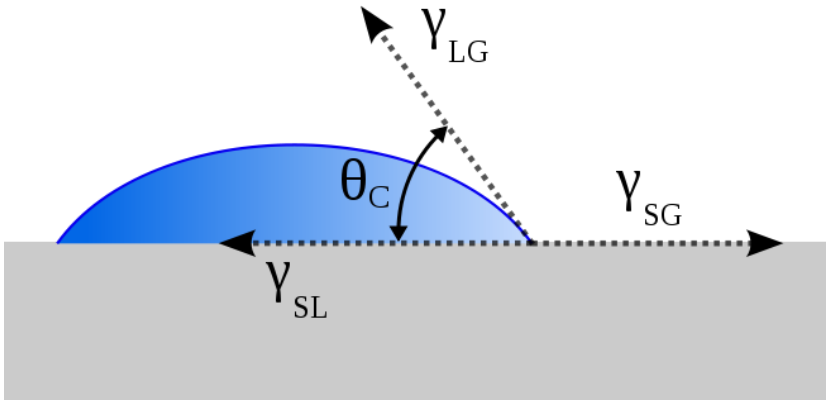

Figure 2.12: Understanding Contact Angle[20]

The contact angle can help to determine the degree of hydrophilicity or hydrophobicity of a thin film. Typically, hydrophilicity is characterised by a CA ≤80° and hydrophobicity >80°.

Complete surface wetting or superhydrophilicity and the opposite, complete surface dewetting or superhydrophobicity are characterised by the CAs <10° and >120° respectively[23].

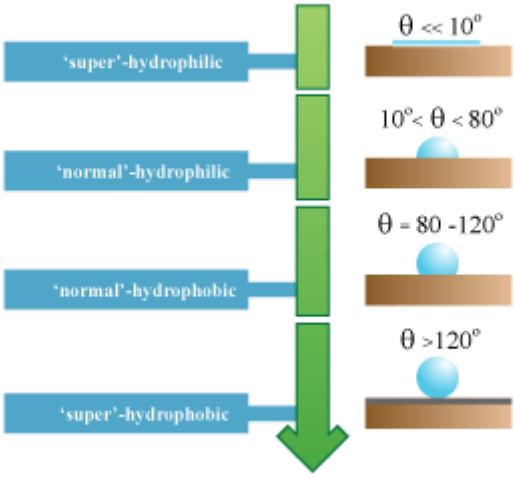

Figure 2.13: Contact angles associated with hydrophilic and hydrophobic surfaces[24]

In this work, contact angle measurements were carried out using a Data Physics OCA 15EC system utilising a sessile drop arrangement at room temperature. This instrument utilises a SCA20 software system. A Hamilton 100 µL syringe was used to dispense 1 µL water droplets onto the surface at medium speed. Small volumes were beneficial to avoid gravity-induced drop shape alteration and to diminish evaporation effects during CA measurements.

CA measurements were performed on samples prior to and after 30 and 60 minutes of UV light irradiation (INTEC standard ISO/WD 27448-1).

2.3.7 Evaluation of Photocatalytic Activity

Various methods of surface organic degradation are used in order to determine the degree of photoactivity that a particular material possesses. These methods include; dye or ink degradation[25-33], microbiological[34] and stearic acid (SA) decomposition[35, 36]. Photocatalytic

inks/dyes undergo oxidative/reductive degradation as a consequence of irradiation via light when present on the surface of an active photocatalyst. Photocatalytic dyes that have been used for the degradation of metal oxides include methylene blue (MB) [26-28, 37-39], methyl orange (MO) [29, 40], rhodamine B[31, 41, 42], basic blue 66 (BB66)[43] and resazurin (Rz)[43]. The SA method involves the mineralisation of SA into CO_2 and H_2O upon irradiation of the surface it is typically spin-coated onto. The photocatalytic degradation is monitored by Fourier Transform Infrared Spectroscopy (FTIR) analysis[44, 45]. With these methods, standardization is an issue. Most of the work reported previously involves disparate ink/dye dilutions, varying photocatalytic material quantities and differing light intensities. Evans and Mills have extensively studied techniques for determining photocatalytic activity[33, 46]. They have developed a self-cleaning surface tester pen that contain sacrificial electron donors (SEDs) and stabilizing polymers which is sold by Ink Intelligent™. The pen tests the activity of a photocatalytic surface by dispensing ink in a convenient and fast method[47].

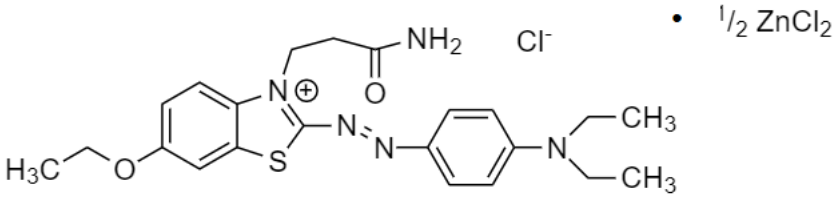

Figure 2.14: Chemical structure of basic blue 66

The work in this thesis employed a standardized INTEC method to measure photocatalytic activity. Evaluation was carried out by degradation of BB66 under UV light irradiation. A dropper was used to add the dye of choice to the top of the film and a metal rod (3 mm K-bar) was used to spread the dye across the film. The dye was allowed to dry and subsequently exposed to UV light (3.30 mV/cm^2). A qualitative approach was applied to monitor and record

the dye degradation over time which involved use of a handheld digital scanner (Skypix handscanner™).

2.3.8 The Hall Effect and Hall Measurements

The Hall Effect was discovered in 1879 by Edwin Hall who measured transverse voltage produced on Au foils. The Nobel Prize in Physics for the years 1985 and 1998 were awarded for work dedicated to the Hall Effect. In 1985, the prize was given to Professor Klaus von Klitzing, Max Planck Institute for the discovery of the quantized Hall Effect[48]. More recently in 1998, Robert Laughlin, Horst Störmer and Daniel Tsui were awarded the prize for noticing that electrons in a magnetic field can act together to form new types of "particles" whose charges have values that are fractions of the charge of an electron[49].

Hall Effect measurements are used to determine electrical properties of a material[50]. It is possible to determine the carrier type (electrons or holes) and the mobility of a material by measuring its Hall voltage. When an electric current flows through a material that is placed within a magnetic field, the magnetic field will exert a transverse force on the mobile charge carriers. This force is called the Lorentz force given in equation 2.7.

$$F_{Lorentz} = q(E + (v\ x\ B) \qquad (2.7)$$

Where:

q - particle charge

E - electric field

v - particle velocity

B - magnetic field (T)

This force separates the charge carriers and forces them to either side of the conductor where charge builds up. The influence of the magnetic field is balanced by the build-up of charge and creates a difference in voltage across the material which can be measured. This is known as the Hall voltage (V_H) and is given in equation 2.8[51].

$$V_H = R_H I B \tag{2.8}$$

V_H is proportional to the magnetic field (B), the current (I) and the Hall coefficient (R_H). V_H is inversely proportional to the thickness (t). The following equations relate R_H and the resistivity (ρ) to the carrier density (n) and mobility (μ).

$$\rho = \frac{1}{ne\mu} \tag{2.9}$$

And

$$R_H = \frac{1}{ne} \tag{2.10}$$

Therefore

$$\mu = \frac{R_H}{\rho} \tag{2.11}$$

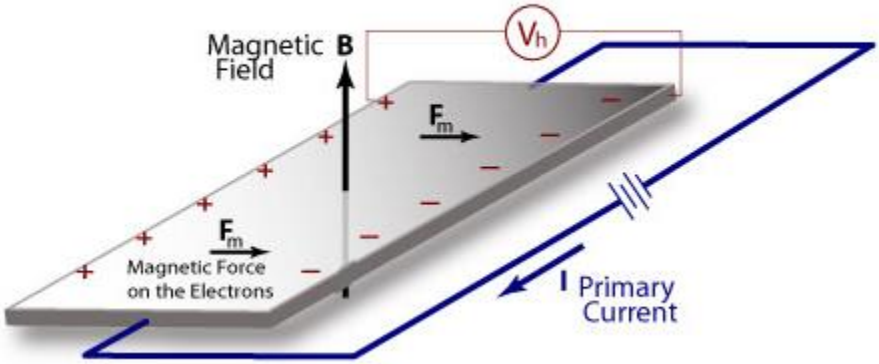

Figure 2.15: Schematic representation of the Hall Effect[52]

Two Hall methods are used, DC and AC. Typically, for a DC field, mobilities less than 10 cm^2/ V.s are difficult to measure. In contrast AC field Hall systems are capable of measuring mobilities on the order of 0.001 cm^2/ V.s.

The measured Hall voltage for a sample with ideal geometry would be zero with zero applied field. However, the measured experimental voltage (V_m) includes a misalignment voltage (V_o) and a thermoelectric voltage (V_{TE}). V_o is a result of asymmetric contact placement on the sample. It is independent of B and therefore it may be removed by field reversal. V_{TE} results as a consequence contacts between two different materials. The unwanted effects of V_{TE} can be removed by current reversal[53].

Drawbacks to the DC method include the following;

For low mobility materials (<10 cm^2/ V.s), V_o and V_{TE} may be quite large in comparison to V_H making it difficult to measure voltage. Systematic errors may be introduced as a consequence of drift of both V_o and V_{TE} as the values may vary over time.

The AC method is a more reliable measurement for low mobility materials. The V_H is proportional to B and so when an AC field is applied, the V_H signal is also an AC signal. As V_o and V_{TE} are both DC signals, they can easily be separated from the V_H signal. A lock-in amplifier is capable of separating AC signals from DC signals to a very high level of accuracy[50, 53].

For the measurements described in this thesis a van der Pauw arrangement was utilized. In this arrangement, the carrier density and resistivity of a flat sample (essentially 2D) that is of arbitrary shape can be measured without knowledge of its current pattern. The following conditions must be satisfied; contacts placed at the edges of the sample must be sufficiently small in size such that the error is on the order of $\frac{D}{L}$ where D is the diameter of contacts and L is the distance between contacts. The sample must have uniform thickness and there must be no isolated holes present[54, 55]. Contacts are typically placed on a square substrate as per figure 2.16. For the van der Pauw measurement, current is applied to the two adjacent contacts and the voltage is then detected between the other two. For Hall measurements, current is applied between opposite contacts (1 and 3) and voltage is detected between the two opposite contacts (2 and 4).

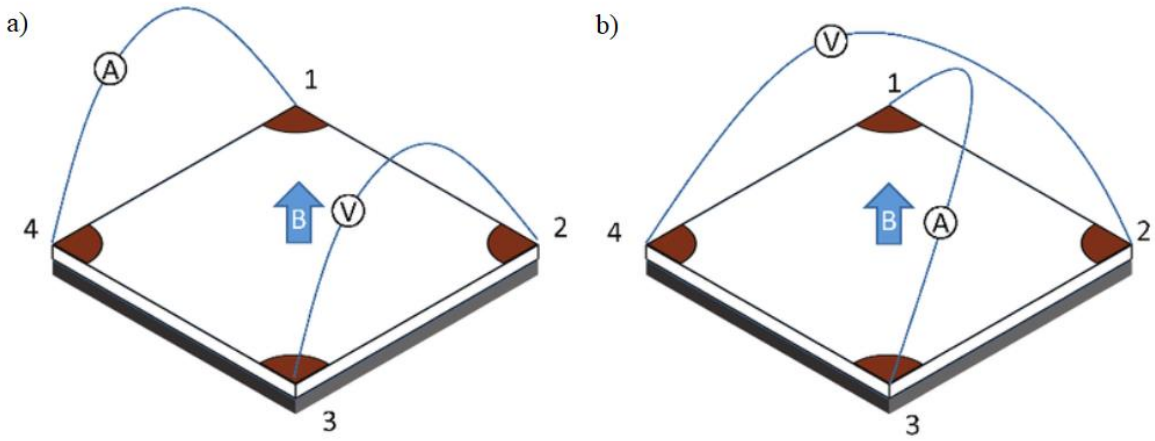

Figure 2.16: Schematic representations of a) Van der Pauw resistivity measurement configuration (one of the eight possible configurations) and b) The Hall Effect measurement configuration[56]

Prior to analysis of films deposited for this work, films deposited on glass substrates were diced into 10 mm^2 squares by Paul Tassie, Tyndall National Institute. The glass was cut along the back side and samples used for analysis were selected from the centre in order to ensure no growth was deposited on edge or back of samples. A van de Pauw arrangement was used with ohmic contacts in place on the 4 corners of the square sample. The average resistivity of the sample was measured by placing a four point probe on each corner point. The measurements were performed using a Lake Shore 8404 AC/DC (alternating current/ direct current) Hall-effect system. The system offers both AC and DC magnetic fields (B) over a variable range up +/- 1.7 T for DC and up to a fixed range of 1.24 T for AC.

References

1. Goldstein, J., Scanning Electron Microscopy and X-ray Microanalysis. 3rd ed.; Springer US: 2003.

2. Goldstein, J. I., Newbury, D. E., Echlin, P., and Joy, D. C., Scanning electron microscopy and x-ray microanalysis (2nd ed.). New York: Plenum Press **1992**.

3. Goldstein, J. K., and Yakowitz, H., Practical scanning electron microscopy: Electron and ion microprobe analysis. New York: Plenum Press **1975**, 582.

4. Brabazon, D., and Raffer, A., Advanced Characterization Techniques for Nanostructures. In Emerging nanotechnologies for manufacturing, Ahmed, W. and J., M. J., Ed. William Andrew Publishing: Boston, 2010; pp 59-91.

5. Akhtar, K., Scanning Electron Microscopy: Principle and Applications in Nanomaterials Characterization. In Handbook of Materials Characterization, Sharma, S. K., Ed. Springer International Publishing: 2018; pp 113-145.

6. Inkson, B. J., Scanning electron microscopy (SEM) and transmission electron microscopy (TEM) for materials characterization, Materials Characterisation using Non Destructive Evaluation (NDE) Methods. University of Sheffield, Sheffield, UK, 2016; pp 17-43.

7. Javed, Y., TEM for Atomic-Scale Study: Fundamental, Instrumentation, and Applications in Nanotechnology. In Handbook of Materials Characterization, Sharma, S. K., Ed. Springer International Publishing: 2018; pp 147-216.

8. Bendersky, L. A. and Gayle, F. W., Electron Diffraction Using Transmission Electron Microscopy. *J Res Natl Inst Stand Technol.* **2001,** 106 (6), 997-1012.

9. Giannini, C., Ladisa, M., Altamura, D., Siliqi, D., Sibillano, T. and De Caro, L., Xray diffraction: a powerful technique for the multiple length scale structural analysis of nanomaterials. *Crystals* **2016,** 6 (8), 1-22.

10. Atkins, P.; de Paula, J., Atkins' Physical Chemistry: Thermodynamics, Structure, and Change. 9th ed.; Oxford University Press: 2014.

11. He, B. B., Preckwinkel, U. and Smith, K. L., *Advances in X-ray Analysis* **2000,** 43, 273.

12. Liu, J. M., Han, L., An, N., Xing, L., Ma, H. Y., Cheng, L., Yang, J. C. and Zhang, Q. C., Enhanced visible-light photocatalytic activity of carbonate-doped anatase TiO_2 based on the electron-withdrawing bidentate carboxylate linkage. *Applied Catalysis B: Environmental* **2017,** 202, 642-652.

13. Georgios, P. and Wolfgang, S. M., X-ray photoelectron spectroscopy of anatase-TiO_2 coated carbon nanotubes. In Solid State Chemistry and Photocatalysis of Titanium Dioxide (Solid State Phenomena), Nowotny, M. K. and N., J., Ed. Trans Tech Publications Ltd: 2010; Vol. 162, pp 163-177.

14. Lin, C., Posadas, A., Hadamek, T. and Demkov, A. A., Final-state effect on x-ray photoelectron spectrum of nominally d1 and n-doped d0 transition-metal oxides. *Phys. Rev. B* **2015,** 92 (3).

15. Kerber, S. J., Bruckner, J. J., Wozniak, K., Seal, S., Hardcastle, S. and Barr, T. L., The nature of hydrogen in x-ray photoelectron spectroscopy: General patterns from hydroxides to hydrogen bonding. *Vacuum Science & Technology A: Vacuum Surfaces and Films* **1996,** 14 (3), 1314-1320.

16. Perkampus, H. H., UV-VIS Spectroscopy and Its Applications. Springer-Verlag Berlin Heidelberg: 1992; p 244.

17. Thomas, M. J. K., Ultraviolet and Visible Spectroscopy: Analytical Chemistry by Open Learning. 2nd ed.; Wiley: 1996.

18. Swinehart, D. F., The Beer-Lambert Law. *J. Chem. Educ.* **1962,** 39 (7), 333.

19. Bordoloi, A. A Detailed Study on Optical and Physical Properties of Rice and its by-products. Tezpur University, 2017.

20. http://chemwiki.ucdavis.edu/Physical_Chemistry/Physical_Properties_of_Matter/Bulk_Properties/Cohesive_And_Adhesive_Forces/Contact_Angles. (accessed 17/08/15).

21. Good, R. J., Contact angle, wetting, and adhesion: a critical review. *Journal of Adhesion Science and Technology* **1992,** 6 (12), 1269-1302.

22. Kontogeorgis, G. M. and Kill, S., Fundamental Equations in Colloid and Surface Science. In Introduction to Applied Colloid and Surface Chemistry, John Wiley & Sons, Ltd.: 2016; pp 74-95.

23. Verplanck, N., Coffinier, Y., Thomy, V. and Boukherroub, R., Wettability Switching Techniques on Superhydrophobic Surfaces. *Nanoscale Res Lett.* **2007,** 2 (12), 577–596.

24. http://www.hk-phy.org/atomic_world/lotus/lotus02_e.html. (accessed 01/09/15).

25. Breault, T. M. and Bartlett, B. M., Lowering the band gap of anatase structured TiO_2 by coalloying with Nb and N: Electronic structure and photocatalytic degradation of methylene blue dye. *Journal of Physical Chemistry C* **2012,** 116 (10), 5986-5994.

26. Dey, N. K., Kim, M. J., Kim, K.-D., Seo, H.O., Kim, D., Kim, Y.D., Lim, D. C. and Lee, K. H., Adsorption and photocatalytic degradation of methylene blue over TiO_2 films on carbon fiber prepared by atomic layer deposition. *Journal of Molecular Catalysis A: Chemical* **2011,** 337 (1-2), 33-38.

27. Kerkez, O. and Boz, I., Efficient removal of methylene blue by photocatalytic degradation with TiO_2 nanorod array thin films. *Reaction Kinetics Mechanisms and Catalysis* **2013,** 110 (2), 543-557.

28. Yogi, C., Kojima, K., Wada, N., Tokumoto, H., Takai, T., Mizoguchi, T. and Tamiaki, H., Photocatalytic degradation of methylene blue by TiO_2 film and Au particles-TiO_2 composite film. *Thin Solid Films* **2008,** 516 (17), 5881-5884.

29. Tian, J., Chen, L., Yin, Y., Wang, X., Dai, J., Zhu, Z., Liu, X. and Wu, P., Photocatalyst of TiO_2/ZnO nano composite film: Preparation, characterization, and photodegradation activity of methyl orange. *Surface & Coatings Technology* **2009,** 204, 205-214.

30. Xu, X., Wang, J. Tian, J., Wang, X., Dai, J. and Liu, X. , Hydrothermal and postheat treatments of TiO_2/ZnO composite powder and its photodegradation behavior on methyl orange. *Ceramics International* **2011,** 37 (7), 2201-2206.

31. Zhang, J., Yan, S., Fu, L., Wang, F., Yuan, M., Luo, G., Xu, Q., Wang, X. and Li, C., Photocatalytic degradation of rhodamine B on anatase, rutile, and brookite TiO_2. *Chinese Journal of Catalysis* **2011,** 32 (6), 983-991.

32. Giwa, A.; Obinna Nkeonye, P.; Bello, K.; Ademola Kolawole, K., Photocatalytic Decolourization and Degradation of C. I. Basic Blue 41 Using TiO_2 Nanoparticles. 2012; Vol. 03, p 1063-1069.

33. Mills, A. and McGrady, M., A study of new photocatalyst indicator inks. *Journal of Photochemistry and Photobiology A: Chemistry* **2008,** 193 (2-3), 228-236.

34. Regmi, C., Joshi, B., Ray, S. K., Gyawali, G. and Pandey, R. P., Understanding Mechanism of Photocatalytic Microbial Decontamination of Environmental Wastewater. *Front Chem*. **2018,** 6 (33).

35. Mills, A. and Wang, J., Simultaneous monitoring of the destruction of stearic acid and generation of carbon dioxide by self-cleaning semiconductor photocatalytic films. *Journal of Photochemistry and Photobiology A: Chemistry* **2006,** 182 (2), 181-186.

36. Smirnova, N., Fesenko, T., Zhukovsky, M., Goworek, J. and Eremenko, A., Photodegradation of stearic acid adsorbed on superhydrophilic TiO_2 surface: In situ FT-IR and LDI study. *Nanoscale Res Lett.* **2015,** 10, 1-7.

37. Kaariainen, M. L., Kaariainen, T. O., and Cameron, D. C., Titanium dioxide thin films, their structure and its effect on their photoactivity and photocatalytic properties. *Thin Solid Films* **2009,** 517 (24), 6666-6670.

38. Binas, V. D., Sambani, K., Maggos, T., Katsanaki, A. and Kiriakidis, G., Synthesis and photocatalytic activity of Mn-doped TiO_2 nanostructured powders under UV and visible light. *Applied Catalysis B: Environmenta*l **2012,** 113, 79-86.

39. Rashad, M. M., Elsayed, E. M., Al-Kotb, M. S. and Shalan, A. E., The structural, optical, magnetic and photocatalytic properties of transition metal ions doped TiO_2 nanoparticles. *Journal of Alloys and Compounds* **2013,** 581, 71-78.

40. Xu, X., Wang, J. Tian, J., Wang, X., Dai, J. and Liu, X., Hydrothermal and postheat treatments of TiO_2/ZnO composite powder and its photodegradation behavior on methyl orange. *Ceramics International* **2011,** 37 (7), 2201-2206.

41. Zhuang, J., Dai, W., Tian, Q., Li, Z., Xie, L., Wang, J., Liu, P., Shi, X. and Wang, D., Photocatalytic degradation of RhB over TiO_2 bilayer films: Effect of defects and their location. Langmuir **2010,** 26 (12), 9686-9694.

42. Banerjee, A. N., Joo, S. W. and Min, B.-K., Photocatalytic degradation of organic dye by sol-gel-derived gallium-doped anatase titanium oxide nanoparticles for environmental remediation. *Journal of Nanomaterials* **2012**, 1-14.

43. Mills, A., O'Rourke, C. and Wells, N., A smart ink for the assessment of low activity photocatalytic surfaces. *Analyst* **2014,** 139, 5409.

44. Mills, A. a. M., M., Current and possible future methods of assessing the activities of photocatalyst films. *Catalysis Today* **2007,** 129 (1-2), 22-28.

45. Mills, A. and Wang, J., Simultaneous monitoring of the destruction of stearic acid and generation of carbon dioxide by self-cleaning semiconductor photocatalytic films. *Journal of Photochemistry and Photobiology A: Chemistry* **2006,** 182 (2), 181-186.

46. Evans, P., Mantke, S., Mills, A., Robinson, A. and Sheel, D. W., A comparative study of three techniques for determining photocatalytic activity. *Journal of Photochemistry and Photobiology A: Chemistry* **2007,** 188 (2-3), 387-391.

47. https://www.inkintelligent.com/ (accessed 18/09/2020).

48. von Klitzing, K., The quantized Hall effect. *Rev. Mod. Phys.* **1986,** 58 (3).

49. Schwarzschild, B., Physics Nobel Prize Goes to Tsui, Stormer and Laughlin for the Fractional Quantum Hall Effect. *Physics Today* **1998,** 51 (12).

50. Schroder, D. K., Semiconductor Material and Device Characterization. 3rd ed.; John Wiley & Sons, Inc.: Hoboken, New Jersey, 2006.

51. Standard Test Methods for Measuring Resistivity and Hall Coefficient and Determining Hall Mobility in Single-Crystal Semiconductors. Annual Book of ASTM Standards. 2000; Vol. 10.05.

52. https://www.ndeed.org/EducationResources/CommunityCollege/MagParticle/Physics/Measuring.htm (accessed 27/06/2016).

53. Lindemuth, J. and Mizuta, S. I., Hall measurements on low mobility materials and high resistivity materials. Proc. SPIE 8110, *Thin Film Solar Technology III* **2011,** 81100I.

54. Van der Pauw, L. J., A Method of Measuring Specific Resistivity and Hall Effect of Discs of Arbitrary Shape. *Phil. Res. Rep.* **1958,** 13 (1), 1-9.

55. Van der Pauw, L. J., A Method of Measuring the Resistivity and Hall Coefficient on Lamellae of Arbitrary Shape. *Philips Technical Review* **1958,** 20 (8), 220-224.

56. Balestrieri, M. Transparent conductive oxides with photon converting properties in view of photovoltaic applications: the cases of rare earth-doped zinc oxide and cerium oxide. Université de Strasbourg, 2014.

Chapter 3: Combinatorial ALD for the Growth of ZnO/TiO_2 Nanolaminates and Mixed ZnO/TiO_2 Nanostructured Films

---

Abstract

In this study, combinatorial atomic layer deposition (C-ALD) has been used to deposit layered ZnO and TiO_2 nanolaminates on both oxide-covered Si (100) wafers and glass substrates in order to assess the influence of substrate and each layer on the structure of the resulting nanolaminates and their photoactivity towards dye degradation. In addition, for comparison to these layered structures, C-ALD has been used to directly create oxide films consisting of an approximately equal mixture of Zn^{2+} and Ti^{4+} ions using the concept of under-dosing in order to deposit sub-monolayer quantities of each oxide per complete C-ALD cycle.

A nucleation delay was observed for ZnO deposited directly on the substrate and on the subsequent TiO_2 layer, the latter to a lesser extent. The reason for the difference in nucleation delay is due to the dissimilar surface groups. For the deliberately-layered structures it was found that on both substrate types, ZnO appeared to possess a templating influence on the TiO_2 layer grown subsequently. XRD analysis showed strong preferential orientation for (002) which indicates the polycrystalline manner of the ZnO film. XRD results also suggested that layer growth was substrate-dependent as crystalline TiO_2 was only identified on glass substrates. The nanolaminate structures were found to be stable in that the layer structure remained intact after annealing at 400 °C for 1 hour in contrast to the mixed ZnO: TiO_2 (1:1) film which showed evidence of ZnO segregation and crystallisation. With respect to

photocatalytic activity, no evidence was found for any enhancement of photoactivity in the mixed or nanolaminate films, the most photoactive films being those consisting of ZnO deposited onto glass substrates.

3.1 Introduction

Thin film materials are an essential part of the modern world being relevant to all aspects of society as may be easily appreciated when one considers electronics, energy, communications and medical issues. Nanostructured materials offer unique, but more often unknown potential benefits that could positively be applied in all of the areas cited arising from the fact that the properties of atoms, groups of atoms and ultra-thin layers are exploited rather than bulk materials.

Hybrid nanolaminate materials have attracted great attention in recent years due to the physical and chemical properties that 2D nanosheets possess that their bulk counterparts do not such as electrical[1, 2], mechanical[3], optical[4-6] and thermal properties[7]. The number of publications on the topic is increasing and is predicted to continue to increase[8]. Noteworthy reviews exist on the topic which explore the fundamentals and importance of these materials[8-10] and also with a focus on specific application fields[11]. The applications of hybrid films are almost endless, ranging from use as capacitors[12-15], dielectrics and insulators[16-25], encapsulation layers/ protective coatings[26-34], lubricants[35] and optical waveguides[36].

Specifically, nanolaminates are multicomponent systems consisting of alternating layers of materials such as metals and metal oxides. Each layer has an associated thickness on the nanometre scale[37]. Mixing a wide variety of materials makes it possible to fine-tune a material in terms of its properties, composition and structure[38]. Films of this type can be readily prepared using atomic layer deposition (ALD) - particularly when deployed in a combinatorial sense using multiple precursors, since ALD is a method that is capable of producing precise films

with constant thickness[39, 40]. Under these conditions the method has been referred to as combinatorial ALD or C-ALD. The unique conformity and precision of ALD enables sub-nanometre design and control of these true nanolaminates thus facilitating the realisation of unique materials properties through this combinatorial approach. Indeed C-ALD provides a route to the fabrication of a truly vast number of potentially new materials, being based on sets of layers of differing materials, layers consisting of mixtures of sub-monolayer quantities of various materials, materials where doping is spread or confined to particular layers or even the creation of new types of alloys.

Using C-ALD it is thus potentially possible to create materials that have new electronic, magnetic and optical properties. Many such properties depend on bulk phenomena which then manifest as new surface phenomena[41]. Photocatalytic activity is a good example of such a phenomenon, in which the creation of excitons via the absorption of light of energy greater than the band gap of the material results in the formation of highly oxidizing surface species, capable of destroying organic materials such as pollutants and micro-organisms. Arguably, the most well-known examples of photocatalytically active metal oxide materials are TiO_2 and ZnO.

Both ZnO and TiO_2 are wide band gap semiconductors with band gap energies in the region of 3.2 eV – 3.4 eV[42, 43]. The similarity in band gap energies of TiO_2 and ZnO and their similar photocatalytic mechanisms suggest TiO_2 and ZnO as suitable materials to be coupled together. Previous work synthesizing ZnO/TiO_2 laminates involved the use of E-beam evaporation[44], sol-gel methods[44-46], ALD[47-49] and spatial ALD[50] with alternative precursors. The findings of these studies showed improvements in crystallinity and quality of ZnO as a direct consequence of a TiO_2 under layer[44], the successful degradation of organic dyes[45, 46], enhanced friction coefficients[49] and increased growth per cycle (GPC) of TiO_2 when deposited on ZnO as opposed to itself[48]. Interestingly, as the number of bilayers increased with the total thickness

and composition of the films remaining the same, an enhancement of the optical transmittance was observed[47, 50]. XRD spectra of nanolaminates revealed weaker signature peaks for the same thickness nanolaminates with more bilayers, suggesting the possibility of tuning nanolaminates from crystalline to amorphous phase. As the number of bilayers decreased for films with the same overall thickness, the refractive index (RI) decreased[50].

In terms of the photocatalytic properties of both ZnO and TiO_2 it is interesting to consider whether the functionalities will both act together and be enhanced or degraded when the materials are combined in various nanolaminate structures. Possible enhancements of photocatalytic activity may arise from greater photocarrier separation arising for example from the ability of ZnO to act as an electron transport layer[51-54]. On the other hand a loss in photocatalytic activity may arise from structural factors related to templating effects.

In order to try to examine these and other potential issues we have studied the growth of nanolaminates of ZnO and TiO_2 using a C-ALD approach. Nanolaminate structures have been prepared with the specific aim of combining the photocatalytic properties and robustness of TiO_2 with the transparent conducting behaviour and photoactivity of ZnO. In addition we have grown a mixed ZnO/TiO_2 layer by deliberately under-dosing during the metal precursor parts of the ALD cycle. Figures 3.1 and 3.2 are schematic representations of the structures grown and examined here. The spacing and thickness of the ZnO and TiO_2 layers in the nanolaminates have been carefully controlled and the resulting materials studied using electron microscopy, atomic force microscopy and UV/visible spectroscopy. In addition the photocatalytic properties of the layers were examined using a combination of contact angle measurements and a simple dye test, comparing TiO_2 layers both with and without ZnO under–layers (and *vice versa*), in order to assess the magnitude and range of ZnO templating influence on the photo active nature of the TiO_2.

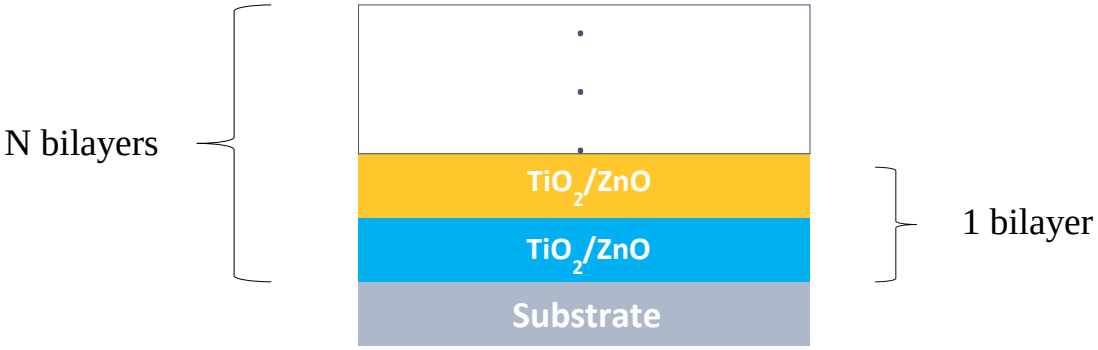

Figure 3.1: Schematic of the TiO_2/ZnO nanolaminates

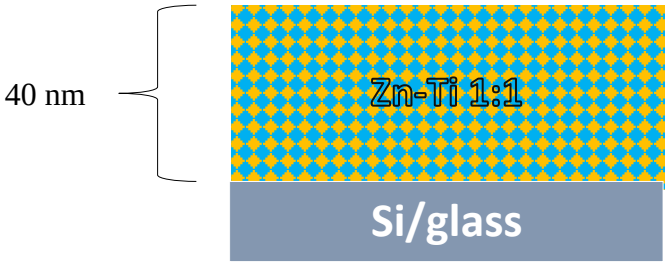

Figure 3.2: Schematic of the true ZnO: TiO_2 1:1 nanolaminate

3.2 Experimental

3.2.1 Preparation of TiO_2/ZnO composites

TiO_2/ZnO bilayer laminate films were deposited on glass and Si (100) substrates using a Cambridge Nanotech Fiji 200 ALD system. Diethyl zinc (DEZn) (min. 95% Strem Chemicals), tetrakis(dimethylamido)titanium(IV) (TDMAT) (99% Strem Chemicals) and water were used as precursors at a growth temperature of 200 °C. Argon (Ar) was used a carrier gas to transport the precursor molecules into the chamber. During the deposition process, the diethyl zinc and water were sustained at room temperature while the temperature of the titanium precursor container; was set to a temperature of 80 °C to ensure sufficient vapour pressure was generated. Pulse times were 0.4 s, 0.2 s and 0.1 s for TDMAT, diethyl zinc and water respectively accompanied with a 10 s argon purge between precursor pulses to remove redundant ligands. The deposition rate was controlled at 2 Å/cycle for ZnO layers and 0.5 Å/cycle for TiO_2 layers. The deposition depth of both ZnO and TiO_2 layers was 40 nm. Films were produced with ZnO layer (40 nm) followed by TiO_2 layer (40 nm) and *vice versa*. For comparison, TiO_2 and ZnO films were grown with a thickness of 40 nm using the same precursors already mentioned. A laminate consisting of ZnO and TiO_2 multilayers, (4 nm ZnO + 4 nm TiO_2) x5 was grown. A deliberately mixed ZnO/TiO_2 1:1 film was also grown by alternating very short (0.05 s) pulses of each precursor until the desired thickness of 40 nm was reached.

3.2.2 Characterization techniques

The surface morphology of the film was observed using scanning electron microscopy (SEM) using a FEI Quanta 650 FEG High Resolution Scanning Electron Microscope. The crystallinity of the TiO_2/ZnO films was analysed by X-ray diffraction (XRD) using a PANalytical X'Pert Pro diffractometer, with Cu Kα (λ = 0.154 nm) radiation from 10 to 70° at a step size of 0.02° under 45 kV and 30 mA. Grazing incidence XRD (GIXRD) was carried out on a Rigaku Ultima

with an incidence angle of 2°. The XRD results were compared to the Joint Committee on the Powder Diffraction Standard cards (JPCDS). The interface of the bilayer was observed using transmission electron microscopy using FIB/TEM. Atomic Force Microscopy (AFM) measurements were carried out in the non-contact mode, with an XE-100 apparatus from Park Systems, using sharp tips. The topographical 3D AFM images were taken over the area of 1 x 1 μm^2. The images were processed with XEI (v.1.8.0) Image Processing Program developed by Park Systems. The UV–Vis transmission spectra were recorded in the range of 200 – 1000 nm using a Perkin Elmer Lambda 950 UV/VIS/NIR spectrometer. The composition and binding energies of the films were investigated by x-ray photoelectron spectroscopy (XPS) using a Kratos AXIS_ULTRA spectrometer with the following parameters; sample temperature: 20-30 °C and X-ray gun: mono Al Kα 1486.58 eV; 150 W (10 mA, 15 kV). Samples were sputtered with Argon Gas Cluster source (10 keV, Ar1000+ clusters) for 2-3 sec in order to remove the carbon over layer Contact angle (CA) measurements were obtained using a Data Physics OCA 15EC system utilising a sessile drop arrangement at room temperature. A Hamilton 100 µL syringe was used to dispense 1 µL water droplets onto the surface. Small volumes were beneficial to avoid gravity-induced drop shape alteration and to diminish evaporation effects during CA measurements.

3.2.3 Evaluation of Photocatalytic Activity

The photocatalytic activity was evaluated by degradation of various dyes under UV light irradiation. A dropper was used to add the dye of choice to the top of the film and a metal rod (3 mm K-bar) was used to spread the dye across the film. The dye was allowed to dry and subsequently exposed to UV light (3.30 mV/cm^2). A qualitative approach was applied to monitor and record the dye degradation over time which involved the use of a handheld digital scanner.

3.3 Results and discussion

3.3.1 The surface morphologies and structural properties of TiO_2/ZnO films

Figure 3.3 shows the GIXRD pattern of selected samples. For both ZnO grown on TiO_2 and *vice versa*, the most predominate peaks can be attributed to hexagonal ZnO with the (002) peak being most evident. Strong preferential orientation for (002) indicates the polycrystalline manner of the ZnO film. This corresponds to wurtzite ZnO. On glass substrates, peaks are again visible for hexagonal ZnO but interestingly also seen are peaks that may be attributed to anatase TiO_2. The GIXRD patterns suggest that ZnO is somewhat crystalline. Interestingly, the XRD pattern of both ZnO: TiO_2 (1:1) and ZnO-TiO_2 (bilayer x5) appear to be strikingly similar on both glass and Si (100) substrates. A crystalline peak at approximately 52° on the Si (100) substrate is seen for both films and is assigned to TiO_2 (105), indicative of the anatase phase. The observed GIXRD peaks compare to standard JCPDS file data.

(a)

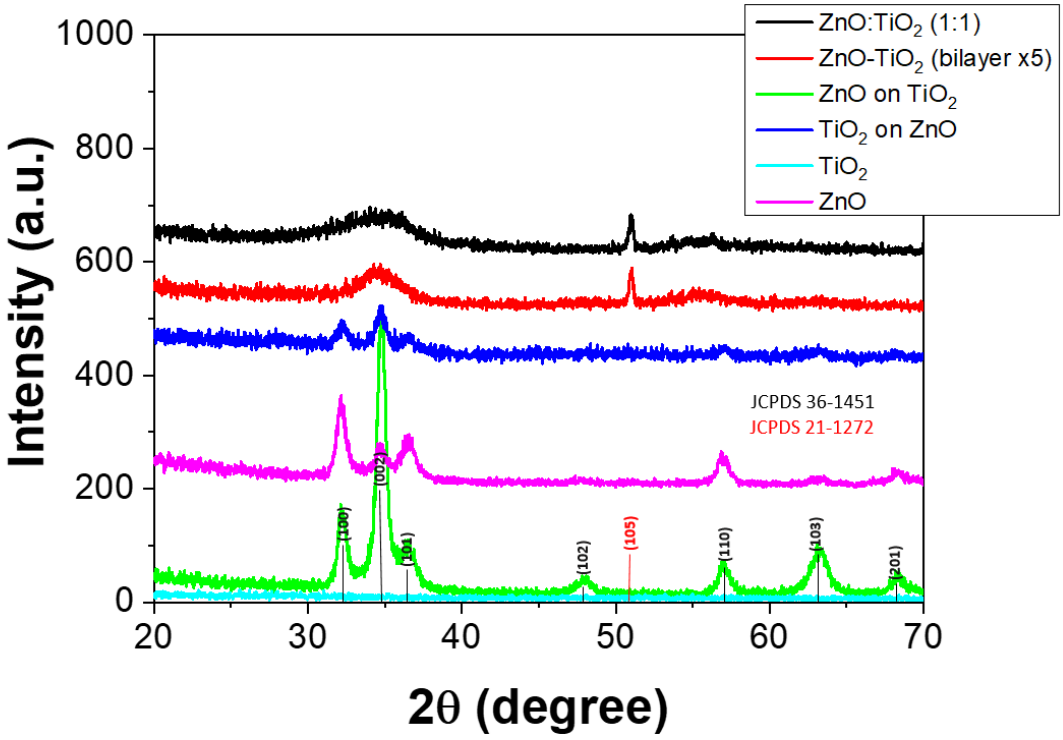

(b)

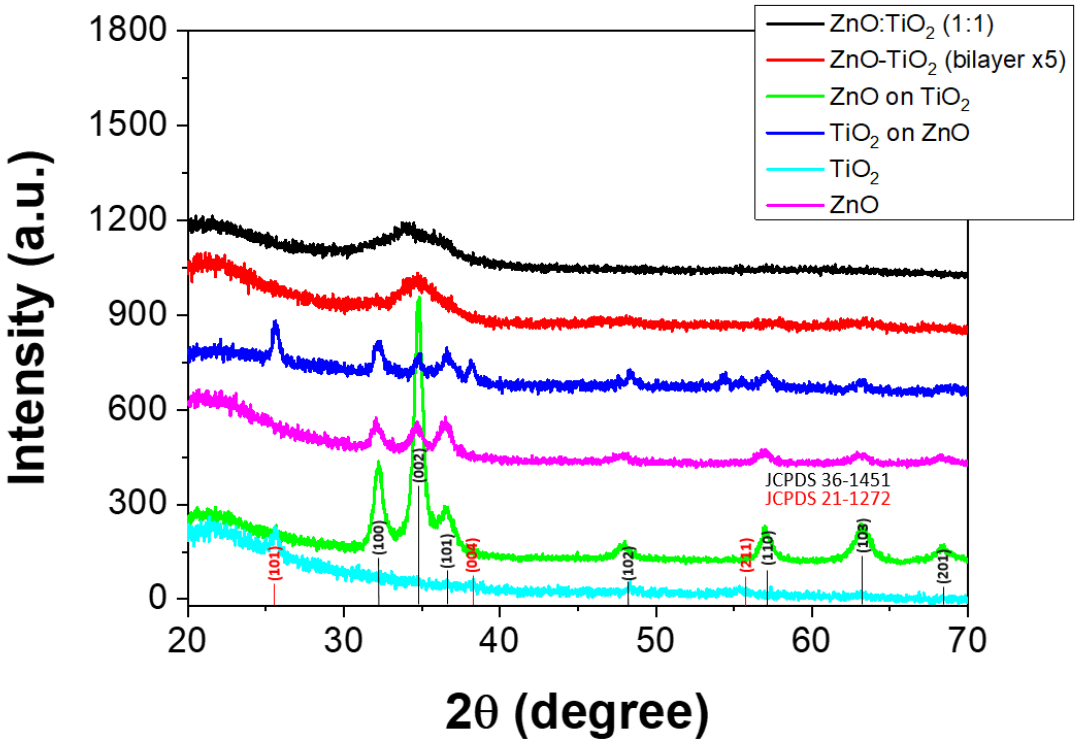

Figure 3.3 GIXRD patterns recorded from TiO_2 (light blue), ZnO (pink), TiO_2 on ZnO (dark blue) and ZnO on TiO_2 (green), ZnO-TiO_2 x5 bilayer (red) and ZnO: TiO_2 1:1 (black) grown on (a), an oxide-covered Si (100) substrate and (b), glass substrates. See insert caption for detail

SEM reveals that the underlying structure of the ZnO layer affects the structure of the TiO_2 grown on top. This can be seen by comparing the morphology of TiO_2 grown directly on the substrate versus TiO_2 grown on ZnO (Figure 3.4 and 3.5). The morphology is comparable to ZnO. Growth also appears to be substrate-dependent based on the SEM images obtained. A difference can be seen between TiO_2 deposited on (a), the oxide-covered Si (100) substrates and (b), the glass substrates. Larger surface features are evident on the glass substrate. These data are analysed further in a later section.

The Scherrer equation (3.1) was applied which relates the full width at half maximum height (FWHM) for the XRD peaks to the grain size.

$$D = \frac{K\lambda}{\beta cos\theta} \tag{3.1}$$

Where K is the shape factor, λ is the X-ray wavelength, β is the FWHM (full width at half maximum) (radians) and θ is the angle of diffraction. The (002) peak was used in the equation. A comparison was made with grain sizes obtained via the Scherrer method[55] and the intercept method[56]. The results are seen below in table 3.1. Grain sizes obtained by the Scherrer method were consistently smaller than those obtained using the intercept method. For the latter, measurements correspond to random but forced fixed placement of a line on an image. Therefore, observer interpretation and variations in patterns must be considered. In the case of ZnO, rod-like grains have random placement which does not lend itself to accurate measurement via the intercept method.

Thin film		**Scherrer method crystallite size (nm)**	**Intercept method crystallite size (nm)**
ZnO on TiO_2	Si	12.1	22.7
	glass	12.0	21.9
TiO_2 on ZnO	Si	14.9	29.3
	glass	15.0	29.5

Table 3.1: Comparison of crystallite size calculated by the Scherrer equation and the intercept method along to ZnO (002) crystal plane

(a)

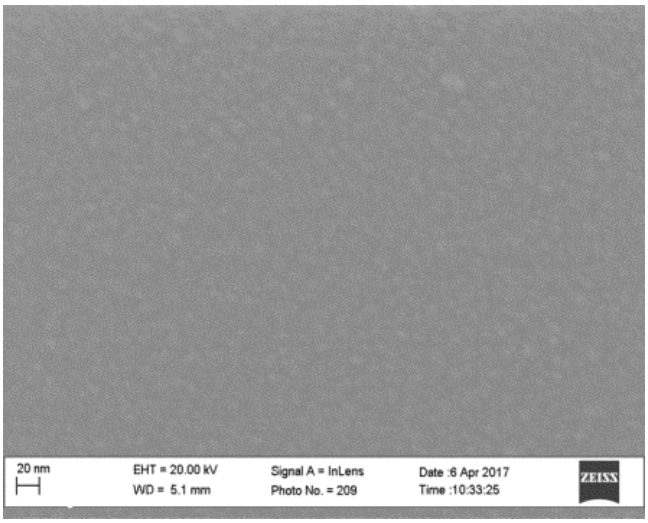
20 nm
EHT = 20.00 kV
WD = 5.1 mm
Signal A = InLens
Photo No. = 209
Date :6 Apr 2017
Time :10:33:25
ZEISS

(b)

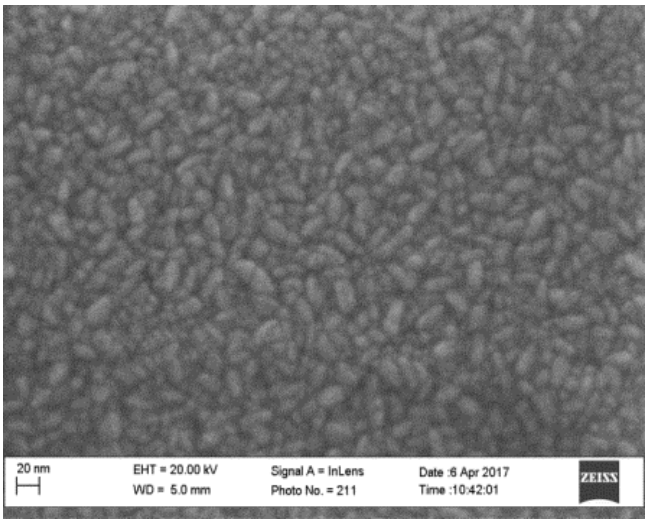
20 nm
EHT = 20.00 kV
WD = 5.0 mm
Signal A = InLens
Photo No. = 211
Date :6 Apr 2017
Time :10:42:01
ZEISS

(c)

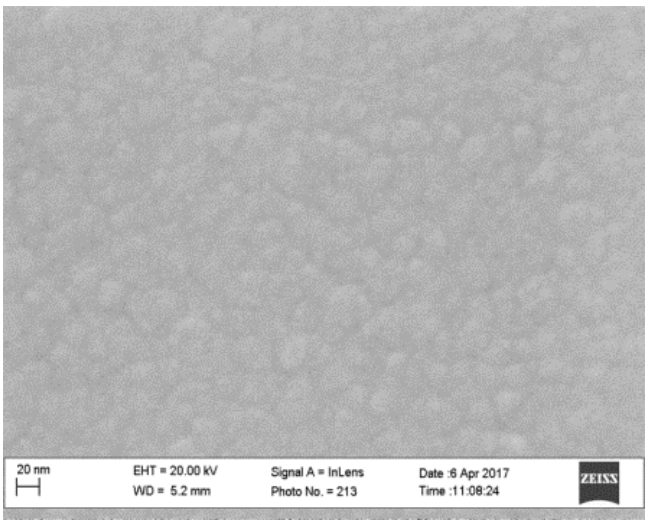
20 nm
EHT = 20.00 kV
WD = 5.2 mm
Signal A = InLens
Photo No. = 213
Date :6 Apr 2017
Time :11:08:24
ZEISS

(d)

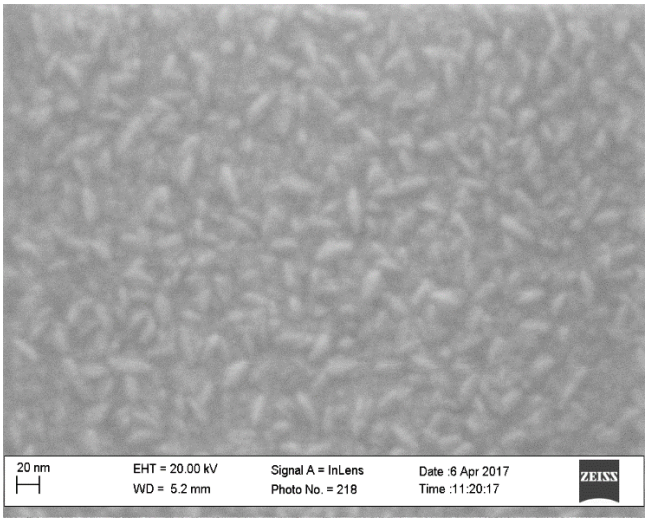

Figure 3.4: SEM images following ALD growth on Si (100) substrates: (a) TiO_2 (b) ZnO (c) TiO_2 on ZnO and (d) ZnO on TiO_2

(a)

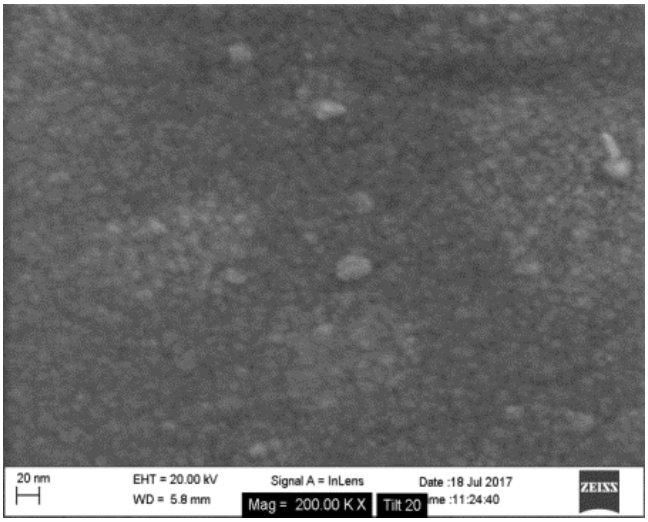
20 nm
EHT = 20.00 kV
WD = 5.8 mm
Signal A = InLens
Mag = 200.00 K X
Tilt 20
Date :18 Jul 2017
me :11:24:40
ZEISS

(b)

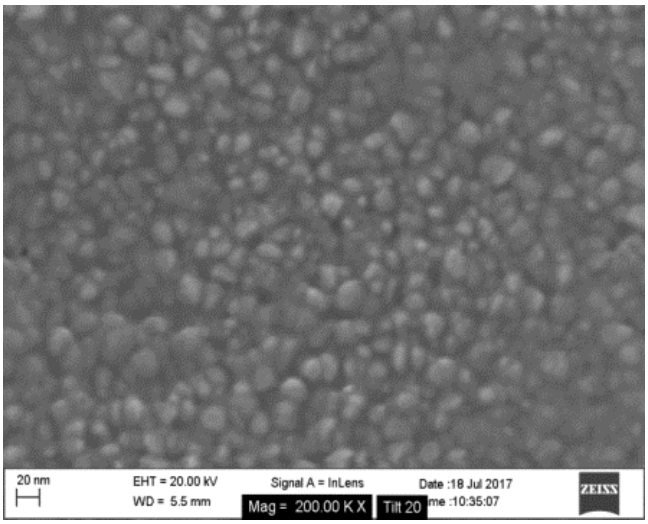
20 nm
EHT = 20.00 kV
WD = 5.5 mm
Signal A = InLens
Mag = 200.00 K X
Tilt 20
Date :18 Jul 2017
me :10:35:07
ZEISS

(c)

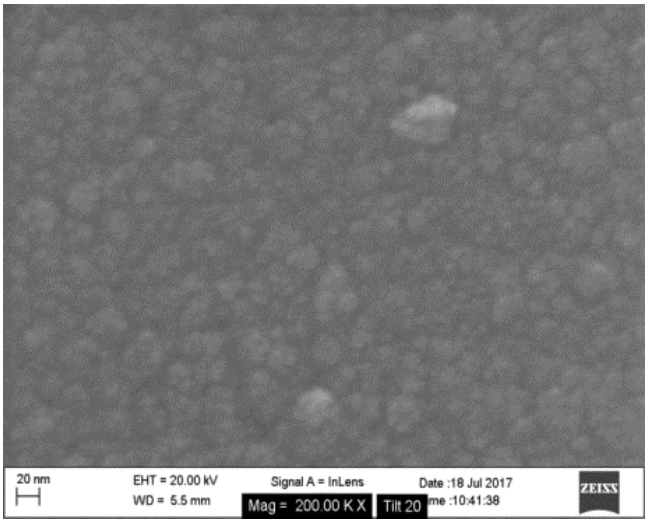
20 nm
EHT = 20.00 kV
WD = 5.5 mm
Signal A = InLens
Mag = 200.00 K X
Tilt 20
Date :18 Jul 2017
me :10:41:38
ZEISS

(d)

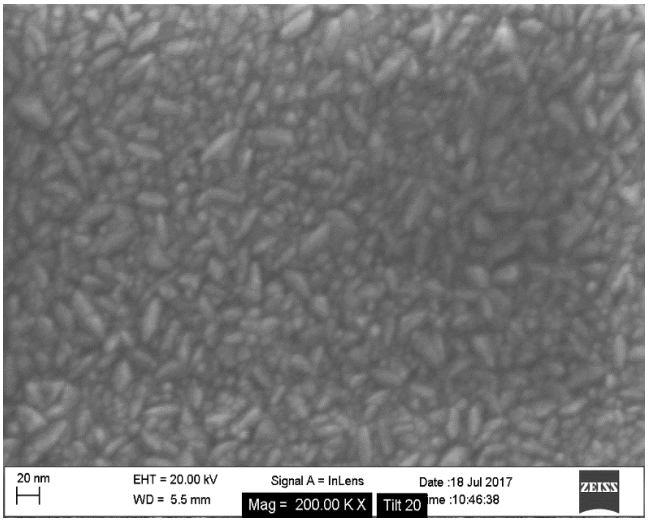

Figure 3.5: SEM images following ALD growth glass substrates: (a) TiO_2 (b) ZnO (c) TiO_2 on ZnO and (d) ZnO on TiO_2

Transmission electron microscopy (TEM) images are presented in figure 3.6. In these images the darker layer is ZnO and the lighter layer is TiO_2. The brighter layer seen below the TiO_2 is a SiO_2 interfacial layer as the Si (100) substrate is naturally oxidized. From figure 3.6 (a) it is seen that the ZnO layer is thinner than the TiO_2 layer despite the fact that the nominal growth rate of 2 Å/cycle was expected for ZnO and 0.5 Å/cycle for TiO_2 which should have resulted in both layers having thicknesses of 40 nm. From the TEM images measured layer thicknesses of 35 nm for ZnO and 55-60 nm for TiO_2 were obtained. This observation suggests that there was a delay in the nucleation of the ZnO layer at the start of the ALD growth process. It is possible that ZnO may self-inhibit when growing on Si and as a result there may be a need to fine tune the recipe to correct this discrepancy.

In support of this proposal it is apparent that in contrast to the SiO_2/ZnO/TiO_2 structure, the SiO_2/TiO_2/ZnO structure shows similar layer thicknesses for the TiO_2 and ZnO layers, figure 3.6 (b). From these TEM images it is evident that ZnO is crystalline due to clear lattice plane

images being present in the TEM image and TiO_2 is amorphous which explains why no diffraction peaks were obtained in the XRD pattern on Si substrate.

(a)

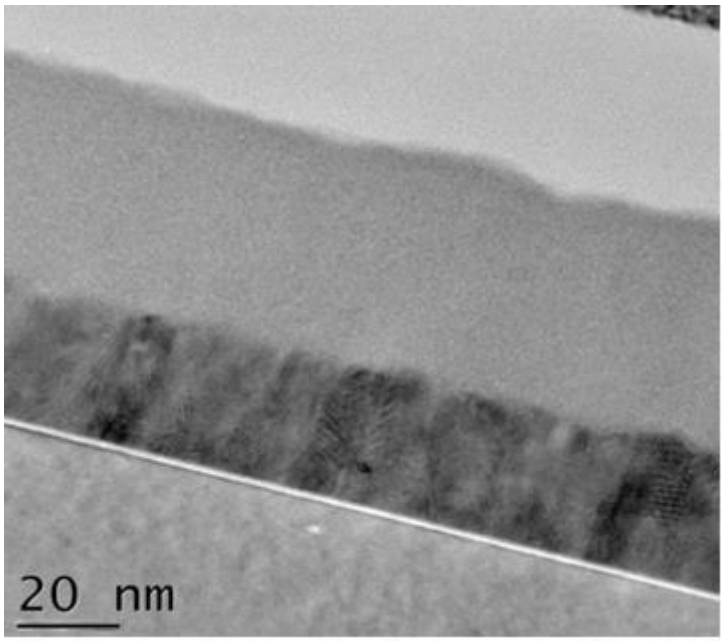

(b)

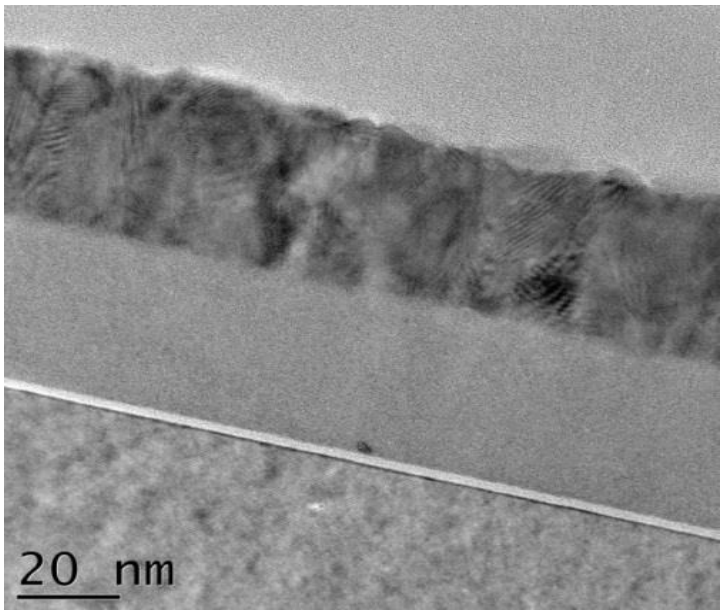

Figure 3.6 (a) TEM images of (a) the Si (100)/ZnO/TiO_2 and (b) the Si (100)/TiO_2/ZnO bilayer structures grown on the naturally-oxidized Si (100) substrates. Note the differences in layer thickness for the darker, ZnO layers when comparing both structures

(a)

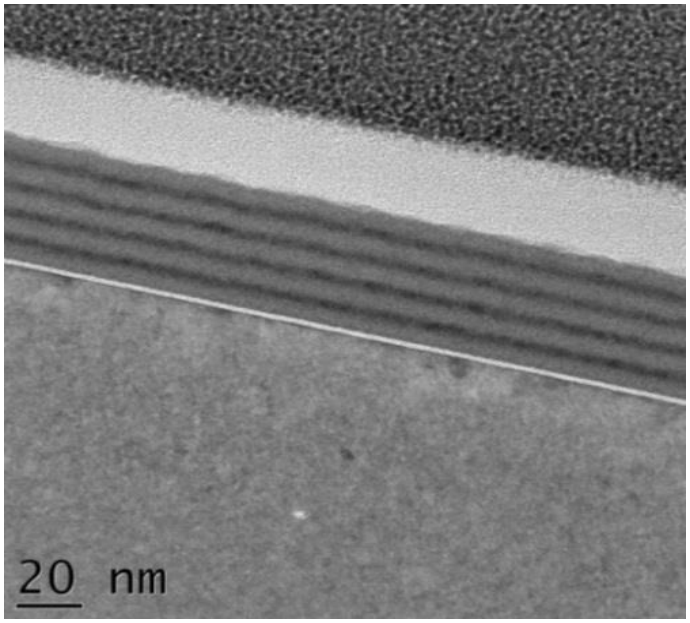

(b)

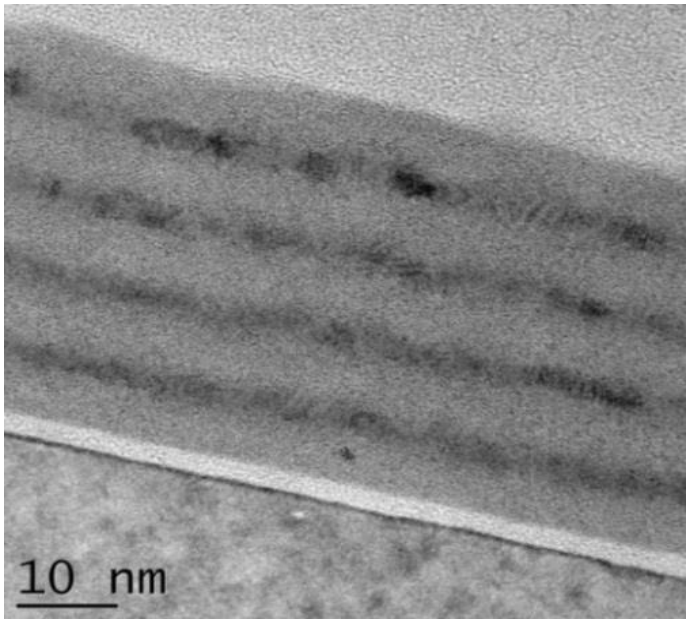

Figure 3.7: TEM images of ZnO and TiO_2 multilayers laminate (4 nm ZnO + 4 nm TiO_2) x5 at (a) 20 nm and (b) 10 nm

Figure 3.7 shows TEM images of true nanolaminate films. Again, the darker layers represent ZnO and the lighter coloured layers represent TiO_2. The nanolaminate remains intact and the layers can clearly be distinguished. In support of the earlier proposal that the growth of the

ZnO on the oxidized Si (100) surface is somewhat inhibited, from figure 3.7 it is possible to see clearly that the first of the very thin ZnO layers simply did not grow due to the proposed delay in nucleation. Interestingly in this example, the TiO_2 layers were thicker than expected, being some 6 nm as opposed to the expected 4 nm. The GPC of TiO_2 grown on ZnO appears to be greater than that of pure TiO_2 deposited directly on substrate. The opposite is observed with ZnO where the GPC of ZnO deposited on TiO_2 is reduced compared to that of pure ZnO grown directly on the substrate. This may be explained by considering surface chemisorption reactions. ALD is very sensitive to the chemical activity of the growth surface. Differences may exist in the chemical activity of the TDMAT and DEZn precursors and these differences could explain the resulting GPC values. A similar result has been observed in other ALD experiments[57, 58].

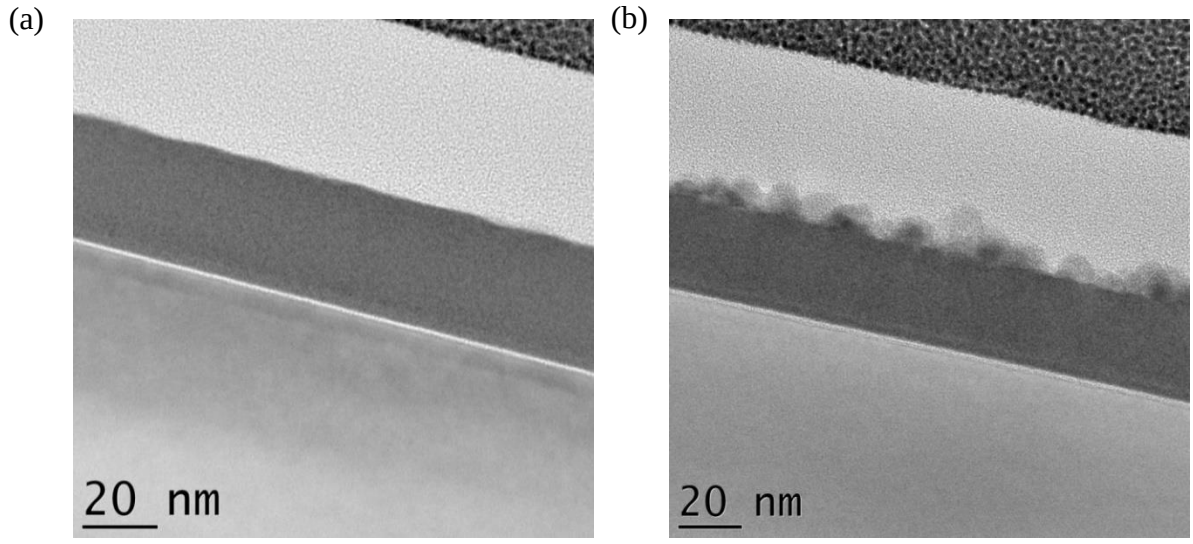

Figure 3.8: TEM images of the mixed 1:1 ZnO/ TiO_2 (1:1) layer (a) before and (b) after, annealing at 400 °C for 60 minutes in air

As seen in figure 3.8 the TEM images of the mixed ZnO/TiO_2 (1:1) layer reveal that after annealing some new deposits appear at the surface of the layer which also appears to have reduced in overall thickness from roughly 32 nm to 29 nm.

Given the tendency of ZnO to readily form crystalline deposits it is proposed that the new deposits consisted on ZnO nanocrystals that form via segregation of Zn^{2+} ions from the mixed layer, oxidation and crystallisation. With this proposal in mind ZnO lattice constants were calculated in accordance with Bragg's law[59] using 1.54 Å for λ (Cu Kα radiation). The values for *d*; the interplanar spacing for ZnO (002) and (100) orientations are 2.68 Å and 2.9 Å respectively, confirming that the deposits were most likely ZnO nanocrystals having a predominant orientation on the (002) direction as the interplanar spacing measurement was in agreement with the theoretical value. It has previously been reported that annealing ALD ZnO produces films preferentially oriented with the c-axis perpendicular to the substrate[60, 61]. Figure 3.9 shows the interplanar spacing within the ZnO nanocrystals as observed using TEM.

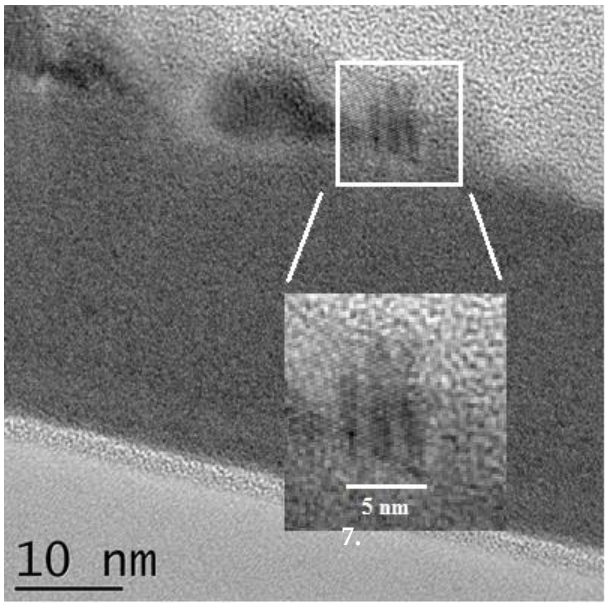

Figure 3.9: TEM image of the annealed mixed ZnO/TiO_2 layer focusing on one of the deposits that appear at the surface of the layer after annealing at 400 °C for 60 minutes in air

Atomic force microscopy (AFM) was employed to evaluate the surface topography of the ZnO, TiO_2 and ZnO/TiO_2 nanolaminate films. AFM images recorded for all films are presented in figures 3.10-3.15. The sampling surface area of the films analysed was 1 x 1 μm^2. The lighter coloured areas in the images indicate higher surface features. The Z scale of the AFM data is situated to the left of each image. The Z scale values vary from sample to sample with a maximum of >20 nm for ZnO deposited on TiO_2 on glass substrate.

The root mean square (RMS) roughness was evaluated for each of the films. These results are displayed in table 3.2. It can be seen from the results that RMS roughness increases for all films grown on glass substrates when compared to the same films deposited on Si substrate. This supports the proposal that growth is substrate-dependent as previously implied from the XRD results. Comparing TiO_2 and TiO_2 grown on ZnO, the RMS roughness values are practically the same on glass substrates, at ca. 1.49 nm and 1.5 nm respectively. However, the RMS roughness value doubles in the case of growth on the Si (100) substrate from 0.64 nm for TiO_2 alone to 1.2 nm for TiO_2 grown onto ZnO on Si (100). In other words the surface of the TiO_2 layer is considerably rougher when deposited onto ZnO grown on Si (100) as compared to that obtained when the TiO_2 was deposited directly on the Si (100) substrate.

Comparing ZnO and ZnO deposited onto TiO_2, again the RMS roughness values are very similar on glass substrates although a slight increase in RMS roughness is observed when the ZnO is deposited onto the TiO_2 layer grown on glass, having a slightly larger value at 1.77 nm as compared to 1.68 nm. Similarly the RMS roughness value obtained from the surface of the ZnO layer deposited onto the TiO_2 layer grown on the Si (100) substrate is again higher than that for ZnO grown directly on the Si (100) substrate, at 1.64 nm versus 1.27 nm, although the increase in RMS roughness isn't as substantial as that observed for the TiO_2 layer. For the nanolaminate stacks, RMS roughness values were found to be lower in comparison to the other films, being ca. 1.24 nm on glass and 0.8 nm on Si (100).

Interestingly, the mixed ZnO/TiO_2 1:1 layer grown on a glass substrate had one of the highest results in terms of RMS roughness, at ca. 1.63 nm. In contrast, the same structure grown on the Si (100) substrate had one of the lowest RMS roughness values, at ca. 0.61 nm.

	RMS roughness of films grown on glass substrates (nm)	**RMS roughness of films grown on Si (100) substrates (nm)**
ZnO	1.49	0.64
TiO_2	1.68	1.27
ZnO on TiO_2	1.77	1.64
TiO_2 on ZnO	1.50	1.21
ZnO: TiO_2 (1:1) mixed layer	1.63	0.61
ZnO/TiO_2 x5	1.24	0.80

Table 3.2: RMS roughness values for the various films produced here as a function of substrate type

Figures 3.10 – 3.15 below present AFM images for the nanolaminate films. For all images, films deposited on glass substrates are the left and films deposited on Si (100) substrates are on the right.

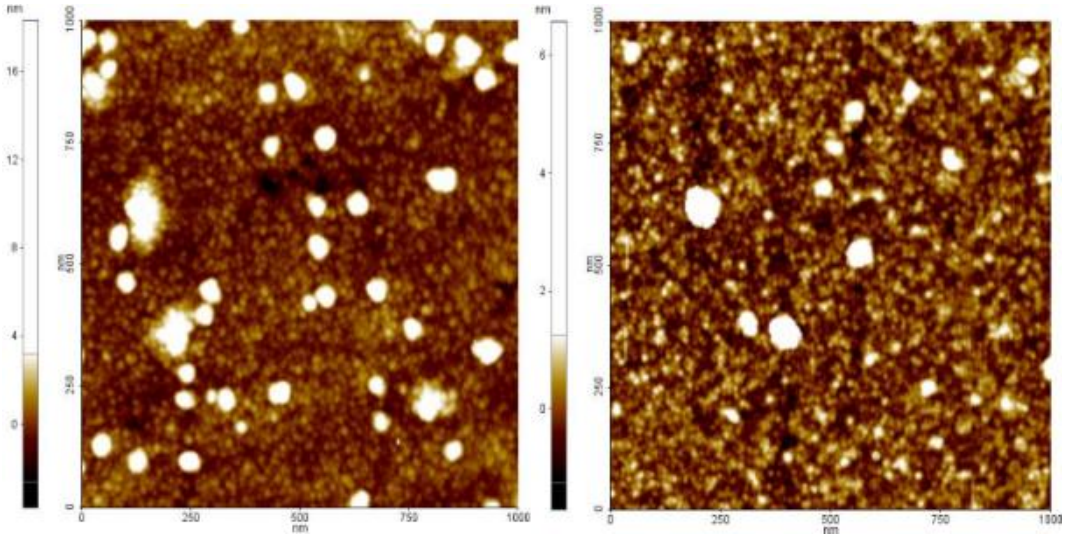

Figure 3.10: AFM images of TiO_2

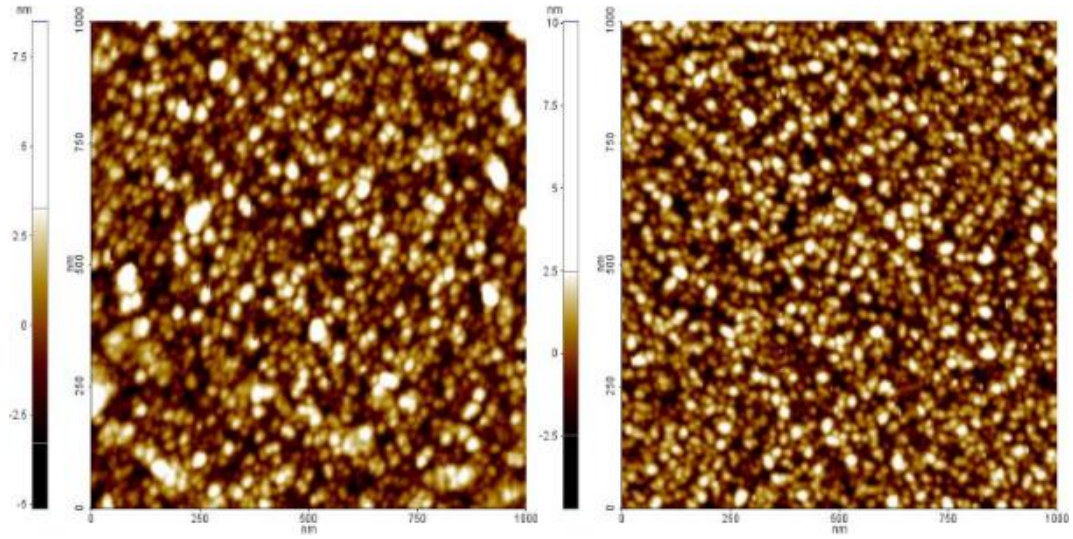

Figure 3.11: AFM images of ZnO

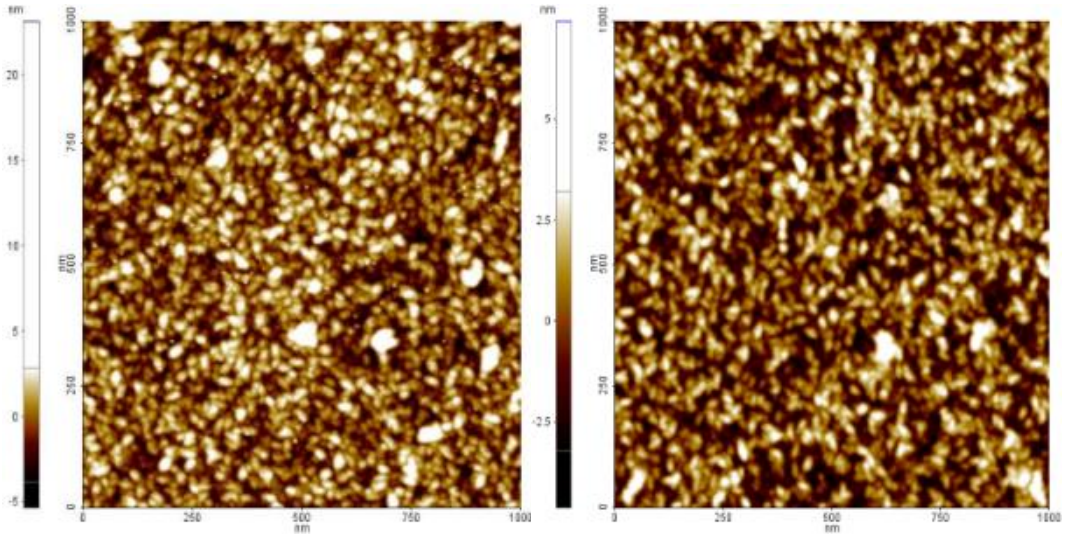

Figure 3.12: AFM images of ZnO on TiO_2

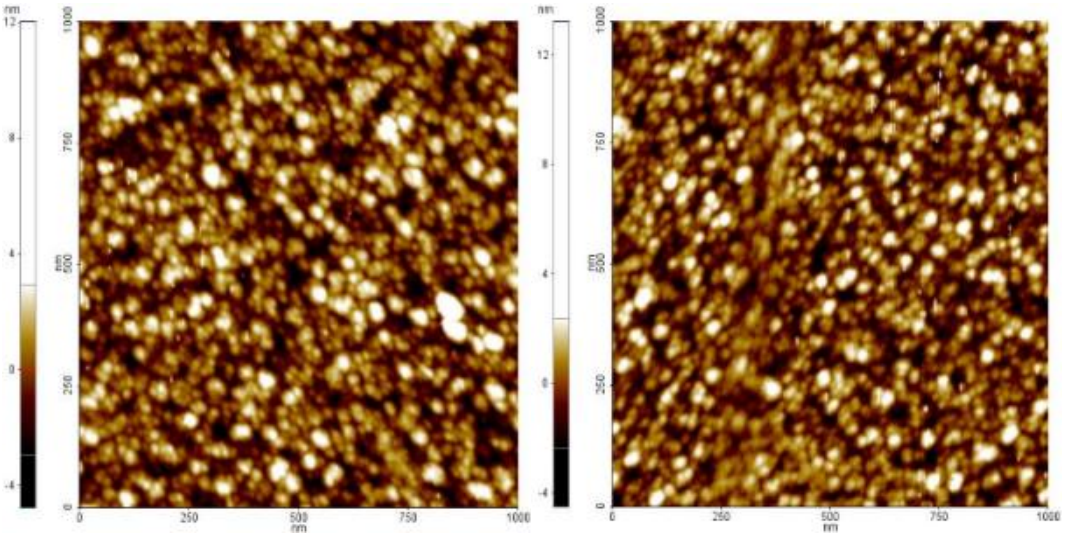

Figure 3.13: AFM images of TiO_2 on ZnO

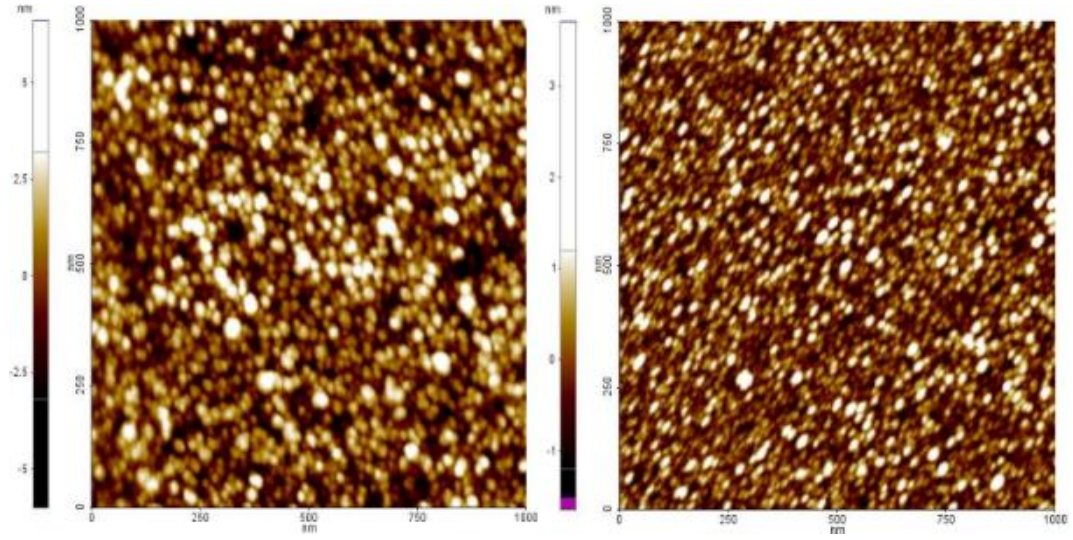

Figure 3.14: AFM images the mixed ZnO: TiO_2 (1:1) layers

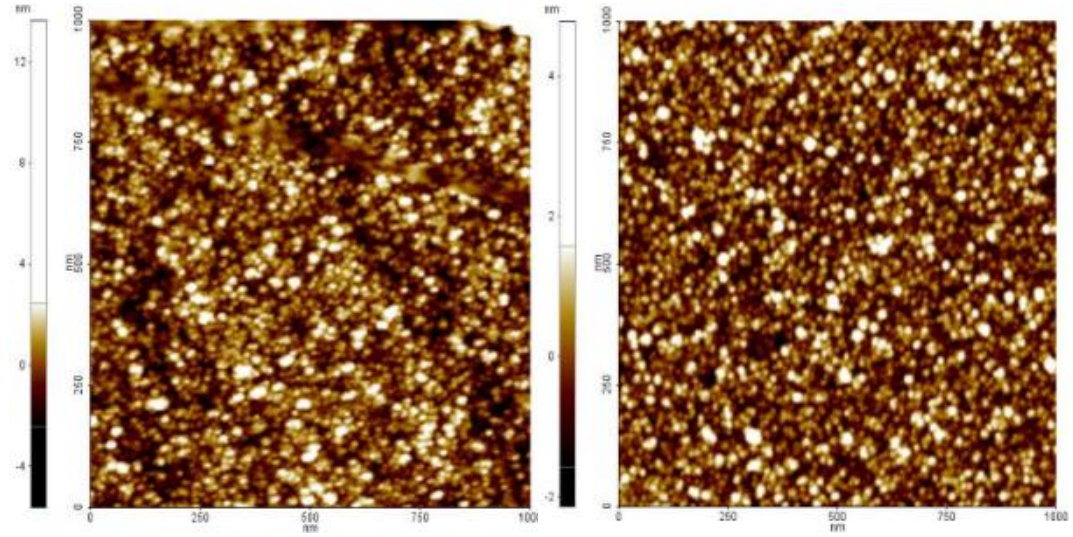

Figure 3.15: AFM images of the x5 bilayers

XPS was employed to characterise the chemical bonding and composition of the films. Figures 3.16 - 3.18 show the XPS spectra of the Ti 2p, Zn 2p and O 1s peaks after mild argon-ion sputtering designed to remove the surface contamination that arises due to handling in air. The major doublet peaks at 459 eV and 465 eV in figure 3.16 can be assigned to Ti $2p_{3/2}$ and Ti $2p_{½}$ peaks of Ti - O bonding, consistent with the literature that exists for TiO_2[48, 62, 63]. The spectra can also be fitted with a second doublet at Ti $2p_{3/2}$ at approx. 457.5 eV which can be attributed

to Ti (III) oxide and hence Ti^{3+}[62,63]. The 2 peaks seen in figure 3.17 at 1021 eV and 1044 eV correspond to Zn $2p_{3/2}$ and Zn $2p_{½}$ and corresponds to accepted XPS data for ZnO found in the literature[48]. The O 1s spectrum depicted in figure 3.18 shows a peak at 529 eV which is attributed to oxygen bound to metal ions in the form of Ti-O and Zn-O species[48].

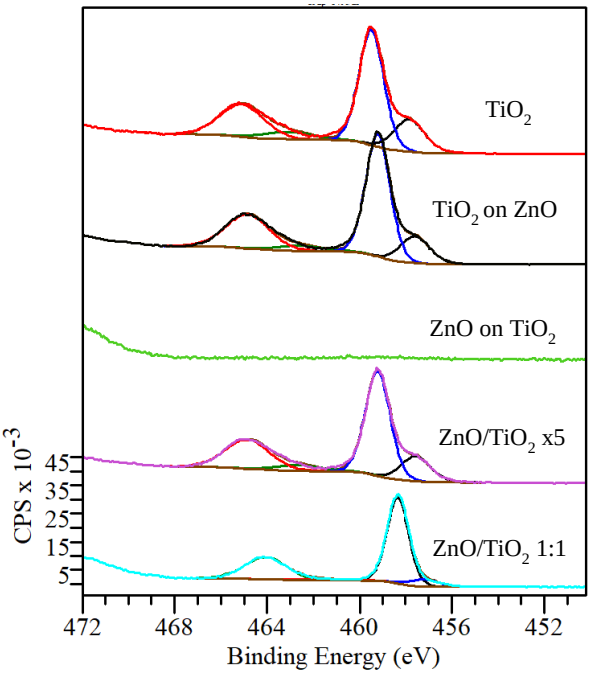

Figure 3.16: Ti 2p XPS spectra for TiO_2, TiO_2 on ZnO, ZnO on TiO_2, ZnO/TiO_2 x5 and ZnO: TiO_2 (1:1) on a Si (100) substrate

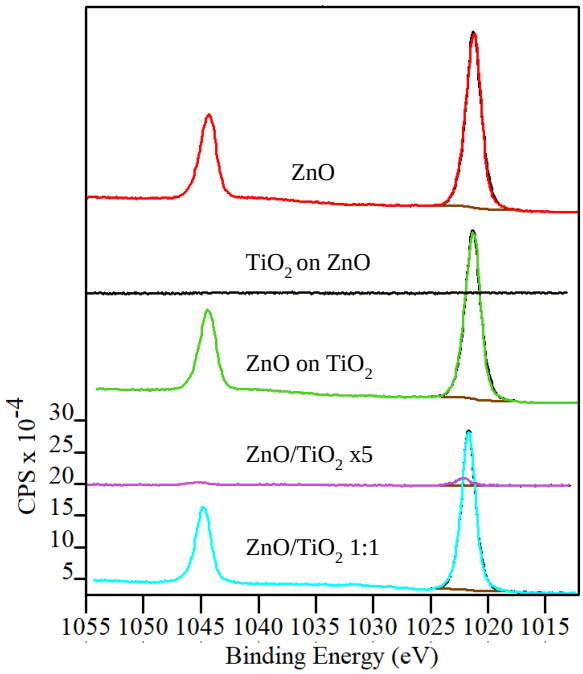

Figure 3.17: Zn 2p XPS spectra for ZnO, TiO_2 on ZnO, ZnO on TiO_2, ZnO/TiO_2 x5 and ZnO: TiO_2 (1:1) on a Si (100) substrate

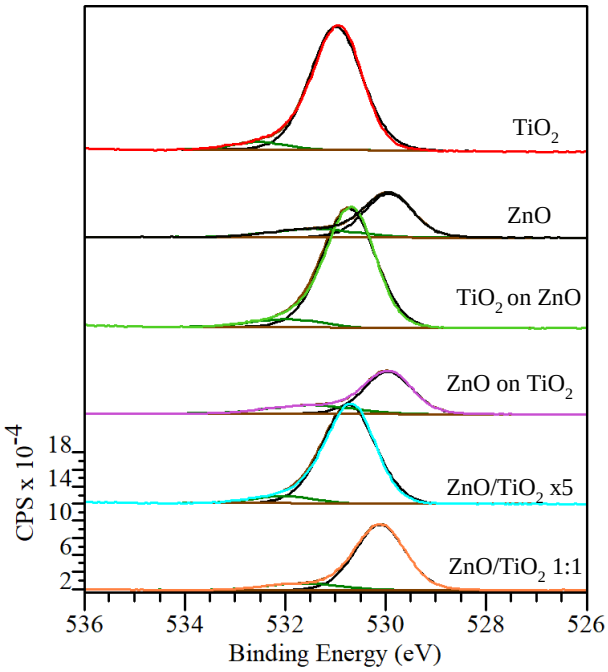

Figure 3.18: O 1s XPS spectra for TiO_2, ZnO, TiO_2 on ZnO, ZnO on TiO_2, ZnO/TiO_2 x5 and ZnO: TiO_2 (1:1) on a Si (100) substrate

The XPS data are entirely consistent with the growth of the target materials and do not indicate that layers are deficient in terms of any particular species. However, for the films which terminate in a TiO_2 layer, or for the deliberately mixed films, XPS can be particularly useful as a means of detecting Ti^{3+} species which have been reported to play a crucial role in determining the photocatalytic activity of the film. Ti^{3+} formation may arise from oxygen vacancies created as a result of oxygen diffusion[64]. Table 3.3 lists the percentage of Ti^{3+} present in the TiO_2 only film, the ZnO/TiO_2 x5 nanolaminate stack, the ZnO/TiO_2 bilayer nanolaminate and the ZnO: TiO_2 (1:1) as determined from the Ti 2p XPS data:

Sample	**% Ti^{3+}**
TiO_2	25.6
ZnO/TiO_2 ×5	21.9
TiO_2 on ZnO	20.5
ZnO: TiO_2 (1:1)	8.8

Table 3.3: Percentages of Ti^{3+} present in the various nanolaminate films studied

From table 3.3 it may be seen that the layered nanolaminate structures has 20-25% of the titanium present as Ti^{3+} and the rest as Ti^{4+}. These surfaces may provide photogenerated hole traps and assist with enhancing photocatalytic activity. Hole traps can increase the excited electron lifetimes located near the surface oxide species. This offers an opportunity for a greater chance of surface reactive oxide species (ROS) generation[65-67]. This will be further discussed in terms of photocatalytic activity later. However, mixed nanolaminate ZnO: TiO_2 (1: 1) is seen to behave differently that it has a lower relative concentration of Ti^{3+} and Ti $2p_{3/2}$ peak of the

dominant Ti(IV)oxide is shifted to lower binding energy of 458.3 eV suggesting that the immediate chemical/structural environment of the Ti^{4+} is different to that of the other layered TiO_2 nanolaminates.

3.3.2 Optical Properties

The optical transmittance spectra for ZnO: TiO_2 (1:1), ZnO/TiO_2 (x5 bilayer), ZnO/TiO_2 and TiO_2/ZnO bilayer nanolaminate structures grown on glass can be seen in figure 3.19. The average transmittance over the entirety of the visible wavelength range 400 to 550 nm is >60% rising to with a hike ~80% at 400 nm for the TiO_2 on ZnO sample and to ~90% for the ZnO on TiO_2 sample. At 380 nm, a strong absorption peak is evident due to the fundamental band gaps of the materials. A slight bump is seen at 350 nm which may be a consequence of the film being a composite of two separate layers. The transmittance values for both films decline to ~0% at lower wavelengths due to near complete absorption in the UV region. The ZnO/TiO_2 and TiO_2/ZnO bilayer nanolaminates absorb more strongly in the UV/visible region in comparison to the ZnO: TiO_2 (1:1) and ZnO/TiO_2 (x5 bilayer) films. A blue shift in the wavelength of the absorption edge is observed with the ZnO: TiO_2 (1:1) and ZnO/TiO_2 (x5 bilayer) films with ZnO: TiO_2 (1:1) possessing the greatest effect on the shift. The blue shift observed may be explained by the Burstein-Moss effect. In this instance, the optical band gap of a semiconductor is increased with increasing electron concentration as the conduction band is occupied with excited electrons. The bottom of the conduction band is filled with donor electrons. According to Pauli's principle no two electrons may occupy the same state hence leading to a blockage in low-energy transitions which in turn enhances the optical band gap[68]. The structure of the latter films resemble that of Ti-doped ZnO (TZO). Hence, the carrier concentration may effectively be increased as Ti could be behaving as a donor material.

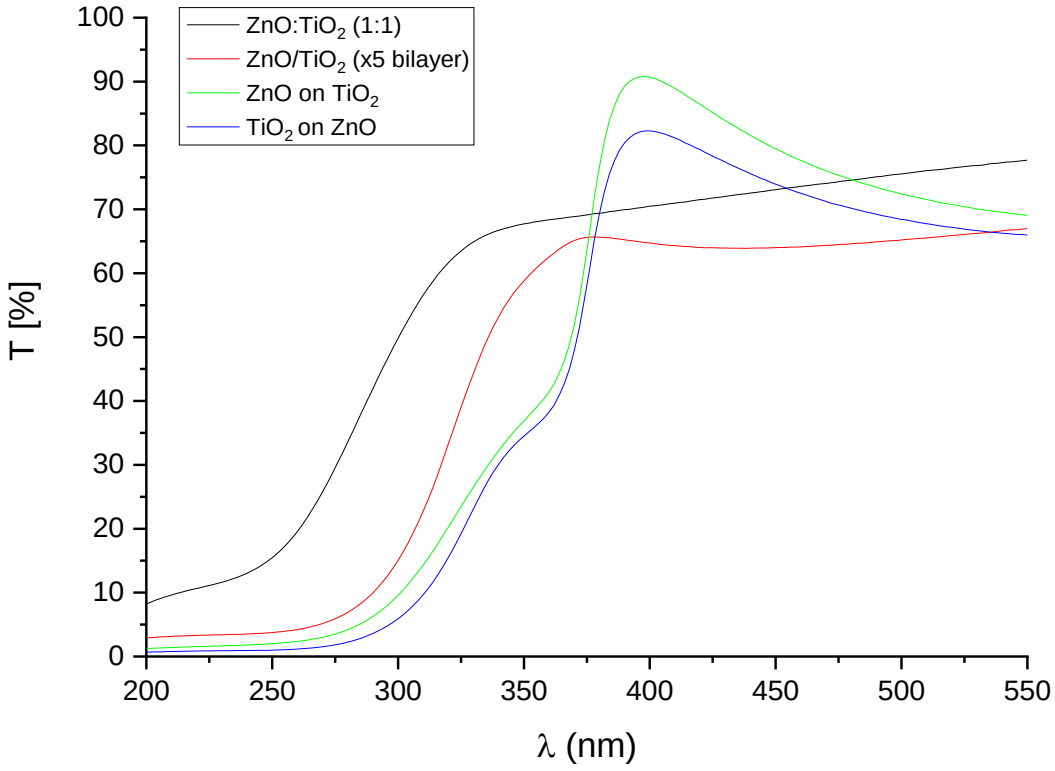

Figure 3.19: Transmittance spectra of the ZnO: TiO_2 (1:1), ZnO/TiO_2 (x5 bilayer), ZnO/TiO_2 bilayer nanolaminate structures grown on glass

3.3.3 Contact angle and photocatalytic activity

Contact angle (CA) measurements were taken in order to get an idea of the hydrophilic or hydrophobic nature of the films. In general a low surface energy and a rough microstructure equate to super-hydrophobicity[69]. The CA was measured prior to UV exposure, after 30 minutes and after 1 hour UV exposure. All values displayed are taken from films that had been annealed at 400 °C for 1 hour in air.

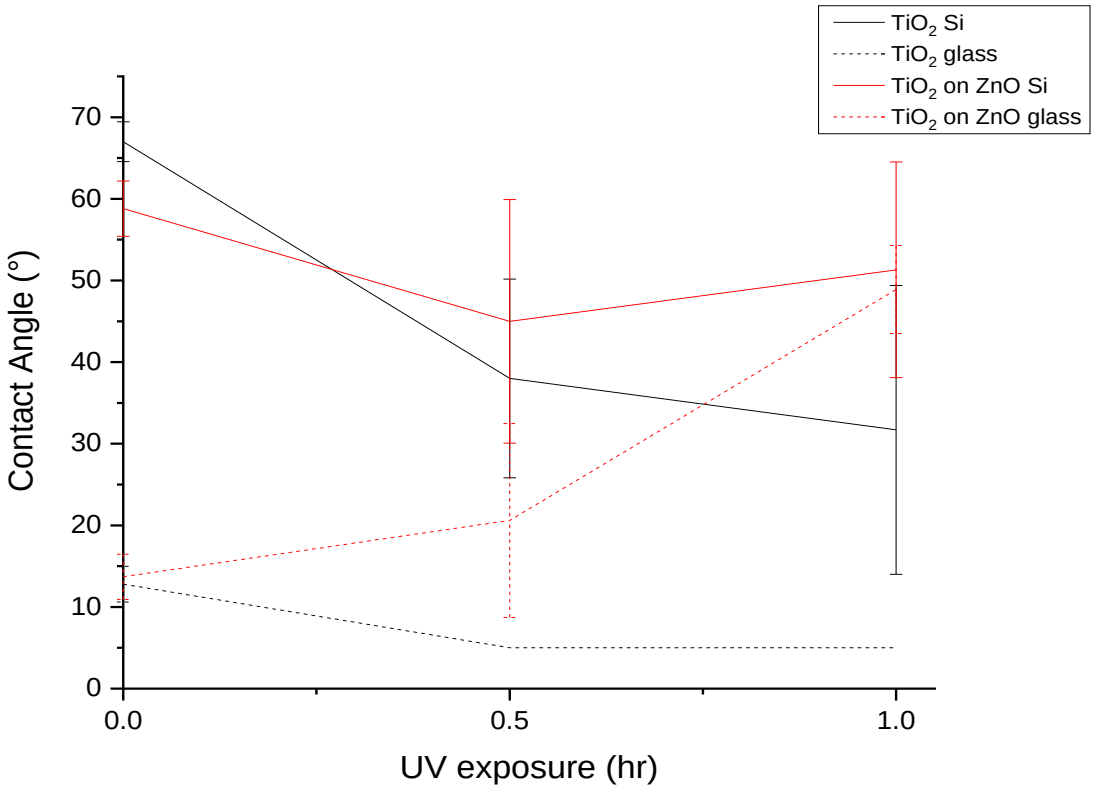

Figure 3.20: Contact angle measurements for TiO_2 and TiO_2 on ZnO grown on both Si (100) and glass substrates, after annealing at 400 °C for 1 hour in air and then exposed to UV radiation, as a function of time

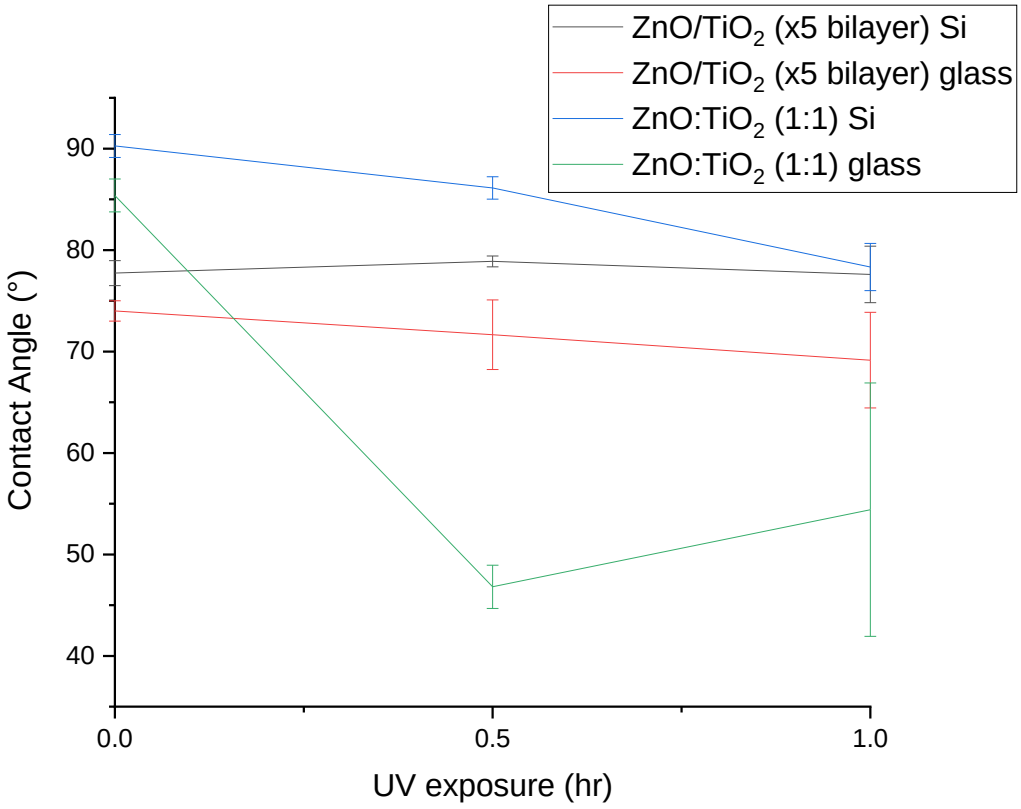

Figure 3.21: Contact angle measurements for ZnO/TiO_2 (x5 bilayers) and ZnO: TiO_2 (1:1) grown on both Si (100) and glass substrates, after annealing at 400 °C for 1 hour in air and then exposed to UV radiation, as a function of time

Initially, films grown on the glass substrates had lower CAs than those grown on Si (100) substrates. In some ways this would not be unexpected since XRD revealed that on these samples there was evidence of anatase formation and anatase is generally found to be the most photoactive form of TiO_2[70]. Following 30 minutes UV irradiation, the CAs decreased for all samples except for the TiO_2 on ZnO grown on glass sample and for ZnO/TiO_2 (x5 bilayers) grown on Si. After 1 hour UV exposure, the CA for TiO_2 on ZnO grown on glass increased dramatically. Out of all the samples, the CAs for the ZnO: TiO_2 (1:1) films were found to be the some of the highest, however a slight decrease in CA with increasing irradiation time was

observed. CAs of <5° were recorded for TiO_2 on glass after UV exposure which is indicative of superhydrophilicity. This is again indicative of some photoactivity arising from the presence of some anatase. Although no general consensus exists to explain why, amorphous TiO_2 surfaces are not found to be particularly photoactive while anatase surfaces are the most photoactive[70].

Morphological influences may also influence CA values. In our case particularly if the TiO_2 adopts the shape of the ZnO grown directly beneath it as in the case of the TiO_2 on ZnO grown on Si (100) substrate sample (see figure 3.4 (c)). The CA data for this sample is shown in the red solid line in figure 3.20 and reveals that the CA remains high despite UV irradiation for an hour. In this particular case it would be tempting to assume that the very prominent texturing of the TiO_2 surface that arises from the ZnO template underneath dominates the CA response completely. However a similar level of texturing, albeit less uniform in nature, arises for TiO_2 on ZnO grown on a glass substrate and as may be seen from the red dotted line in figure 3.20 this material has a low CA value to start with which actually increases during UV exposure. Such potentially conflicting results are indicative of the fact that CA measurements are at best only a very rough guide to wards understanding the hydrophobicity or hydrophilicity of a sample surface.

Photocatalytic activity was also investigated via dye degradation experiments. Films were coated with an even layer of Basic Blue 66 dye and exposed to UV light and the change in the colour of the ink monitored and recorded over time by use of a handheld digital scanner. Digital image analysis as described by Mills et al. was used to assess photo-activity of the films[71]. Figure 3.22 below shows the films initially covered with a thin layer of dye before UV exposure and after 150 minutes of UV bleaching.

By comparing the before and after images presented in figure 3.22, it is concluded that the dye did not degrade to any visual degree on the ZnO/TiO_2 x5 nanolaminate stack grown on glass suggesting nearly complete inactivity (samples (e) in figure 3.22). For the samples shown in (c) in these figures which were the ZnO/TiO_2 bilayer samples grown on glass with the TiO_2 layer on top of the ZnO layer, the dye only showed slight discolouration suggesting that this sample had some, albeit minimal levels of photoactivity.

Comparing the samples shown in (c) TiO_2 on ZnO and (d) ZnO on TiO_2 in these figures, the dye was again degraded suggesting that these films also possessed some degree of photoactivity. Similarly the sample shown in (f) also degraded the dye to some extent showing photoactivity.

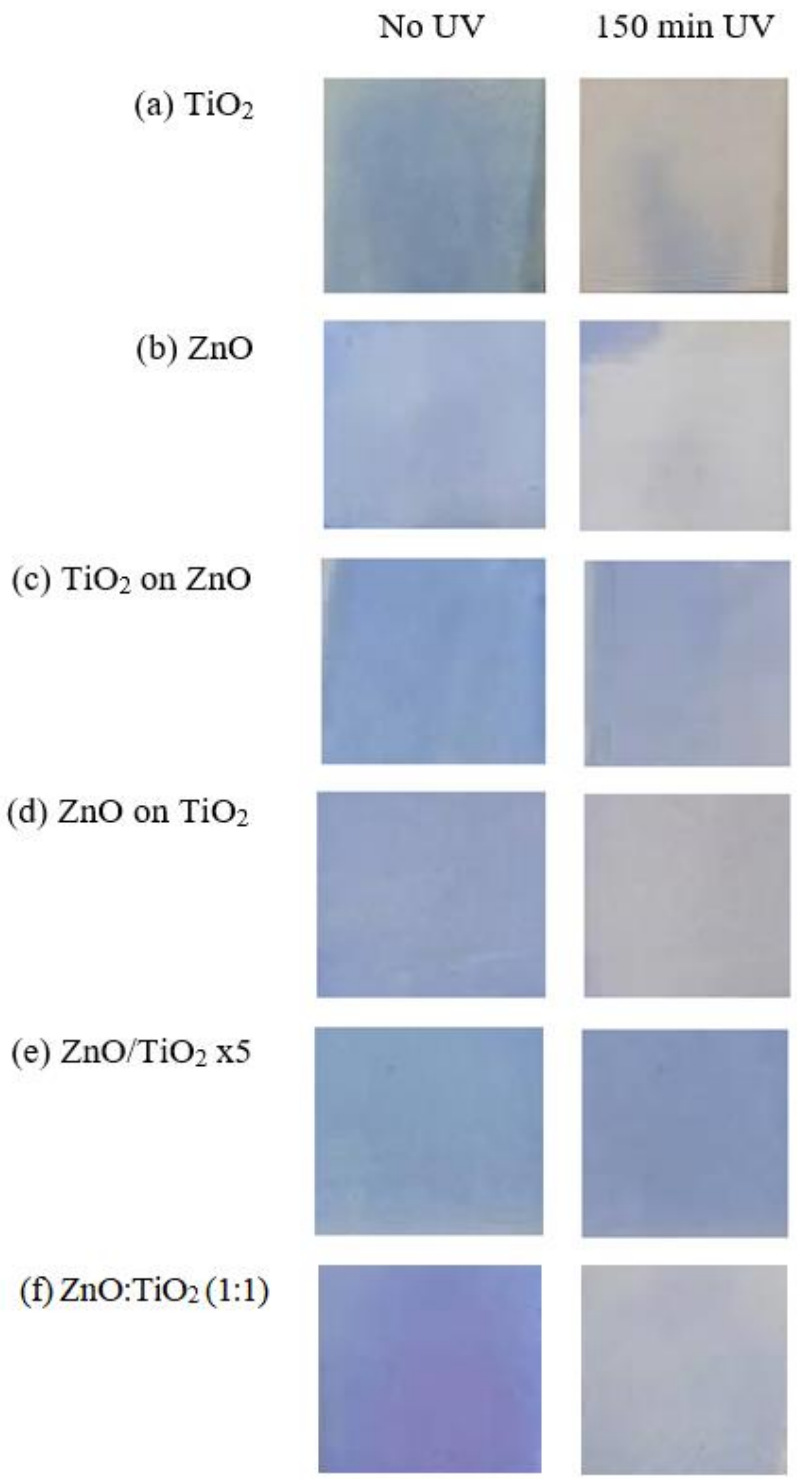

Figure 3.22: Images of the samples before and after 150 minutes UV irradiation on glass substrate: (a) TiO_2 (b) ZnO (c) TiO_2 on ZnO (d) ZnO on TiO_2 (e) ZnO/TiO_2 x5 (f) ZnO: TiO_2 (1:1)$^+$

Although some of the films display some degree of photoactivity, the shortest time-to-bleach as determined by visual inspection was around 69 minutes exposure.

	Time to bleach (minutes)
TiO_2	75.8
ZnO	69.3
ZnO on TiO_2*	116.4
TiO_2 on ZnO	130.8
ZnO/TiO_2 x5	-
ZnO: TiO_2 (1:1)+	77.2

Table 3.4: Times to bleach for TiO_2, ZnO, ZnO on TiO_2, TiO_2 on ZnO, ZnO/TiO_2 x5 and ZnO: TiO_2 (1:1) films

*Two separate films of ZnO on TiO_2 were analysed so the average of both values is being used for time to bleach.

+Sample has been annealed at 400 ℃ for 60 minutes in air

By assessment of the time-to-bleach values given in table 3.4, it may be seen that the ZnO and TiO_2 films are the most photoactive, followed closely by ZnO: TiO_2 (1:1). A value for the time to bleach ZnO/TiO_2 x5 bilayer could not be calculated.

The results from the dye degradation experiments are in good agreement with the CA values obtained for the films after 1 hour UV exposure. The layered nanolaminate structures has 20-25% of the titanium present as Ti^{3+} and the rest as Ti^{4+}. The presence of Ti^{3+} influences the electronic structure and surface activity of TiO_2[72]. In particular it is likely that the presence of Ti^{3+} extends the wavelength range where the material absorbs into the visible region of the

spectrum. If this were the case then it might provide a mechanism whereby the visible light-induced photocatalytic activity could become significant[73-77]. However as noted above, these samples were not found to be photoactive using the tests employed.

3.4 Conclusions

TiO_2/ZnO nanolaminates were deposited via an ALD process which revealed a slight delay in nucleation with ZnO. SEM showed that TiO_2 morphology follows that of the ZnO underneath. XRD results suggested that layer growth was substrate-dependent as crystalline TiO_2 was only identified on glass. The ZnO was polycrystalline as evidenced by the appearance lattice fringes in the TEM images while the TiO_2 was amorphous. TEM revealed that the laminates remained intact after annealing. Nanocrystals were seen on top of the mixed ZnO: TiO_2 (1:1) film and thus it is apparent that the mixed film is not stable towards high temperature annealing. These results suggest that formation of a nanolaminate structure may help with stability. After 1 hour UV exposure, the TiO_2 yielded a CA value of <5°, suggesting superhydrophilicity.

This study highlights how the use of an under layer may act as a template of morphology. It also suggests the possible role of nanolaminates in stabilizing materials. In a practical sense, TiO_2 may act as a stabilizer for ZnO in a TiO_2/ZnO bilayer stack when used as an anode material in lithium ion batteries (LIBs)[78].

References

1. Radisavljevic, B., Radenovic, A., Brivio, J., Giacometti, V. and Kis, A., Single-layer MoS_2 transistors. *Nature Nanotechnology* **2011,** *6*.

2. Lopez-Sanchez, O., Lembke, D., Kayci, M., Radenovic, A. and Kis, A., Ultrasensitive photodetectors based on monolayer MoS_2. *Nat. Nanotechnol.* **2013,** *8* (7), 497–501.

3. Bertolazzi, S., Brivio, J., and Kis, A., Stretching and Breaking of Ultrathin MoS_2. *ACS Nano* **2011,** *5* (12), 9703–9709.

4. Zeng, H., Dai, J., Yao, W., Xiao, D. and Cui, X., Valley polarization in MoS2 monolayers by optical pumping. *Nat. Nanotechnol.* **2012,** *7*, 490–493.

5. Zhang, W., Chuu, C. P., Huang, J. K., Chen, C. H., Tsai, M. L., Chang, Y. H.. Liang, C. T., Chen, Y. Z., Chueh, Y. L., He, J. H., Chou, M. Y. and Li, L. J., Ultrahigh-Gain Photodetectors Based on Atomically Thin Graphene-MoS_2 Heterostructures. *Sci. Rep* **2014,** *23* (4), 3826.

6. Cong, C., Shang, J., Wu, X., Cao, B., Peimyoo, N., Qiu, C., Sun, L. and Yu, T., Synthesis and Optical Properties of Large-Area Single-Crystalline 2D Semiconductor WS_2 Monolayer from Chemical Vapor Deposition. *Adv. Optical Mater.* **2014,** *2*, 131–136.

7. Cai, Y., Lan, J., Zhang, G. and Zhang, Y. W., Lattice vibrational modes and phonon thermal conductivity of monolayer MoS_2. *Phys. Rev. B* **2014,** *89*, 035438.

8. Azadmanjiri, J., Berndt,C. C., Wang, J., Kapoor A. J. and Srivastavac, V. K., Nanolaminated composite materials: structure, interface role and applications. *RSC Adv.* **2016,** *6*, 109361.

9. Sundberg, P. and Karppinen., M., Organic and inorganic-organic thin film structures by molecular layer deposition: a review. *Beilstein Journal of Nanotechnology* **2014,** *5*, 1104-1136.

10. Schmidt, D. F., Nanolaminates - Bioinspired and beyond. *Materials Letters* **2013,** *108*, 328-335.

11. Azadmanjiri, J., Berndt, C. C., Wang, J., Kapoor, A.J., Srivastavac, V. K. and Wen, C., A review on hybrid nanolaminate materials synthesized by deposition techniques for energy storage applications. *J. Mater. Chem. A* **2014,** *2*, 3695-3708.

12. Puttaswamy, M., Vehkamäki, M., Kukli, K., Dimri, M. C., Kemmel, M., Hatanpää, T., Heikkilä, M. J., Mizohata, K., Stern, R., Ritala, M. and Leskelä, M., Bismuth iron oxide thin films using atomic layer deposition of alternating bismuth oxide and iron oxide layers. *Thin Solid Films* **2016,** *611*, 78-87.

13. Zhang, G., Wu, H., Wang, X., Zhang, D., Wang, T. and Liu, C., Modulation of the dissipation factor in transparent AlZnO/ZrO_2/AlZnO capacitors. *Journal of Alloys and Compounds* **2017,** *690*, 777-782.

14. Martínez-Castelo, J. R., López, J., Domínguez, D., Murillo, E., Machorro, R., Borbón-Nuñez, H. A., Fernandez-Alvarez, I., Arias, A., Curiel, M., Nedev, N., Farías, M. H. and Tiznado, H., Structural and electrical characterization of multilayer Al_2O_3/ZnO nanolaminates grown by atomic layer deposition. *Materials Science in Semiconductor Processing* **2017,** *71*, 290-295.

15. Onaya, T., Nabatame, T., Sawada, T., Kurishima, K., Sawamoto, N., Ohi, A., Ogura, A., Improved leakage current properties of ZrO_2/(Ta/Nb)O_x -Al_2O_3/ZrO_2 nanolaminate

insulating stacks for dynamic random access memory capacitors. *Thin Solid Films* **2018,** *655*, 48–53.

16. Chen, W., Ren, W., Zhang, Y., Liu, M. and Ye, Z. G., Preparation and properties of ZrO_2 and TiO_2 films and their nanolaminates by atomic layer deposition. *Ceramics International* **2015,** *41*, S278–S282.

17. Rodríguez, A., Gonzalez, M. B., Campabadal, F., Suñé, J. and Miranda, E., Electrical characterization of multiple leakage current paths in HfO_2/Al_2O_3-based nanolaminates. *Microelectronics Reliability* **2015,** *55* (9-10), 1442-1445.

18. Cho, H., Park, K. W., Park, C. H., Cho, H. J., Yeom, S. J., Hong, K., Kwak, N. J. and Ahn, J. H., Abnormally enhanced dielectric constant in ZrO_2/Ta_2O_5 multi-laminate structures by metallic Ta formation. *Materials Letters* **2015,** *154*, 148-151.

19. López, J., Martínez, J., Abundiz, N., Domínguez, D., Murillo, E., Castillón, F., Machorro, R., Farías, M. and Tiznado, H., Thickness effect on the optical and morphological properties in Al_2O_3/ZnO nanolaminate thin films prepared by atomic layer deposition. *Superlattices Microstruct.* **2016,** *90*, 265-273.

20. Lo Nigro, R., Schilirò, E., Greco, G., Fiorenza, P. and Roccaforte, F., Laminated Al_2O_3–HfO_2 layers grown by atomic layer deposition for microelectronics applications. *Thin Solid Films* **2016,** *601*, 68-72.

21. Mahata, C., An, Y., Choi, S., Byun, Y. C., Kim, D. K., Lee, T., Kim, J., Cho, M. H. and Kim, H., Electrical properties of the HfO_2–Al_2O_3 nanolaminates with homogeneous and graded compositions on InP. *Current Applied Physics* **2016,** *16* (3), 294-299.

22. Zhang, J., Ding, X., Li, J. Zhang, H., Jiang, X. and Zhang, Z., Performance enhancement in InZnO thin-film transistors with compounded ZrO_2–Al_2O_3 nanolaminate as gate insulators. *Ceramics International* **2016,** *42* (7), 8115–8119.

23. Gao, J., He, G., Sun, Z., Chen, H., Zheng, C., Jin, P., Xiao, D. and Liu, M., Modification of electrical properties and carrier transportation mechanism of ALD-derived HfO_2/Si gate stacks by Al_2O_3 incorporation. *Journal of Alloys and Compounds* **2016,** *667*, 352-358.

24. Rodriguez, A., Gonzalez, M. B., Campabadal, F., Suñé, J. and Miranda, E., Breakdown time statistics of successive failure events in constant voltage-stressed Al_2O_3/HfO_2 nanolaminates. *Microelectronic Engineering* **2015,** *147*, 85-88.

25. Mahata, C., Byun, Y. C., An, C. H., Choi, S., An, Y. and Kim, H., Comparative study of atomic-layer-deposited stacked (HfO_2/Al_2O_3) and nanolaminated ($HfAlO_x$) dielectrics on $In_{0.53}Ga_{0.47}As$. *ACS Appl Mater Interfaces* **2013,** *5* (10), 4195-201.

26. Kim, L. H., Kim, K., Park, S., Jeong, Y. J., Kim, H., Chung, D. S., Kim, S. H. and Park, C. E., Al_2O_3/TiO_2 Nanolaminate Thin Film Encapsulation for Organic Thin Film Transistors via Plasma-Enhanced Atomic Layer Deposition. *ACS Applied Materials & Interfaces* **2014,** *6*, 6731−6738.

27. Singh, A., Nehm, F., Müller-Meskamp, L., Hoßbach, C., Albert, M., Schroeder, U., Leo, K. and Mikolajick, T., OLED compatible water-based nanolaminate encapsulation systems using ozone based starting layer. *Organic Electronics* **2014,** *15*, 2587–2592.

28. Oh, J., Shin, S., Park, J., Ham, G. and Jeon, H., Characteristics of Al_2O_3/ZrO_2 laminated films deposited by ozone-based atomic layer deposition for organic device encapsulation. *Thin Solid Films* **2016,** *599*, 119-124.

29. Jeong, E. G., Han, Y. C., Im, H. G., Bae, B. S. and Choi, K. C., Highly reliable hybrid nano-stratified moisture barrier for encapsulating flexible OLEDs. *Organic Electronics* **2016,** *33*, 150-155.

30. Nehm, F., Dollinger, F., Klumbies, H., Müller-Meskamp, L., Leo, K., Singh, A., Richter, C., Schroeder, U., Mikolajick, T., Hossbach, C., Albert, M. and Bartha, J. W., Atomic layer deposited TiO_x/AlO_x nanolaminates as moisture barriers for organic devices. *Organic Electronics* **2016,** *38*, 84-88.

31. Leppäniemi, J., Sippola, P., Broas, M., Aromaa, J., Lipsanen, H. & Koskinen, J., Corrosion protection of steel with multilayer coatings: Improving the sealing properties of physical vapor deposition CrN coatings with Al_2O_3/TiO_2 atomic layer deposition nanolaminates. *Thin Solid Films* **2017,** *627*, 59–68.

32. Radi, P. A., Testoni, G. E., Pessoa, R. S., Maciel, H. S., Rocha, L. A. and Vieira, L., Tribocorrosion behavior of TiO_2/Al_2O_3 nanolaminate, Al_2O_3, and TiO_2 thin films produced by atomic layer deposition. *Surface and Coatings Technology* **2018,** *349*, 1077-1082.

33. Díaz, B., Härkönen, E., S´wiatowska, J., Seyeux, A., Maurice, V., Ritala, M. and Marcus, P., Corrosion properties of steel protected by nanometre-thick oxide coatings. *Corrosion Science* **2014,** *82*, 208–217.

34. Härkönen, E., Tervakangas, S., Kolehmainen, J., Díaz, B., Swiatowska, J., Maurice, V., Seyeux, A., Marcus, P., Fenker, M., Tóth, L., Radnöczi, G. and Ritala, M., Interface control of atomic layer deposited oxide coatings by filtered cathodic arc deposited sublayers for improved corrosion protection. *Materials Chemistry and Physics* **2014,** *147*, 895-907.

35. Mohseni, H. and Scharf, T. W., Role of atomic layer deposited solid lubricants in the sliding wear reduction of carbon–carbon composites at room and higher temperatures. *Wear* **2015,** *332-333* (1303–1313).

36. López, J., Borbón-Nuñez, H. A., Lizarraga-Medina, E. G., Murillo, E., Machorro, R., Nedev, N. & Soto, G., Al_2O_3 -Y_2O_3 ultrathin multilayer stacks grown by atomic layer deposition as perspective for optical waveguides applications. *Optical Materials* **2017,** *72*, 788–794.

37. *Atomic Layer Deposition of Nanostructured Materials*. Wiley-VCH: Weinheim, Germany, 2012.

38. Lee, H. B., Anderson, V. R. and George, S. M., Growth and Properties of Hafnicone and HfO_2/Hafnicone Nanolaminates and Alloy Films Using Molecular Layer Deposition Techniques. *ACS Applied Materials & Interfaces* **2014,** *6*, 16880-16887.

39. Ritala, M. and Leskela, M., Chapter 2 – Atomic layer deposition. In *Handbook of Thin Films*, Nalwa, H. S., Ed. Academic Press: San Diego, CA, 2002; Vol. Volume 1: Deposition and processing of thin films.

40. Johnson, R. W., Hultqvist, A. and Bent, S. F., A brief review of atomic layer deposition: from fundamentals to applications. *Materials Today* **2014,** *17* (5), 236-246.

41. Handwerker, C. and Pollock, T. M., Emerging Science and Research Opportunities for Metals and Metallic Nanostructures. *JOM* **2014,** *66* (7), 1321–1341.

42. Janotti, A. and Van de. Walle, C. G., Fundamentals of zinc oxide as a semiconductor. *Rep. Prog. Phys.* **2009,** *72*.

43. Reyes-Coronado, D., Rodríguez-Gattorno, G., Espinosa-Pesqueira, M. E., Cab, C., de Coss R. and Oskam, G., Phase-pure TiO_2 nanoparticles: anatase, brookite and rutile. *Nanotechnology* **2008,** *19* (145605).

44. Xu, L., Shi, L. and Li, X., Effect of TiO_2 buffer layer on the structural and optical properties of ZnO thin films deposited by E-beam evaporation and sol-gel method. *Applied Surface Science* **2008,** *255*, 3230-3234.

45. Tian, J., Chen, L., Yin, Y., Wang, X., Dai, J., Zhu, Z., Liu, X. and Wu, P., Photocatalyst of TiO_2/ZnO nano composite film: Preparation, characterization, and photodegradation activity of methyl orange. *Surface & Coatings Technology* **2009,** *204*, 205-214.

46. Prasannalakshmi, P. a. S., N., Fabrication of TiO_2/ZnO nanocomposites for solar energy driven photocatalysis. *Materials Science in Semiconductor Processing* **2017,** *61*, 114-124.

47. Gu. Y. Z., L., H. L., Geng, Y., Ye, Z. Y., Zhang, Y., Sun, Q. Q., Ding, S. J. and Zhang, D. W., Optical and microstructural properties of ZnO/TiO_2 nanolaminates. *Nanoscale Research Letters* **2013,** *8*, 107.

48. Qian, X., Gao, M. Y., Cao, Y. Q., Guo,B. L. and Li, A .D., Preparation and phase structures of Zn–Ti–O ternary compounds by atomic layer deposition. *J. Vac. Sci. Technol. A* **2013,** *31*.

49. Wang, W. K., Wen, H. C., Cheng, C. H., Hung, C. H., Chou, W. C., Yau, W. H., Yang, P. F. and Lai, Y. S., Nanotribological properties of ALD-processed bilayer TiO_2/ZnO films. *Microelectronics Reliability* **2014,** *54*, 2754–2759.

50. Chen, R., Lin, J. L., He, W. J., Duan, C. L., Peng, Q. and Wang, X. L., Spatial atomic layer deposition of ZnO/TiO_2 nanolaminates. *J. Vac. Sci. Technol. A* **2016,** *34* (5).

51. Leelavathi, A., Madras, G. & Ravishankar, N., Origin of enhanced photocatalytic activity and photoconduction in high aspect ratio ZnO nanorods. *Phys. Chem. Chem. Phys.* **2013,** *15*, 10795-10802.

52. Han, C., Yang, M.-Q., Weng, B. and Xu, Y.-J., Improving the photocatalytic activity and anti-photocorrosion of semiconductor ZnO by coupling with versatile carbon. *Phys. Chem. Chem. Phys.* **2014,** *16*, 16891-16903.

53. Li, W., Wang, G., Chen, C., Liao, J. and Li, Z., Enhanced Visible Light Photocatalytic Activity of ZnO Nanowires Doped with Mn^{2+} and Co^{2+} Ions. *Nanomaterials* **2017,** *7* (1), 20.

54. Rokhsat, E. and Akhavan, O., Improving the photocatalytic activity of graphene oxide/ZnO nanorod films by UV irradiation. *Appl. Surf. Sci.* **2016**, 371.

55. Scherrer, P., Bestimmung der Größe und der inneren Struktur von Kolloidteilchen mittels Röntgenstrahlen. *Nachrichten von der Gesellsschaft der Wissenschaften zu Göttingen, Mathematisch-Physikalische Klasse* **1918**, 98.

56. Abrams, H., Grain Size Measurement by the Intercept Method. *Metallography* **1971,** *4* (1), 59-78.

57. Poodt, P., Lankhorst, A., Roozeboom, F., Spee, K., Maas, D. and Vermeer, A., High-Speed Spatial Atomic-Layer Deposition of Aluminum Oxide Layers for Solar Cell Passivation. *Advanced Materials* **2010,** *22* (32), 3564-3567.

58. Vehkamäki, M., Hatanpää, T., Ritala, M. & Leskelä, M., Bismuth precursors for atomic layer deposition of bismuth-containing oxide films. *J. Mater. Chem.* **2004,** *14* (21), 3191–3197.

59. Bragg, W. H., The Reflection of X-rays by Crystals. *Proc. R. Soc. Lond. A.* **1913,** *88* (605), 428-438.

60. Tian, J.-L., Zhang, H.-Y., Wang, G.-G., Wang, X.-Z., Sun, R., Jin, L., & Han, J.-C., Influence of film thickness and annealing temperature on the structural and optical properties of ZnO thin films on Si (100) substrates grown by atomic layer deposition. *Superlattices and Microstructures* **2015,** *83*, 719–729.

61. Yen, C.-Y., Jian, S.-R., Chen, G.-J., Lin, C.-M., Lee, H.-Y., Ke, W.-C., Juang, J.-Y., Influence of annealing temperature on the structural, optical and mechanical properties of ALD-derived ZnO thin films. *Applied Surface Science* **2011,** *257* (17), 7900–7905.

62. Bharti, B., Kumar, S., Lee, H.N. and Kumar, R., Formation of oxygen vacancies and Ti^{3+} state in TiO_2 thin film and enhanced optical properties by air plasma treatment. *Scientific Reports* **2016,** *6*, 1-13.

63. Chen, P., A novel synthesis of Ti^{3+} self-doped Ag_2O/TiO_2 (p-n) nanoheterojunctions for enhanced visible photocatalytic activity. *Materials Letters* **2016,** *163*, 130-133.

64. Zhang, Y., Xing, Z. P., Liu, X. F., Li, Z. Z., Wu, X. Y., Jiang, J. J., Li, M., Zhu, Q. and Zhou, W., Ti^{3+} self-doped blue TiO_2 single-crystalline nanorods for efficient solar driven photocatalytic performance. *ACS Applied Materials & Interfaces* **2016,** *8* (40), 26851-26859.

65. Linsebigler, A. L., Lu, G. Q. and Yates, J. T., Photocatalysis on TiO_2 surfaces - Principles, mechanisms and selected results. *ACS Applied Materials & Interfaces* **1995,** *8* (40), 26851-26859.

66. Muruganandham, M. and Swaminathan, M., Solar photocatalytic degradation of a reactive azo dye in TiO_2-suspension. *Solar Energy Materials and Solar Cells* **2004,** *81* (4), 439-457.

67. Fox, M. A. and Dulay, M. T., Heterogeneous photocatalysis. *Chemical Reviews* **1993,** *93* (1), 341-357.

68. Shan, F. K., Liu, G. X., Lee, W. J. and Shin, B. C., Stokes shift, blue shift and red shift of ZnO-based thin films deposited by pulsed-laser deposition. *Journal of Crystal Growth* **2006,** *291*, 328–333.

69. Roughness-Induced Superhydrophobicity. In *Multiscale Dissipative Mechanisms and Hierarchical Surfaces. NanoScience and Technology*, Springer, Berlin, Heidelberg: 2008.

70. Luttrell, T., Halpegamage, S., Tao, J., Kramer, A., Sutter, E. and Batzill, M., Why is anatase a better photocatalyst than rutile? - Model studies on epitaxial TiO_2 films. *Sci Rep.* **2015,** *4*, 4043.

71. Mills, A., O'Rourke, C. and Wells, N., A smart ink for the assessment of low activity photocatalytic surfaces. *Analyst* **2014,** *139*, 5409.

72. Xu, Y., Wu, S., Wan, P., Sun, J., and Hood, Z. D., Introducing $Ti3^+$ defects based on lattice distortion for enhanced visible light photoreactivity in TiO2 microspheres. *RSC Adv.* **2017,** *7*, 32461.

73. Grabstanowicz, L. R., Gao, S., Li, T. et al., Facile Oxidative Conversion of TiH_2 to High-Concentration Ti^{3+} - Self-Doped Rutile TiO_2 with Visible-Light Photoactivity. *Inorg. Chem.* **2013,** *52*, 3884-3890.

74. Chen, X., Liu, L. and Huang, F., Black Titanium Dioxide (TiO_2) Nanomaterials. *Chem. Soc. Rev.* **2015,** *44*, 1861-1885.

75. Deak, P., Aradi, B. and Frauenheim, T., Oxygen deficiency in TiO_2: Similarities and differences between the Ti self-interstitial and the O vacancy in bulk rutile and anatase. *Physical Review B* **2015,** *92* (4), 045204-045210.

76. Aïnouche, H., L., A.Kadri, A., Benbrahim, N. and Bradai, D., Ti^{3+} states induced band gap reduction and enhanced visible light absorption of TiO_2 nanotube arrays: Effect of the surface solid fraction factor. *Solar Energy Materials and Solar Cells* **2016,** *151*, 179-190.

77. Lui, X., Du, G. and Li, M., True Photoreactivity Origin of Ti^{3+} - Anatase TiO_2 crystals with Respectively Dominated Exposed {001}, {101}, and {100} Facets. *ACS Omega* **2019,** *4*, 14902-14912.

78. Cao, Y. Q., Wang, S.-S., Liu, C., Wu, D. and Li, A.-D., Atomic layer deposition of ZnO/TiO_2 nanolaminates as ultra-long life anode material for lithium-ion batteries. *Sci Rep* **2019,** *9* (11526).

Chapter 4: A Comparative Study of the Growth of ZnO on Si (100) and Glass Substrates by both Thermal and Remote Plasma-Assisted ALD

Abstract

The deposition of ZnO onto Si (100) wafers and glass substrates by both thermal and remote plasma atomic layer deposition (ALD) was studied. The same reactor, in this case a Picosun™ R200 ALD reactor, was used for both sets of experiments so as to minimise the influence of reactor design on the nature of the deposited materials. For both sets of experiments diethyl zinc (DEZn) was used as the zinc precursor while water was used as the oxygen source for the thermal process and O_2 was used as the oxygen source for the plasma-assisted process.

The growth per cycle (GPC) for the thermal process was found to be higher than that of the plasma process with the exception of growth at a substrate temperature of 100 °C. The maximum GPC for the thermal process was found to be 2.1 Å/cycle at a substrate temperature of 150 °C which was achieved on glass substrate whereas on the Si (100) substrate the GPC under the same conditions was found to be 1.76 Å/cycle. In contrast, for the plasma process, the maximum GPC observed was 1.4 Å/cycle at 200 °C which was achieved on the Si (100) substrate. The differences between the thermal and plasma-assisted processes are discussed in terms of the mechanisms of nucleation and growth.

In addition, significant variations in film morphology and crystallinity were observed between process type and substrate. In terms of morphology, the thermal ALD films presented cylindrical, tear drop-like surface features. In contrast, PE-ALD films showed more spherical

surface features on both Si (100) and glass substrates. For both thermal and PE-ALD, features became more defined as the substrate temperature increased. In terms of crystallinity the PE-ALD films showed a preference for c-axis orientation with the XRD spectrum dominated by the (002) reflection, while the thermal ALD process showed no particular preference between the (100) and (002) directions for films deposited at 100 °C on both Si (100) and glass substrates. As the substrate temperature increased to 150 and 200 °C, the (100) direction was more prevalent.

Electrically the films produced were found to be highly resistive irrespective of the type of ALD process used to deposit them. These results are interpreted in terms of variations in the initial nucleation of the ZnO films and differences in their subsequent rates of growth.

4.1 Introduction

Within the scientific community zinc oxide (ZnO) has long been at the forefront of semiconductor research. The first evidence of this material being studied links as far back as 1935 in which C. W. Bunn determined the lattice dimensions of pure zinc oxide[1]. Still to this day, the material is heavily relied on. The basic properties and applications of ZnO have been well documented over the years and interest is constantly being renewed in this material. ZnO is an n-type semiconductor with a direct band gap of 3.37 eV at room temperature[2-6]. Due to its large band gap, ZnO exhibits considerable potential in areas such as electronics, optoelectronics and sensors[2, 7]. The material has been extensively studied by both thermal and plasma ALD processes. Tynell et al.[8] produced an exhaustive review on ALD of ZnO in which they discuss in depth both thermal ALD and PE-ALD. It is well known that the quality of films depends on the deposition method used. Another crucial factor to consider is the growth temperature as it directly influences the growth rate for the deposition. Borylo et al.[9] reported the influence that the process temperature has on the structure on the thin film. Their results

show that the temperature of the ALD process significantly affects the structure and transparency of ZnO thin films.

Atomic layer deposition is a vapour phase technique that allows for self-limiting growth of thin films. Since the process involves a self-limiting approach, only one atomic or molecular layer can be deposited each time. The surface of the activated substrate becomes saturated with precursor molecules. Due to this fact, ALD is potentially the best method for achieving growth of films with precisely controlled thickness in both the nanometre and sub-nanometre range[10]. Once, ALD was predominately a thermal process in which the thermal energy drives the surface reactions[11]. However, in recent times with demand for improving quality films and lowering of the deposition temperature, research has surged in the area of plasma enhanced ALD or PE-ALD. This method allows for lower temperature processes to be employed while still providing a self-limiting growth and maintaining thickness control. A lower temperature may be required if the substrate is particularly delicate or temperature sensitive. Low-temperature ALD processes may be required for application in perovskite solar cells (PSCs) where ALD is used to deposit charge carrier transports layers or act as encapsulation layers. Low-temperature deposition is essential in order to prevent the degradation of thermally sensitive perovskites[12, 13]. In PE-ALD, the plasma provides the energy to break the bonds in the substrate to chemically activate it while eliminating the need for elevated process temperatures.[14]. The desired precursor can then proceed to bond to the activated surface. PE-ALD is a suitable method if it is necessary to remove water as a precursor which may be important for eliminating the possibility of hydrogen contamination of the film or for speeding up the process, since water is generally more difficult to remove from a vacuum chamber by conventional pumping than some radical or ionic species which necessarily results in increased purge times.

Here, a comparative study of the growth of ZnO on Si (100) and glass substrates by both thermal and remote PE-ALD is presented with focus on the films crystallinity and morphology as well as optical and electrical performance. The same reactor, in this case a Picosun™ R200 ALD reactor, was used for both sets of experiments so as to minimise the influence of reactor design on the nature of the deposited materials. For both sets of experiments DEZn was used as the zinc precursor while water was used as the oxygen source for the thermal process and O_2 was used as the oxygen source for the plasma-assisted process.

4.2 Experimental

4.2.1 Preparation of ZnO films

ZnO films were deposited using both thermal and plasma processes on a 200 mm Picosun™ R200 ALD reactor. Diethyl zinc (DEZn) (min. 95% Strem Chemicals) was used as a metal precursor. The growth temperatures for the thermal and plasma ZnO films were 100 °C, 150 °C and 200 °C. Nitrogen (N_2) was used a carrier gas to transport the precursor molecules into the chamber. During the deposition process, DEZn and water were sustained at room temperature. Pulse times were 0.05 s and 0.1 s for diethyl zinc and water respectively accompanied with a 6.0 s Ar purge between precursor pulses in order to remove both residual precursor and reaction products. The PE-ALD ZnO growth consisted of 0.05 s of DEZn exposure, 6 s Ar purge, 28.0 s of oxygen plasma exposure with RF power of 2800 and 3000 W, followed by 6.0 s of Ar purge. The flow rate of the oxygen was 80 sccm. Prior to all depositions, glass substrates were cleaned by ultrasonication in Decon 90, acetone, and IPA successively. Si (100) wafers (SI-MAT) were cleaned using ozone followed by treatment in hydrogen fluoride (HF) to remove any oxide from the surface of the wafer.

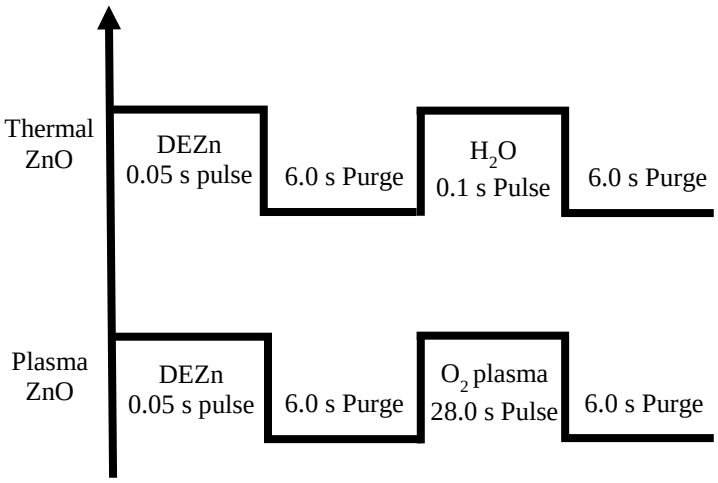

Figure 4.1: A schematic representation of the thermal and plasma ZnO ALD recipes used in this work

4.2.2 Characterisation techniques

The surface morphology of the films was observed using scanning electron microscopy (SEM) using a FEI Quanta 650 FEG High Resolution Scanning Electron Microscope. The crystallinity of the ZnO films was analysed by X-ray diffraction (XRD) using a PANalytical X'Pert Pro Diffractometer, with Cu Kα (λ = 0.154 nm) radiation from 10 to 70° at a step size of 0.02° under 45 kV and 30 mA. The XRD results were compared to the Joint Committee on the Powder Diffraction Standard Card (JPCDS: 36-1451). Optical measurements (UV-Vis) were obtained in the range of 200 – 800 nm using a Perkin Elmer Lambda 950 UV/VIS/NIR Spectrometer. AC and DC field Hall Measurements were performed using a Lake Shore 8400 Series system.

4.3 Results and Discussion

4.3.1 The surface morphologies, growth rate and structural properties of ZnO films

SEM was used to study the morphology of the ZnO thin films deposited. Viewing the samples at a tilt angle of 30° allowed for cross-sectional analysis and in turn facilitated measurement of film thickness. Figure 4.2 shows the GPCs of the thermal and plasma ALD ZnO films deposited as a function of substrate temperature. Each point represents the results of 3 separate experiments. From previous studies a nominal growth rate of ca. 2 Å/cycle was expected for the thermal ZnO[15-17] and 2.2 Å/cycle for the plasma ZnO[18]. However, from figure 4.2(b) (black data points) it may be seen that in our experiments this GPC was only achieved on glass substrates over the temperature range studied. Based on these results plus the results from the nanolaminate study in section 3.3, it is suggested that a delay in nucleation occurred on both substrate types which is tentatively attributed to the initial state of the Si (100) substrate prior to growth.

For growth on Si (100) substrates, the thermal ALD process achieved a maximum GPC of 1.82 Å/cycle at 200 °C. Decreasing the temperature to 150 °C resulted in a slight drop in GPC to 1.76 Å/cycle while further decreasing the temperature to 100 °C resulted in a further drop in GPC to 0.13 Å/cycle. A variation in growth rate of this nature may be accounted for by invoking a mechanism which is essentially thermally activated. Interestingly a similar trend in GPC was observed for the PE-ALD growth on the Si (100) substrates although for all substrate temperatures studied the variation in the measured GPCs was considerably less than that seen for the thermal ALD process (figure 4.2(a)). This is perhaps not surprising since it might be expected in PE-ALD that the activation energy for the process would be largely delivered by the plasma rather than from the substrate. However since the substrate temperature still influences the GPC to a degree this highlights the fact that the process is not solely determined

by gas-phase activation- which again would be entirely consistent with the self-limiting nature of an ALD process.

The values of GPC for the films deposited by the plasma process range from 0.87 – 1.4 Å/cycle. Comparing the GPC value for both the thermal and plasma films grown at 100 °C shows a higher GPC for the plasma film. As implied above, for the thermal process the low GPC value can be explained by the lower reactivity of the DEZn precursor at lower temperatures. At 150 °C and 200 °C, GPC values for the plasma grown films on Si (100) substrates are lower than those for the thermally grown films.

(a)

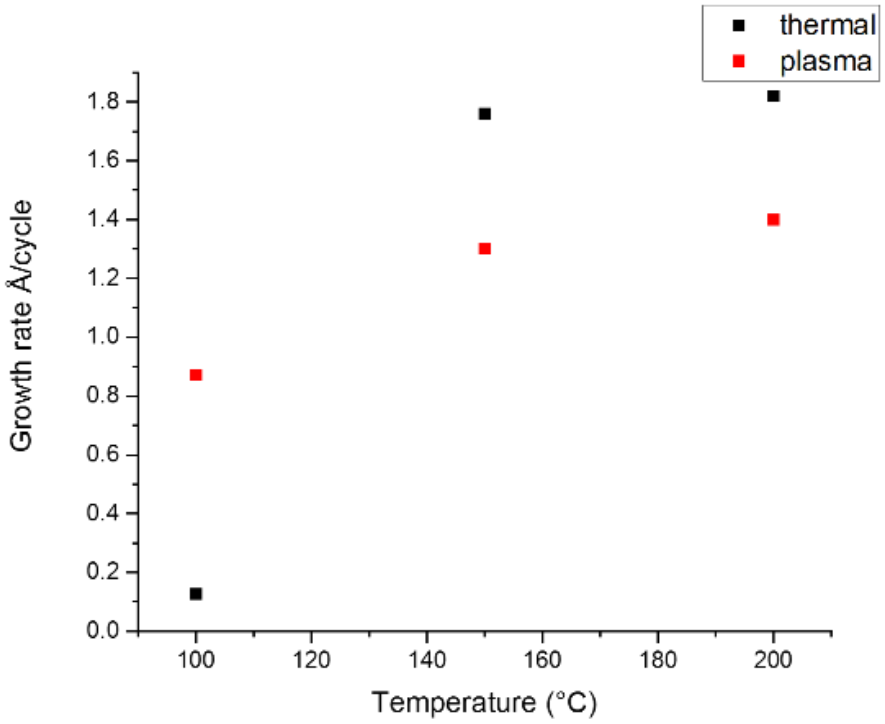

(b)

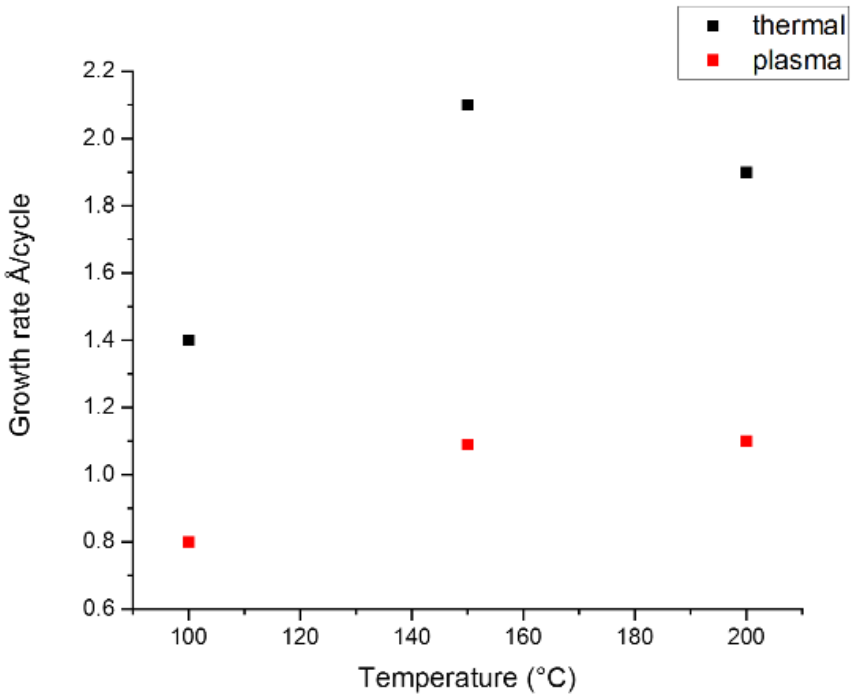

Figure 4.2: Graph of growth rate per cycle vs. temperature for thermal and PE-ALD ZnO on (a) Si and (b) glass substrate at 100 °C, 150 °C and 200 °C

From figure 4.2 (b) (black data points) it may be seen that the maximum GPC achieved on glass substrates was 2.1 Å/cycle deposited by the thermal ALD process at 150 °C. Increasing the growth temperature still further resulted in a slight drop in GPC to 1.9 Å/cycle. These values are similar to the nominal growth rate of 2 Å/cycle[15-17]

Overall, the plasma GPC values were much lower on the glass substrates than on the Si (100) substrates (figure 4.2, red data points). Similar to the pattern seen on the Si (100) substrates, the glass substrate plasma GPC values at 150 °C and 200 °C were practically the same at both temperatures, being 1.1 Å/cycle in this case.

As with the growth on the Si (100) substrates the overall behaviour of the GPC as a function of substrate temperature for both the thermal and plasma ALD processes is indicative of processes which are thermally activated in that in general increasing the substrate temperature increases or at least maintains the GPC. The exception here is the thermal process on glass at 200 °C, where a decrease in GPC is observed.

There is nothing particularly unusual about such behaviour since it is generally-known that ALD growth can decrease at higher temperatures due to desorption effects. However, what is unusual is the influence of the substrates.

On the Si (100) substrates increasing the substrate temperature results in an increase in GPC while on glass substrates the GPC decreases. In addition on the Si (100) substrates reducing the temperature to 100 °C results in the lowest GPC value measured while on glass substrates growth at the same temperature results in a GPC which is over 10 times larger.

These differences are highlighted in table 4.1, below:

Substrate/ growth mode	**GPC @100 °C (Å)**	**GPC @ 150 °C (Å)**	**GPC @200 °C (Å)**
Si (100)/ thermal	0.13	1.76	1.82
Glass/ thermal	1.4	2.1	1.9
Si (100)/ plasma	0.87	1.3	1.4
Glass/ plasma	0.8	1.1	1.1

Table 4.1: A comparison of the GPC values recorded for ZnO ALD on both Si (100) wafers and glass substrates as a function of substrate temperature and growth mode

From table 4.1 it may be seen that in terms of the thermal process, the Si (100) substrates appear to be considerably less reactive than the glass substrates at the lowest temperature studied, 100 °C. This trend is maintained at the higher temperatures but to a lesser degree.

This is quite surprising since both surfaces are effectively SiO_2 in terms of chemical composition. This trend is reversed for the plasma process although here the differences are much less marked. Again this is quite surprising.

A possible reason behind the variations in GPC values are the magnitudes of the sticking coefficients of the species impinging on the surface. In the case of the thermal process the adsorption of DEZn is likely to dominate the growth process. Using this argument we might assume that if this is the case then logically the sticking coefficient of DEZn must higher on the glass surface than on the Si (100) surface.

Plan-view SEM images (figure 4.3 and 4.4) highlight the differences in morphology of ZnO grown by thermal and plasma ALD at 100 °C, 150 °C and 200 °C. Thermal ZnO films display cylindrical, tear drop-like surface features on both the Si (100) and glass substrates. In contrast, plasma ZnO films on both substrates have more scattered, spherical features on the surface. These features become more defined with an increase in growth temperature due to increased thermal energy. The PE-ALD ZnO SEM images are very similar to each other which suggests that the substrate temperature has little influence on the morphology as a consequence of the high reactivity of the O_2 plasma[19]. All films are free from discontinuities or defects.

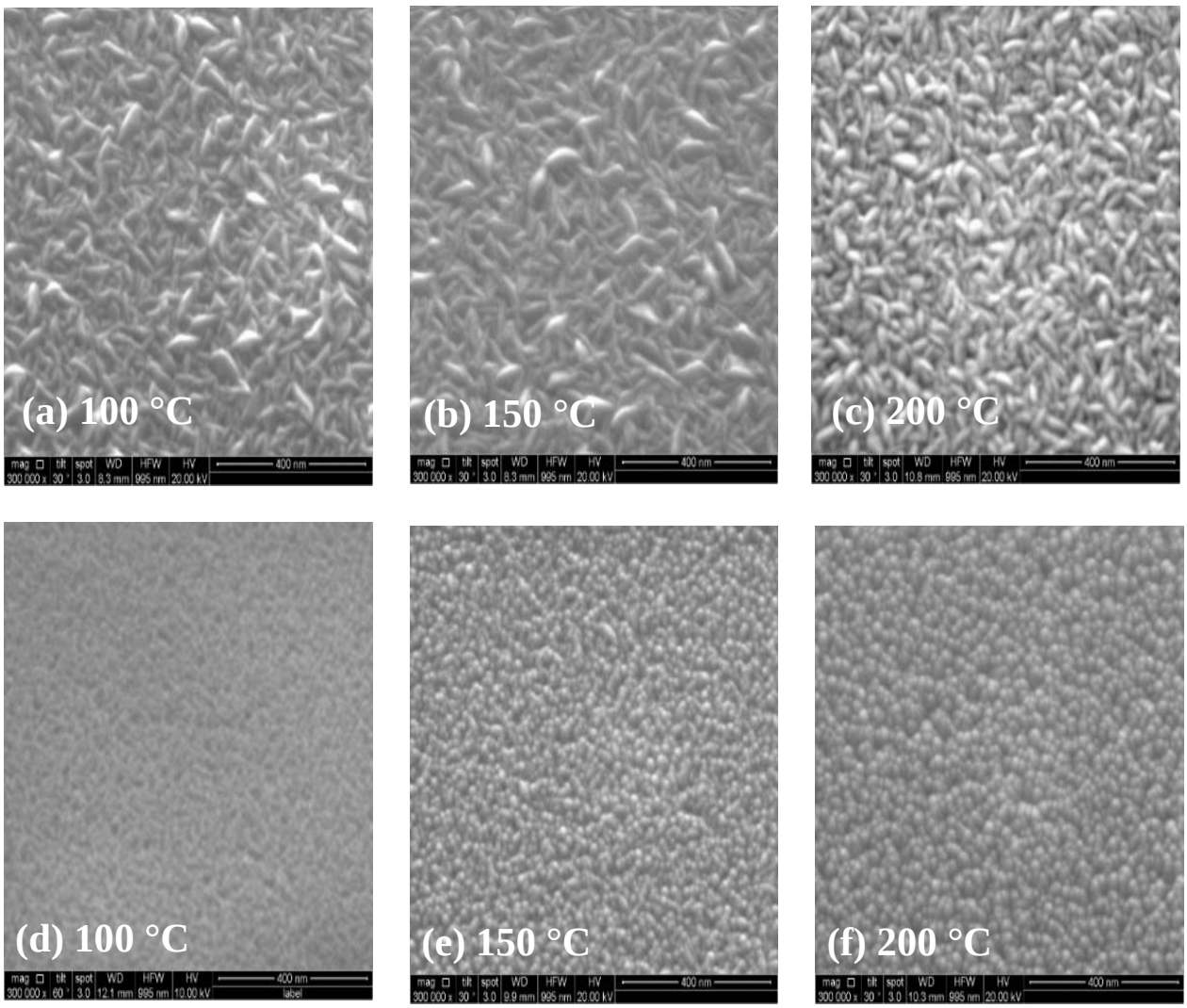

Figure 4.3: Plan-view SEM of (a) - (c) thermal ZnO and (d) - (f) plasma ZnO at various temperatures on Si (100) substrate

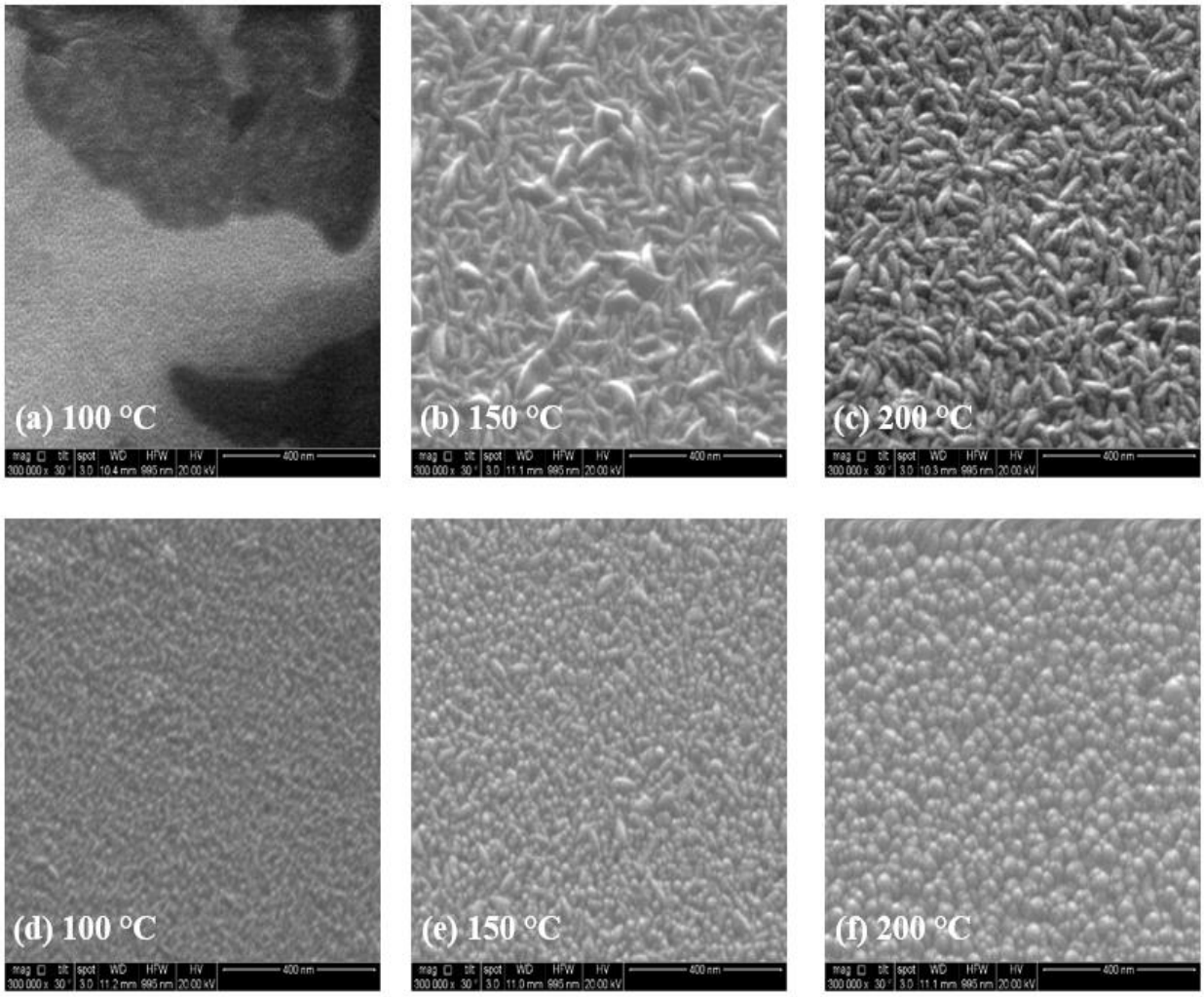

Figure 4.4 Plan-view SEM of (a) - (c) thermal ZnO and (d) - (f) plasma ZnO at various temperatures on glass substrate

XRD patterns of all ZnO films grown by both thermal ALD and PE-ALD are presented in figure 4.5. All films characterized by XRD were grown using 900 ALD cycles. XRD patterns for thermal ALD ZnO show characteristic peaks at 2θ values of 31.8°, 34.4°, 36.2° and 56.6° corresponding to reflections having the Miller indices, (100), (002), (101) and (110) respectively. The broad peak at 20° (2θ) is characteristic of the glass substrate. Similarly, the broad peak at 70° (2θ) is attributed to Si (100) substrate. All films apart from the film deposited using thermal ALD ZnO at 100 °C exhibited a preferred *c*-axis oriented (100) phase of the wurtzite structure. XRD patterns for PE-ALD ZnO show the characteristic peak at 2θ value of 34.4° (002) being present in all samples except for the PE-ALD ZnO on deposited on glass at 200 °C. This film also lacked any characteristic peaks suggesting that it was amorphous. One peak at 31.8° (2θ) corresponding to the (100) of wurtzite ZnO was present in all of the ZnO films deposited using thermal ALD. In contrast, this peak was only observed in the spectra obtained from the PE-ALD deposited samples grown at 100 °C on both substrate types.

Further interpretation may be made by considering the ALD window for ZnO as described by Pilz et al. in which the GPC was constant in the temperature range of 125 to 200 °C[20]. Below the ALD window (100 °C), a mixture of both (100) and (002) orientations is evident. As the temperature increases, the (002) orientation becomes more dominant. Therefore, inside the ALD window (>100 °C) the PE-ALD ZnO films are (002) textured. The expected GPC of the PE-ALD process has previously been stated in section 4.3.1 as ca. 2.2 Å/cycle. This is closely related to the interplanar distance of 2.6 Å of the (002) orientation. For the atomic arrangement of the (002) plane, one species lies parallel to the substrate. For the (100) plane, it consists of both Zn and O species. Therefore, in the (100) direction, a full crystalline plane could not be formed with one ALD cycle and the GPC would restricted to half of the lattice spacing (2.82 Å) for the (100) plane (depicted by Pilz et al.[20]). This may explain the low GPC observed at

lower temperatures[21]. It has previously been reported that for PE-ALD ZnO, a switch in preferred orientation from (100) to (002) occurs as substrate temperature increased[18-21].

A switch from no preferential orientation to (002) preferential orientation was also observed by Kim et al.[22] In all of these cases, the temperature at which this preferential orientation switch occurs is similar to the start of the ALD window for ZnO.

Interestingly in this work, for the PE-ALD ZnO deposited on Si (100), the intensity of the (002) peak increased with increasing temperature (figure 4.5 (b)) but in contrast, for the PE-ALD ZnO deposited on glass substrates, the (002) peak disappears completely as the temperature increases (figure 4.5 (d)).

(a)

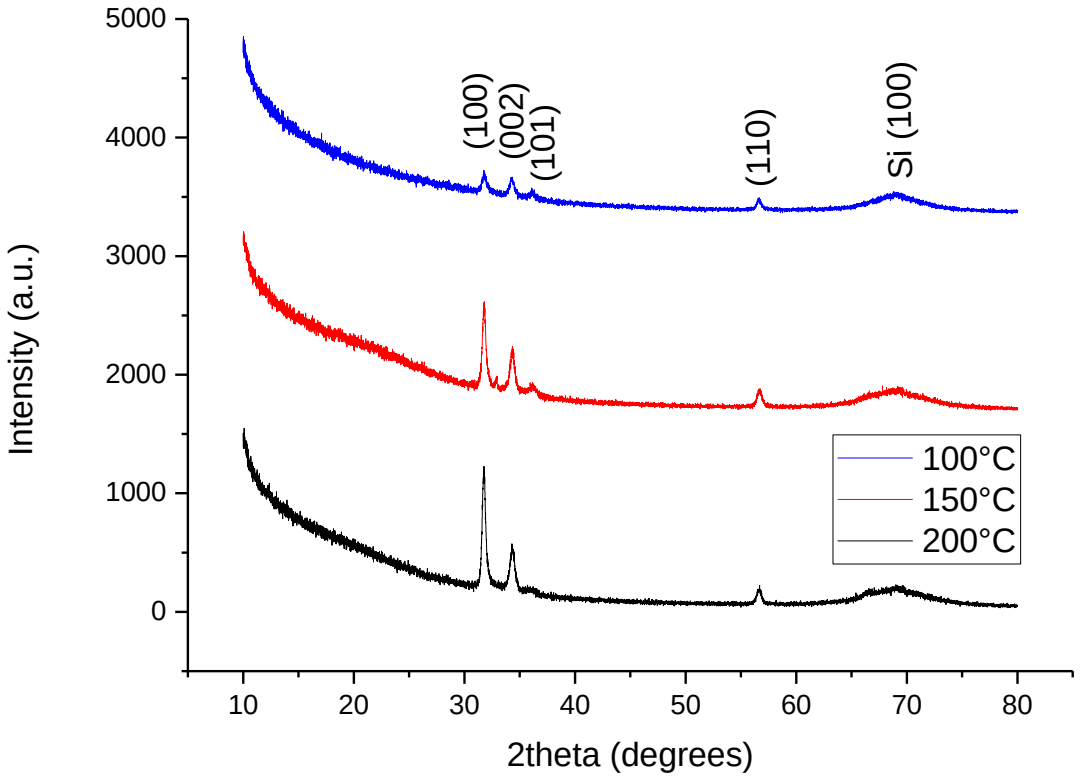
5000
4000
3000
2000
1000
0
Intensity (a.u.)
(100)
(002)
(101)
(110)
Si (100)
100°C
150°C
200°C
10
20
30
40
50
60
70
80
2theta (degrees)

(b)

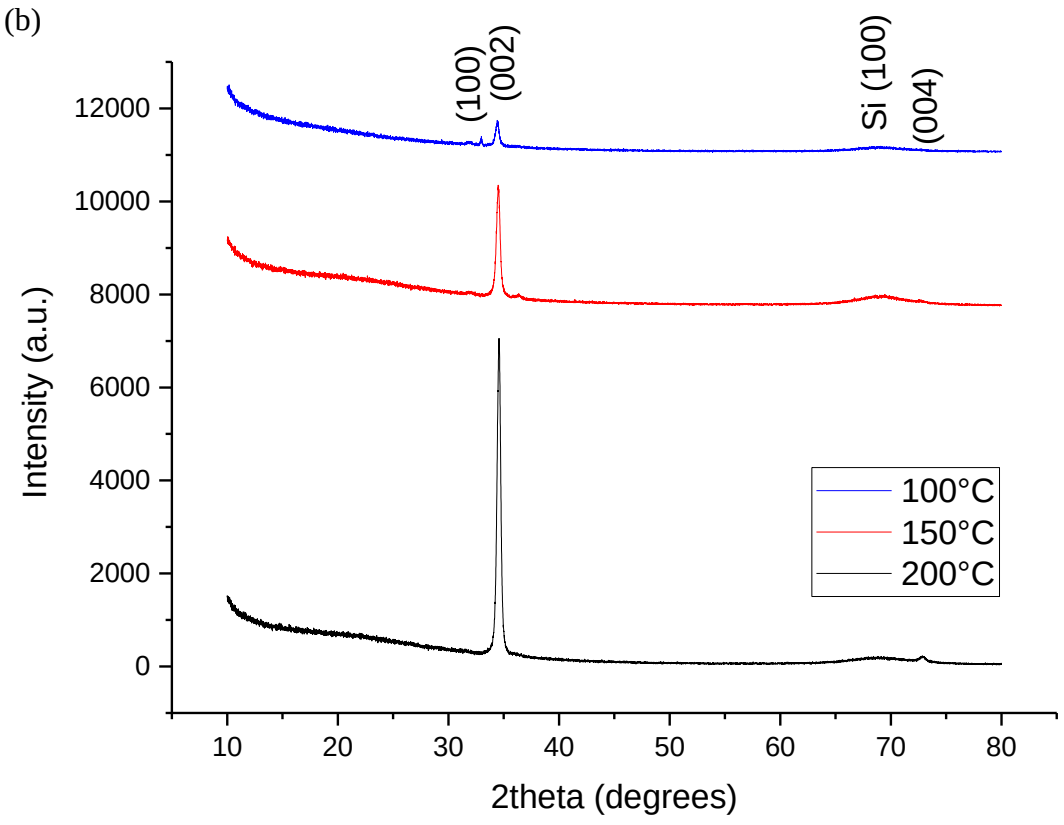
12000
10000
8000
6000
4000
2000
0
Intensity (a.u.)
(100)
(002)
Si (100)
(004)
100°C
150°C
200°C
10
20
30
40
50
60
70
80
2theta (degrees)

(c)

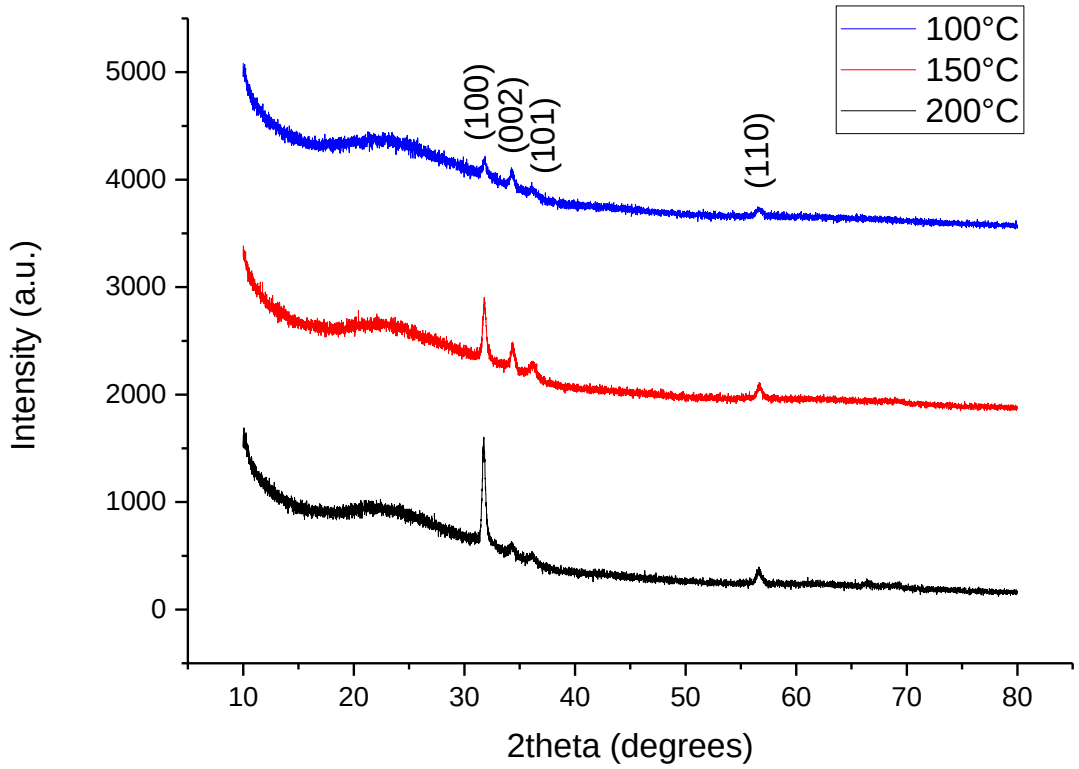

(d)

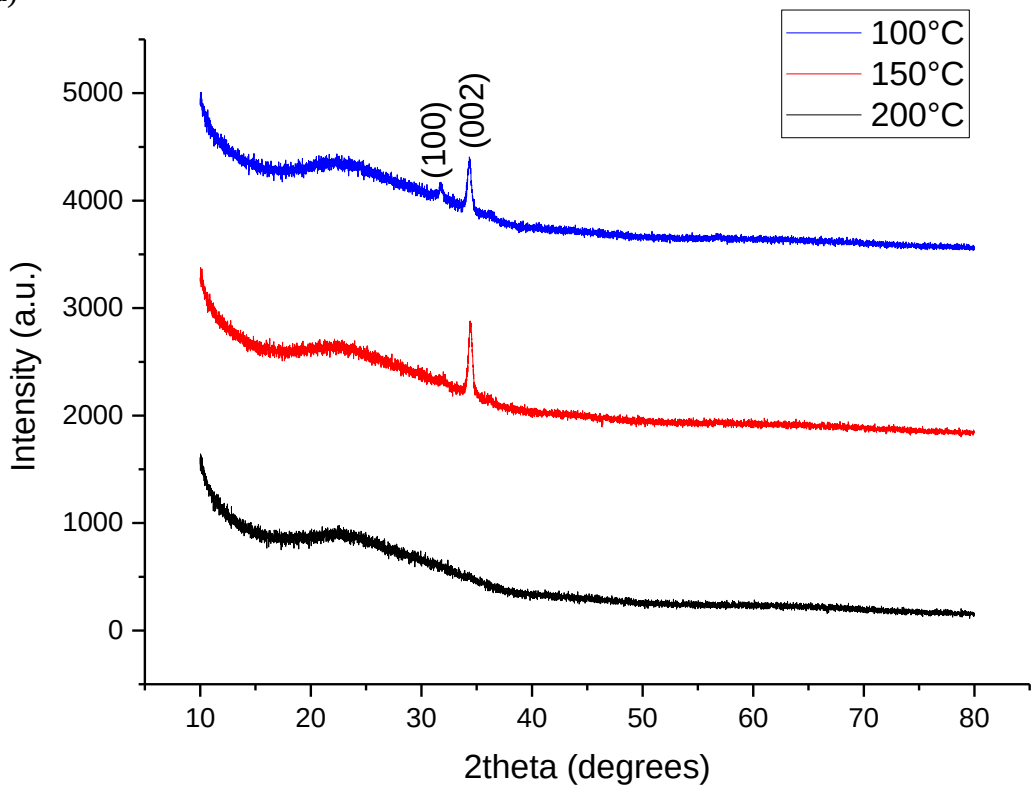

Figure 4.5 XRD patterns of (a) thermal ALD ZnO on Si, (b) PE-ALD ZnO on Si, (c) thermal ALD ZnO on glass and (d) PE-ALD ZnO on glass

In general, the thermal ALD ZnO films appear to display more evidence of crystallinity than those grown via PE-ALD although the film that gave rise to the most intense (002) peak was the PE-ALD film deposited on Si (100) substrates at 200 °C, see figure 4.5 (b), black trace. Interestingly, a peak at 73.8° (2θ) (004) was present on PE-ALD ZnO on glass growth at 200 °C which is usually characteristic of ZnO nanoparticles.

The average grain size was estimated using the Scherrer equation (section 3.3) along the ZnO (100) crystal plane for thermal ALD process and the ZnO (002) crystal plane for the PE-ALD process[23]. The results are seen below in table 4.2. In general, the grain sizes for the thermal ALD process were larger than those for the PE-ALD process. The films deposited on glass substrates had larger grains than those deposited on Si (100) substrates for both ALD processes with the exception of the films grown using thermal ALD ZnO at 100 °C on glass.

Growth temperature (°C)	**Scherrer method crystallite size (nm)**			
	Thermal		**Plasma**	
	Si (100)	**glass**	**Si (100)**	**glass**
100	27.0	23.0	24.4	26.1
150	26.5	28.5	24.5	25.5
200	27.3	28.8	25.7	-

Table 4.2: Comparison of crystallite size calculated by the Scherrer equation for thermal and plasma ALD deposited ZnO on both Si (100) and glass along to ZnO (002) crystal plane

Comparing the grain sizes estimated via the Scherrer method and those measured from the SEM images, it was found that the grain sizes as determined using the two approaches were consistent.

4.3.2 Optical Properties

Optical measurements in the form of UV/Visible spectroscopy were carried out by recording transmittance spectra for the films grown using 900 ALD cycles of both the thermal and PE-ALD processes on glass substrates at 100 °C, 150 °C and 200 °C, figure 4.6.

Thermal ALD films (figure 4.6 (a)) grown at 150 °C and 200 °C on glass appear to follow a similar pattern with transmittance at 90% above 600 nm. Transmittance decreases from 90% down to 70% steadily from 600 nm to 450 nm. An increase is seen at 400 nm to 80% before dropping as expected in the UV region to 0%. Films grown at 100 °C on glass show a slight difference and once in the UV region, the percentage transmittance for these films inclines to 0% more slowly. Figure 4.6 (b) shows UV/Visible transmittance spectra for ZnO PE-ALD films at 100 °C, 150 °C and 200 °C. The average transmittance over the entirety of the visible wavelength range 400 to 550 nm is >60%. A higher transmittance at ~90% is observed for films grown at a higher temperature. At 360-380 nm, a strong absorption edge is evident near the ultraviolet region due to the fundamental band gap of the material for both the thermal and PE-ALD processes. Transmittance of all films incline to ~0% in the UV region as expected. Once in the UV region, the percentage transmittance for films grown at 150 °C and 200 °C comparatively much lower than the 100 °C film. This result was also seen in the thermally grown film and may be attributed to the quality of the material being affected at different temperatures. A sharper transition in the spectra can be attributed to a thin films with a higher optical quality and less defect absorption states[20, 24].

(a)

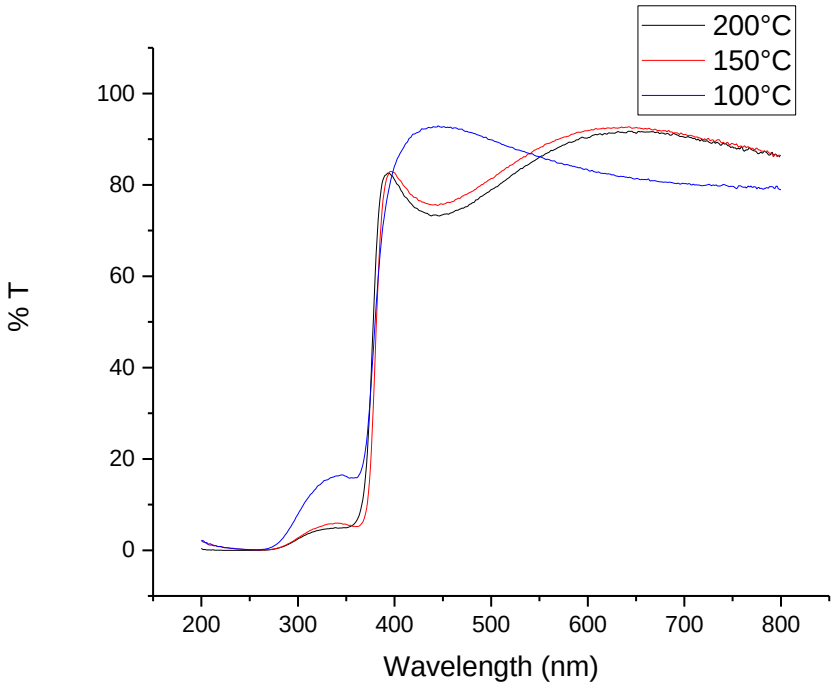

(b)

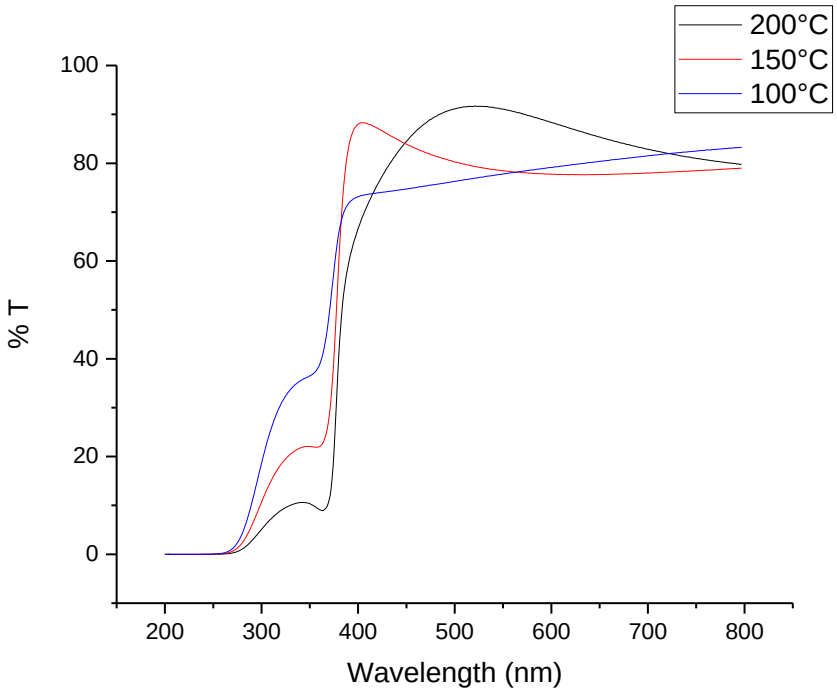

Figure 4.6 UV/Visible Spectroscopy transmittance spectra for 900 cycles (a) ZnO thermal ALD and (b) PE-ALD films at 100 °C 150 °C and 200 °C on glass substrates

It is worth noting that UV/Vis measurements on thin films deposited by ALD are used as a guide only. This is due to the fact that ALD is capable of coating high aspect ratio films. Although this is generally considered as an advantage, for the purpose of obtaining UV/Vis measurements it presents a disadvantage. An overgrowth occurs where the ALD films deposits on the underside of the substrate and leads to an overlap of growth. An incorrect decrease in percentage transmission may be measured due to additional absorption caused by this overlap. The use of a mask may prevent this overgrowth and allow for more accurate optical measurements.

4.3.3 Electrical Properties

The Hall mobility (μ_H), carrier concentration (n) and the sheet resistance (R_s) were obtained with Hall Effect measurements carried out at room temperature using a van der Pauw structure (1 cm x 1 cm). The measurements were performed using a Lake Shore 8404 AC/DC (alternating current/ direct current) Hall-effect system as described in section 2.3.8. Table 4.3 summarises the Hall data measured. Figure 4.7 displays the effect of the growth temperature on the resistivity of thermal and PE-ALD ZnO.

T (°C)	**μ_H (cm^2/Vs)**		**n ($1/cm^3$)**		**R_s (Ω/□)**	
	plasma	thermal	plasma	thermal	plasma	thermal
100	0.8	0.7	2.3E16	1.9E17	6.0E7	3.6E6
150	1.5	10.5	2.4E16	8.8E18	2.4E7	6.1E3
200	1.7	27.2	8.3E15	2.9E19	2.6E7	4.4E2

Table 4.3: Hall mobility, carrier concentration and sheet resistance measurements for 900 cycles thermal and PE-ALD ZnO films at 100 °C, 150 °C and 200 °C

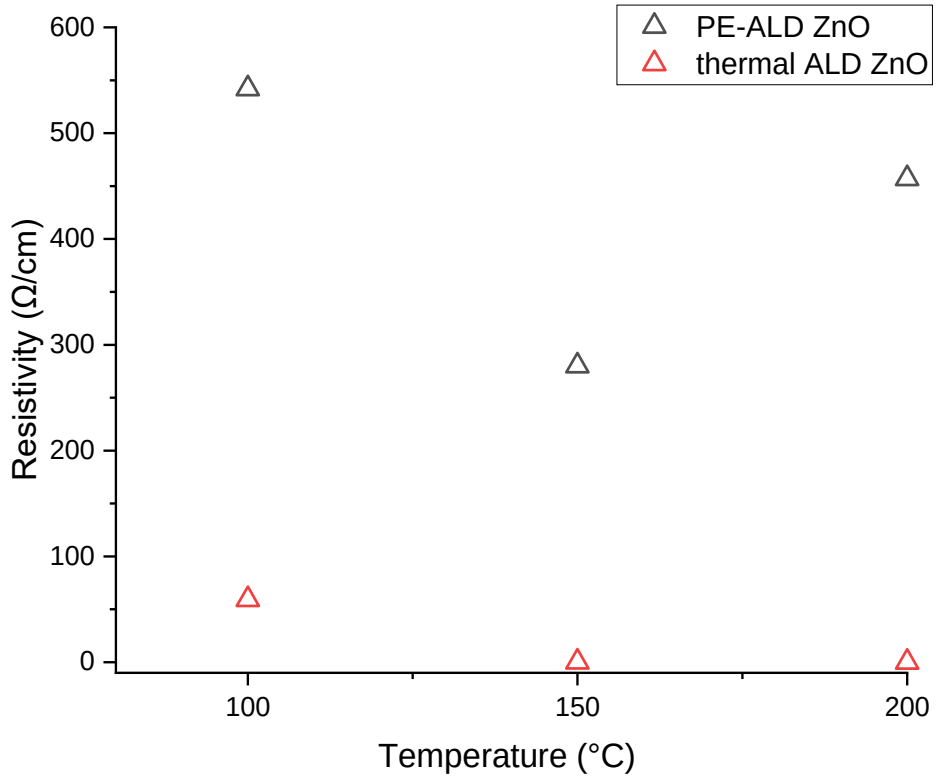

Figure 4.7: Resistivity of thermal and PE-ALD ZnO deposited on glass substrates as a function of substrate temperature

From table 4.3 it may be seen that in general for all samples the Hall mobility increases with increasing substrate temperature during growth, while the sheet resistance decreases accordingly. Interestingly in terms of carrier concentrations, for the samples grown by thermal ALD an increase in carrier concentration is observed with increasing substrate temperature while for the PE-ALD grown samples the reverse trend is observed. Similarly for these latter samples the sheet resistance values are very high for all samples prepared, meaning that the PE-ALD samples are essentially resistive. In contrast the samples grown by thermal ALD have

much lower sheet resistance values by several orders of magnitude, as might be expected from the higher carrier concentrations and mobilities.

In more detail, the Hall mobility's for both ALD processes deposited at 100 °C were very similar with thermally grown ZnO having a slightly higher Hall mobility of 0.7 cm^2/Vs versus 0.8 cm^2/Vs for the plasma grown film. Similarly, the carrier concentrations for both films are of the same order of magnitude. However, the sheet resistance of the plasma grown film was an order of magnitude higher than that of the thermally grown film.

For the films deposited at 150 °C, the thermal ALD ZnO films had Hall mobilities that were approximately 7 times those of the plasma films, being some 10.5 cm^2/Vs as compared with 1.5 cm^2/Vs. The carrier concentration of the thermal ALD ZnO films was 2 orders of magnitude higher than that of the plasma-grown films. The sheet resistance of the plasma grown ZnO was 2.4E7 Ω/□ which was much higher than the thermally grown film which has a sheet resistance of 6.1E3 Ω/□.

The most significant difference in Hall mobility between the ALD processes was seen for the films deposited at 200 °C. The Hall mobility for the thermal ALD ZnO was approximately 16 times higher than that of the plasma film. It has been reported that the microstructure of a thin film can influence its electrical properties[25-27]. As the grain size increases, the Hall mobility has been reported to increase[25]. The surface features observed in figures 4.3 an 4.4 may explain the large Hall mobility for this film. The carrier concentration of thermal ALD ZnO was 5 orders of magnitude higher than the plasma grown film. The sheet resistance was much lower for the thermal film than the plasma films, 4.4E2 Ω/□ for thermal ZnO and 2.6E7 Ω/□ for the plasma grown ZnO. Thermally deposited ZnO at 200 °C was the best performing across Hall mobility, carrier concentration and sheet resistance.

The results show that for all substrates temperatures and both substrate types, the thermal process leads to films that are more conducting than their plasma-grown counterparts. All films grown by thermal ALD have higher carrier concentrations as compared to their plasma-grown counterparts. As the substrate temperature was increased, the carrier concentrations of the films grown by thermal ALD increased whereas the opposite trend was observed for their plasma-grown counterparts. The plasma grown films are much more resistive than the thermally grown films at the same temperature. The optimum growth temperature with respect to the minimum resistivity was found to be 150 °C as reflected in both the thermal and plasma processes. Hence, this temperature was selected to continue growth of doped-ZnO films.

The Hall mobility (μ_H), carrier concentration (n) and the sheet resistance (R_s) were obtained for two other PE-ALD ZnO films deposited at 150 °C in which all growth parameters remained the same except one was deposited with a reduced plasma power of 2500 W (compared to 2800 W for all other films) and the other, a reduced O_2 plasma pulse time of 22.0 s (28.0 s all other films). The results are displayed in table 4.4.

Film	**μ_H (cm^2/Vs)**	**n ($1/cm^3$)**	**R_s (Ω/□)**
PE-ALD ZnO 150 °C	1.5	2.4E16	2.7E7
↓ pulse	0.6	1.9E16	3.0E7
↓ power	0.4	2.0E16	4.2E7

Table 4.4: Hall mobility, carrier concentration and sheet resistance measurements for 900 cycles PE-ALD ZnO films at 150 °C, PE-ALD ZnO deposited with a reduced plasma power and PE-ALD ZnO deposited with a reduced plasma pulse

From the results in table 4.4, neither the Hall mobility, carrier concentration or sheet resistance improve for PE-ALD ZnO deposited with a reduced plasma power and PE-ALD ZnO deposited with a reduced plasma pulse when compared to PE-ALD ZnO films at 150 °C.

Jin et al. have reported a possible explanation to the decrease of sheet resistance of PE-ALD ZnO thin films grown with an extended plasma pulse[28]. The decrease in sheet resistance may be attributed to the fact that as the O_2 plasma pulse time is extended, the ZnO crystal size also increase[28]. This larger crystal size allows for a longer carrier mean free path within the ZnO film layer[29, 30]. Secondly, the excess of oxygen present from a longer plasma pulse time leads to the formation of Zn vacancies and a breakdown of the intrinsic stoichiometry of ZnO. High quality and strictly stoichiometric ZnO is typically insulating. Generally, the conductivity of ZnO is largely dependent on the presence of impurities[31, 32]. The nature of the ALD process can lead to the formation of impurities such as hydrogen or hydroxyls which can act as shallow donors. The presence of impurities can positively increase the carrier concentration of ZnO thin films[33-40].

As previously mentioned, ITO is the TCO commercial standard in many applications with sheet resistance values in the range of 8-100 Ω/□. In order for ZnO and doped-ZnO to compete with ITO, it needs to possess at least comparable electrical properties. The best performing ZnO film in terms of sheet resistance in this study was thermally deposited at 200 °C, with a sheet resistance of 440 Ω/□. This does not compete with commercial ITO hence explaining why doping of ZnO is necessary in order to improve the electrical properties.

4.4 Conclusion

The growth of ZnO has been demonstrated by ALD and PE-ALD on a 200 mm Picosun™ R200 ALD reactor. Both processes are substrate and temperature dependant. The GPC for the thermal process was found to be higher than that of the plasma process with the exception of growth at a substrate temperature of 100 °C. The maximum GPC for the thermal process was found to be 2.1 Å/cycle at a substrate temperature of 150 °C which was achieved on glass substrate whereas on the Si (100) substrate the GPC under the same conditions was found to be 1.76 Å/cycle. In contrast, for the plasma process, the maximum GPC observed was 1.4 Å/cycle at 200 °C which was achieved on the Si (100) substrate. The differences between the thermal and plasma-assisted processes are discussed in terms of the mechanisms of nucleation and growth. In addition, significant variations in film morphology and crystallinity were observed between process type and substrate. In terms of morphology, the thermal ALD films presented cylindrical, tear drop-like surface features. In contrast, PE-ALD films showed more spherical surface features. For both thermal and PE-ALD, features became more defined as the substrate temperature increased. In terms of crystallinity the PE-ALD films showed a preference for c-axis orientation with the XRD spectrum dominated by the (002) reflection, while the thermal ALD process showed no particular preference between the (100) and (002) directions. For all films, the average transmittance over the entirety of the visible wavelength range 400 to 750 nm is >60% with a sharp cut off in the UV region due to the band gap.

Electrically the films produced were found to be highly resistive irrespective of the type of ALD process used to deposit them.

References

1. Bunn, C. W., The lattice-dimensions of zinc oxide. *Proc. Phys. Soc.* **1935,** *47* (835).

2. Janotti, A. and Van de Walle., C. G., Fundamentals of zinc oxide as a semiconductor. *Rep. Prog. Phys.* **2009,** *72*.

3. Reynolds, D. C., Look, D. C., Jogai, B., Litton, C. W., Cantwell, G. and Harsch, W. C., Valence-band ordering in ZnO. *Physical Review B* **1999,** *60* (4), 2340-2344.

4. Srikant, V. and Clarke, D. R., On the optical band gap of zinc oxide. *Journal of Applied Physics* **1998,** *83* (10), 5447-5451.

5. Thomas, D. G., The exciton spectrum of ZnO. *Journal of Physics and Chemistry of Solids* **1960,** *15* (1-2).

6. Liang, W. Y. and Yoffe, A. D., Transmission Spectra of ZnO Single Crystals. *Physical Review Letters* **1968,** *20* (2), 59-62.

7. Boyadjieva, S. I., Georgievab, V., Yordanovc, R., Raichevab, Z. and Szilágyia, I. M., Preparation and characterization of ALD deposited ZnO thin filmsstudied for gas sensors. *Applied Surface Science* **2016,** *387*, 1230–1235.

8. Tynell, T. and Karppinen, M., Atomic layer deposition of ZnO: a review. *Semicond. Sci. Technol.* **2014,** *29* (043001).

9. Borylo, P., Matus, K., Lukaszkowicz, K., Kubacki, J., Balin, K., Basiaga, M., Szindler, M. and Mikuła, J., The influence of atomic layer deposition process temperature on ZnO thin film structure. *Applied Surface Science* **2017,** *474*, 177–186.

10. Johnson, R. W., Hultqvist, A. and Bent, S. F., A brief review of atomic layer deposition: from fundamentals to applications. *Materials Today* **2014,** *17* (5), 236-246.

11. Ritala, M. and Leskala., M., Chapter 2 – Atomic layer deposition. In *Handbook of Thin Films*, Nalwa, H. S., Ed. Academic Press: San Diego, CA, 2002; Vol. Volume 1: Deposition and processing of thin films.

12. Meng, L., Hu, S., Yan, W., Feng, J., Li, H. and Yan, X., Controlled synthesis of large scale continuous monolayer WS_2 film by atmospheric pressure chemical vapor deposition. *Chemical Physics Letters* **2020,** *739*, 136945.

13. Lv, Y., Xu, P., Ren, G., Chen, F., Nan, H., Liu, R., Wang, D., Tan, X., Liu, X., Zhang, H. and Chen, Z.-K., Low-Temperature Atomic Layer Deposition of Metal Oxide Layers for Perovskite Solar Cells with High Efficiency and Stability under Harsh Environmental Conditions. *ACS Appl. Mater. Interfaces* **2018,** (10), 23928−23937.

14. Profijt, H. B., Potts, S. E., van de Sanden, M. C. M. and Kessels, W. M. M., Plasma-Assisted Atomic Layer Deposition: Basics, Opportunities and Challenges. *J. Vac. Sci. Technol. A* **2011,** *29* (5).

15. Lee, D.-J. K., H.-M. Kwon, J.-Y. Choi, H., Kim, S.-H. and Kim, K.-B., Structural and Electrical Properties of Atomic Layer Deposited Al-Doped ZnO Films. *Adv. Funct. Mater.* **2011,** *21* (3), 448-455.

16. Jensen, J. M., Oelkers, A. B., Toivola, R., Johnson, D. C., Elam, J. W. and George, S. M., X-ray Reflectivity Characterization of ZnO/Al_2O_3 Multilayers Prepared by Atomic Layer Deposition. *Chem. Mater.* **2002,** *14* (5), 2276-2282.

17. Banerjee, P., Lee, W.-J., Bae, K.-R., Lee, S. B. and Rubloff, G. W., Structural, electrical, and optical properties of atomic layer deposition Al-doped ZnO films. *J. Appl. Phys.* **2010,** *108*, 043504.

18. Park, S.-H. K., Hwang, C.-S., Kwack, H.-S., Lee, J.-H. and Chu, H. Y., Characteristics of ZnO Thin Films by Means of Plasma-Enhanced Atomic Layer Deposition. *Electrochem. Solid State* **2006,** *9* (10), G299.

19. Zhang, J., Yang, H., Zhang, Q.-I., Dong, S. and Luo, J. K., Structural, optical, electrical and resistive switching properties of ZnO thin films deposited by thermal and plasma-enhanced atomic layer deposition. *Appl. Surf. Sci.* **2013,** *282*, 390-395.

20. Pilz, J., Perrotta, A., Leising, G. and Coclite, A. M., ZnO Thin Films Grown by Plasma-Enhanced Atomic Layer Deposition: Material Properties Within and Outside the "Atomic Layer Deposition Window". *Physica Status Solidi A* **2020,** *217* (8), 1900256.

21. Rowlette, P. C., Allen, C. G., Bromley, O. B., Dubetz, A. E. and Wolden, C. A., Plasma-Enhanced Atomic Layer Deposition of Semiconductor Grade ZnO Using Dimethyl Zinc. *9 Chem. Vapor Depos.* **2009,** *15* (1-3), 15-20.

22. Kim, D., Kang, H., Kim, J.-M. and Kim, H., The properties of plasma-enhanced atomic layer deposition (ALD) ZnO thin films and comparison with thermal ALD. *Appl. Surf. Sci.* **2011,** *257* (8), 3776-3779.

23. Scherrer, P., Bestimmung der Größe und der inneren Struktur von Kolloidteilchen mittels Röntgenstrahlen. *Nachrichten von der Gesellsschaft der Wissenschaften zu Göttingen, Mathematisch-Physikalische Klasse* **1918**, 98.

24. Viezbicke, B. D., Patel, S., Davis, B. E. and Birnie, D. P., Evaluation of the Tauc method for optical absorption edge determination: ZnO thin films as a model system. *Physica Status Solidi (B) Basic Research* **2015,** *252* (8), 1700-1710.

25. Calnan, S. and Tiwari, A. N., High mobility transparent conducting oxides for thin film solar cells. *Thin Solid Films* **2010,** *518* (77), 1839-1849.

26. Lee, J. H., Ko, K. H. and Park, B. O., Electrical and Optical Properties of ZnO Transparent Conducting Films by the sol-gel method. *Journal of Crystal Growth* **2003,** *247* (1-2), 119-125.

27. Bandyopadhyay, S., Paul, G. K., Roy, R., Sen, S. K. and Sen, S., Study of structural and electrical properties of grain-boundary modified ZnO films prepared by sol–gel technique. *Mater. Chem. Phys.* **2002,** *74* (1), 83-91.

28. Jin, M. J., Jo, J., Neupane, G. P., Kim, J., An, K.-S. and Yoo, J. W., Tuning of undoped ZnO thin films via plasma enhanced atomic layer deposition and its application for an inverted polymer solar cell. *AIP Advances* **2013,** *3* (10), 102114.

29. Seah, M. P. and Dench., W. A., Quantitative electron spectroscopy of surfaces: A standard data base for electron inelastic mean free paths in solids. *Surf. Interface Anal.* **1979,** *1* (1), 1-10.

30. Zhang, W., Brongersma, S. H., Richard, O., Brijs, B., Palmans, R., Froyen, L. and Maex, K., Influence of the electron mean free path on the resistivity of thin metal films. *Microelectronic Engineering* **2004,** *76* (1-4), 146-152.

31. Tuomisto, F., Saarinen, K., Look, D. C. and Farlow, G. C., Introduction and recovery of point defects in electron-irradiated ZnO. *Phys. Rev. B* **2005,** *72*, 08520.

32. Janotti, A. and Van de. Walle, C. G., Native point defects in ZnO. *Phys. Rev. B* **2007**, 165202.

33. Zhang, L., Jiang, Y., Ding, Y., Povey, M. and York, D., Investigation into the antibacterial behaviour of suspensions of ZnO nanoparticles (ZnO nanofluids). *Journal of Nanoparticle Research volume* **2007,** *9*, 479 – 489.

34. Thomas, M. A. and Cui., J. B., Highly Tunable Electrical Properties in Undoped ZnO Grown by Plasma Enhanced Thermal-Atomic Layer Deposition. *ACS Appl. Mater. Interfaces* **2012,** *4* (6), 3122–3128.

35. Zhang, B. P., Wakatsuki, K., Binh, N. T., Usami, N. and Segawa, Y., Effects of growth temperature on the characteristics of ZnO epitaxial films deposited by metalorganic chemical vapor deposition. *Thin Solid Films* **2004,** *449* (1-2), 12-19.

36. Cheun, H., Fuentes-Hernandez, C., Zhou, Y., Potscavage, W. J. Jr., Kim, S.-J., Shim, J., Dindar, A. and Kippelen, B., Electrical and Optical Properties of ZnO Processed by Atomic Layer Deposition in Inverted Polymer Solar Cells. *J. Phys. Chem. Commun.* **2010,** *114* (48), 20713–20718.

37. Wang, J.-C., Weng, W.-T., Tsai, M.-Y., Lee, M.-K., Horng, S.-F., Perng, T.-P., Kei, C.-C., Yu, C.-C. and Meng, H.-F., Highly efficient flexible inverted organic solar cells using atomic layer deposited ZnO as electron selective layer. *J. Mater. Chem.* **2010,** *20* (5), 862-866.

38. Marichy, C., Bechelany, M. and Pinna, N., Atomic Layer Deposition of Nanostructured Materials for Energy and Environmental Applications. *Advanced Materials* **2012,** *24* (8), 1017-1032.

39. Van de Walle, C. G., Hydrogen as a Cause of Doping in Zinc Oxide. *Phys. Rev. Lett.* **2000,** *85* (5-31), 1012.

40. Zhou, Z., Kato, K., Komaki, T., Yoshino, M., Morinaga, M. and Morita, K., Effects of dopants and hydrogen on the electrical conductivity of ZnO. *J. Eur. Ceram. Soc.* **2004,** *24* (1), 139-146.

Chapter 5: The Growth of Nanolaminate Doped ZnO binaries by ALD

Abstract

In this chapter, the growth of thin ZnO films doped with aluminium (AZO), gallium (GZO), tin (SZO) and titanium (TZO) by both thermal and PE-ALD is described. As previously mentioned in chapter 4, the best performing undoped ZnO film did not compete with the electrical properties of commercial ITO. As a result, doping of ZnO with the intention of improving the electrical properties has been investigated.

It was found that neither the thermal nor PE-ALD doped films could compare in terms of the Hall mobilities obtained for as-grown ZnO (10.5 and 1.5 $cm^2/V.s$ for thermal and PE-ALD ZnO respectively). However, for both the thermal and PE-ALD doped films, the carrier concentration values were higher than those obtained for as-grown ZnO. The best Hall mobility at 6.77 $cm^2/V.s$ was achieved for thermal TZO (19:1). The doped films had lower values of sheet resistance than that of as-grown ZnO (6.1 kΩ/□ and 240 MΩ/□ for thermal and PE-ALD ZnO respectively). These results show how the incorporation of dopants can influence the electrical properties of ALD-grown ZnO. XRD results displayed varying degrees of crystallinity for the doped-ZnO films. From studies of the growth per cycle (GPC) of the various processes it is suggested that the dopant may cause inhibited nucleation of ZnO due to the dopant blocking sites and hindering DEZ absorption[1, 2]. SEM results showed similarities between as-grown thermal ALD ZnO and thermal ALD AZO, SZO and TZO on both glass and Si (100) substrates. On glass substrates, PE-ALD AZO, GZO, SZO and TZO all mirror what

is observed with as-grown PE-ALD ZnO. PE-ALD AZO also shows similar surface features on Si (100) substrates. The reduction in the growth rates observed were confirmed via TEM imaging which revealed the presence of layers that were thinner than expected.

5.1 Introduction

The introduction of dopants into a host material allows for the manipulation of the composition and structure that can impact both electrical and optical properties of the material. ZnO is frequently doped and to date, some 22 elements have been reported as dopants in ZnO by ALD where Al is the most popular choice[3]. ALD is particularly advantageous for controlled doping due to the cyclic, self-limiting manner which allows for precise thickness control that can theoretically allow for accurate control over the dopant level[4, 5]. Despite the advantages of doping thin films via the method of ALD, drawbacks exist and ALD doping presents its limitations- the most obvious of which is the fact that the dopant atoms are not uniformly distributed throughout the material as might be required under 'ideal' conditions. One of the principal reasons for doping a material in the first place is to enhance a particular property of said material. However, this is not always a straightforward process. For ALD-grown materials there are many reports which present the etching effect dopants can have, leading to a reduction of the overall growth rate of the film and a reduction in the efficiency of the doping process[6,7]. As well as decreased growth rates for doped ALD films, increased growth rates have also been reported. This has been observed for Ti- doping of ZnO with the titanium precursor titanium(IV) isopropoxide (TTIP) where adsorption of TTIP appears to increase the overall ZnO growth rate[8].

ZnO is doped by ALD for the fabrication of transparent conducting oxides (TCOs) in which the overall aim is to improve the resistivity of the material without losing transparency. TCOs are electrically conductive materials, usually designed so as to minimize the absorption of light in the visible region. The most widely used TCO material is indium tin oxide (ITO) however its use is limited by the commercial difficulties associated with the acquisition of indium. ZnO is an extremely promising material for application in TCOs owing to its wide band gap and its earth abundance. Hence, it offers a cost effective alternative to ITO. The wide band gap of ZnO causes the creation of excess charge carriers when doped[9, 10]. In many applications, one of the key requirements for TCOs is a film resistivity on the order of 1 mΩ cm or lower[11]. This can be achieved by cation doping ZnO with group III, IV and V elements.

Here, doped ZnO films were deposited via thermal and PE-ALD with the intention of improving the electrical properties of the material as compared to undoped ZnO. ZnO thin films were doped with Al, Ga, Sn and Ti dopants.

5.2 Experimental

5.2.1 Preparation of doped ZnO films

Doped ZnO films were deposited using both thermal and plasma ALD processes on a 200 mm Picosun™ R200 ALD reactor. ZnO thin films were doped with Al (AZO), Ga (GZO), Sn (SZO) and Ti (TZO). The supercycle method was followed as shown in figure 5.1 below in which X = Al, Ga, In, Ti and Sn. Dopant ratios of 9:1 and 19:1 were used. Films were deposited at 150 °C.

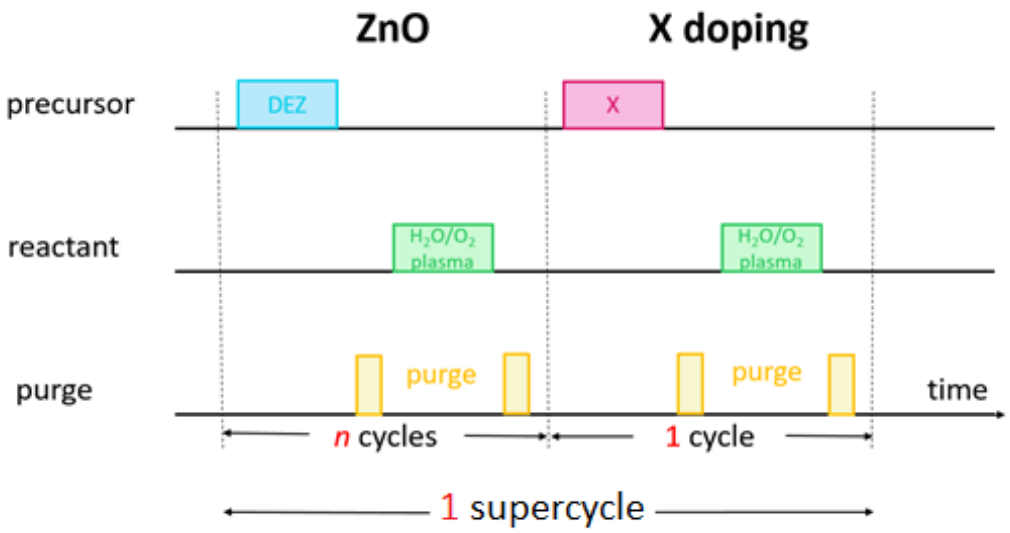

Figure 5.1: The supercycle method schematic for doped ZnO thin films in which X = Al, Ga, In, Ti and Sn

A typical supercycle recipe used for the growth of ZnO: Al with a 19:1 dopant ratio was as follows: firstly the zinc precursor; DEZ, was introduced to the chamber for a pulse time of 0.05 s followed by a 6 s purge. Next, a 28.0 s pulse of O_2 plasma was introduced (0.1 s pulse of H_2O for thermal ALD process). These two steps were then repeated a further 18 times giving a total of 19 ZnO growth cycles. The dopant was then introduced into the chamber. In the case of

aluminium dopant, a 0.01 s pulse of TMA was employed followed by a 28.0 s pulse of O_2 plasma. The pulse times for trimethylgallium (TMG), tetrakis(dimethylamino)tin(IV) (TDMASn) and tetrakis(dimethylamino)titanium(IV) (TDMAT) were 0.03 s, 1.6 s and 1.8 s respectively. This supercycle was repeated until the desired number of cycles was completed. Similar recipes were employed for 9:1 dopant ratio films. A further 10 nm of ZnO was deposited after the above recipe in order to ensure that the growth did not cease on a dopant layer.

5.2.2 Film Characterisation

The surface morphology of the films was observed via SEM using a FEI Quanta 650 FEG high-resolution scanning electron microscope. Scanning transmission electron microscopy (STEM) analysis was carried out using a Thermo-Fisher Scientific double tilt STEM holder in the Thermo-Fisher Scientific FEI double aberration-corrected monochromated Titan Themis Z. The microscope was operated at 300 kV. The imaging mode used was STEM at 146 mm camera length with a 50-µm C2 aperture. EDS mapping was done using a Bruker Super X detector. All Titan STEM and EDS data processing was done using Thermo-Fisher Scientific Velox Software. The crystallinity of the ZnO films was analysed by X-ray diffraction (XRD) using a PANalytical X'Pert Pro Diffractometer, with Cu Kα (λ = 0.154 nm) radiation from 10 to 70° at a step size of 0.02° under 45 kV and 30 mA. The XRD results were compared to the Joint Committee on the Powder Diffraction Standard Card (JPCDS: 36-1451). Optical measurements (UV-Vis) were obtained in the range of 200 – 800 nm using a Perkin Elmer Lambda 950 UV/VIS/NIR Spectrometer. AC and DC field Hall Measurements were performed using a Lake Shore 8400 Series system.

5.3 Results and discussion

5.3.1 The morphologies, growth rate and structural properties of doped ZnO films

Plan-view SEM images were obtained for thermal and PE-ALD doped ZnO thin films. Figures 5.2-5.5 compare plan-view images for thermal and PE-ALD AZO, GZO, SZO and TZO (19:1) films deposited at 150 °C on both glass and Si (100) substrates. Figure 5.6 shows plan-view SEM images of as-grown thermal and PE-ALD ZnO on glass and Si (100) substrates.

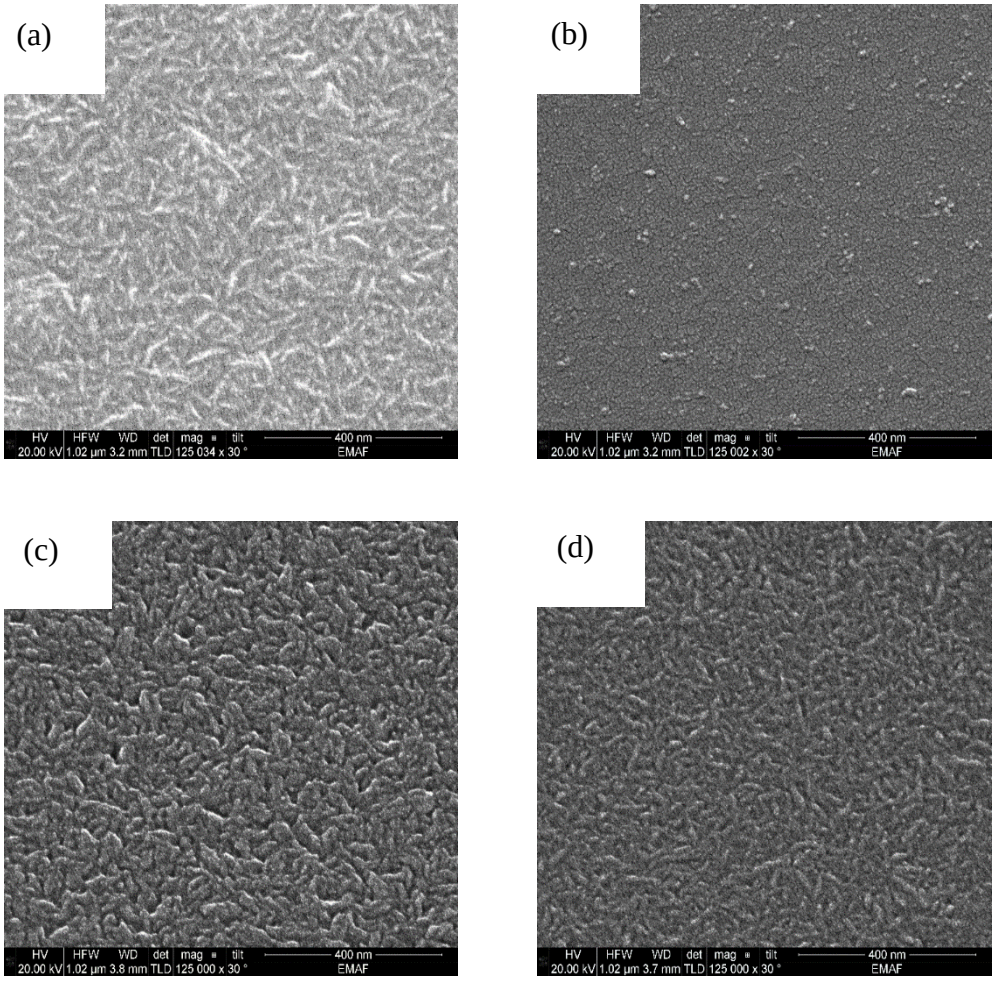

Figure 5.2: Plan-view SEM images of thermal ALD (a) AZO, (b) GZO, (c) SZO and (d) TZO (19:1) films deposited at 150 °C on glass substrates, Au-coated

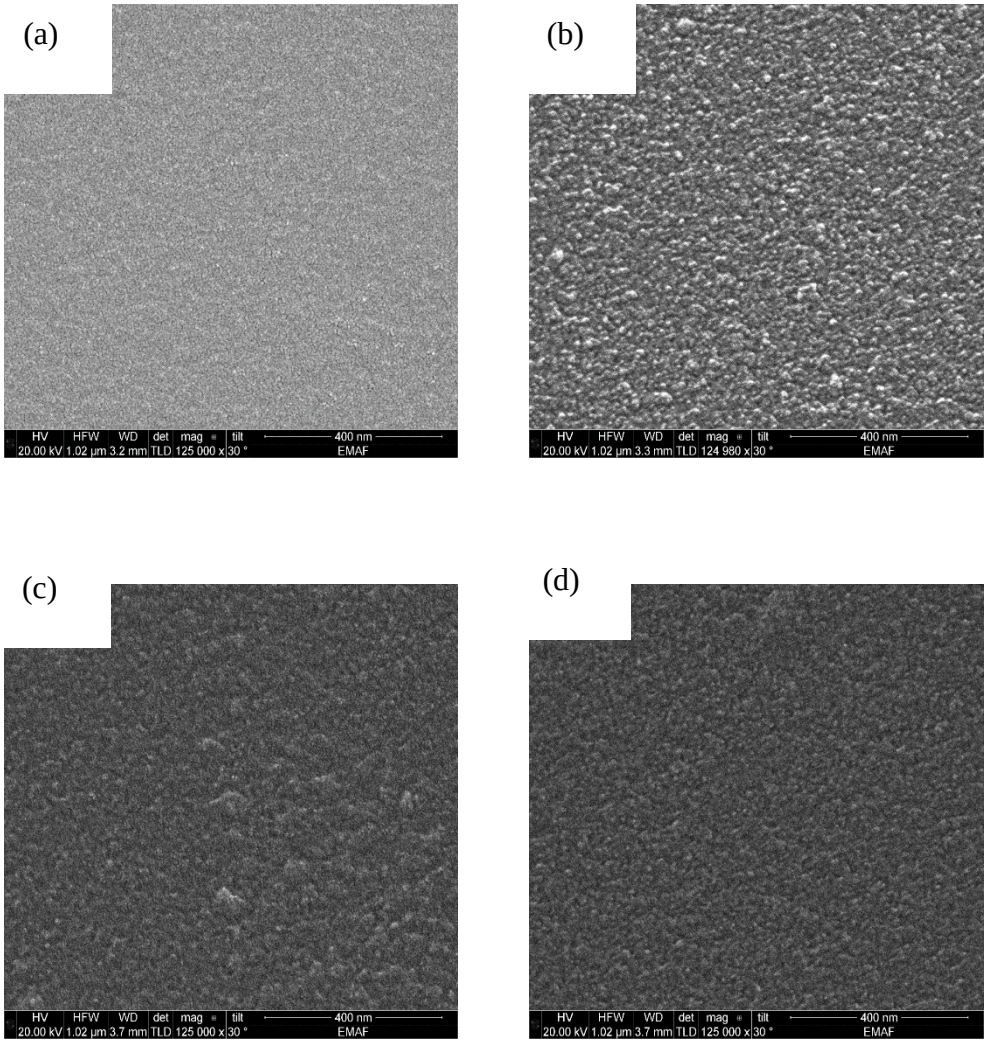

Figure 5.3: Plan-view SEM images of PE-ALD (a) AZO, (b) GZO, (c) SZO and (d) TZO (19:1) films deposited at 150 °C on glass substrates, Au-coated

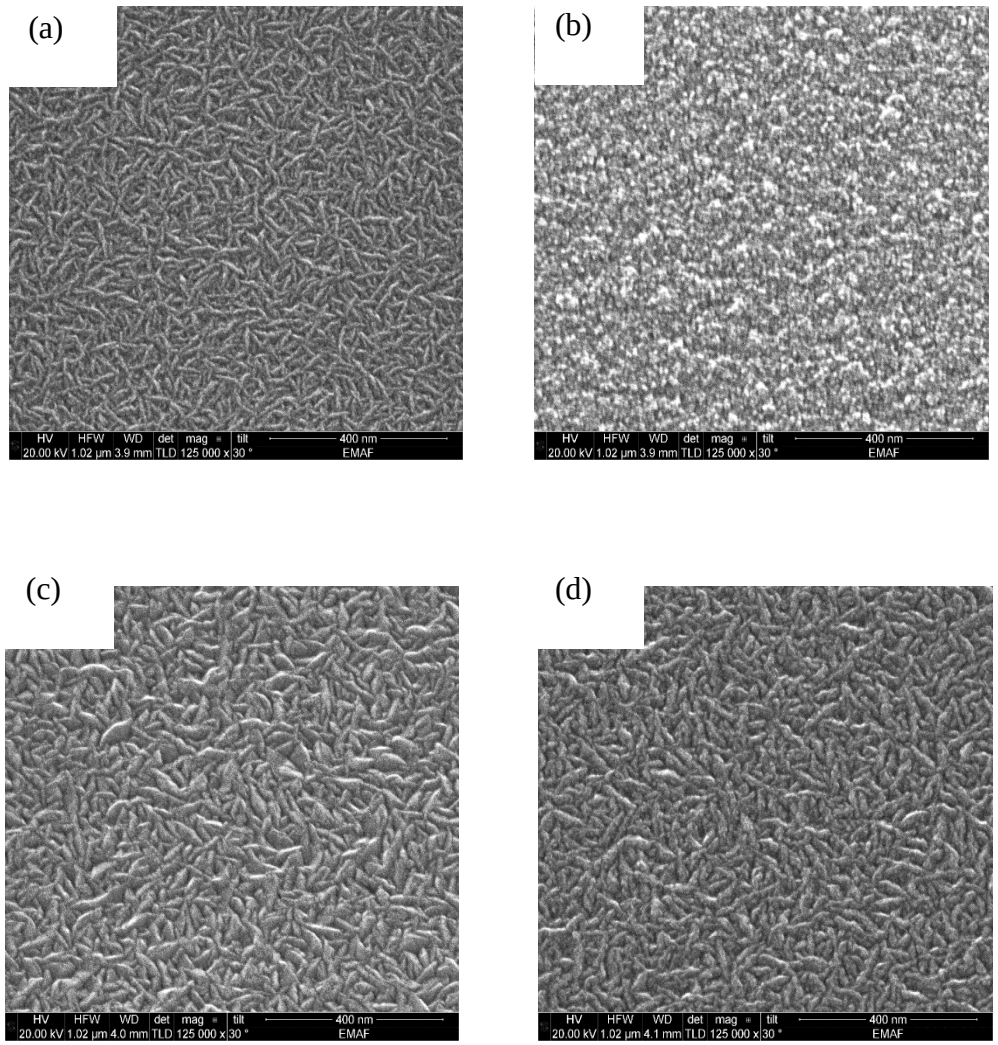

Figure 5.4: Plan-view SEM images of thermal ALD (a) AZO, (b) GZO, (c) SZO and (d) TZO (19:1) films deposited at 150 °C on Si (100) substrates, Au-coated

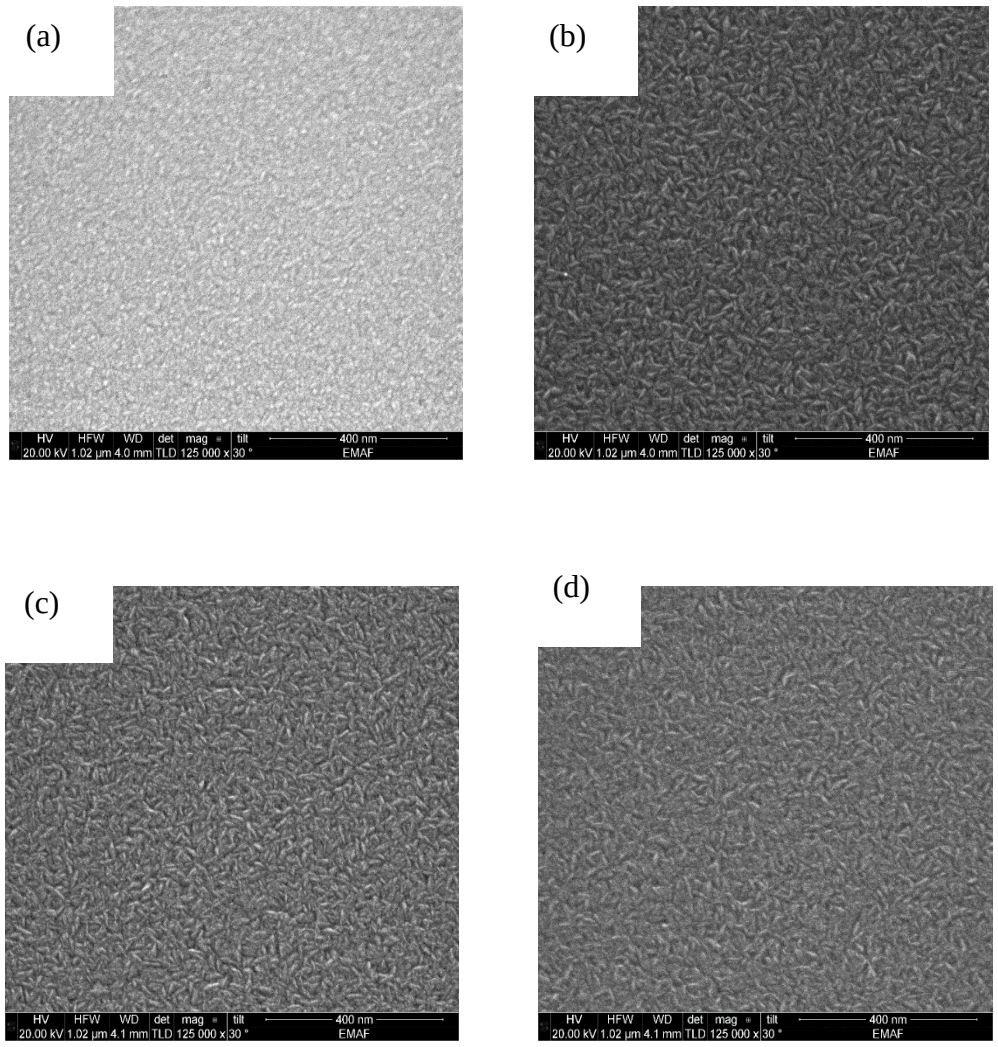

Figure 5.5: Plan-view SEM images of PE-ALD (a) AZO, (b) GZO, (c) SZO and (d) TZO (19:1) films deposited at 150 °C Si (100) substrates, Au-coated

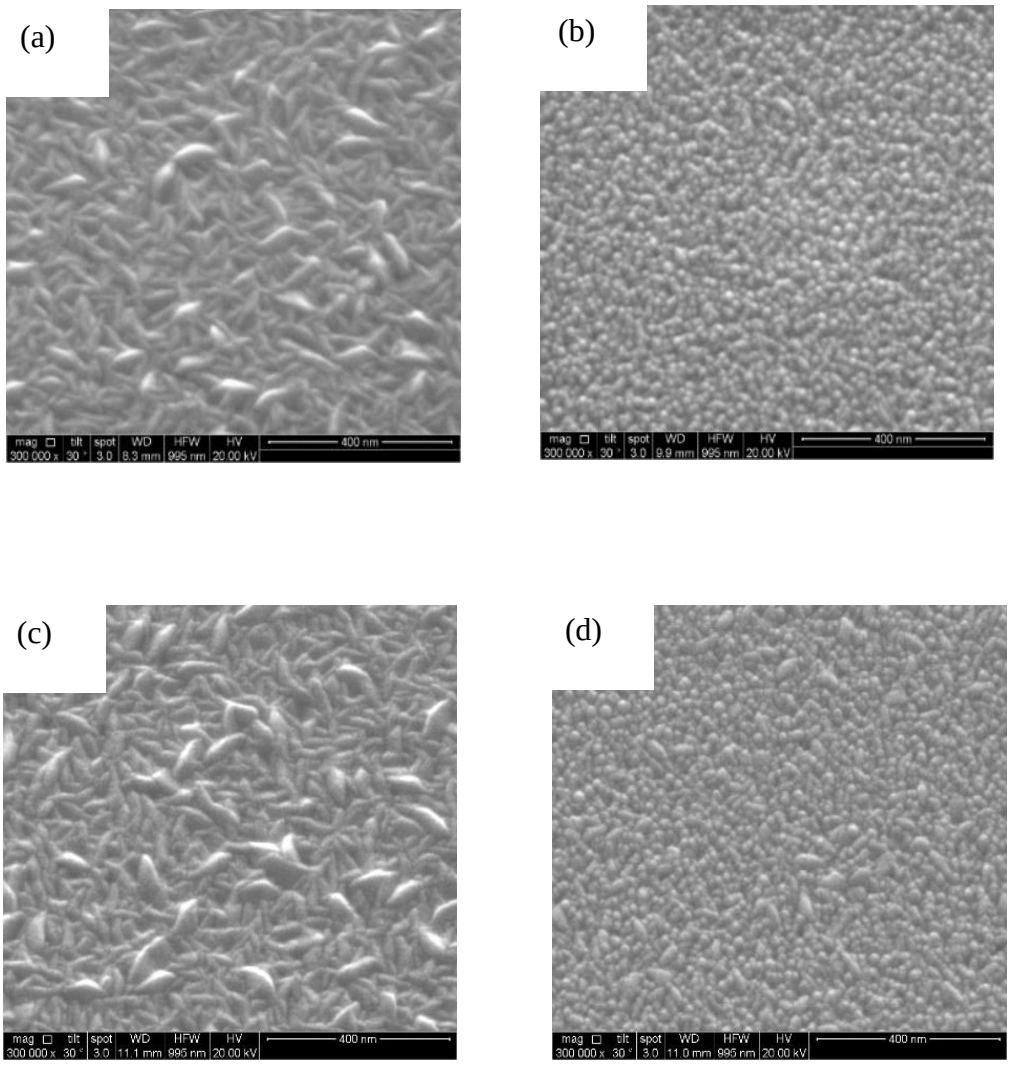

Figure 5.6: Plan-view SEM images of as-grown ZnO on Si (100) substrates by (a) thermal ALD and (b) PE-ALD, and on glass substrates, Au-coated by (c) thermal ALD and (d) PE-ALD deposited at 150 °C

Similar to as-grown thermal ALD ZnO, thermal ALD AZO, SZO and TZO layers show grains on the surface of the films on both glass and Si (100) substrates. AZO appears to have the thinnest columnar surface features of the three. GZO differs from the above as no columnar grains are presents but rather smaller, more random surface particles are apparent. For PE-ALD films on glass substrates, AZO, GZO, SZO and TZO all reflect what is observed with as-grown PE-ALD ZnO, namely small densely packed surface features. PE-ALD AZO also shows similar surface features on Si (100) substrate. However, GZO, SZO and TZO differ, displaying columnar surface features.

It is well known that a correlation between microstructure and electrical properties of thin films exists[12]. Polycrystalline films tend to possess a lower sheet resistivity. Larger grain sizes on the surface of a film may cause promotion of electron movement due to overlapping of the individual grains. A densely packed film can also lead to an increase in the electron mobility. On the contrary, grain boundaries that form around large surface grains can result in an increase in sheet resistivity as a consequence of charge trapping[13]. Table 5.1 displays the approximate grain sizes for all films obtained via the intercept method[14]. Following this, Scherrer calculations (section 3.3) were employed to determine the crystallite size for comparison purposes.

Due to the fact that XRD analysis for many films revealed a lack of crystallinity, the calculation of crystallite size via the Scherrer equation was not possible for all samples. Therefore, the comparison of crystallite size via both methods was impractical. For all films, the grain sizes obtained by the Scherrer method were consistently smaller than those obtained by the intercept method. For the latter, measurements correspond to the random but forced fixed placement of a line. Observer interpretation and variations in patterns must be considered. Another point to consider is that rod-like grains with random placement do not allow for accurate measurement via the intercept method.

Thin film		ALD Process	Intercept method crystallite size (nm)	Scherrer method crystallite size (nm)
AZO	Si	thermal	23.78	2.70
		plasma	11.93	-
	glass	thermal	28.71	-
		plasma	10.53	0.18
GZO	Si	thermal	17.62	2.78
		plasma	19.01	-
	glass	thermal	17.21	-
		plasma	19.79	-
SZO	Si	thermal	19.53	2.76
		plasma	21.10	2.66
	glass	thermal	30.48	-
		plasma	19.40	-
TZO	Si	thermal	30.08	4.09
		plasma	36.06	2.68
	glass	thermal	33.24	-
		plasma	18.05	-

Table 5.1: Comparison of crystallite size as determined by both the Scherrer equation and the intercept method for both thermal and PE-ALD 19:1 AZO, GZO, SZO and TZO on Si (100) and glass substrates

TEM imaging, figures 5.7-5.8, 5.10-5.15, does not show any evidence of true nanolaminate formation for the AZO, GZO, SZO and TZO samples. This may result from intermixing between the layers. However, the dopant layer thickness would be very small compared to the overall thickness of the films making it difficult to view. Typically, the mass differences of the component elements causes the visible contrast in the imaging mode. Although this difference in contrast is seen in the TEM images, it does not reveal the existence of laminate layers as might be expected from the film deposition recipe.

From the TEM images, more information about the morphology was obtained and the presence of ZnO columnar grains in the bulk was identified. The interface plays an important role in the properties of a thin film[15]. Discernible lattice planes suggest that all films are crystalline.

Defects or imperfections present at the interface may cause electronic trapping or even formation of undesirable phases which would invoke degradation and deterioration of any device made from this material[16]. For example, in ferroelectric field transistors where the electronic properties of oxide–oxide interfaces are utilised[17]. In addition optical guided wave device structures have been fabricated in which the oxide-oxide interface is very important[18].

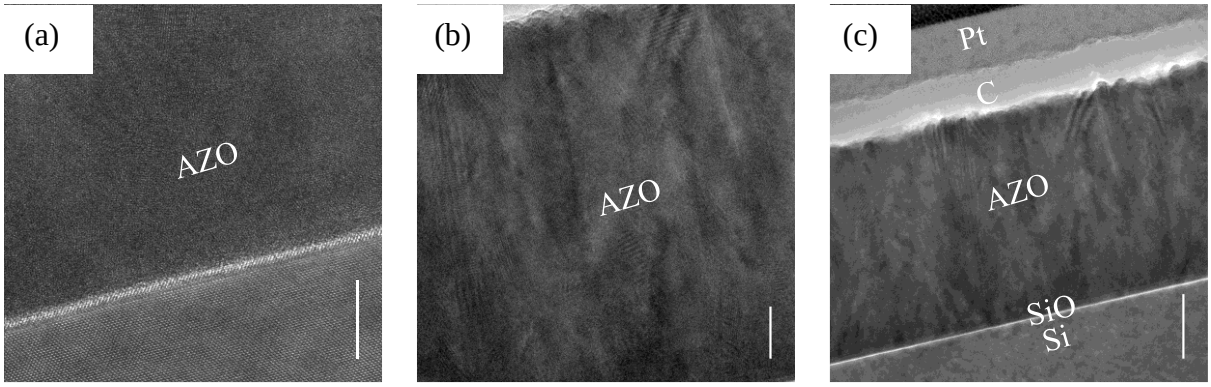

Figure 5.7: TEM image of thermal AZO at scale of (a) 10 nm (b) 20 nm and (c) 50 nm on Si (100) substrates

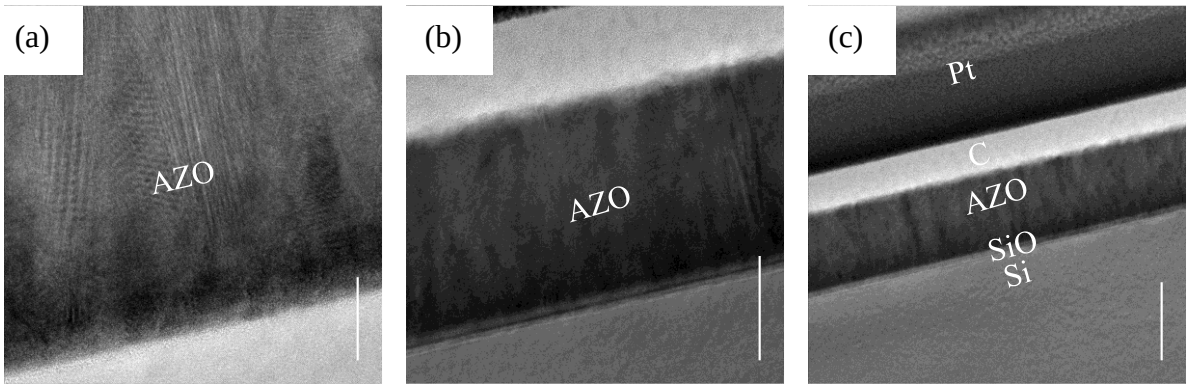

Figure 5.8: TEM image of PE-ALD AZO at scale of (a) 20 nm (b) 50 nm and (c) 100 nm on Si (100) substrates

Thermal AZO films appear to be polycrystalline in nature as evidenced by the presence of oriented planes. For PE-ALD AZO, figure 5.8 (a), the planes seem to be mainly be oriented in one direction. As will be presented in section 5.3.1, the XRD pattern for this film shows (100) orientation. The measured thickness of the films were less than the theoretical values. As mentioned in section 1.5.3, etching of ZnO is commonly reported with the DEZ, TMA and

H_2O ALD reaction. The etching of surface Zn-alkyls may therefore account for the reduced thickness.

Fast Fourier transform (FFT) images recorded from the TEM images for PE-ALD AZO displayed in figure 5.9 showed the periodic structured pattern which confirmed the formation of ZnO in hexagonal wurtzite structure.

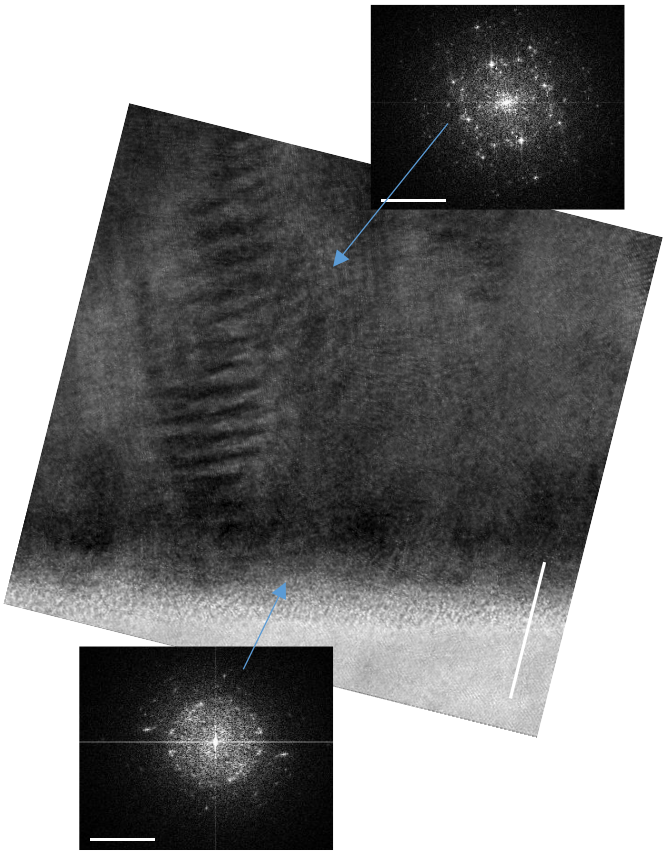

Figure 5.9: TEM image and FFT images of PE-ALD AZO confirming the presence of ZnO in hexagonal wurtzite structure on a Si (100) substrate

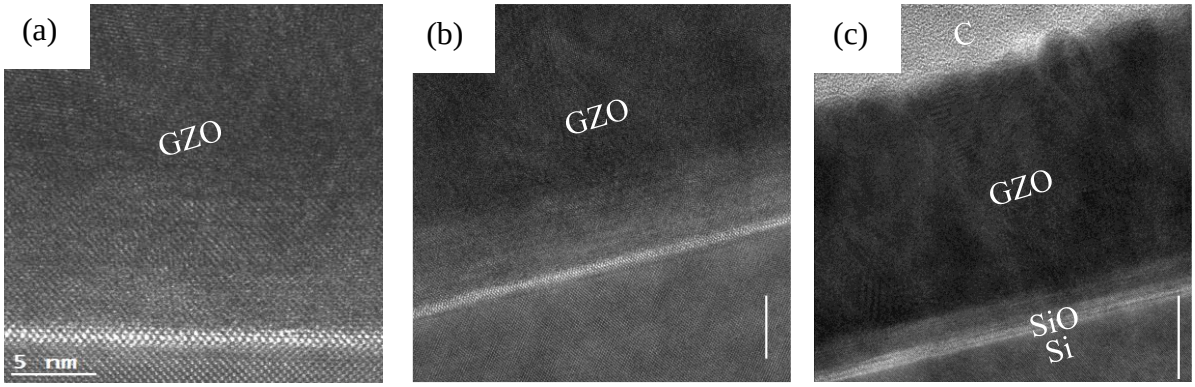

Figure 5.10: TEM images of thermal ALD GZO at scales of (a) 5 nm (b) 10 nm and (c) 20 nm on Si (100) substrates

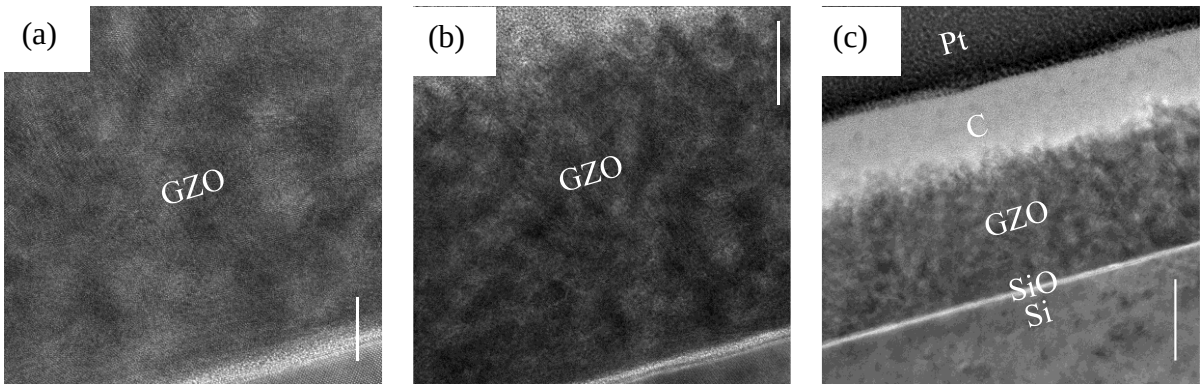

Figure 5.11: TEM images of PE-ALD GZO at scales of (a) 10 nm (b) 20 nm and (c) 50 nm on Si (100) substrates

For thermal GZO, based on previous studies by Comstock, the thermal TMGa and H_2O ALD process does not occur which would suggest the film most likely consists of ZnO with residual TMGa precursor/ or products from this randomly scattered throughout the film. This is further discussed later in this section. Comparing the TEM of both the thermal and PE-ALD films, the images for the latter show no obvious signs of crystallinity. This is consistent with the XRD data for PE-ALD GZO, which reveals the films to be amorphous.

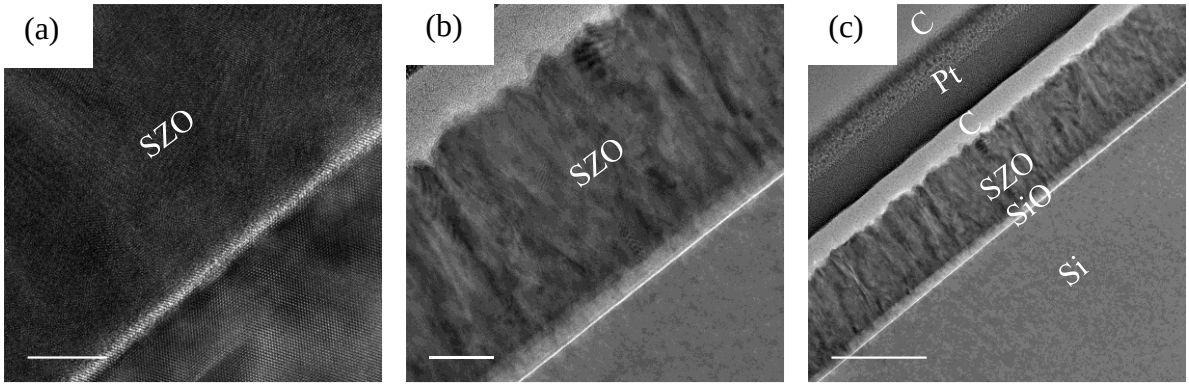

Figure 5.12: TEM images of thermal ALD SZO at scales of (a) 10 nm (b) 50 nm and (c) 200 nm on Si (100) substrates

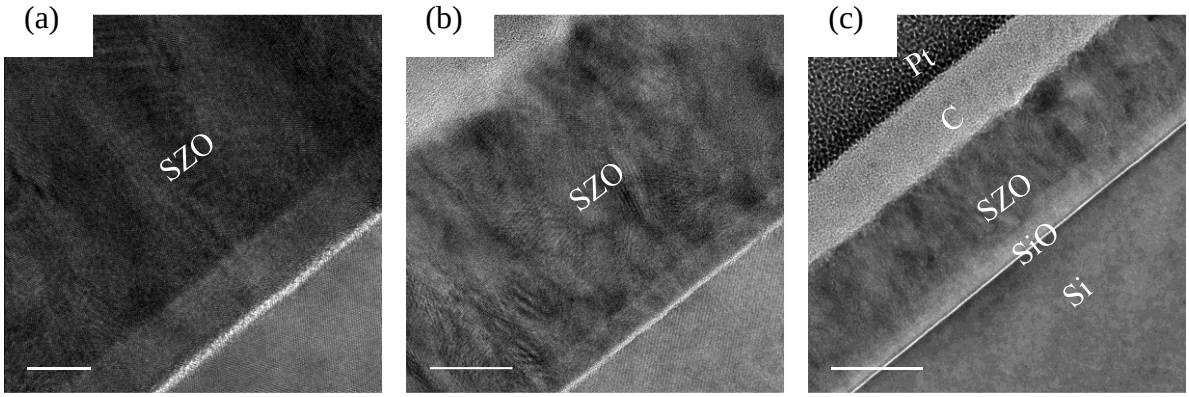

Figure 5.13: TEM images of PE-ALD SZO at scales of (a) 10 nm (b) 20 nm and (c) 50 nm on Si (100) substrates

Thermal SZO displayed columnar features in the bulk (figure 5.12). For both thermal and PE-ALD SZO, discernible lattice planes are present. The measured thickness for SZO was also less than the theoretically calculated value. Mullings et al. have explained how etching in SZO ALD could take place[19].

With these ideas in mind, it is suggested that the following may occur; cleavage of a C-N bond in an $N(CH_3)_2$ ligand of the Sn precursor, TDMASn followed by formation of DMZ and the associated C-Zn bonds. However, this is likely to be hindered by the fact that the C-N bond is stronger than a C-Zn bond, being some 82 kcal/mol[20] as measured in $HN(CH_3)_2$ versus ca. 64 kcal/mol[21]. A reduction in surface hydroxyl group density and/or the presence of less reactive surface hydroxyl groups is likely the cause of a reduced SZO growth rate[19].

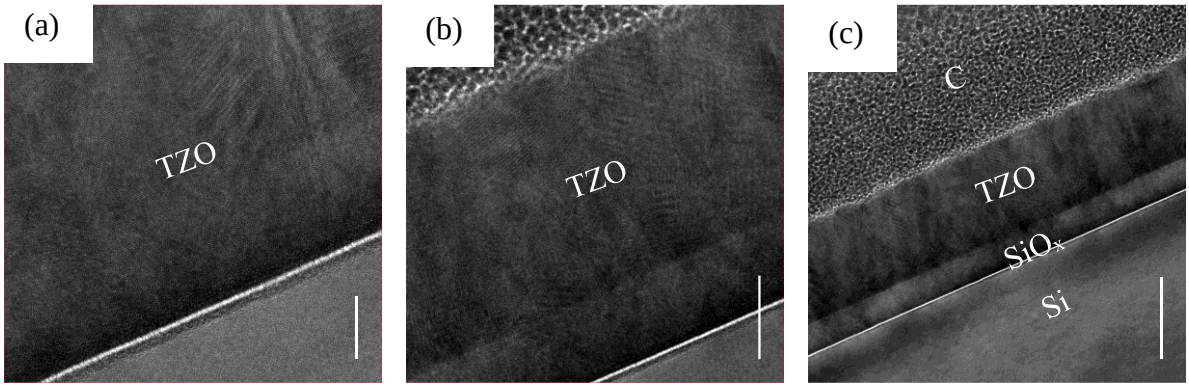

Figure 5.14: TEM images of thermal ALD TZO at scales of (a) 10 nm (b) 20 nm and (c) 50 nm on Si (100) substrates

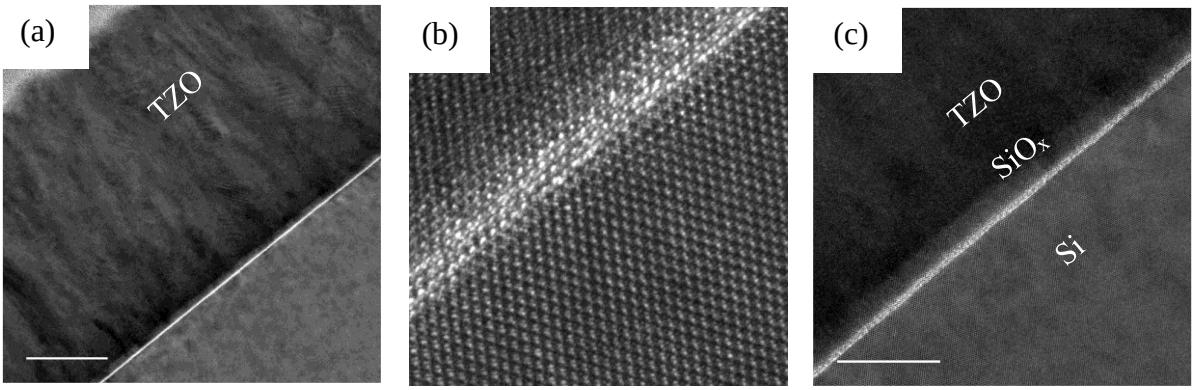

Figure 5.15: TEM images of PE-ALD TZO at scales of (a) 50 nm, (b) 5 nm and (c) 20 nm in which the film-substrate interface is highlighted on Si (100) substrates

For both thermal and PE-ALD SZO, Discernible lattice planes are observed in the TEM images, figures 5.14-5.15.

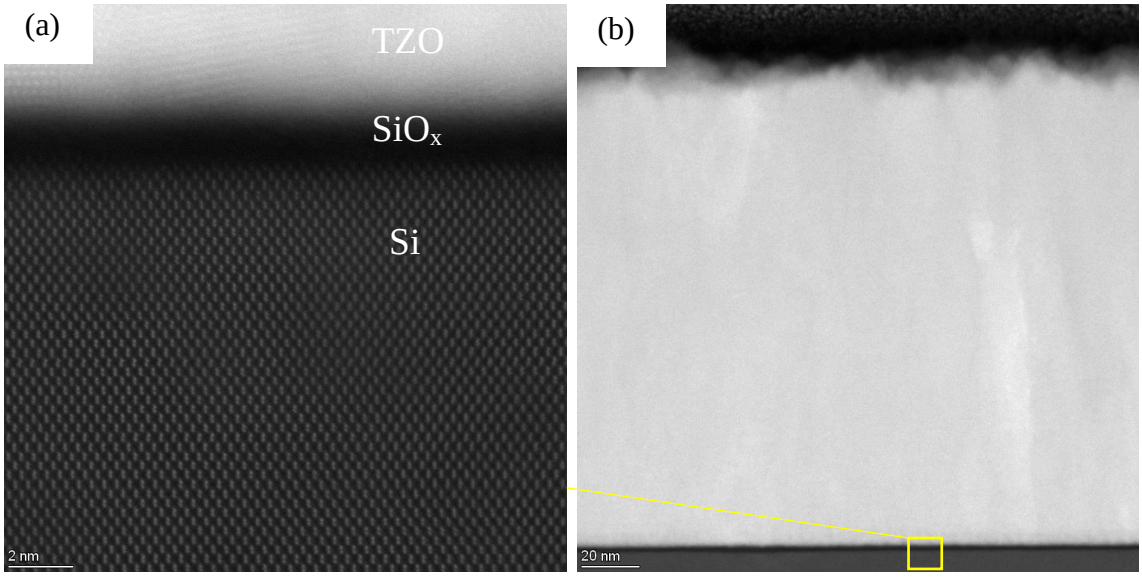

Figure 5.16: TEM images of PE-ALD TZO in which the film-substrate interface is highlighted at (a) 2 nm and (b) 20 nm on a Si (100) substrate

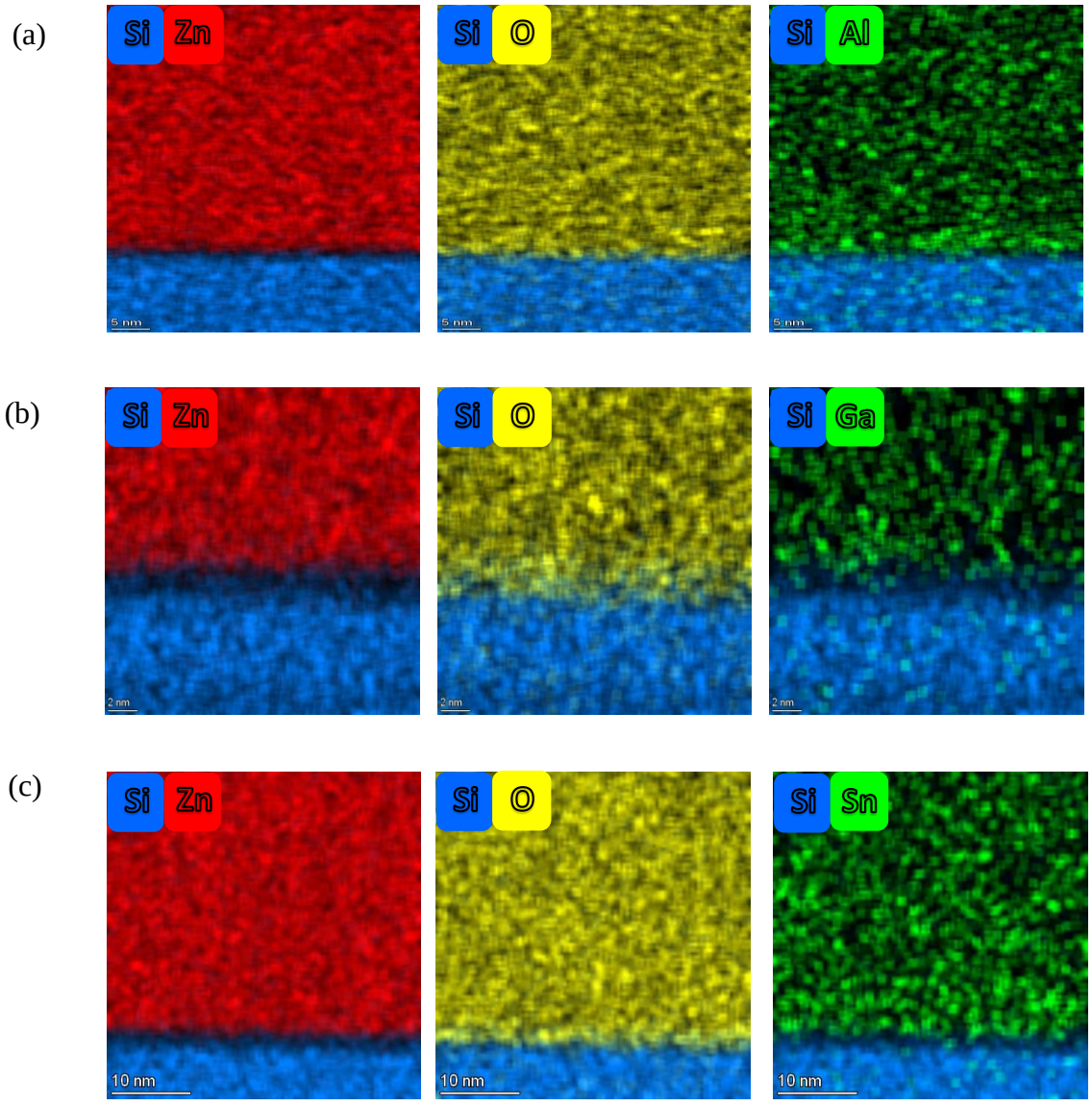

Figure 5.17: EDS elemental mapping of thermal ALD (a) AZO, (b) GZO and (c) SZO on Si (100) substrates

(a)

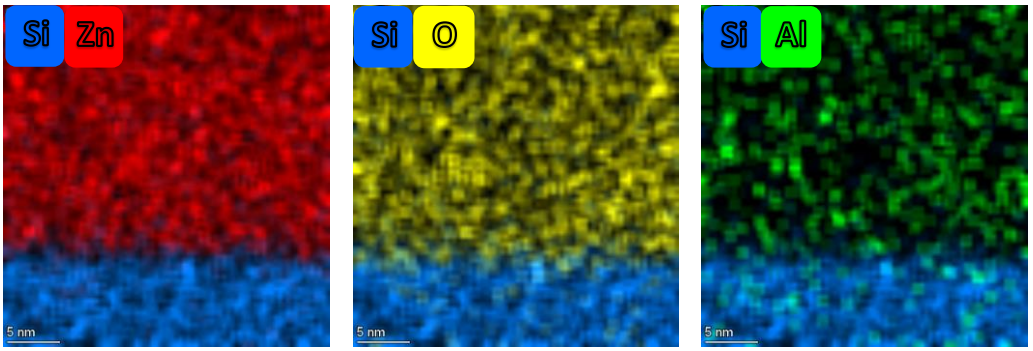

(b)

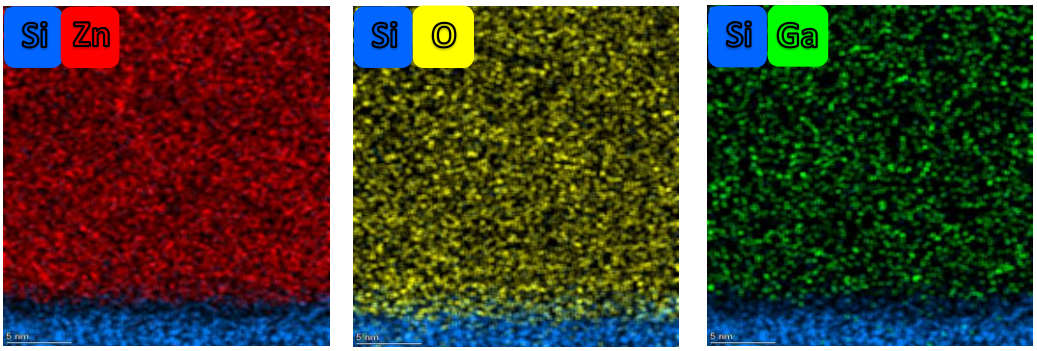

(c)

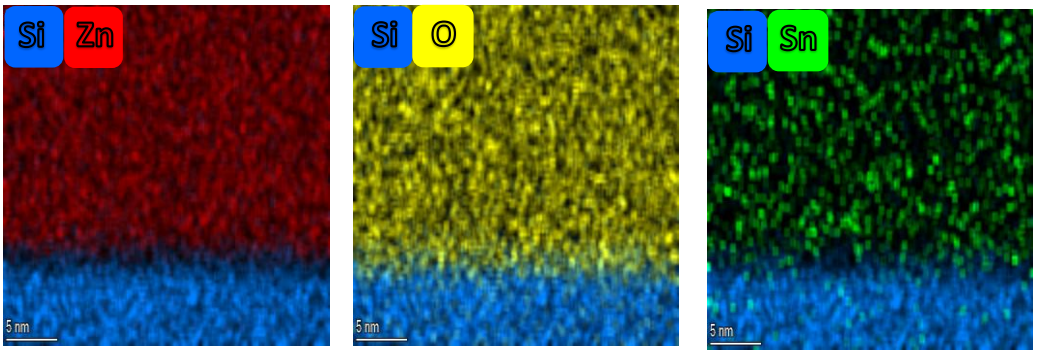

(d)

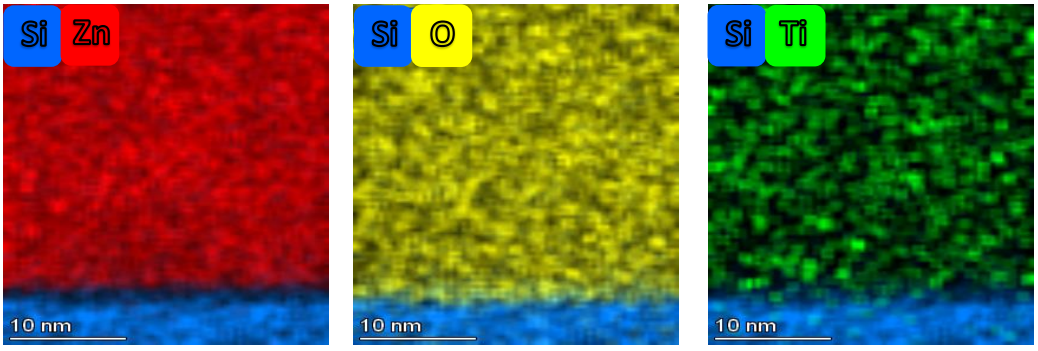

Figure 5.18: EDS elemental mapping of PE-ALD (a) AZO, (b) GZO, (c) SZO and (d) TZO on Si (100) substrates

Energy dispersive X-ray spectrometry (EDS) elemental mapping images (figures 5.17 and 5.18), indicate the incorporation of dopants into the ZnO films. The EDS mapping results of the dopants show lower densities in comparison with the mapping of Zn and O as a consequence of the lower concentrations in the samples.

The deposition of binary films utilises the supercycle method. In theory, the film composition and growth rate should follow that described by the rule of mixtures (ROM) in which a linear change in growth rate with film composition is expected[6, 22, 23] (equation 5.1).

$$Thickness = \frac{Total\ number\ of\ cycles}{[(CR_1 gpc_1 + CR_2 gpc_2)]} \qquad (5.1)$$

In which;

CR_x (>1) is the cycle ratio relevant to the particular metal oxide and gpc_x is the growth per cycle of each metal oxide. The growth rates per cycle used for each calculation are based off literature values for the deposition of each binary metal oxide. For thermal ALD, the GPC values used for Al_2O_3, SnO_2, TiO_2 and ZnO were 1[24], 0.6[25], 0.5[26, 27] and 2.0[28-30] Å/cycle respectively. For PE-ALD they are 1.2[31], 0.66[32], 1.7[33], 0.5[34] and 2.2[35] Å/cycle for Al_2O_3, Ga_2O_3, SnO_2, TiO_2 and ZnO respectively.

The thickness predicted by both the ROM and that measured by TEM of doped ZnO are presented in table 5.2.

Film	Thermal/Plasma	ROM thickness (nm)	Measured thickness (nm)
AZO	thermal	175.5	155-158
	plasma	193.5	94-96
GZO	thermal	-	63-68
	plasma	191.1	78-88
SZO	thermal	173.7	170-172
	plasma	195.8	65-68
TZO	thermal	173.3	75-77
	plasma	190.4	167-174

Table 5.2: Estimated and measured thickness for thermal and PE-ALD 19:1 AZO, GZO, SZO and TZO on Si (100) substrates

Comparing the ROM values to the experimentally-determined values, all films deviated from the expected values albeit to different degrees. It is possible that the inhibition of ZnO growth on the dopant layers may have occurred. This has previously been reported by Kessels et al. in which Al_2O_3 ALD cycles interrupted the growth of the ZnO grains[36]. This has also been reported by Elam et al. for AZO[6] and by Lee et al. for IZO[7]. In both of these cases the actual growth rate per cycle was lower than expected. In contrast an increase in growth rate per cycle has also been reported

in which adsorption of TTIP molecules caused a deviation in expected growth rate of TiO_2[8]. Nucleation effects can occur due to the differing surface reaction sites possessed by different metal oxides. In the case of AZO, it has been reported that it takes 4-6 ALD cycles of ZnO for the growth rate to return to full potential when deposited on Al_2O_3 and 2-3 cycles for the growth rate of Al_2O_3 to return to its full value when deposited on ZnO[6]. This can be explained by the surface density of the hydroxyl species being lower for Al_2O_3 than ZnO. The crystallinity of a material also has an effect on the growth rate per cycle. ALD-deposited ZnO is typically crystalline whereas ALD deposited Al_2O_3 is amorphous. The surface density is effected by the difference in crystallinity as it influences the formation of microstructures during growth[22]. This also emphasises the necessity to use sheet resistance as opposed to resistivity when evaluating the electrical properties of these thin films Thickness variations are highly likely due to the different growth rates of different dopants. Using the sheet resistance also takes into account the possibility of nucleation delays between the nanolaminate layers. From table 5.2, it is clear that a large deviation in thickness was obtained for thermal TZO. For this particular sample it was suspected that the DEZn precursor ran out during deposition. This was highlighted further in the Hall Effect measurements as the film was too resistive to measure. As a consequence of these uncertainties the film was re-grown and all electrical measurements were taken from the new sample.

For AZO and GZO, the PE-ALD counterparts had a considerably lower overall thickness compared to the thermal ALD films. This may be explained by the high ion energy of the plasma causing etching of the thin films and precursor desorption[37]. Zhu et al. explained how the decreased GPC is likely a consequence of film densification[38].

The crystal structure and different structural parameters of the films were analysed from the XRD data obtained for the thermal and PE-ALD ZnO (as-grown), AZO, GZO, SZO and TZO thin films, deposited at 150 °C at both 9:1 and 19:1 dopant ratios. The XRD patterns of these films are shown in figures 5.19 – 5.23.

As previously discussed in section 4.3, the XRD pattern for thermal ALD ZnO exhibits well defined reflections at 2θ values of 31.8°, 34.4°, 36.2° and 56.6° corresponding to reflections having the Miller indices, (100), (002), (101) and (110) respectively. The presence of these multiple peaks suggest the polycrystalline nature of the film. The broad peak at 20° (2θ) is attributed to the glass substrate. Similarly, the broad peak at 70° (2θ) is characteristic of a Si (100) substrate. XRD patterns for PE-ALD ZnO show the characteristic peak at 2θ value of 34.4° (002) being present. A preference for c-axis orientation was identified as the XRD pattern is dominated by the (002) reflection. The (110) reflection was only present in the data obtained from the thermal ALD ZnO films.

The introduction of dopants caused a deterioration of the ZnO crystal structure. The deposition was clearly substrate dependent with Si (100) substrate films displaying weak crystallinity and glass substrate films being amorphous with the exception of the PE-ALD AZO (19:1) sample grown on a glass substrate. The intensity of the characteristic ZnO peaks decreased with doping due to loss of crystallinity and perhaps incorporation of defects into the lattice sites of ZnO. However, it must be noted that the XRD depth of analysis is only ca. 10 nm under the conditions employed.

A shift in the (100) XRD peak towards higher angle was observed with the introduction of Al. This can be attributed to the smaller ionic radius of Al^{3+} (0.053 nm) compared to that of Zn^{2+} (0.074 nm) as the lattice parameters of AZO are smaller than those of ZnO. This signifies

the incorporation of Al^{3+} due to doping[39]. Depending on what dopant is introduced, the crystallinity of doped-ZnO films differs accordingly[1, 2].

It has been reported that the (002) plane in ZnO films is suppressed once Al^{3+} is incorporated[40, 41]. Banerjee et al.[42] suggested that since the (100) plane is charge neutral due to it consisting of alternating rows of Zn^{2+} and O^{2-} ions, the Al^{3+} ions may cause a disturbance to the charge neutrality and cause the (100) surface energy to be the most favourable[43].

The deformation of the ZnO lattice is reported to be significantly lower in GZO than in AZO as the covalent bond lengths of Ga-O and Zn-O (1.92 Å and 1.97 Å, respectively) are very similar when compared to that of Al-O (2.7 Å). The Ga^{3+} dopant ions cause lattice disordering due to the ionic radius mismatch of Ga^{3+} (0.62 Å) and Zn^{2+} (0.74 Å)[44]. Hence, a shift in the XRD peaks towards a higher angle was observed with the introduction of Ga. This was seen for the thermal GZO (19:1) films where the upward shift of the (100) plane was slightly less than that observed for the thermal AZO (19:1) sample. The PE-ALD GZO (19:1) sample was completely amorphous in terms of the XRD data.

In the case of SZO, PE-ALD (on Si (100) substrates) films exhibited an a-axis orientation preference. The (100) component is observed, indicating that the a-axis of the wurtzite crystal is growing parallel to the substrate. Compared to as-grown ZnO, the XRD pattern for the SZO film was significantly broader and weaker. This result is consistent with previous reports of ALD as-grown SZO which showed that the films were largely amorphous as is also the case for SnO_x deposited by the TDMASn and H_2O ALD process[19, 45-49].

Finally, the XRD results for TZO showed that the films were largely amorphous on glass substrates. The PE-ALD TZO (9:1) sample showed preferential c-axis orientation with a peak at 34.1°. The presence of the (002) plane may be explained by the following; the surface energy is reduced when Ti ions are substituted at zinc sites of the wurtzite structure. The (002) plane

possesses a high atomic density and is therefore capable of producing the lowest surface energy when doped with Ti. This may then be the reason why growth proceeds with the preferred orientation along the c-axis[50, 51]. All other TZO films on Si (100) substrates displayed a weak (100) peak, while the peak associated with the (101) plane was also present for both the 9:1 and 19:1 PE-ALD TZO samples. A preferential a-axis orientation was found by Bergum et al[52]. The overall low crystallinity of TZO may be attributed to the presence of amorphous TiO_2 interlayers and thinner, crystalline ZnO layers which possess smaller crystal size[53]. It has been shown that increasing the Ti at% in TZO completely suppresses the appearance of peaks associated with the (100) and (101) planes[54]. Ti^{4+} ions have a smaller ionic radius of 0.68 Å when compared to the Zn^{2+} that has an ionic radius of 0.74 Å and therefore the Ti can substitute in place of the Zn ions in the ZnO lattice[54]. This can be seen by an upward shift of the peaks associated with the (100) plane to higher angles.

(a)

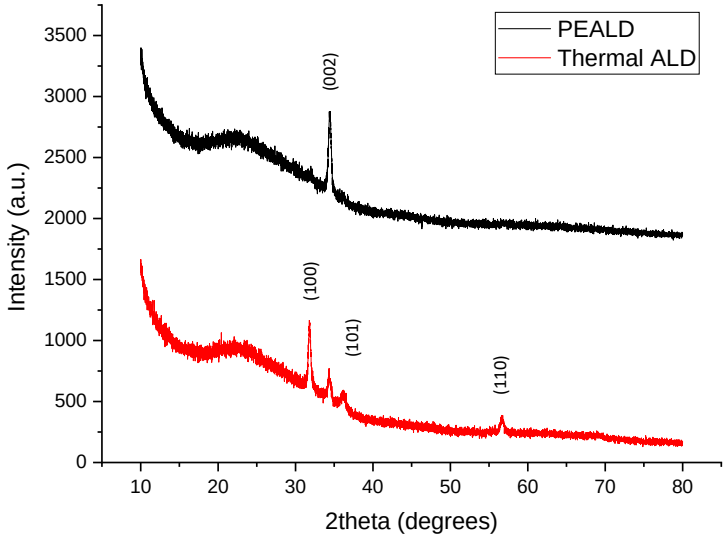

(b)

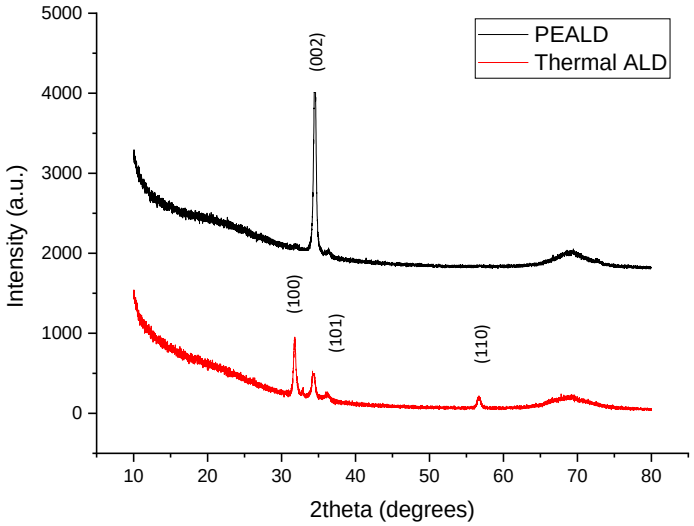

Figure 5.19: XRD patterns of as-grown ZnO films deposited at 150 °C on (a) glass substrates and (b) Si (100) substrates

(a)

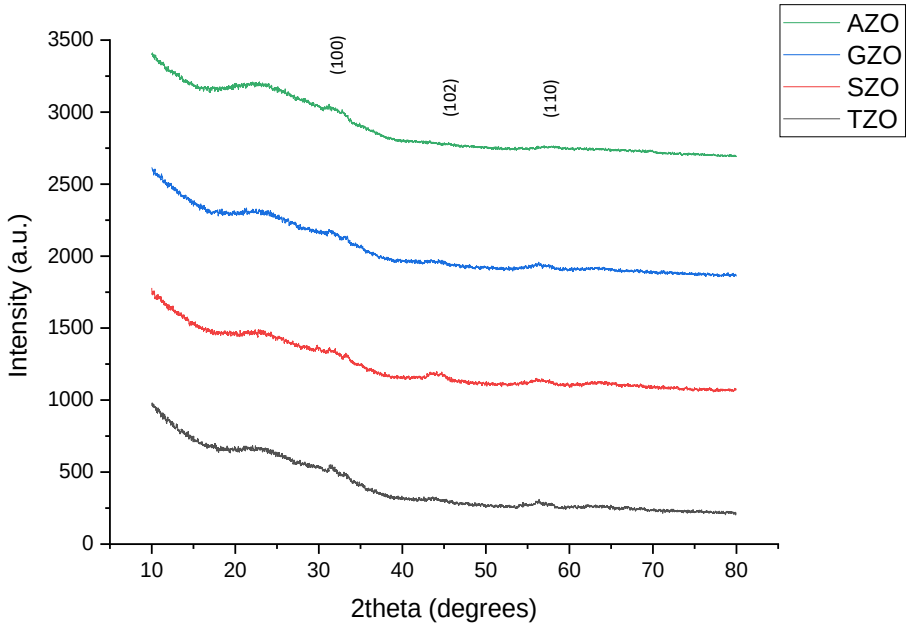

(b)

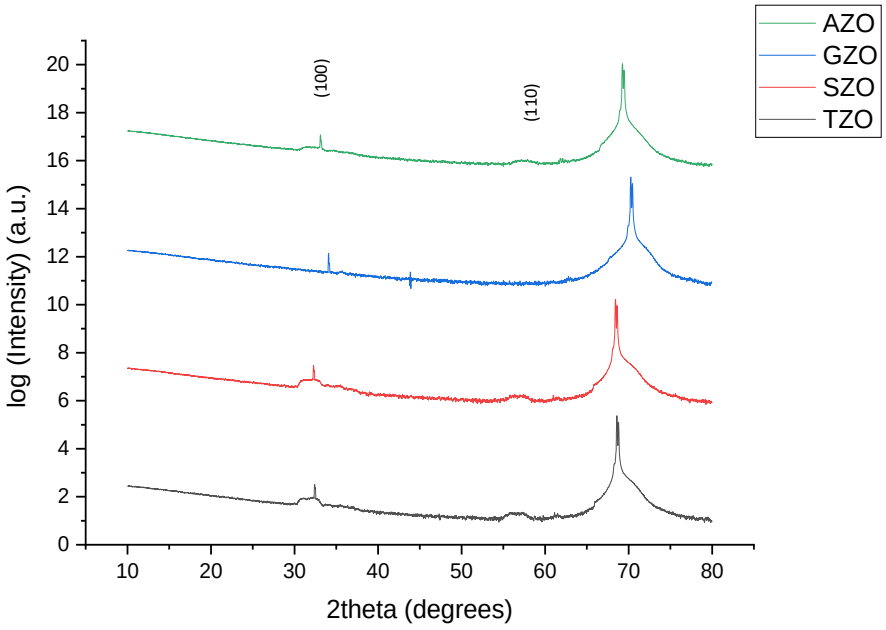

Figure 5.20: XRD patterns of thermal ALD AZO, GZO, SZO and TZO (9:1) films deposited at 150 °C on (a), glass substrates and (b) Si (100) substrates

(a)

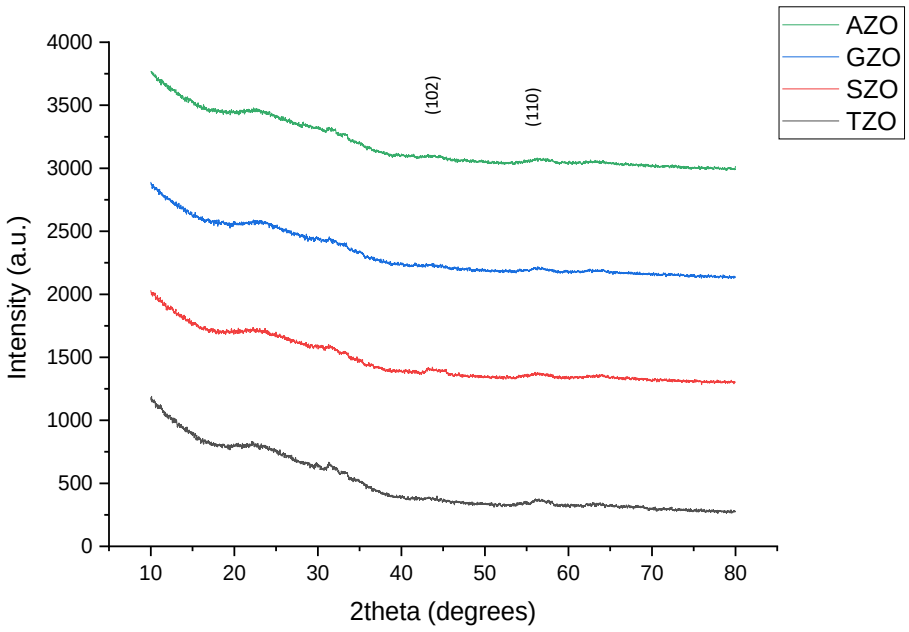

(b)

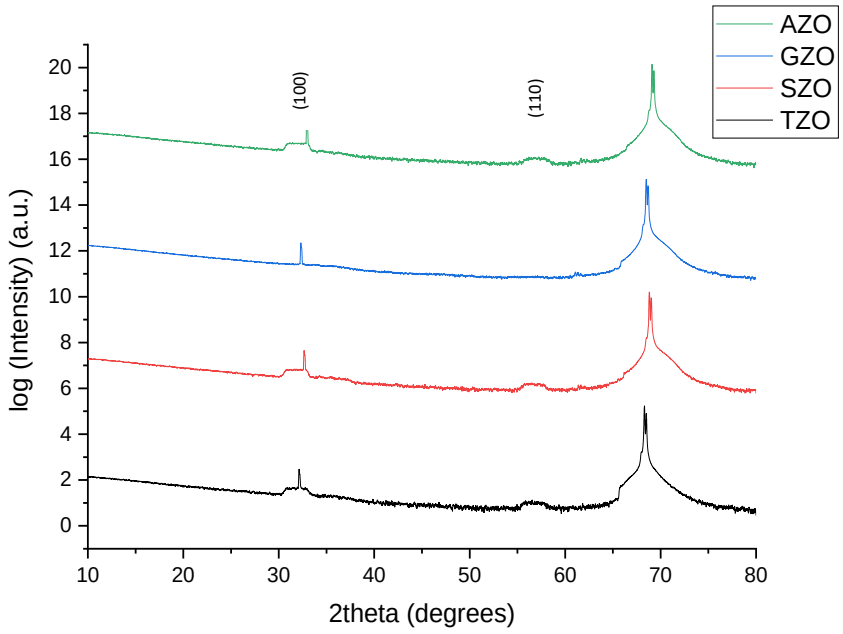

Figure 5.21: XRD patterns of thermal ALD AZO, GZO, SZO and TZO (19:1) films deposited at 150 °C on (a) glass substrates and (b) Si (100) substrates

(a)

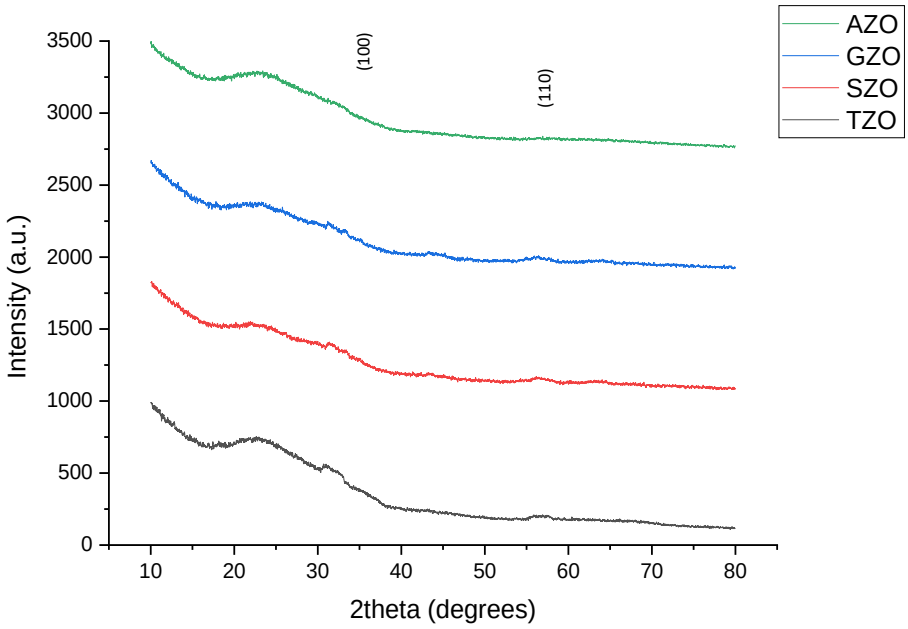

(b)

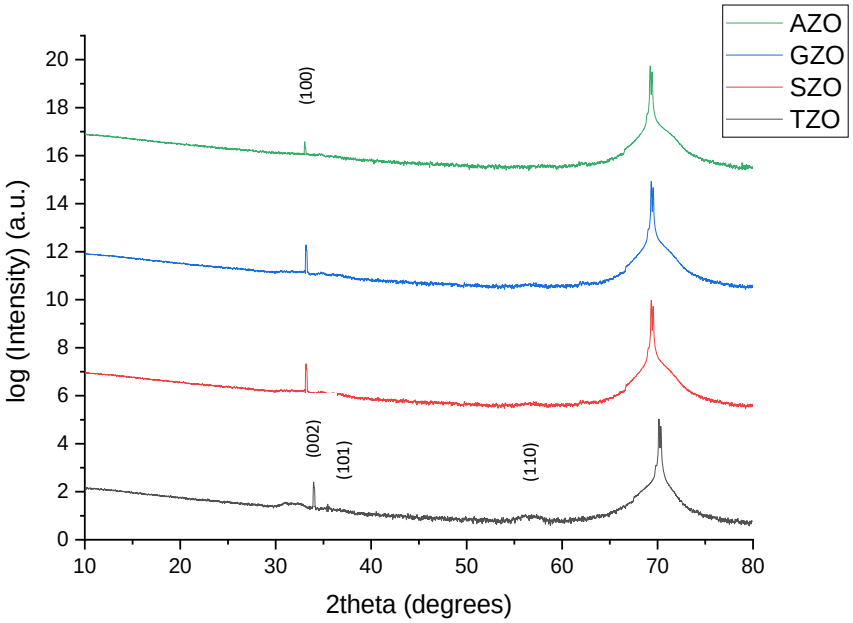

Figure 5.22: XRD patterns of PE-ALD AZO, GZO, SZO and TZO (9:1) films deposited at 150 °C on (a) glass substrates and (b) Si (100) substrates

(a)

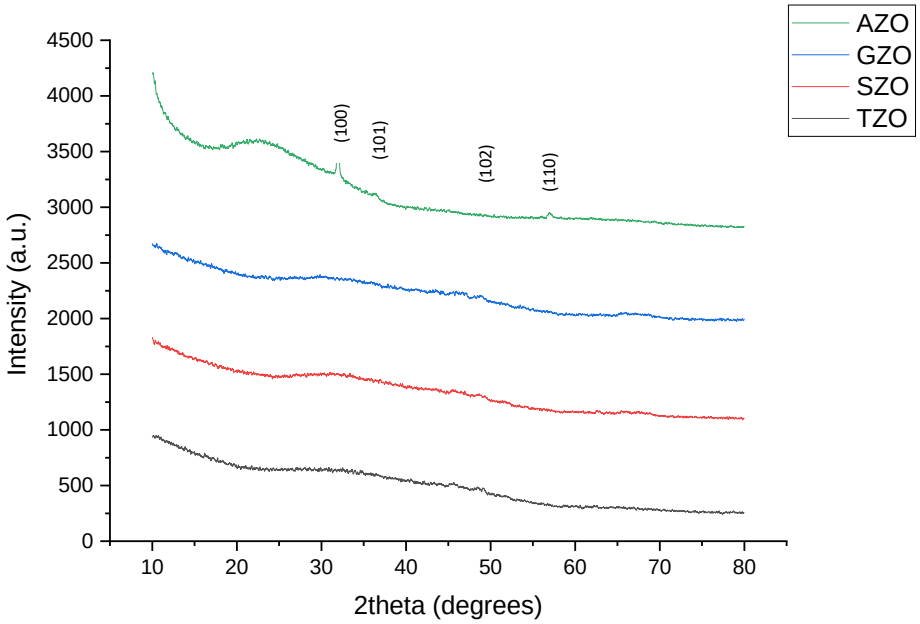

(b)

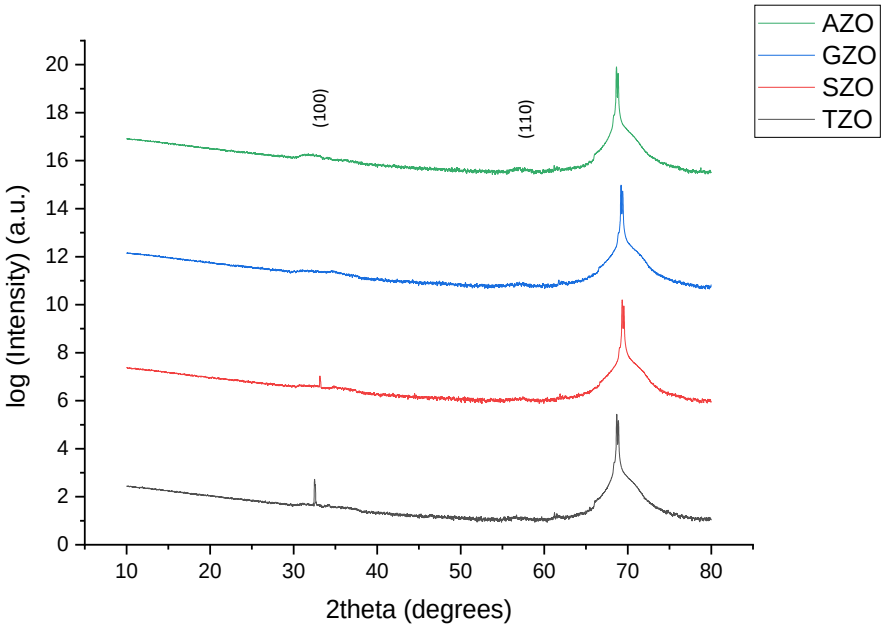

Figure 5.23: XRD patterns of PE-ALD AZO, GZO, SZO and TZO (19:1) films deposited at 150 °C on (a) glass substrates and (b) Si (100) substrates

Table 5.3 and 5.4 below displays the results obtained from XPS analysis and depth profiling of thermal and PE-ALD ZnO, AZO, GZO, SZO and TZO. Depth profiling was carried out as depth of analysis for typical XPS is typically ca. 10 nm. An etch time of 600 s relates to a depth of analysis of 24 nm and an etch time of 900 s relates to a depth of analysis of 36 nm.

Film	**Name**	**Thermal/Plasma**	**% Conc.**
ZnO	Zn 2p	thermal	44.5
		plasma	46.4
	O 1s	thermal	53.8
		plasma	52.3
	C 1s	thermal	1.7
		plasma	1.2

Table 5.3: Quantification of high resolution XPS data for both thermal ALD and plasma ALD grown ZnO at 600 s etch time, equivalent to 24 nm depth profiling

Film	Name	Thermal/Plasma	% Conc.
AZO	Zn 2p	thermal	42.1
		plasma	44.4
	O 1s	thermal	52.0
		plasma	49.3
	C 1s	thermal	1.4
		plasma	1.4
	Al 2p	thermal	4.5
		plasma	4.9
GZO	Zn 2p	thermal	43.2
		plasma	39.9
	O 1s	thermal	40.2
		plasma	50.4
	C 1s	thermal	5.4
		plasma	7.2
	Ga 2p	thermal	11.2
		plasma	2.5
SZO	Zn 2p	thermal	44.2
		plasma	52.5
	O 1s	thermal	53.0
		plasma	43.3
	C 1s	thermal	2.4
		plasma	0.5
	Sn 3d	thermal	0.3
		plasma	3.8
TZO	Zn 2p	thermal	46.7
		plasma	51.8
	O 1s	thermal	48.4
		plasma	45.5
	C 1s	thermal	2.9
		plasma	-
	Ti 2p	thermal	2.0
		plasma	2.7

Table 5.4: Quantification of high resolution XPS data for both thermal ALD and plasma ALD-grown AZO, GZO, SZO and TZO (19:1) samples at 900 s etch time, equivalent to 36 nm depth profiling

Dopants were incorporated into the ZnO films as reflected in the results outlined in tables 5.3 and 5.4. For the thermal ALD process, the most effectively doped film was GZO with a Ga atomic percentage of 11.2%. Szabó et al. reported the optimal Ga doping concentration to be 3 at% in which films had excellent homogeneous resistivity[55]. However, Al was the most effective dopant for the plasma process at 4.9 at%. For all doped ZnO films except GZO, the plasma ALD process films had a higher incorporation of dopants than their thermal ALD process counterparts. In terms of electrical characterisation, thermal ALD AZO, SZO and TZO (19:1) possessed a higher Hall mobility and carrier concentration and a lower sheet resistance than their PE-ALD counterparts. Therefore, electrically, the thermal ALD films can be said to perform better than the PE-ALD films. From this it can be concluded that a higher dopant incorporation alone does not necessarily equate to the best film electrically. As discussed in chapter 1, the doping efficiency is important. The presence of residual carbon was detected in all films except for plasma ALD TZO (etch time 900 s). This is due to precursor ligand reactions at the low temperatures at which the ALD process was carried out, or possibly just ligand incorporation. The highest carbon concentration was found at 0 s etch time which equates to surface contamination which is expected for samples handled in air.

The binding energies of Zn $2p_{3/2}$ and Zn $2p_{1/2}$ were observed at 1021.8 and 1044.8 eV, which is consistent with the literature for Zn in bulk ZnO[56]. From figure 5.24, it can be seen that the O peak contains two components with different binding energies. The lower binding energy component of the O 1s peak at ca. 530 eV can be assigned to O^{2-} ions surrounded by Zn^{2+} ions, indicating the presence of Zn-O bonds[36, 57-59]. The second O component at the binding energy of ca. 532 eV can be attributed mainly to surface hydroxyl groups[36, 57-59].

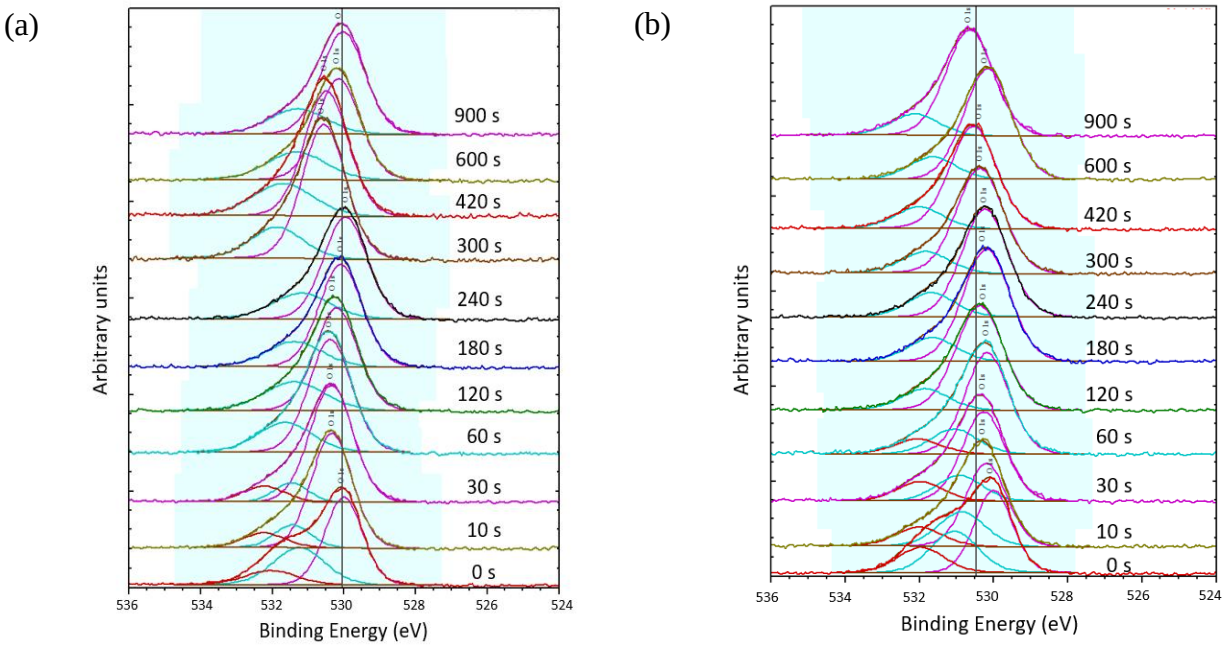

Figure 5.24: XPS spectra of the O 1s region for (a) thermal and (b) PE-ALD AZO at a depth of 0-36 nm. The oxygen peak was composed of two components with different binding energies

The peak at 532 eV can also be attributed to O^{2-} ions coupled with Al^{3+} which might be present as Al_{Zn}^{+} in the ZnO phase, but also as AlO_x clusters. The low binding energy component at ca. 73 eV is indicative of the presence of Al_2O_3[60-62]. Low concentrations of Al doping would most likely not be detectable from the Al 2p peak such that it would be difficult to investigate the chemical environment[36, 63]. Gupta et al. reported that Al 2p peaks which exhibit a low energy 'shoulder' indicates presence of non-oxidised Al atoms[64]. This was not observed here which suggested that all Al is oxidised.

For GZO, the Ga $2p_{3/2}$ peak was at ca. 1118 eV, consistent with the literature values for Ga^{3+}[65]. The Ga concentration differed hugely between the thermally grown and PE-ALD grown GZO, 11.2% and 2.5% respectively. Comstock et al. reported that H_2O is not sufficiently reactive with the TMGa-terminated surface resulting in no thermally-driven growth of Ga_2O_3[66]. The carbon contamination was also significantly higher in the thermal ALD GZO films as compared to the PE-ALD GZO films. A high Ga and C content may suggest the somewhat unreactive nature of TMGa and water under the conditions employed. The carbon ligands from the TMGa precursor may have been incorporated into the film. The precursor may not have decomposed as intended and/or was not sufficiently purged. The Ga atoms may have segregated together in the layer, to give an apparent concentration which is much higher than would be achieved just from the pulse ratio of 19:1

The Sn $3d_{5/2}$ spectral peak was observed at a binding energy of ca. 486 eV which is consistent with the standard values of SnO at 486.4 eV as given in the literature[67]. Differentiating between SnO and SnO_2 from the XPS Sn 3d peaks alone is quite difficult. A valence band spectrum is normally required to distinguish between these two oxides[68].

The binding energies of Ti $2p_{3/2}$ and $2p_{1/2}$ corresponding to Ti^{4+} states were ca. 458 and 464 eV, in agreement with the reported literature[72]. A shoulder associated with Ti^{3+} species was observed at 456.9 eV[73]. Interestingly, this film had the best electrical properties, a finding which is discussed in section 5.3.3.

The nominal dopant fraction based on GPC values for both the thermal and PE-ALD processes were calculated using equation 5.2[36]. The nominal dopant fraction may be defined as the atomic percentage (at%) of dopant incorporated into the ZnO film.

$$Nominal\ at.\% = \frac{GPC_{dopant}}{GPC_{dopant} + GPC_{ZnO}}\ x\ 100\% \qquad (5.2)$$

The GPCs used for each calculation are based on literature values for the deposition of each binary metal oxide. For thermal ALD, the GPC values used for Al_2O_3, SnO_2, TiO_2 and ZnO were 1[24], 0.6[25], 0.5[26, 27] and 2.0[28-30] Å/cycle respectively. The PE-ALD GPCs used were 1.2[31], 0.66[32], 1.7[33], 0.5[34] and 2.2[35] Å/cycle for Al_2O_3, Ga_2O_3, SnO_2, TiO_2 and ZnO respectively. Thermal Ga_2O_3 does not appear due to the fact that H_2O is not sufficiently reactive with the TMGa-terminated surface[66] and to the best of the knowledge of the author, no GPC values for this process exist in the literature. It also must be noted that AZO GPC is highly dependent on the growth temperature. The GPC increases rapidly with growth temperature[74].

Film	**Thermal/Plasma**	**Nominal dopant at%**
AZO	thermal	2.6
	plasma	2.8
GZO	thermal	-
	plasma	1.6
SZO	thermal	1.6
	plasma	3.9
TZO	thermal	1.3
	plasma	1.2

Table 5.5: Nominal dopant atomic percentage (at%) for thermal and PE-ALD AZO, GZO, SZO and TZO calculated based on GPC values using equation 5.2, dopant ratio 19:1

5.3.2 Optical Properties

The optical spectra displaying the transmittance results for ZnO and doped-ZnO grown at 150 °C for thermal and PE-ALD are shown in figures 5.25-5.27. The optical transparency exceeded 70% in the visible range. The absorption edge for all samples lay within the region 275-370 nm as expected due to the absorption of the glass substrates. Incorporation of the Al, Ga, Sn and Ti-dopants produced a blue shift in the wavelength of the absorption edge. The Ga dopant caused the greatest shift for the 9:1 thermal and PE-ALD films and 19:1 thermal films. However, the Al dopant produced the greatest effect on the shift for the 19:1 PE-ALD films. This may be explained by considering Burstein-Moss theory. This theory explains how the optical band gap of a semiconducting material with a direct band gap increases with increasing electron concentration due to the conduction band being highly populated with excited electrons from shallow donor states[50]. The electronic valence structure of Al and Ga are the same ($3s^2$, $3p^1$ for Al and $4s^2$, $4p^1$ for Ga) and so it may be expected that AZO and GZO would be similar in terms of their optical properties. However, GZO is metallic-like and produces a larger Burstein-Moss shift with respect to undoped ZnO which is seen in figures 5.26 and 5.27. In contrast, AZO behaves as a semiconductor and shows a smaller Burstein-Moss shift. Gabás et al, have attributed the difference to the fact that Al atoms occupy both substitutional and interstitial sites, whereas it was suggested that Ga occupies substitutional sites only[75].

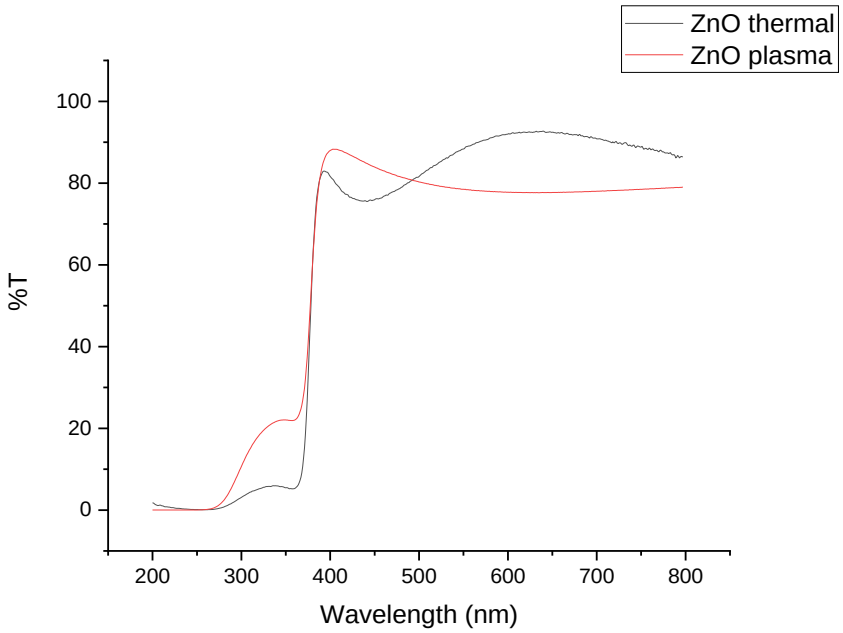

Figure 5.25: UV/visible spectra of thermal and PE-ALD ZnO films deposited at 150 °C on glass substrates

(a)

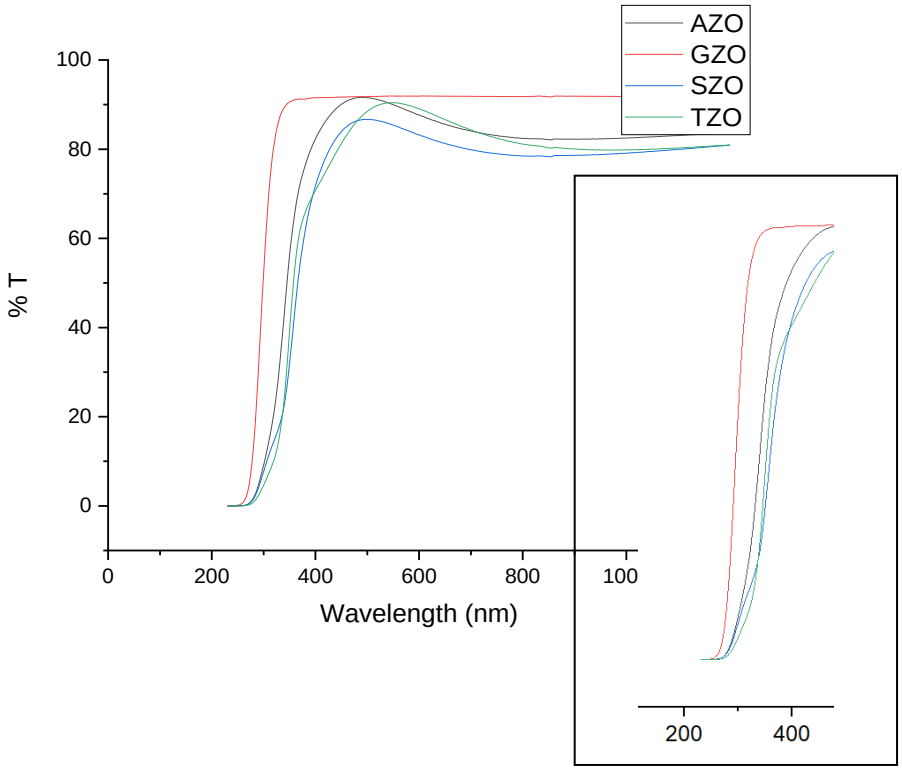

(b)

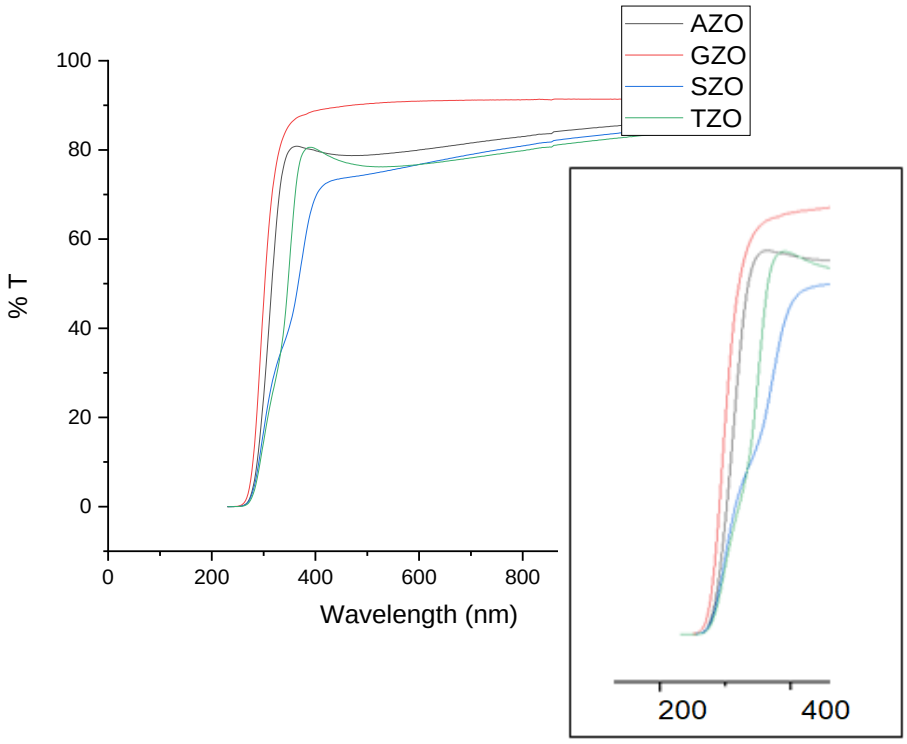

Figure 5.26: UV/visible spectra of (a), thermal and (b), PE-ALD AZO, GZO, SZO and TZO (9:1) films deposited at 150 °C on glass substrates

(a)

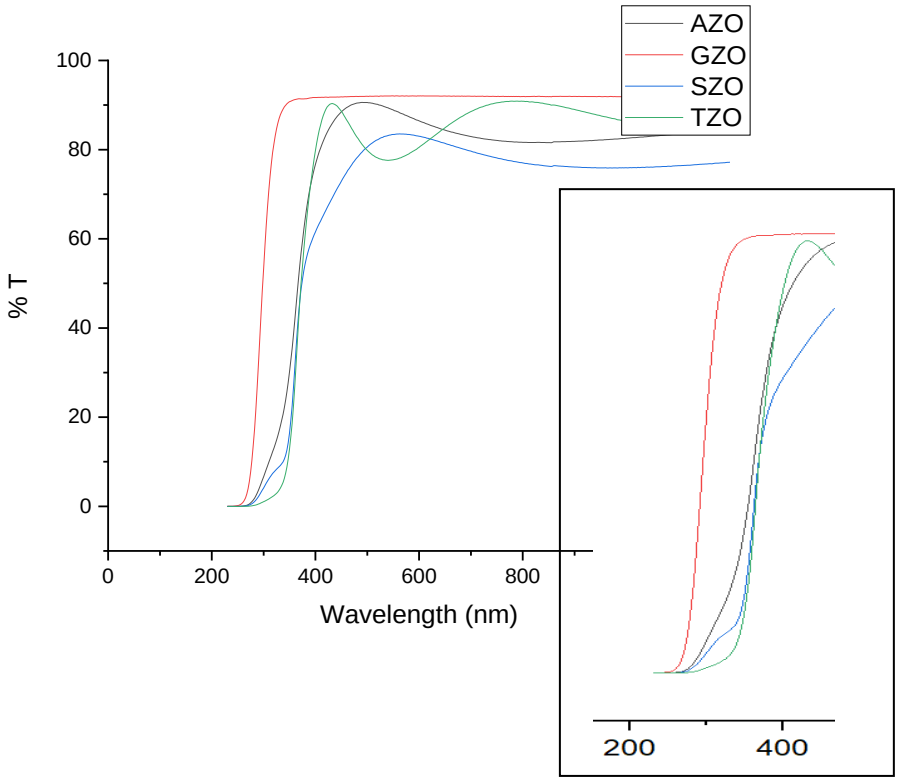

(b)

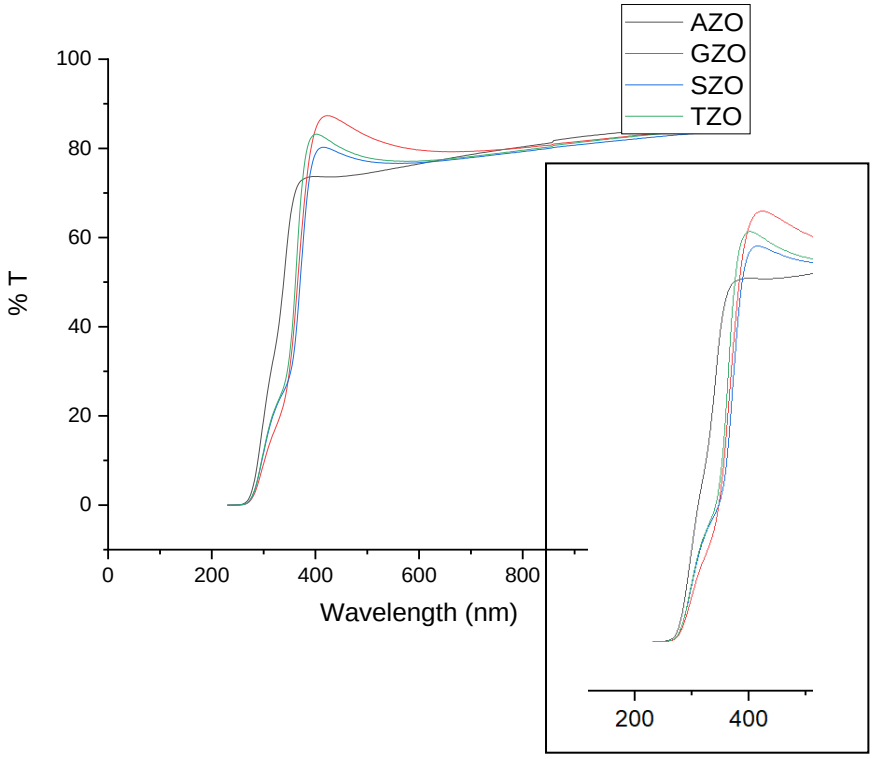

Figure 5.27: UV/visible spectra of (a), thermal and (b), PE-ALD AZO, GZO, SZO and TZO (19:1) films deposited at 150 °C on glass substrates

The band gaps of 19:1 thermal and PE-ALD films were determined using the Tauc plot method (equation 5.3). A graph plotting $(\alpha h\nu)^2$ versus photon energy ($h\nu$) was generated. The band gap energies were determined by the extrapolation of the linear region of the optical absorption edge. The absorption coefficient (α) was calculated via equation 5.4[76] where A is the absorbance and t is the thickness of the ALD layer.

$$(\alpha h\nu)^{\frac{1}{n}} = A(h\nu - E_g) \quad (5.3)$$

Where:

α - absorption coefficient

h - Plank's constant

ν - frequency of light

n - nature of the transition

A - absorbance

E_g - band gap energy

The nature of the transition, n may take on the following values; n = ½ for direct allowed transitions, n = $^3/_2$ for direct forbidden transitions, n = 2 for indirect allowed transitions and n = 3 for indirect forbidden transitions.

$$\alpha = \frac{2.303\,A}{t} \tag{5.4}$$

The Tauc plot (figure 5.28) exhibits band gap energies of 3.7, 3.8 and 3.86 eV for thermal AZO, SZO and TZO (19:1) respectively on glass substrate. Table 5.6 presents the results for the previously mentioned films and also PE-ALD AZO, GZO, SZO and TZO (19:1).

Hou et al. reported band gap energies of 3.27 – 3.58 eV for thermal ALD AZO (0% to 4.42%)[77]. Swatowska et al. reported band gap energies in the range of 3.4-3.9 eV for thermal ALD AZO (1.6% to 7.9%)[78]. In the case of thermal ALD TZO, Lee et al. found an enhanced band gap of 3.51 eV when compared to undoped ZnO (3.25 eV)[8]. An increase in band gap energy can be explained by the Burstein-Moss theory as previously mentioned[50]. Valencia et al. suggested that the morphology of thin films may be determined by band gap analysis[79]. Various TiO_2 films (amorphous, amorphous-crystalline, and crystalline) were deposited via sol-gel methods. The films that were confirmed to be amorphous by XRD had band gap values in the range of 3.5 eV, much higher than the crystallised TiO_2 films. Welte et al. also observed a higher band gap for amorphous TiO_2 films[80]. XRD analysis proved that films in this chapter are practically amorphous which coincides with the higher band gap values measured.

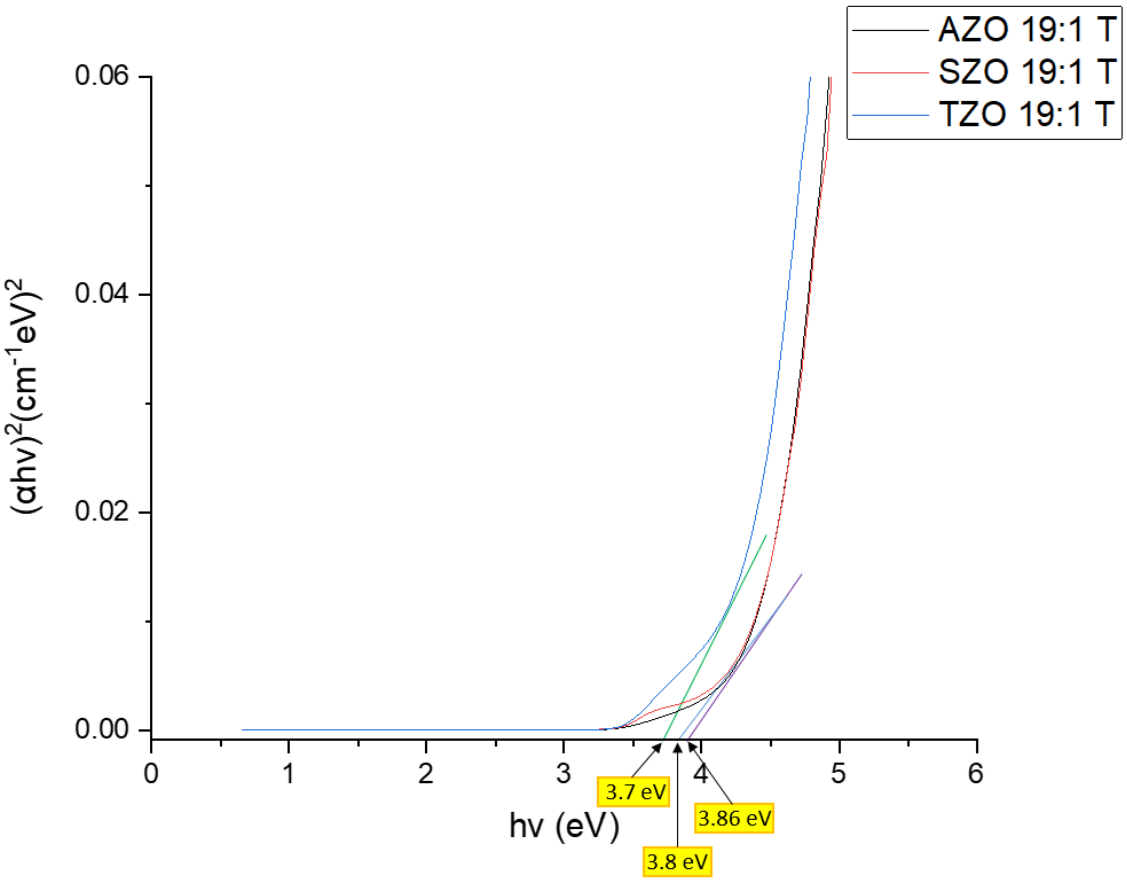

Figure 5.28: Band gap energies calculated via Tauc plot method for thermal ALD 19:1 AZO, SZO and TZO on glass substrates

Thin film		ALD Process	Band gap (eV)
AZO	19:1	thermal	3.7
		plasma	4.3
GZO	19:1	thermal	-
		plasma	4.2
SZO	19:1	thermal	3.8
		plasma	4.26
TZO	19:1	thermal	3.86
		plasma	4.24

Table 5.6: Band gap energies calculated via Tauc plot method for 19:1 thermal and PE-ALD AZO, GZO, SZO and TZO on glass substrates

5.3.3 Electrical Properties

The electrical properties of doped ZnO films were assessed by means of Hall Effect measurements. These measurements were carried out on a Lake Shore 8404 Hall-effect system and the results obtained are displayed in tables 5.7 and 5.8. The Hall mobility, carrier concentration and sheet resistance for each film were measured. The sheet resistance was measured as opposed to resistivity. This is due to the fact that thickness variations are highly likely due to the different growth rates of different dopants. Using the sheet resistance also takes into account the possibility of nucleation delays between the nanolaminate layers.

Film	**Thermal/Plasma**	**Hall mobility ($cm^2/V.s$)**	**Carrier concentration (cm^{-3})**	**Sheet resistance (Ω/□)**
AZO	thermal	1.26	3.41×10^{19}	8.0×10^{3}
	plasma	N/A	N/A	N/A
GZO	thermal	N/A	N/A	N/A
	plasma	N/A	N/A	N/A
SZO	thermal	1.54	2.19×10^{19}	10.3×10^{3}
	plasma	0.43	7.16×10^{17}	1237.6×10^{3}
TZO	thermal	2.89	7.65×10^{19}	1.7×10^{3}
	plasma	0.19	1.42×10^{19}	124.5×10^{3}

Table 5.7: Electrical properties of AZO, GZO, SZO and TZO (9:1) deposited by thermal and PE-ALD at 150 °C on glass substrate

Film	Thermal/Plasma	Hall mobility ($cm^2/V.s$)	Carrier concentration (cm^{-3})	Sheet resistance ($\Omega/\square$)
AZO	thermal	5.98	1.58×10^{20}	400
	plasma	0.11	6.35×10^{17}	5062.5×10^{3}
GZO	thermal	N/A	N/A	N/A
	plasma	0.15	1.20×10^{19}	215.0×10^{3}
SZO	thermal	2.66	2.74×10^{19}	4.8×10^{3}
	plasma	0.20	3.88×10^{17}	4826.9×10^{3}
TZO	thermal	6.77	1.51×10^{20}	339.0
	plasma	0.06	6.19×10^{17}	8817.8×10^{3}

Table 5.8: Electrical properties of AZO, GZO, SZO and TZO (19:1) deposited by thermal and PE-ALD at 150 °C on glass substrates

A common trend observed for all doped films was that thermally-grown doped ZnO had a significantly higher carrier concentration and Hall mobility and a lower sheet resistance than the plasma doped films. Thomas et al. have attributed an increase in resistivity and hence sheet resistance to a lower concentration of oxygen vacancies as a result of their neutralization by oxygen radicals[81]. Ideally, the optimum film would have a high carrier concentration and Hall mobility with a low sheet resistance.

The electrical properties for PE-ALD AZO 9:1 could not be obtained via Hall measurements. This film was extremely resistive and displayed no ohmic behaviour.

The low sheet resistance of 400 Ω/□ for thermal AZO (19:1) may also be attributed to the fact that the film had small surface features. Smaller surface grains mean less trapping and a lower sheet resistance. A more densely packed film may explain why this film had a relatively high Hall mobility of 5.98 $cm^2/V.s$. Previously, AZO films grown using a dopant ratio of 19:1 have been reported to have the best electrical characteristics[82-84]. Dhakal et al. reported a 575 nm thick AZO film grown at 325 °C with a sheet resistance of 100 Ω/□ and a carrier concentration of 1.86 $x10^{20}$ cm^{-3}. Following annealing of the films at 400 °C for 30 minutes, a sheet resistance of 25 Ω/□ (corresponding to a resistivity of 1.4 $x10^3$ cm^{-3})[82]. Qian et al. reported 60 nm thick AZO films deposited at 120 °C with a resistivity of 9.4×10^{-4} Ω cm[83]. A resistivity of 1.7 $x10^{-3}$ Ω cm and a carrier concentration 4.7 $x10^{20}$ cm^{-3} was reported by Lee et al.[85].

The Hall mobility for thermal SZO was found to be 2.66 $cm^2/V.s$ for the 19:1 film while the value obtained for the 9:1 film was 1.54 $cm^2/V.s$. This result is reflected for the carrier concentration values of thermal SZO where the value obtained for the 19:1 film is higher than the 9:1 film. The opposite results are seen for plasma SZO where both the Hall mobility and the carrier concentration show higher values in the 9:1 film as opposed to the 19:1 doped film. In terms of sheet resistance, the thermal SZO 19:1 film had a lower value than the 9:1 film, 475.5 $x10^1$ versus 102.5 $x10^2$ Ω/□. For plasma SZO, the 19:1 film had a higher sheet resistance than the 9:1 film, 482.7 $x10^4$ versus 123.8 $x10^4$ Ω/□. These results suggests that the film ratio of 19:1 is best for the thermal process and a ratio of 9:1 is best for the plasma process in order to achieve the best electrical properties for the particular films. At higher dopant levels, inactive dopant atoms can act as scattering centres which in turn negatively impact the electrical properties of a material. The contrary seems to be the case for plasma grown films. The higher levels of introduced dopants may be incorporated more effectively. Plasma etching effects

(supported by the lower thickness of plasma grown films) caused by the high ion energy of the plasma may be compensated by the higher level of dopants leaving no excess dopants present for scattering to occur – effectively the atoms lost by etching are replaced[37].

The electrical data for thermal ALD-grown TZO 19:1 proved to be the most optimal with the largest Hall mobility at 6.77 $cm^2/V.s$ and also the best sheet resistance value at 339 Ω/□. Thermal TZO (19:1) also had a high carrier concentration at 1.51 $x10^{20}$ cm^{-3}. It has previously been reported that in ALD, Ti is incorporated into the film as Ti^{4+}. Therefore, when Ti^{4+} substitutes Zn^{2+}, two free electrons are available to contribute to the conductivity of the film[8]. The optimal dopant ratio for thermal TZO has been reported as 19:1[8, 86] which was reflected in this study. Films prepared at the higher doping level of 9:1 displayed similar electrical results (Hall mobility 2.89 $cm^2/V.s$, carrier concentration 7.65 $x10^{19}$ cm^{-3} and sheet resistance 1200 Ω/□). Although the mobilities and carrier concentrations for the thermal 9:1 TZO were lower than those of the 19:1 films, while the sheet resistance values were higher, the results are encouraging when compared to the other 9:1 doped films and the 19:1 films of GZO and SZO.

The electrical properties of GZO films could not be determined except for the plasma GZO (19:1) film where a Hall mobility of 0.15 $cm^2/V.s$, a carrier concentration of 1.20 $x10^{19}$ cm^{-3} and a sheet resistance of 215.0 $x10^3$ Ω/□ were obtained. Although the value for carrier concentration is quite respectable, the film was very resistive as reflected by the high sheet resistance. It has previously been reported that after a certain level of Ga-doping, Ga atoms tend to occupy interstitial sites as neutral defects and can even substitute oxygen sites. This leads to a decrease in carrier concentration as the Ga act as neutral point defects and no longer contribute the free electrons[87, 88]. Roberts et al. reported a nuclear magnetic resonance (NMR) study in which Ga-O bonding formed with an increase in Ga-doping. This lead to the formation of non-conducting Ga_2O_3 phase which acted as a charge trapping centre and further reducing carrier concentration and mobility[89]. Even though in this thesis the electrical properties of a

GZO film with a higher Ga % could not be compared, this is a very interesting observation that should be explored as future work.

Overall, the thermal TZO (19:1) film had the best Hall mobility at 6.77 $cm^2/V.s$ and also the best sheet resistance at 339 Ω/□. The thermal AZO (19:1) film had the best carrier concentration at 1.58 $x10^{20}$ cm^{-3} with the thermal TZO film having a comparable value at 1.51 $x10^{20}$ cm^{-3}.

For films marked N/A in the tables, the resistance was too high to measure. The upper limit of the Hall system is 200 GΩ.

5.4 Conclusions

When compared to as-grown ZnO, neither the thermal ALD nor plasma ALD doped films could compare in terms of the Hall mobilities achieved. The Hall mobilities of the thermal and plasma as-grown ZnO at 150 °C were 10.5 and 1.5 $cm^2/V.s$, higher than that of any of the corresponding doped films. However, in terms of carrier concentrations, for both the thermal and plasma doped films, the values were higher than those obtained for as-grown ZnO (8.8 $x10^{18}$ and 2.4 $x10^{16}$ cm^{-3} for thermal and PE-ALD ZnO respectively). Of the doped films, the thermal TZO (19:1) film displayed the highest Hall mobility at 6.77 $cm^2/V.s$ which may be explained in terms of the presence of more active dopants that can also act as scattering centres. The blue-shift observed based on the Burstein-Moss theory indicates an increase in the carrier concentration[50]. Similarly, a reduction was seen in terms of sheet resistance values as the doped films had lower values than that of as-grown ZnO. These results show that the incorporation of dopants improved the electrical properties of ZnO but with no obvious correlation between Hall mobility and sheet resistance. Ellmer et al. have stated that ionized impurity scattering is responsible for decreased electron mobility but with an increased carrier concentration[90].

It has previously been reported that the intensity of the (002) XRD peak from doped ZnO films is inversely proportional to sheet resistance[40, 91]. In contrast, the work presented here suggests that this is not necessarily always the case since the thermally deposited AZO (19:1) films grown here possessed one of the lowest sheet resistance values at 400 Ω/□ but the (002) plane was absent from the XRD spectrum for the film. Interestingly, thermal TZO (19:1) had a lower sheet resistance of 339 Ω/□ but was completely amorphous and no (002) peak was present in the XRD spectrum.

Varying degrees of crystallinity were observed across the doped-ZnO films. This may be as a result of how materials nucleates on the substrate directly or on or near the introduced dopant.

In addition the dopant may cause inhibited nucleation of ZnO due to the dopant blocking sites and hindering DEZn absorption[1, 2].

Similar to as-grown thermal ALD ZnO, thermal ALD AZO, SZO and TZO show columnar grains on the surface of the films on both glass and Si (100) substrates. On glass substrates, PE-ALD AZO, GZO, SZO and TZO all reflect what is observed with as-grown PE-ALD ZnO. PE-ALD AZO also shows similar surface features on Si (100) substrate. However, GZO, SZO and TZO differs showing columnar surface features.

TEM imaging revealed deviations from the expected growth rates resulting in films with a reduced thickness. As previously mentioned, the dopant may inhibit nucleation of ZnO due to the dopant blocking sites and hindering DEZn absorption.

References

1. Bandyopadhyay, S., Paul, G. K., Roy, R., Sen, S. K. and Sen, S., Study of structural and electrical properties of grain-boundary modified ZnO films prepared by sol–gel technique. *Mater. Chem. Phys.* **2002,** *74* (1), 83-91.

2. Kim, K.-H., Park, K.-C. and Ma, D.-Y., Structural, electrical and optical properties of aluminum doped zinc oxide films prepared by radio frequency magnetron sputtering. *J. Apply. Phys.* **1997,** *81*, 7764.

3. Gao, Z. a. B., P., Review Article: Atomic layer deposition of doped ZnO films. *Journal of Vacuum Science & Technology A* **2019,** *37* (5), 050802.

4. George, S. M., Atomic Layer Depostion: An Overview. *Chem. Rev.* **2010,** *110*, 111-131.

5. Wu, Y., Devin Giddings, A., Verheijen, M. A., Macco, B., Prosa, T. J., Larson, D. J., Roozeboom, F. and Kessels, W. M. M., Dopant Distribution in Atomic Layer Deposited ZnO:Al Films Visualized by Transmission Electron Microscopy and Atom Probe Tomography. *Chem. Mater.* **2018,** *30*, 1209-1217.

6. Elam, J. W. a. G. S. M., Growth of ZnO/Al_2O_3 Alloy Films Using Atomic Layer Deposition Techniques. *Chem. Mater.* **2003,** *15* (4), 1020-1028.

7. Lee, D.-J., Kwon, J.-Y., Kim, J., Kim, K.-J., Cho, Y.-H., Cho, S.-Y., Kim, S.-H., Xu, J. and Kim, K.-B., Ultrasmooth, High Electron Mobility Amorphous In–Zn–O Films Grown by Atomic Layer Deposition. *J. Phys. Chem. C* **2014,** *118* (1), 408-415.

8. Lee, D.-J., Kim, K.-J., Kim, S.-H., Kwon, J.-Y., Xu, J. and Kim, K.-B. , Atomic layer deposition of Ti-doped ZnO films with enhanced electron mobility. *J. Mater. Chem. C* **2013,** *1* (31), 4761-4769.

9. Dixon, S. C., Scanlon, D. O., Carmalt, C. J. and Parkin, I. P., n-Type doped transparent conducting binary oxides: an overview. *J. Mater. Chem. C* **2016,** *4* (29), 6946-6961.

10. Ellmer, K., Klein, A. and Rech, B., Transparent Conductive Zinc Oxide Basics and Applications in Thin Film Solar Cells Springer, Heidelberg: 2008; Vol. 104.

11. Minami, T., Transparent Conducting Oxide Semiconductors for Transparent Electrodes. *Semicond. Sci. Technol.* **2005,** *20* (4), S35-S44.

12. Calnan, S. a., A. N., High mobility transparent conducting oxides for thin film solar cells. *Thin Solid Films* **2010,** *518* (77), 1839-1849.

13. Igasaki, Y. S., H., Substrate temperature dependence of electrical properties of ZnO:Al epitaxial films on sapphire ($12\bar{1}0$). *Journal of Applied Physics* **1991,** *69* (4), 2190.

14. Abrams, H., Grain Size Measurement by the Intercept Method. *Metallography* **1971,** *4* (1), 59-78.

15. Henrich, V. E., Oxide Surfaces. In *The Chemical Physics of Solid Surfaces*, Woodruff, D. P., Ed. 2001; Vol. 9, pp 1-34.

16. Mathews , S., Ramesh , R., Venkatesan , T. and Benedetto, J., Ferroelectric Field Effect Transistor Based on Epitaxial Perovskite Heterostructures. *Science* **1997,** *276* (531), 238-240.

17. Kim, T. S. K., C. H., The effect of buffer layer on the structural and electrical properties of (BaSr)TiO3thin films deposited on indium tin oxide-coated glass substrate by using a rf magnetron sputtering method. *J. Appl. Phys.* **1994,** *76* (7), 4316.

18. Glass, A., Materials for Photonic Switching and Information Processing. *MRS Bulletin* **1988,** *13* (8), 16-20.

19. Mullings, M. N., Hägglund, C., Tanskanen, J. T., Yee, Y., Geyer, S. and Bent, S. F., Thin film characterization of zinc tin oxide deposited by thermal atomic layer deposition. *Thin Solid Films* **2014,** *556*, 186-194.

20. Luo, Y., *Comprehensive Handbook of Chemical Bond Energies*. CRC Press: University of Science and Technology, Hefei, China, 2007.

21. Jackson, R. L., Metal-alkyl bond dissociation energies for $(CH_3)_2Zn$, $(C_2H_5)Zn$, $(CH_3)_2Cd$, and $(CH_3)_2Hg$. *Chemical Physics Letters* **1989,** *163* (4-5), 315-322.

22. Mackus, A. J. M., Schneider, J. R., MacIsaac, C., Baker, J. G. and Bent, S. F., Synthesis of Doped, Ternary, and Quaternary Materials by Atomic Layer Deposition: A Review. *Chem. Mater.* **2019,** *31*, 1142−1183.

23. Askeland D. R., F., P. P. and Wright, W. J., *The Science and Engineering of Materials*. 6th ed. ed.; Cengage Learning: 2010.

24. Puurunen, R. K., Surface chemistry of atomic layer deposition: A case study for the trimethylaluminum/water process. *Journal of Applied Physics* **2005,** *97* (121301).

25. Elam, J.; W., B., D. A., Hryn, A. J., Martinson, A. B. F., Pellin, M. J. and Hupp, J. T., Atomic Layer Deposition of Tin Oxide Films Using Tetrakis(dimethylamino) Tin. *J. Vac. Sci. Technol. A* **2008,** *26* (2), 244−252.

26. Reiners, M., Xu, K., Aslam, N., Devi, A., Waser, R. and Hoffmann-Eifert, S., Growth and Crystallization of TiO_2 Thin Films by Atomic Layer Deposition Using a Novel Amido Guanidinate Titanium Source and Tetrakis-dimethylamido-titanium. *Chem. Mat.* **2013,** *25*, 2934–2943.

27. Jin, C., Liu, B., Lei, Z. and Sun, J., Structure and photoluminescence of the TiO_2 films grown by atomic layer deposition using tetrakis-dimethylamino titanium and ozone. *Nanoscale Research Letters* **2015,** *10* (95).

28. Tapily, K., Gu, D., Baumgart, H., Namkoong, G., Stegall, D. and Elmustafa, A. A., Mechanical and structural characterization of atomic layer deposition-based ZnO films. *Semicond. Sci. Technol.* **2011,** *26*, 115005.

29. Lin, M.-C., Wu, M.-K., Yuan, K.-Y., Chen, M.-J., Yang, J.-R. and Shiojiri, M., Structural and Photoluminescence Properties of ZnO Films Grown on 6H-SiC Substrates by Low-Temperature Atomic Layer Deposition. *J. Electrochem. Soc.* **2011,** *158* (H1213).

30. Nam, T., Kim, J.-M., Kim, M.-K., Kim, H. and Kim, W.-H. , Low-temperature Atomic Layer Deposition of TiO_2, Al_2O_3, and ZnO Thin Films. *J. Korean Phys. Soc.* **2011,** *59* (2), 452-457.

31. Hemmen, v., J. L., Heil, S. B. S., Klootwijk, J. H., Roozeboom , F., Hodson, C. J., Sanden, van de , M. C. M. and Kessels W. M. M., Plasma and thermal ALD of Al_2O_3 in a commercial 200 mm ALD reactor. *Journal of the Electrochemical Society* **2007,** *154* (7), G165-G169.

32. Mahmoodinezhad, A., Janowitz, C., Naumann, F., Plate, P., Gargouri, H., Henkel, K., Schmeißer, D. and Flege, J. I., Low-temperature growth of gallium oxide thin films by plasma-enhanced atomic layer deposition. *J. Vac. Sci. Technol. A* **2020,** *38*, 022404.

33. Wang, C., Zhao, D., Grice, C., Liao, W., Yu, Y., Cimaroli, A., Shrestha, N., Roland, P., Chen, J., Yu, Z., Liu, P., Cheng, N., Ellingson, R., Zhao, X. and Yan, Y., Low-Temperature Plasma-Enhanced Atomic Layer Deposition of Tin Oxide Electron Selective Layers for Highly Efficient Planar Perovskite Solar Cells. *J. Mater. Chem. A.* **2016,** *4* (31), 12080-12087.

34. Xie, Q., Musschoot, J., Deduytsche, D., Van Meirhaeghe, R., Detavernier, C., Van; Den Berghe, S., Jiang, Y.-L., Ru, G.-P., Li, B.-Z. and Qu, X.-P., Growth Kinetics and Crystallization Behavior of TiO_2 Films Prepared by Plasma Enhanced Atomic Layer Deposition. *J. Electrochem. Soc.* **2008,** *155* (9), H688-H692.

35. Park, S.-H. K., Hwang, C.-S., Kwack, H.-S., Lee, J.-H. and Chu, H. Y., Characteristics of ZnO Thin Films by Means of Plasma-Enhanced Atomic Layer Deposition. *Electrochem. Solid State* **2006,** *9* (10), G299.

36. Wu, Y., Hermkens, P. M., van de, Loo, B. W. H., Knoops, H. C. M., Potts, S. E., Verheijen, M. A., Roozeboom, F. and Kessels, W. M. M., Electrical transport and Al doping efficiency in nanoscale ZnO films prepared by atomic layer deposition. *J. Appl. Phys.* **2013,** *114*, 024308.

37. Chae, H. S., H. H., Removal with Fluorocompounds in a Plasma-Enhanced Chemical Vapor Deposition Chamber. *J. Korean Phys. Soc.* **2007,** *51*, 978.

38. Zhu, Z., Sippola, P., Lipsanen, H., Savin, H. and Merdes, S., Influence of plasma parameters on the properties of ultrathin Al_2O_3 films prepared by plasma enhanced atomic layer deposition below 100 °C for moisture barrier applications. *Japanese Journal of Applied Physics* **2018,** *57*, 125502.

39. Islam, M. R., Rahman, M., Farhad, S. F. U. and Podder, J., Structural, optical and photocatalysis properties of sol–gel deposited Al-doped ZnO thin films. *Surfaces and Interfaces* **2019,** *16*, 120-126.

40. Zhou, H.-M., Yi, D.-G., Yu, Z.-M., Xiao, L.-R. and Li, J., Preparation of aluminum doped zinc oxide films and the study of their microstructure, electrical and optical properties *Thin Solid Films* **2007,** *515*, 6909–6914.

41. Zhaochun, Z., Huang, B., Yu, Y. and Deliang, C., Electrical properties and Raman spectra of undoped and Al-doped ZnO thin films by metalorganic vapor phase epitaxy. *Materials Science and Engineering B* **2001,** *86* (2), 109-112.

42. Banerjee, P., Lee, W.-J., Bae, K.-R., Lee, S. B. and Rubloff, G. W., Structural, electrical, and optical properties of atomic layer deposition Al-doped ZnO films. *J. Appl. Phys.* **2010,** *108*, 043504.

43. Ahn, C. H., Lee, S. Y. and Cho, H. K., Influence of growth temperature on the electrical and structural characteristics of conductive Al-doped ZnO thin films grown by atomic layer deposition. *Thin Solid Films* **2013,** *545*, 106-110.

44. Zhou, X., Xie, Z., Bian, L., Li, W., Zhou, X., Wu, X., Yang, Z., Han, N., Zhang, J. and Chen, Y., Enhanced NO_2 Sensing Property of ZnO by Ga doping and H_2 Activation. *Physica Status Solidi A* **2018,** *215* (11), 1700861.

45. Hultqvist, A., Platzer-Björkman, C., Zimmermann, U., Edoff, M. and Törndahl, T., Growth kinetics, properties, performance, and stability of atomic layer deposition Zn–Sn–O buffer layers for Cu(In,Ga)Se_2 solar cells. *Prog. Photovoltaics Res. Appl.* **2012,** *20* (7), 883-891.

46. Choi, W.-S., Preparation of zinc-tin-oxide thin film by using an atomic layer deposition methodology. *Journal of the Korean Physical Society* **2010,** *57* (6), 1472-1476.

47. Hultqvist, A., Edoff, M. and Törndahl, T., Evaluation of Zn-Sn-O buffer layers for $CuIn_{0.5}Ga_{0.5}Se_2$ solar cells. *Progress in Photovoltaics: Research and Applications* **2011,** *19* (4), 478-481.

48. Kapilashrami, M., Kronawitter, C.X., Törndahl, T., Lindahl, J., Hultqvist, A., Wang, W.-C., Chang, C.-L., Mao, S.S. and Guo, J., Soft X-ray characterization of $Zn_{1-x}Sn_xO_y$

electronic structure for thin film photovoltaics. *Physical Chemistry Chemical Physics* **2012,** *14* (29), 10154-10159.

49. Mullings, M. N., Hägglund, C. and Bent, S. F., Tin oxide atomic layer deposition from tetrakis(dimethylamino)tin and water. *Journal of Vacuum Science & Technology A* **2013,** *31*, 061503.

50. Bergum, K., Hansen, P.-A., Fjellvåg, H. and Nilsen, O., Structural, electrical and optical characterization of Ti-doped ZnO films grown by atomic layer deposition. *J. Alloys Compounds* **2014,** *616*, 618-624.

51. Jayakrishnan, R., Mohanachandran, K., Sreekumar, R., Sudha Kartha, C. and Vijayakumar, K. P., ZnO thin films with blue emission grown using chemical spray pyrolysis. *Mater. Sci. Semicond. Process.* **2013,** *16*, 326–331.

52. Bergum, K., Fjellvåg, H. and Nilsen, O., Thickness dependent structural, optical and electrical properties of Ti-doped ZnO films prepared by atomic layer deposition. *Appl. Surf. Sci.* **2015,** *332*, 494-499.

53. Chen, R., Lin, J. L., He, W. J., Duan, C. L., Peng, Q. and Wang, X. L., Spatial atomic layer deposition of ZnO/TiO_2 nanolaminates. *J. Vac. Sci. Technol. A* **2016,** *34* (5).

54. Rajasekaran, M., Arunachalam, A. and Kumaresan, P., Structural, morphological and optical characterization of Ti-doped ZnO nanorod thin film synthesized by spray pyrolysis technique. *Mater. Res. Express* **2020,** *7*, 036412.

55. Szabó, Z. B., Z., Basa, P., Czigány, Z., Bársony, I., Wang, H.-Y. and Volk, J., Homogeneous transparent conductive ZnO:Ga by ALD for large LED wafers. *Appl. Surf. Sci.* **2016,** *379*, 304-308.

56. Wang, F.-H., Chang, H.-P., Tseng, C.-C. and Huang, C.-C., Effects of H_2 plasma treatment on properties of ZnO:Al thin films prepared by RF magnetron sputtering. *Surface and Coatings Technology* **2011,** *205* (23-24), 5269-5277.

57. Kwon, S., Bang, S., Lee, S., Jeon, S., Jeong, W., Kim, H., Gong, S. C., Chang, H. J., Park, H.-H. and Jeon, H., Characteristics of the ZnO thin film transistor by atomic layer deposition at various temperatures. *Semiconductor Science and Technology* **2009,** *24* (3), 035015.

58. Tong, H., Deng, Z., Liu, Z., Huang,C., Huang, J., Lan, H., Wang, C. and Cao, Y., Effects of post-annealing on structural, optical and electrical properties of Al-doped ZnO thin films. *Applied Surface Science* **2011,** *257* (11), 4906-4911

59. Gao, M., Wu, X., Liu, J. and Liu, W., The effect of heating rate on the structural and electrical properties of sol–gel derived Al-doped ZnO films. *Applied Surface Science* **2011,** *257* (15), 6919-6922

60. Chen, M., Wang, X., Yu, Y. H., Pei, Z. L., Bai, X. D., Sun, C., Huang, R. F. and Wen, L. S., X-ray photoelectron spectroscopy and auger electronspectroscopy studies of Al-doped ZnO films. *Applied Surface Science* **2000,** *158*, 134-140.

61. Chung, Y. M., Moon, C. S., Jung, W. S. and Han, J. G., The low temperature synthesis of Al doped ZnO films on glass and polymerusing pulsed co-magnetron sputtering: H_2 effect. *Thin Solid Films* **2006,** *515*, 567–570.

62. Li, L., Liang, F., Zhou, X., Liu, Z. Y., Zhao, L. and Jiang, S., X-ray photoelectron spectroscopy study and thermoelectric properties of Al-doped ZnO thin films. *Journal of Electron Spectroscopy and Related Phenomena* **2009,** *173* (1), 7-11.

63. Islam, M. N., Ghosh, T. B., Chopra, K. L. and Acharya, H. N., XPS and X-ray diffraction studies of aluminum-doped zinc oxide transparent conducting films *Thin Solid Films* **1996,** *280*, 20–25.

64. Gupta, S., Hannah, S., Watson, C. P., Šutta, P., Pedersen, R. H., Gadegaard, N. and Gleskova, H., Ozone oxidation methods for aluminum oxide formation: Application to low-voltage organic transistors. *Organic Electronics* **2015,** *21*, 132-137.

65. Park, S. M., Ikegami, T. and Ebihara, K., Effects of substrate temperature on the properties of Ga-doped ZnO by pulsed laser deposition. *Thin Solid Films* **2006,** *513*, 90-94.

66. Comstock, D. J. a. E., J. W., Atomic Layer Deposition of Ga2O3 Films using Trimethylgallium and Ozone. *Chem. Mater.* **2012,** *24* (21), 4011–4018.

67. Weber, J., Jeedigunta, S. and Kumar, A., Fabrication and Characterization of ZnO Nanowire Arrays with an Investigation into Electrochemical Sensing Capabilities. *Journal of Nanomaterials* **2008**, 1-5.

68. https://www.jp.xpssimplified.com/elements/tin.php. (accessed 07/10/2021).

69. Kim, J. N., Shin, K. S., Kim, D. H., Park, B. O., Kim, N. K. and Cho, S. H., Changes in chemical behavior of thin film lead zirconate titanate during Ar^{+}-ion bombardment using XPS. *Appl. Surf. Sci.* **2003,** *206*, 119–128.

70. Wagner, C. D., Riggs, W. M., Davis, L. E., Moulder, J. F. and Muilenberg, G. E., Handbook of X-ray Photoelectron Spectroscopy. **1979,** *3* (4), 68–69.

71. Dey, N. K., Kim, M. J., Kim, K.-D., Seo, H.O., Kim, D., Kim, Y.D., Lim, D. C. and Lee, K. H., Adsorption and photocatalytic degradation of methylene blue over TiO_2 films on carbon fiber prepared by atomic layer deposition. *Journal of Molecular Catalysis A: Chemical* **2011,** *337* (1-2), 33-38.

72. Younis, A., Chu, D. and Li, S., Bi-stable resistive switching characteristics in Ti-doped ZnO thin films *Nanoscale Research Letters* **2013,** *8*, 154.

73. Bharti, B., Kumar, S., Lee, H.-N. and Kumar, R., Formation of oxygen vacancies and Ti^{3+} state in TiO_2 thin film and enhanced optical properties by air plasma treatment. *Scientific Reports* **2016,** *6*, 32355.

74. Baji, Z., Lábadi, Z., Horváth, Z. E., Fried, M., Szentpáli, B. and Bársony, I., Temperature dependent in situ doping of ALD ZnO. *J. Therm. Anal. Calorim.* **2011,** *105*, 93–99.

75. Gabás, M., Torelli, P., Barrett, N. T., Sacchi, M. and Ramos Barrado, J. R., Electronic structure of Al- and Ga-doped ZnO films studied by hard X-ray photoelectron spectroscopy. *APL Mater.* **2014,** *2*, 012112.

76. Al-Saadi, T. M., Hussein, B. H., Hasan, A. B. and Shehab, A. A., Study the Structural and Optical Properties of Cr doped SnO2 Nanoparticles Synthesized by Sol-Gel Method *Energy Procedia* **2019,** *157*, 457-465.

77. Hou, Q., Meng, F. and Sun, J., Electrical and optical properties of Al-doped ZnO and $ZnAl_2O_4$ films prepared by atomic layer deposition. *Nanoscale Res. Lett.* **2013,** *8* (144).

78. Swatowska, B., Powroznik, W., Czternastek, H., Lewinska, G., Stapinski, T., Pietruszka, R., Witkowski, B. S. and Godlewski, M., Application Properties of ZnO and AZO Thin Films Obtained by the ALD Method. *Energies* **2021,** *14*, 6271.

79. Valencia, S., Marín, J. M. and Restrepo, G., Study of the Bandgap of Synthesized Titanium Dioxide Nanoparticules Using the Sol-Gel Method and a Hydrothermal Treatment. *The Open Materials Science Journal* **2010,** *4*, 9-14.

80. Welte, A., Waldauf, C., Brabec, C. J. and Wellmann, P., Application of optical absorbance for the investigation of electronic and structural properties of sol-gel processed TiO_2 films. *Thin Solid Films* **2008,** *516* (20), 7256-7259.

81. Thomas, M. A. a. C., J. B., Highly Tunable Electrical Properties in Undoped ZnO Grown by Plasma Enhanced Thermal-Atomic Layer Deposition. *ACS Appl. Mater. Interfaces* **2012,** *4* (6), 3122–3128.

82. Dhakal, T., Nandur, A. S., Christian, R., Vasekar, P., Desu, S., Westgate, C., Koukis, D. I., Arenas, D. J. and Tanner, D. B., Transmittance from visible to mid infra-red in AZO films grown by atomic layer deposition system. *Sol. Energy Mater. Sol. Cells* **2012,** *86* (5), 1306-1312.

83. Qian, X., Cao, Y., Guo, B., Zhai, H. and Li, A., Atomic Layer Deposition of Al-doped ZnO Films Using Aluminum Isopropoxide as the Al Precursor. *Chem. Vap. Deposition* **2013,** *19* (4-6), 180-185.

84. Lee, J. H., Lee, J.-W., Hwang, S., Kim, S. Y., Cho, H. K., Lee, J. Y. and Park, J.-S., Effects of Al Concentration on Microstructural Characteristics and Electrical Properties of Al-Doped ZnO Thin Films on Si Substrates by Atomic Layer Deposition. *J. Nanosci. Nanotechnol.* **2012,** *12* (7), 5598-5603.

85. Lee, D.-J. x., Kwon, J.-Y., Kim, S.-H., Kim, H.-M. and Kim, K.-B., Effect of Al Distribution on Carrier Generation of Atomic Layer Deposited Al-Doped ZnO Films. *J. Electrochem. Soc.* **2011,** *158* (5), D277-D281.

86. Qian, X., Gao, M. Y., Cao, Y. Q., Guo,B. L. and Li, A .D., Preparation and phase structures of Zn–Ti–O ternary compounds by atomic layer deposition. *J. Vac. Sci. Technol. A* **2013,** *31*.

87. Ye, J. D., Gu, S. L., Zhu, S. M., Liu, S. M., Zheng, Y. D., Zhang, R., Shi, Y., Yu, H. Q. and Ye, Y. D., Gallium doping dependence of single-crystal n-type Zno grown by metal organic chemical vapor deposition. *J. Cryst. Growth* **2005,** *283* (3-4), 279-285.

88. Chalker, P. R., Marshall, P. A., Romani, S. and Roberts, J. W., Atomic layer deposition of Ga-doped ZnO transparent conducting oxide substrates for CdTe-based photovoltaics. *Journal of Vacuum Science & Technology A* **2013,** *31*, 01A120.

89. Roberts, N., Wang, R.-P., Sleight, A. W. and Warren, W. W., ^{27}Al and ^{69}Ga impurity nuclear magnetic resonance in ZnO:Al and ZnO:Ga *Phys. Rev. B* **1998,** *57*, 5734.

90. Ellmer, K. a. M., R., Carrier transport in polycrystalline transparent conductive oxides: A comparative study of zinc oxide and indium oxide. *Thin Solid Films* **2008,** *516* (14), 4620-4627.

91. Lee, J. H., Ko, K. H. and Park, B. O., Electrical and Optical Properties of ZnO Transparent Conducting Films by the sol-gel method. *Journal of Crystal Growth* **2003,** *247* (1-2), 119-125.

Chapter 6: A Study of the Growth of Ternary Compounds Based on ZnO by Plasma-Assisted ALD

Abstract

This chapter describes the growth and characterisation of ZnO: Ga_2O_3: Al_2O_3, ZnO: SnO_2: Al_2O_3 and ZnO: TiO_2:Al_2O_3 using PE-ALD at 150 °C as described in section 2.2.4. XRD analysis revealed that growth was substrate dependent with Si (100) substrate films displaying crystallinity and glass substrate films being significantly less crystalline. A shift in the (100) XRD peak towards a higher angle occurred due to the incorporation of the dopants into the ZnO matrix. In terms of both carrier concentration and sheet resistance, the best performing ternary was found to be the ZnO: Ga_2O_3: Al_2O_3 (9:1 Ga, 19:1 Al) material with a carrier concentration of 1.36 x10^{19} cm^{-3} and a Hall mobility of 0.17 cm^2/V.s.

6.1 Introduction

One of the main applications of ALD involves the use of doped, binary metal oxides[1]. However, there is increasing interest in the fabrication of ternary and quaternary materials in terms of applications such as catalysis[2, 3], energy storage[4, 5] and photovoltaics[6-8].

Coll *et al.* have published a review on the topic of functional multicomponent oxides focusing on pervoskites (ABO_3), spinels (AB_2O_4), delafossites (ABO_2) and scheelites (ABO_4)[9]. This review exploits the fact that the exact same metal cation can be either stable or metastable in different structures. In contrast this present chapter focuses exclusively on ZnO-based ternary oxides which are composed of Zn^{2+} ions combined with two other metal ions in an oxide matrix-so-called ternary oxides. The use of ternary oxides provides more opportunities to tune the

composition and both the atomic and electronic structures. ALD is a particularly suitable deposition method for the fabrication of ternary or even quaternary oxides as it possible to tailor the growth recipe to a precise sequence. Mackus et al. have published an extensive review on the growth of doped, ternary and quaternary materials by ALD[1]. Previous ZnO-based ternaries studied include ZnO: Al_2O_3: ZrO_2[10], ZnO: MgO: Al_2O_3[11] and ZnO: TiO_2: ZrO_2[12]. The co-reactant used in the growth of these films was H_2O. In this thesis, O_2 plasma was the chosen co-reactant. A more reactive co-reactant can lead to the elimination of nucleation effects such as etching by persistent ligands or memory issues associated with the persistence of H_2O in the chamber. Use of O_2 plasma may also functionalize the surface of the film with more reactive sites. If nucleation effects can be minimized, the deposition of complex materials may become more viable as switching between different binary oxides is aided[1].

6.2 Experimental

6.2.1 Preparation of ZnO ternary films

As listed in section 2.2.4 of this thesis, the following ternary samples of ZnO: Ga_2O_3: Al_2O_3, ZnO: SnO_2: Al_2O_3 and ZnO: TiO_2: Al_2O_3 were prepared using PE-ALD at 150 °C via the supercycle method:

Case	Dopant 1 ratio	Dopant 2 ratio
1	9:1	19:1
2	19:1	9:1
3	19:1	19:1

Table 6.1: Dopant ratios used for the growth of ternary films

6.2.2 Characterisation techniques

The crystallinity of the ZnO ternary films was analysed by X-ray diffraction (XRD) using a PANalytical X'Pert Pro Diffractometer, with Cu Kα (λ = 0.154 nm) radiation from 10 to 70° at a step size of 0.02° under 45 kV and 30 mA. The XRD results were compared to the Joint Committee on the Powder Diffraction Standard Card (JPCDS: 36-1451). AC and DC field Hall Measurements were performed using a Lake Shore 8400 Series system.

6.3 Results and discussion

6.3.1 X-ray Diffraction

Figures 6.1-6.3 show XRD patterns for ZnO: Ga_2O_3: Al_2O_3, ZnO: SnO_2: Al_2O_3 and ZnO: TiO_2: Al_2O_3 deposited by PE-ALD at 150 °C on both Si (100) and glass substrates.

Peaks observed at 31.8° was assigned to the (100) plane of ZnO. This was observed in ZnO: Ga_2O_3: Al_2O_3 and ZnO: SnO_2: Al_2O_3 for all three dopant ratios studied, see table 6.1 above. The intensity of this peak was highest in the 19:1 dopant, 19:1 dopant ratio film. Indeed for the ZnO: TiO_2: Al_2O_3 sample the (100) plane was only observed in the 19:1, 19:1 ratio film.

A shift in the (100) XRD peak towards a higher angle was observed when comparing the ternary films to as-grown PE-ALD ZnO. For ZnO: SnO_2: Al_2O_3, the (100) peaks were found at approximately 32.7°, 33.2° and 33.1° for the ratios 9:1 Sn 19:1 Al, 19:1 Sn 9:1 Al and 19:1 Sn 19:1 Al respectively. For ZnO: Ga_2O_3: Al_2O_3, the (100) peaks were found at approximately 32.8°, 32.9° and 33.1° for the ratios 9:1 Ga 19:1 Al, 19:1 Ga 9:1 Al and 19:1 Ga 19:1 Al respectively. The (100) peak in the 19:1, 19:1 ratio ZnO: TiO_2: Al_2O_3 material was shifted to 32.5°.

The deposition was clearly substrate dependent with films grown on Si (100) substrates films displaying clear evidence of crystallinity in the form of sharp, well-defined XRD features while films deposited on glass gave rise to significantly broader and weaker XRD features, suggesting reduced crystallinity in comparison. In all the ternary oxides deposited, with the exception of the ZnO: TiO_2: Al_2O_3 materials, a broad peak ranging from 31-36° was seen for the films deposited on glass substrates.

(a)

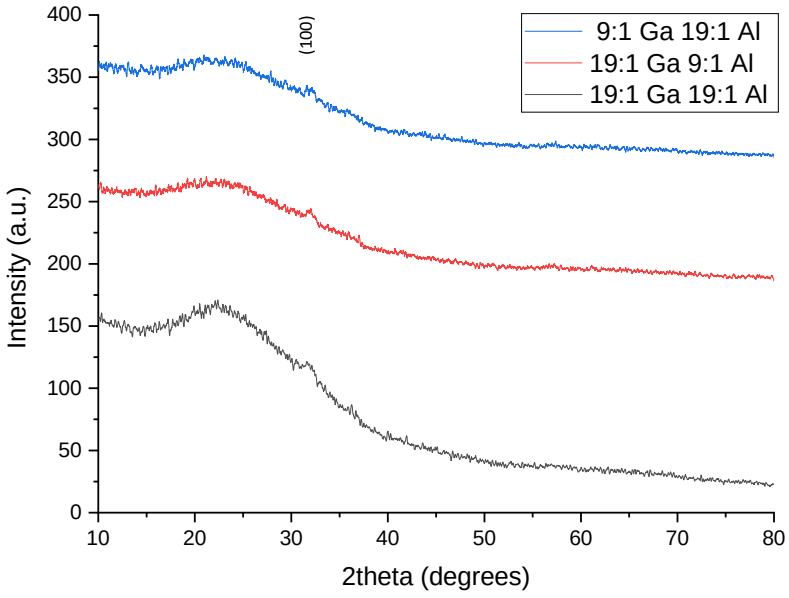

(b)

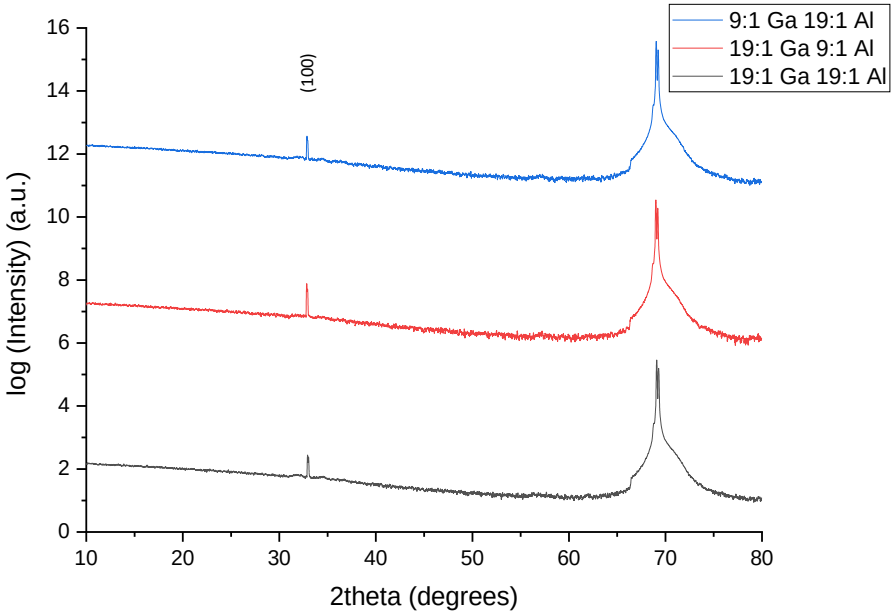

Figure 6.1: XRD patterns of ZnO: Ga_2O_3: Al_2O_3 materials deposited using various dopant ratios at 150 °C on (a) glass substrates and (b) Si (100) substrates

(a)

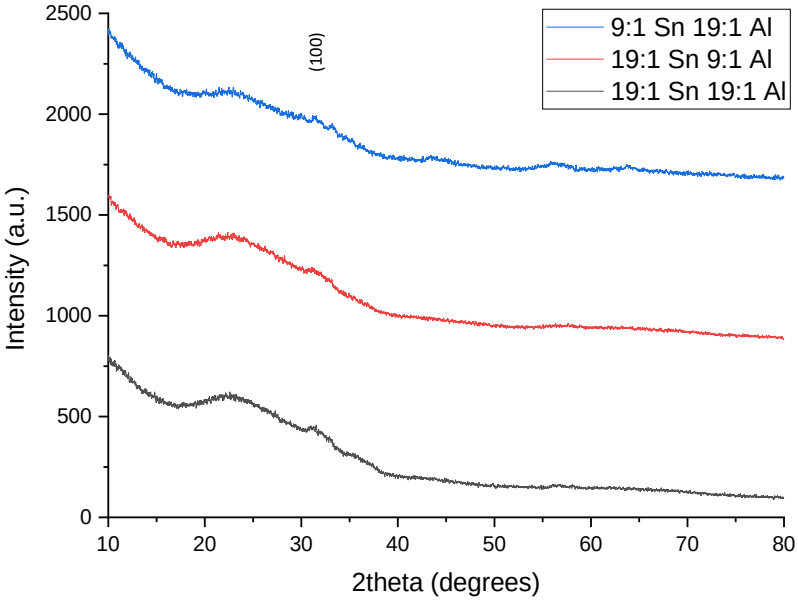

(b)

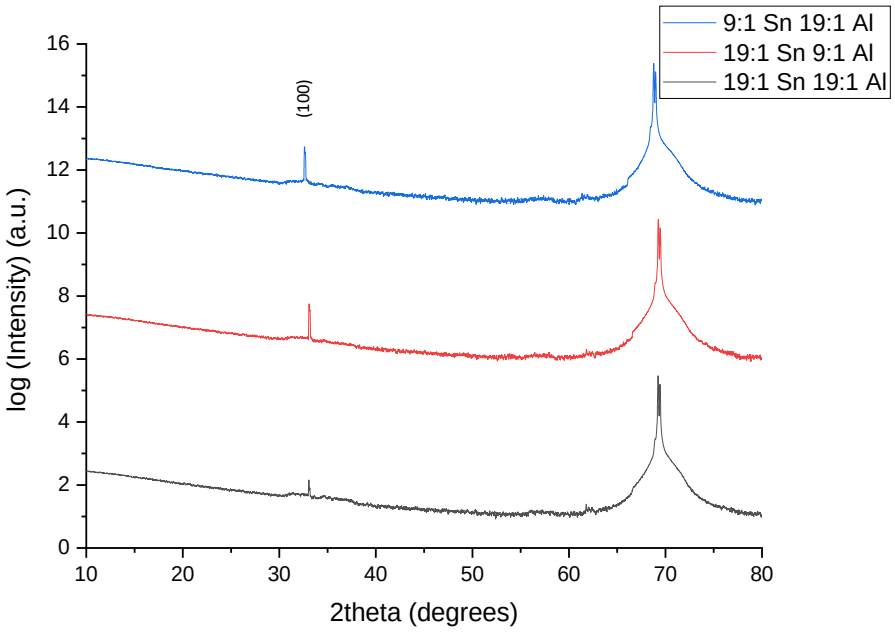

Figure 6.2: XRD patterns of ZnO: SnO_2: Al_2O_3 materials deposited using various dopant ratios at 150 °C on (a) glass substrates and (b) Si (100) substrates

(a)

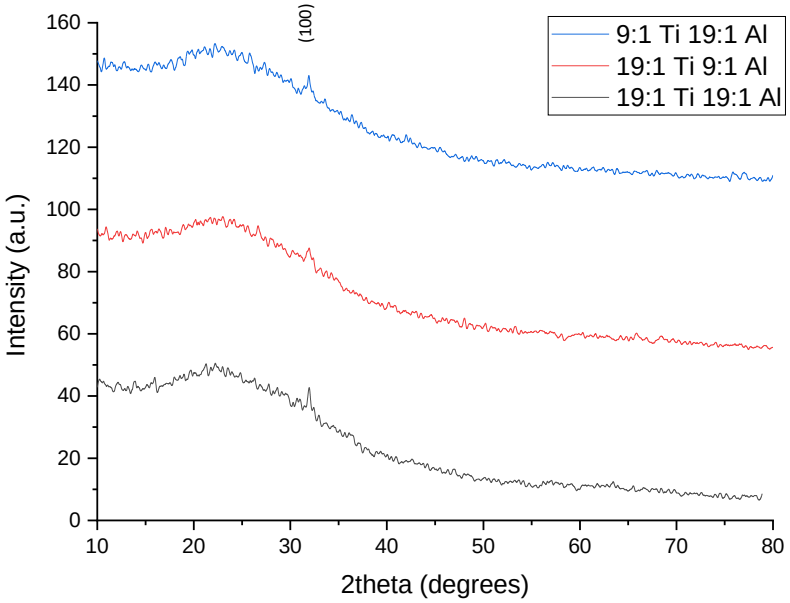

(b)

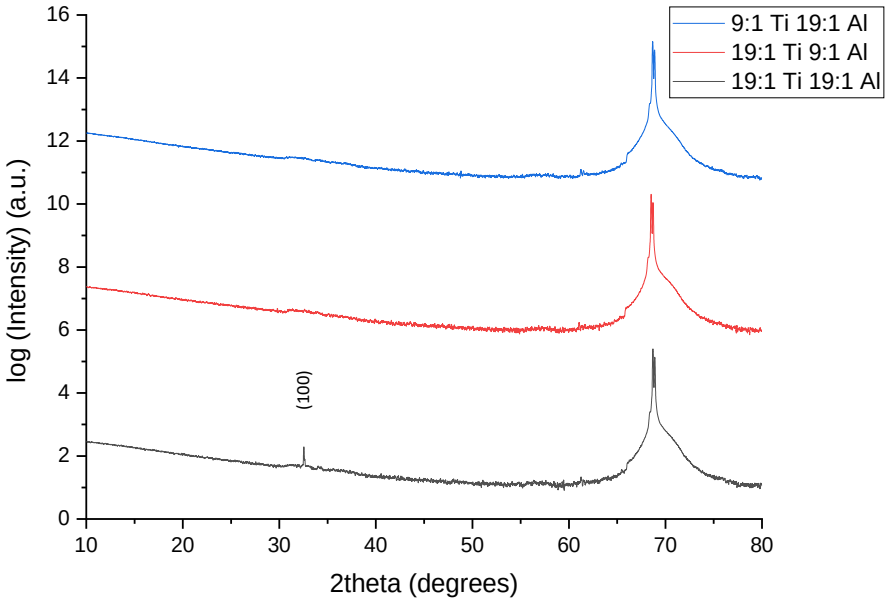

Figure 6.3: XRD patterns of ZnO: TiO_2: Al_2O_3 materials deposited using various dopant ratios at 150 °C on (a) glass substrates and (b) Si (100) substrates

6.3.2 Hall Effect Measurements

The Hall mobilities, carrier concentrations and sheet resistance values for the ZnO: Ga_2O_3: Al_2O_3, ZnO: SnO_2: Al_2O_3 and ZnO: TiO_2: Al_2O_3 ternary materials deposited by PE-ALD at 150 °C on glass substrates are given in table 6.2.

Film	**Dopant ratio**	**Hall mobility (cm^2/V.s)**	**Carrier concentration (cm^{-3})**	**Sheet resistance (Ω/□)**
ZnO:Ga_2O_3:Al_2O_3	9:1 Ga, 19:1 Al	0.17	1.36 x10^{19}	169.0 x10^3
	19:1 Ga, 9:1 Al	0.08	5.59 x10^{18}	709.0 x10^3
	19:1 Ga, 19:1 Al	0.11	4.18 x10^{18}	882.4 x10^3
ZnO:SnO_2:Al_2O_3	9:1 Sn, 19:1 Al	0.18	1.06 x10^{18}	1797.1 x10^3
	19:1 Sn, 9:1 Al	0.14	2.29 x 10^{17}	1115.2 x 10^3
	19:1 Sn, 19:1 Al	0.09	7.51 x 10^{16}	50343.2 x 10^3
ZnO:TiO_2:Al_2O_3	9:1 Ti, 19:1 Al	0.10	4.89 x10^{17}	6214.3 x10^3
	19:1 Ti, 9:1 Al	0.09	7.70 x10^{17}	4148.6 x10^3
	19:1 Ti, 19:1 Al	0.10	1.09 x10^{18}	2844.0 x10^3

Table 6.2: Electrical properties of ZnO: Ga_2O_3: Al_2O_3, ZnO: SnO_2: Al_2O_3 and ZnO: TiO_2: Al_2O_3 deposited by PE-ALD at 150 °C on glass substrates

For the ZnO: Ga_2O_3: Al_2O_3 materials, the best Hall mobility, 0.17 $cm^2/V.s$ was obtained for the 9:1 Ga, 19:1 Al material. This same material also had the highest carrier concentration and the lowest sheet resistance.

For the ZnO: SnO_2: Al_2O_3 materials, the highest Hall mobility of 0.18 $cm^2/V.s$ was achieved by the film with a ratio of 9:1 Sn, 19:1 Al. Again, this film also had the highest carrier concentration. The 19:1 Sn, 19:1 Al film had the highest sheet resistance being some 28 times that of the 9:1 Sn, 19:1 Al material and 45 times that of the 19:1 Sn, 9:1 Al material.

For the ZnO: TiO_2: Al_2O_3 materials, very little difference in terms of Hall mobility was seen between the different dopant ratios. The highest carrier concentration obtained was for the 19:1 Ti, 19:1 Al material while the lowest sheet resistance was obtained for the 9:1 Ti, 19:1 Al material, but as may be seen from table 6.2 above, the sheet resistance values for all films are of similar order of magnitude, being some kΩ/□.

Overall, for all films studied, there is really very little variation in the measured Hall mobilities. The ZnO: SnO_2: Al_2O_3 (9:1 Sn, 19:1 Al) material has the highest Hall mobility at 0.18 $cm^2/V.s$ while across all ratios studied it is the ZnO: Ga_2O_3: Al_2O_3 materials that have the highest carrier concentrations, the highest value being measured for the 9:1 Ga, 19:1 Al material at 1.36 $x10^{19}$ cm^{-3}. The ternary with the best (lowest) sheet resistance was found to be the ZnO: Ga_2O_3: Al_2O_3 material for the ratio 9:1 Ga, 19:1 Al, at 169.0 $x10^3$ Ω/□. Overall, the ZnO: Ga_2O_3: Al_2O_3, (9:1 Ga, 19:1 Al material is the best performing ternary in terms of both carrier concentration and sheet resistance while its Hall mobility at 0.17 $cm^2/V.s$ is very close to the highest value recorded across the series, at 0.18 $cm^2/V.s$

As noted earlier, the measured values for Hall mobility for all ternary samples are quite comparable. These values may be compared to the values recorded for the binary-doped materials reported in Chapter 5.

The Hall mobility values range between 0.06 and 0.43 $cm^2/V.s$ for the plasma-grown binaries and between 0.08 and 0.18 $cm^2/V.s$ for the ternaries. Interestingly although there are some variations, these are not particularly pronounced suggesting that there is no particular advantage in terms of depositing ternaries as compared to binaries in terms of mobility.

Comparing both the binaries and ternaries to the nominally undoped ZnO materials grown at the same temperature ((2.4×10^{16} cm^{-3}, Chapter 4) it may be seen that the carrier concentration values were generally higher for the binaries and ternaries than those obtained from the nominally undoped materials, as might be expected if the doping is indeed influencing the electrical properties as per design.

The carrier concentration values for the ternaries varied from 10^{16}-10^{20} cm^{-3}. The lowest sheet resistance for the ternaries was for the ZnO: Ga_2O_3: Al_2O_3 (9:1 Ga, 19:1 Al) material at 169 $\times 10^3$ Ω/□. The only plasma-grown binary that gave rise to a comparable value GZO (19:1) at 215 $\times 10^3$ Ω/□. Interestingly, the best performing films for both binaries and ternaries in terms of sheet resistance both contained Ga. The values obtained for these films were also lower than the sheet resistance measured for plasma-grown nominally-undoped ZnO at 150 °C (240×10^5 Ω/□.

6.4 Conclusions

ZnO: Ga_2O_3: Al_2O_3, ZnO: SnO_2: Al_2O_3 and ZnO: TiO_2: Al_2O_3 ternaries were deposited via PE-ALD at 150 °C. XRD analysis identified that growth was substrate dependent with Si (100) substrate films displaying crystallinity and glass substrate films being significantly less crystalline. A shift in the (100) XRD peak towards a higher angle was observed when comparing the ternary films to as-grown PE-ALD ZnO implying that lattice constants decrease. This was due to the incorporation of the dopants into the ZnO matrix.

The best performing ternary in terms of both carrier concentration and sheet resistance was found to be the ZnO: Ga_2O_3: Al_2O_3 (9:1 Ga, 19:1 Al) material. At 0.17 cm^2/V.s, this sample also displayed a Hall mobility which was comparable to the highest value recorded across the series 0.18 cm^2/V.s.

Overall, the best performing films in terms of mobility, sheet resistance and carrier concentration were those films containing Ga, which suggests that of the additional ions included, Ga^{3+} ions perform better than Sn^{4+} ions or Ti^{4+} ions as dopants. We may speculate as to why this should be the case when in theory Ga^{3+} ions can contribute one extra electron to the conduction band of the ZnO while both Sn^{4+} or Ti^{4+} ions can contribute two electrons. In terms of the size of the ions, in increasing order, the ionic radii are as follows 0.53, 0.62, 0.68, 0.69 and 0.74 Å for Al^{3+}, Ga^{3+}, Ti^{4+}, Sn^{4+} and Zn^{2+} respectively[13]. Both Ti^{4+}, Sn^{4+} are very comparable in size with Ga^{3+} being smaller. From the XRD results, it can be seen that the ternary containing Ti^{4+} is the least crystalline while ternaries containing Ga^{3+} and Sn^{4+} show similar degrees of crystallinity.

References

1. Mackus, A. J. M., Schneider, J. R., MacIsaac, C., Baker, J. G. and Bent, S. F. Synthesis of Doped, Ternary, and Quaternary Materials by Atomic Layer Deposition: A Review. *Chem. Mater.* **2019**, *31*, 1142−1183.

2. O'Neill, B. J., Jackson, D. H. K., Lee, J., Canlas, C., Stair, P. C., Marshall, C. L., Elam, J. W., Kuech, T. F., Dumesic, J. A. and Huber, G. W. Catalyst Design with Atomic Layer Deposition. *ACS Catal.* **2015**, *5* (3), 1804–1825.

3. Singh, J. A., Yang, N. and Bent, S. F. Nanoengineering Heterogeneous Catalysts by Atomic Layer Deposition. *Annu. Rev. Chem. Biomol. Eng.* **2017**, *8* (1), 41–62.

4. Meng, X., Yang, X.-Q. and Sun, X. Emerging Applications of Atomic Layer Deposition for Lithium Ion Battery Studies. *Adv. Mater.* **2012**, *24*, 3589–3615.

5. Peng, Q., Lewis, J. S., Hoertz, P. G., Glass, J. T. and Parsons, G. N. Atomic Layer Deposition for Electrochemical Energy Generation and Storage Systems. *J. Vac. Sci. Technol. A* **2012**, *30* (1), 010803-010801–010814.

6. Bakke, J. R., Pickrahn, K. L., Brennan, T. P. and Bent, S. F. Nanoengineering and Interfacial Engineering of Photovoltaics by Atomic Layer Deposition *Nanoscale* **2011**, *3*, 3482–3508.

7. van Delft, J. A., Garcia-Alonso, D. and Kessels, W. M. M. Atomic Layer Deposition for Photovoltaics: Applications and Prospects for Solar Cell Manufacturing. *Semicond. Sci. Technol.* **2012**, *27* (7), 074002.

8. Palmstrom, A. F., Santra, P. K. and Bent, S. F. Atomic Layer Deposition in Nanostructured Photovoltaics: Tuning Optical, Electronic and Surface Properties *Nanoscale* **2015**, *7* (29), 12266– 12283.

9. Coll, M. and Napari, M. Atomic layer deposition of functional multicomponent oxides. *APL Materials* **2019**, *7*, 110901.

10. Mohseni; H. and Scharf, T. W. Atomic layer deposition of $ZnO/Al_2O_3/ZrO_2$ nanolaminates for improved thermal and wear resistance in carbon-carbon composites. *J. Vac. Sci. Technol. A* **2012**, *30* (1), 01A149.

11. Luka; G., G., M., Guziewicz, E., Stakhira, P., Cherpak, V. and Volynyuk, D. ZnO Films Grown by Atomic Layer Deposition for Organic Electronics. *Semicond. Sci. Technol.* **2012**, *27* (7), 07400.

12. Ageh, V., Choudhuri, D. and Scharf, T. W. Reciprocating Sliding Wear Behavior and Mechanisms of Quaternary Metal Oxide Coatings. *Wear* **2015**, *330−331*, 390−399.

13. Shannon, R.D. Revised effective ionic radii and systematic studies of interatomic distances in halides and chalcogenides. Acta Crystallographica Section A **1976**, *32* (5), 751-767.

Chapter 7: Conclusion and Suggestions for Future Work

The initial work presented in this thesis studied the growth of TiO_2/ZnO nanolaminates. The concept of combinatorial ALD or C-ALD was introduced in order to facilitate the deposition of layered ZnO and TiO_2 nanolaminates on both Si (100) wafers and glass substrates. Films grown included; ZnO (40 nm), TiO_2 (40 nm), ZnO layer (40 nm) followed by TiO_2 layer (40 nm) and *vice versa*, a multilayered laminate (4 nm ZnO + 4 nm TiO_2) x5 and a deliberately mixed ZnO/TiO_2 1:1 film grown by alternating very short (0.05 s) pulses of each precursor until the desired thickness of 40 nm was reached.

A nucleation delay was observed for ZnO deposited directly on the substrate and on the subsequent TiO_2 layer, albeit the latter to a lesser extent. The reason for the difference in nucleation delay may be explained by the dissimilar surface groups, SiO_2 with surface hydroxyl groups for Si (100) substrate and hydroxyl groups bonded to Ti in the case of the TiO_2 layer. ZnO appeared to possess a templating influence on the TiO_2 layer grown subsequently on both substrate types. XRD analysis revealed a strong preference for the (002) orientation which indicated the polycrystalline manner of the ZnO film. XRD results also suggested that layer growth was substrate-dependent as shown by crystalline TiO_2 only being present on glass substrates. The nanolaminate structures showed stability such that the layer structure remained intact after undergoing annealing at 400 °C for 1 hour. In contrast, the mixed ZnO: TiO_2 (1:1) film showed evidence of ZnO segregation and crystallisation. In regards to photocatalytic activity, no evidence was found for any enhancement of photoactivity in the mixed or

nanolaminate films. After 1 hour UV exposure, the TiO_2 yielded a CA value of <5°, suggesting superhydrophilicity. The most photoactive films were found to be those consisting of ZnO deposited onto glass substrates.

Next, a comparative study of the deposition of ZnO onto Si (100) wafers and glass substrates by both thermal and remote plasma atomic layer deposition (ALD) was investigated. In order to minimise the influence of reactor design on the nature of the deposited materials, the same reactor, in this case a Picosun™ R200 ALD reactor, was used for both sets of experiments.

The GPC values for both ALD processes were investigated and the thermal process was found to have a higher GPC than that of the plasma process with the exception of growth at a substrate temperature of 100 °C. The maximum GPC for the thermal process was found to be 2.1 Å/cycle at a substrate temperature of 150 °C deposited on glass substrate whereas on the Si (100) substrate the GPC under the same conditions was found to be 1.76 Å/cycle. In contrast, the maximum GPC observed for the plasma process was 1.4 Å/cycle at 200 °C which was achieved on the Si (100) substrate. The differences between the thermal and plasma-assisted processes prompted a discussion of the mechanisms of nucleation and growth for both processes that concluded that overall, involved in both processes are essentially thermally activated to some extent. For the PE-ALD process, although the activation energy for the reaction is largely delivered by the plasma rather than from the substrate, the overall process is not solely determined by gas-phase activation since the substrate temperature still influenced the GPC to a degree. This is consistent with the self-limiting nature of an ALD process. When comparing the GPC values for both the thermal and plasma films grown at 100 °C, a higher GPC for the plasma film was obtained. The low GPC value for the thermal process can be explained by the lower reactivity of the DEZn precursor at lower temperatures. Further to this, at 150 °C and

200 °C, GPC values for the plasma grown films on Si (100) substrates are lower than those for the thermally grown films.

In terms of morphology, differences were observed between the thermal and plasma grown films. The thermal ALD films showed cylindrical, tear drop-like surface features whereas the PE-ALD films showed more spherical surface features on both Si (100) and glass substrates. As the substrate temperature increased, features became more defined for both thermal and PE-ALD. In terms of crystallinity, the XRD spectrum for PE-ALD films was dominated by the presence of the (002) reflection, showing a preference for c-axis orientation. In contrast, the thermal ALD process displayed no particular preference between the (100) and (002) directions for films deposited at 100 °C on both Si (100) and glass substrates. The (100) direction became more prevalent as the substrate temperature increased to 150 and 200 °C.

Optically, all films possessed an average transmittance over the entirety of the visible wavelength range 400 to 750 nm of >60% with a sharp cut off in the UV region due to the band gap of the material.

The electrical properties of the films was investigated via Hall Effect measurements. Hall mobilities were found to increase with increasing substrate temperature, while the sheet resistance decreased accordingly. Interestingly in terms of carrier concentrations, an increase was observed for thermal ALD process films with increasing substrate temperature while for the PE-ALD grown samples the reverse trend was observed. Similarly for these latter samples the sheet resistance values are very high for all samples prepared, meaning that the PE-ALD samples produced were essentially resistive. In contrast, the samples grown by thermal ALD

have much lower sheet resistance values by several orders of magnitude, as might be expected due to the higher carrier concentrations and mobilities.

Next, ZnO was intentionally doped with Al, Ga, Sn and Ti with the aim of improving the electrical properties of the thin films**.** Dopant ratios of 9:1 and 19:1 were employed. Electrically, the 19:1 films outperformed their 9:1 counterparts with the exception of PE-ALD TZO.

For thermally deposited AZO, SZO and TZO on both glass and Si (100) substrates, SEM imaging revealed columnar grains on the surface of the films. As-grown thermal ALD ZnO also showed similar surface features. No columnar grains were present on the surface of thermal GZO in which more random smaller surface particles were observed. AZO, GZO, SZO and TZO deposited by PE-ALD on glass all display similar surface features to those observed on as-grown PE-ALD ZnO, small densely packed surface features**.** Comparing these results to the PE-ALD films deposited on Si (100) substrate, AZO shows similar surface features but GZO, SZO and TZO differ displaying columnar surface features.

Neither the thermal nor plasma doped films could compete in terms of the Hall mobilities measured when compared to as-grown ZnO. On the contrary, as might be expected, both the thermal and plasma doped films had higher carrier concentration values than those obtained for the as-grown ZnO**.** The blue-shift observed via UV-Visible Spectroscopy can indicate an increase in the carrier concentration (Burstein-Moss theory)[24]. A similar improvement was observed for sheet resistance values as the doped films had lower values than that of as-grown ZnO. These results suggest that the incorporation of dopants improved the electrical properties of ZnO however with no direct correlation between Hall mobility and sheet resistance.

From TEM imaging it was observed that the expected growth rates deviated from the actual growth rates. This may be explained by dopant atoms inhibiting nucleation of ZnO due to the dopant blocking sites and hindering DEZn absorption[12, 13]. This highlights the idea that there are differences in the nucleation of ZnO on different dopant atoms and *vice versa*. This may also be used to explain the varying degrees of crystallinity observed across all doped ZnO films.

Next, the growth of the ternary oxides ZnO: Ga_2O_3: Al_2O_3, ZnO: SnO_2: Al_2O_3 and ZnO: TiO_2: Al_2O_3 by PE-ALD was studied. By nature ternary films are more complex and it was demonstrated that by fabricating these materials by ALD allows for precise control over film design.

The incorporation of dopant atoms was confirmed by the observation of a shift in the (100) XRD peak towards higher angles. Growth of ternaries proved to be substrate dependent as Si (100) substrate films displayed crystallinity while glass substrate films were weakly crystalline.

For all ternaries, the best ratio in terms of electrical measurements was found to be 9:1 Ga/Sn/Ti, 19:1 Al. At this ratio, the best Hall mobility was for the ZnO: SnO_2: Al_2O_3 at 0.18 $cm^2/V.s$, the best carrier concentration was by ZnO: Ga_2O_3: Al_2O_3 at 1.36 $x10^{19}$ cm^{-3} and the lowest sheet resistance was by ZnO: Ga_2O_3: Al_2O_3 at 169.0 $x10^3$ Ω/□.

The ZnO: Ga_2O_3: Al_2O_3 (9:1 Ga, 19:1 Al) ternary was the best performing overall across carrier concentration and sheet resistance. The Hall mobility was comparable to that of the best performing ternary; ZnO: SnO_2: Al_2O_3 (0.18 $cm^2/V.s.$) at 0.17 $cm^2/V.s.$

Comparing the binaries and ternaries to as-grown ZnO, for both the thermal and plasma process, the carrier concentration values were higher than that obtained for plasma as-grown ZnO also deposited at 150 °C (2.4 $x10^{16}$ cm^{-3}).

The plasma-grown doped ZnO film with the lowest sheet resistance was GZO (19:1) at 215 $x10^{3}$ Ω/□. This value is comparable to that obtained for the ZnO: Ga_2O_3: Al_2O_3 ternary (9:1 Ga, 19:1 Al) which was found to have a sheet resistance of 169 $x10^{3}$ Ω/□. As previously mentioned, the best performing films in terms of sheet resistance both included Ga atoms. These sheet resistance values above were lower than the sheet resistance obtained for plasma-grown ZnO at 150 °C which was 240 $x10^{5}$ Ω/□.

In order to build upon the work presented in this thesis the following studies may be considered for future work:

- A wider range of dopant ratios should be investigated in order to assess the potential benefits on electrical and optical properties and also to determine the optimal doping ratio for different dopants in ZnO matrix thin films.

- Other precursors could be explored in order to improve the electrical and optical properties of the films.

- Depositing the doped films at different temperatures would be beneficial to have a wider range of data. A higher temperature such as 200 °C may have a positive effect on film properties.

- It would be beneficial to dope ZnO at various dopant concentrations. XPS analysis could be employed in order to investigate if all dopant atoms were incorporated as dopants that substituted in place of Zn atoms e.g. Al_{Zn}^{+} in the case of AZO. Al-doping should not lead to any additional oxygen atoms. If an increase in oxygen content is detected by XPS, it would suggest the formation of an Al_2O_3 phase which would negatively impact the electrical properties of the film as Al is not acting as an electron donor.

- Further analysis is required on the ternary films in order to fully make an interpretation of the results. SEM would prove beneficial to see the surface morphology of the films. TEM would be extremely beneficial to see the cross-section of the films. From this, the confirmation of laminate structure may be possible. It may also be possible to see how the dopants have been incorporated. XPS would allow for the true atomic percentages of the ternary films to be measured.

Appendix I

Publications

- **Shóna Doyle**, Louise Ryan, Melissa M. McCarthy, Mircea Modreanu, Michael Schmidt, Fathima Laffir, Ian M. Povey and Martyn E. Pemble
  "Combinatorial ALD for the growth of ZnO/TiO_2 nanolaminates and mixed ZnO/TiO_2 nanostructured films."
  Mater. Adv., 2022, 3, 2896-2907

Conference Presentations

- Joint EuroCVD 21 – Baltic ALD 15 Conference

  Linköping, Sweden

  Oral Presentation: "New Materials via Combinatorial Atomic Layer Deposition"

- 7th International Symposium on Transparent Conductive Materials, IS-TCM 2018

  Chania, Crete, Greece

  Poster: "Atomic layer deposition applied in a combinatorial approach for the growth of ZnO and TiO_2 nanolaminates possessing tuneable photoactivity"

- ALD/ALE 2019 – The 19th International Conference on Atomic Layer Deposition

  Bellevue, Seattle, Washington, USA

  Poster: "Atomic layer deposition of ZnO thin films for BEOL Applications"

Appendix II

The recipes for the preparations of TiO_2/ZnO composites are given in tables I-V below.

Step	Instruction	Valve number	Value (unit)
0	flow	0	40 sccm
1	flow	1	180 sccm
2	wait		1 s
3	wait		20 s
4	wait		1 s
5	pulse	3	0.2 s
6	wait		10 s
7	pulse	5	0.1 s
8	wait		10 s
9	go to	5	200
10	wait		10 s
11	flow	0	0 sccm
12	flow	1	0 sccm

Table I: Recipe for the deposition of thermal ALD ZnO (40 nm) by Cambridge Nanotech Fiji 200

Referring to table I, in steps 0 and 1 precursor carrier flow rate and plasma source purge flow rate are set and measured in standard cubic centimetres per minute (sccm) at atmospheric pressure and temperature. In steps 2, 3 and 4, 1 s and 20 s wait times occur to allow for

stabilisation of flow rates. Step 5 involves a DEZn precursor pulse for 0.2 s. Step 6 is a wait time of 10 s to allow for purge of DEZn and any reaction by-products. Step 7 is a water pulse for 0.1 s. Step 8 is a wait time of 10 s to allow for purge of water and reaction by-products. In step 9, "go to" returns the recipe to step 5 and the reaction repeats itself for 200 cycles. Step 10 is a wait time of 10 s. In steps 11 and 12, the precursor flow rate and plasma source flow rate are set to the stand-by rate of 0 sccm.

Step	**Instruction**	**Valve number**	**Value (unit)**
0	flow	0	40 sccm
1	flow	1	180 sccm
2	wait		1 s
3	wait		20 s
4	wait		1 s
5	pulse	0	0.4 s
6	wait		10 s
7	pulse	5	0.1 s
8	wait		10 s
9	go to	5	670
10	wait		10 s
11	flow	0	0 sccm
12	flow	1	0 sccm

Table II: Recipe for the deposition of thermal ALD TiO_2 (40 nm) by Cambridge Nanotech Fiji 200

Referring to table II, in steps 0 and 1 the precursor carrier flow rate and plasma source purge flow rate are set and measured in standard cubic centimetres per minute (sccm) at atmospheric pressure and temperature. In steps 2, 3 and 4, 1 s and 20 s wait times occur to allow for stabilisation of flow rates. Step 5 involves a TDMAT precursor pulse for 0.4 s. Step 6 is a wait time of 10 s to allow for purge of TDMAT and any reaction by-products. Step 7 is a water pulse for 0.1 s. Step 8 is a wait time of 10 s to allow for purge of water and reaction by-products. In step 9, “go to” returns the recipe to step 5 and the reaction repeats itself for 670 cycles. Step 10 is a wait time of 10 s. In steps 11 and 12, the precursor flow rate and plasma source flow rate are set to the stand-by rate of 0 sccm.

Step	Instruction	Valve number	Value (unit)
0	flow	0	40 sccm
1	flow	1	180 sccm
2	wait		1 s
3	wait		20 s
4	wait		1 s
5	pulse	3	0.2 s
6	wait		10 s
7	pulse	5	0.1 s
8	wait		10 s
9	go to	5	200
10	wait		10 s
11	pulse	0	0.4 s
12	wait		10 s
13	pulse	5	0.1 s
14	wait		10 s
15	go to	11	670
16	wait		1 s
17	wait		10 s
18	flow	0	0 sccm
19	flow	1	0 sccm

Table III: Recipe for the deposition of thermal ALD ZnO (40 nm) on TiO_2 (40 nm) by Cambridge Nanotech Fiji 200

Referring to table III, in steps 0 and 1, the precursor carrier flow rate and plasma source purge flow rate are set and measured in standard cubic centimetres per minute (sccm) at atmospheric pressure and temperature. In steps 2, 3 and 4, 1 s and 20 s wait times occur to allow for stabilisation of flow rates. Step 5 involves a DEZn precursor pulse for 0.2 s. Step 6 is a wait time of 10 s to allow for purge of DEZn and any reaction by-products. Step 7 is a water pulse for 0.1 s. Step 8 is a wait time of 10 s to allow for purge of water and reaction by-products. In step 9, “go to” returns the recipe to step 5 and the reaction repeats itself for 200 cycles. Step 10 is a wait time of 10 s. Step 11 involves a TDMAT precursor pulse for 0.4 s. Step 12 is a wait time of 10 s to allow for purge of TDMAT and any reaction by-products. Step 13 is a water pulse for 0.1 s. Step 14 is a wait time of 10 s to allow for purge of water and reaction by-products. In step 15, “go to” returns the recipe to step 11 and the reaction repeats itself for 670 cycles. Steps 16 and 17 are wait times of 1 and 10 s. In steps 18 and 19, the precursor flow rate and plasma source flow rate are set to the stand-by rate of 0 sccm.

Step	Instruction	Valve number	Value (unit)
0	flow	0	40 sccm
1	flow	1	180 sccm
2	wait		1 s
3	wait		20 s
4	wait		1 s
5	pulse	0	0.4 s
6	wait		10 s
7	pulse	5	0.1 s
8	wait		10 s
9	go to	5	670
10	wait		10 s
11	pulse	3	0.2 s
12	wait		10 s
13	pulse	5	0.1 s
14	wait		10 s
15	go to	11	200
16	wait		1 s
17	wait		10 s
18	flow	0	0 sccm
19	flow	1	0 sccm

Table IV: Recipe for the deposition of thermal ALD TiO_2 (40 nm) on ZnO (40 nm) by Cambridge Nanotech Fiji 200

Referring to table IV, in steps 0 and 1 the precursor carrier flow rate and plasma source purge flow rate are set and measured in standard cubic centimetres per minute (sccm) at atmospheric pressure and temperature. In steps 2, 3 and 4, 1 s and 20 s wait times occur to allow for stabilisation of flow rates. Step 5 involves a TDMAT precursor pulse for 0.4 s. Step 6 is a wait time of 10 s to allow for purge of TDMAT and any reaction by-products. Step 7 is a water pulse for 0.1 s. Step 8 is a wait time of 10 s to allow for purge of water and reaction by-products. In step 9, “go to” returns the recipe to step 5 and the reaction repeats itself for 670 cycles. Step 10 is a wait time of 10 s. Step 11 involves a DEZn precursor pulse for 0.2 s. Step 12 is a wait time of 10 s to allow for purge of DEZn and any reaction by-products. Step 13 is a water pulse for 0.1 s. Step 14 is a wait time of 10 s to allow for purge of water and reaction by-products. In step 15, “go to” returns the recipe to step 11 and the reaction repeats itself for 200 cycles. Steps 16 and 17 are wait times of 1 and 10 s. In steps 18 and 19, the precursor flow rate and plasma source flow rate are set to the stand-by rate of 0 sccm.

Step	Instruction	Valve number	Value (unit)
0	flow	0	40 sccm
1	flow	1	180 sccm
2	wait		1 s
3	wait		20 s
4	wait		1 s
5	pulse	2	0.2 s
6	wait		10 s
7	pulse	5	0.06 s
8	wait		10 s
9	go to	5	20
10	wait		10 s
11	pulse	0	0.4 s
12	wait		10 s
13	pulse	5	0.06 s
14	wait		10 s
15	go to	11	80
16	go to	5	5
17	wait		1 s
18	wait		10 s
19	flow	0	0 sccm
20	flow	1	0 sccm

Table V: Recipe for the deposition of thermal ALD ZnO and TiO_2 multilayers laminate

(4 nm ZnO + 4 nm TiO_2) x5 by Cambridge Nanotech Fiji 200

Referring to table V, in steps 0 and 1, the precursor carrier flow rate and plasma source purge flow rate are set and measured in standard cubic centimetres per minute (sccm) at atmospheric pressure and temperature. In steps 2, 3 and 4, 1 s and 20 s wait times occur to allow for stabilisation of flow rates. Step 5 involves a DEZn precursor pulse for 0.2 s. Step 6 is a wait time of 10 s to allow for purge of DEZn and any reaction by-products. Step 7 is a water pulse for 0.06 s. Step 8 is a wait time of 10 s to allow for purge of water and reaction by-products. In step 9, “go to” returns the recipe to step 5 and the reaction repeats itself for 20 cycles. Step 10 is a wait time of 10 s. Step 11 involves a TDMAT precursor pulse for 0.4 s. Step 12 is a wait time of 10 s to allow for purge of TDMAT and any reaction by-products. Step 13 is a water pulse for 0.06 s. Step 14 is a wait time of 10 s to allow for purge of water and reaction by-products. In step 15, “go to” returns the recipe to step 11 and the reaction repeats itself for 80 cycles. In step 16, “go to” returns the recipe to step 5 and the reaction repeats itself for 5 cycles. Steps 17 and 18 are wait times of 1 and 10 s. In steps 19 and 20, the precursor flow rate and plasma source flow rate are set to the stand-by rate of 0 sccm.

(a)

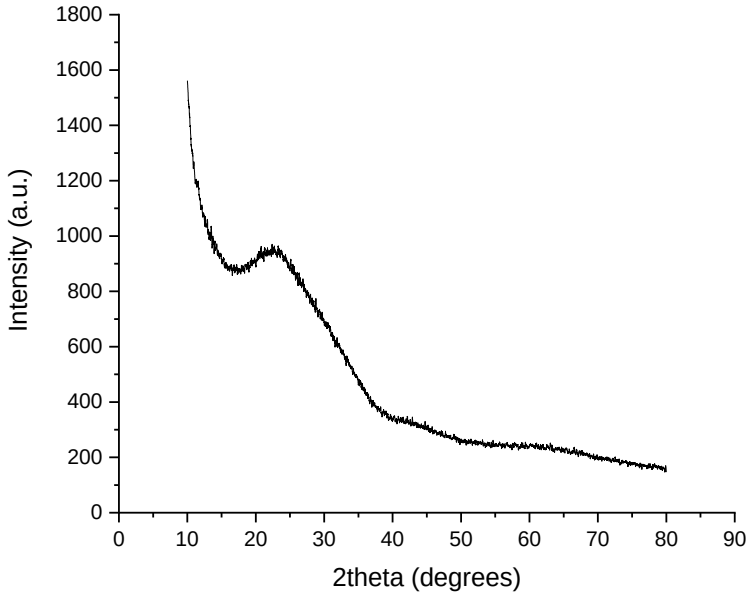

(b)

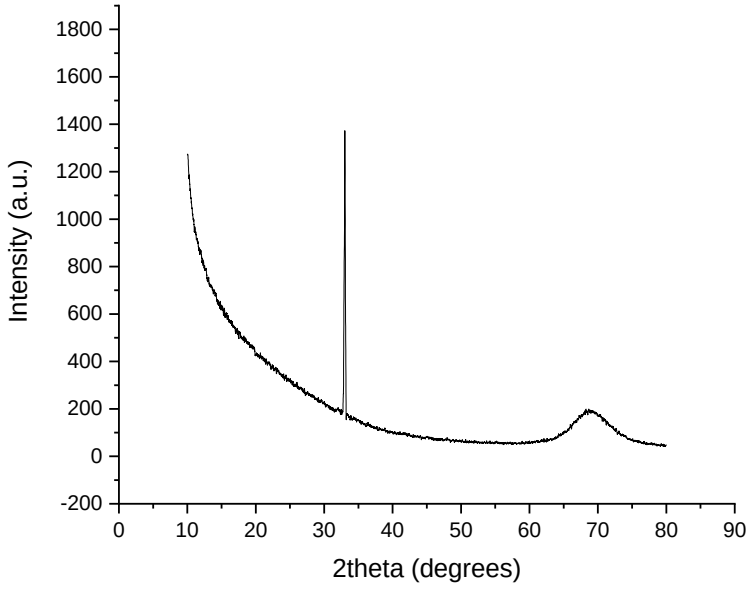

Figure I: XRD patterns (a) glass substrate and (b) Si (100) substrate

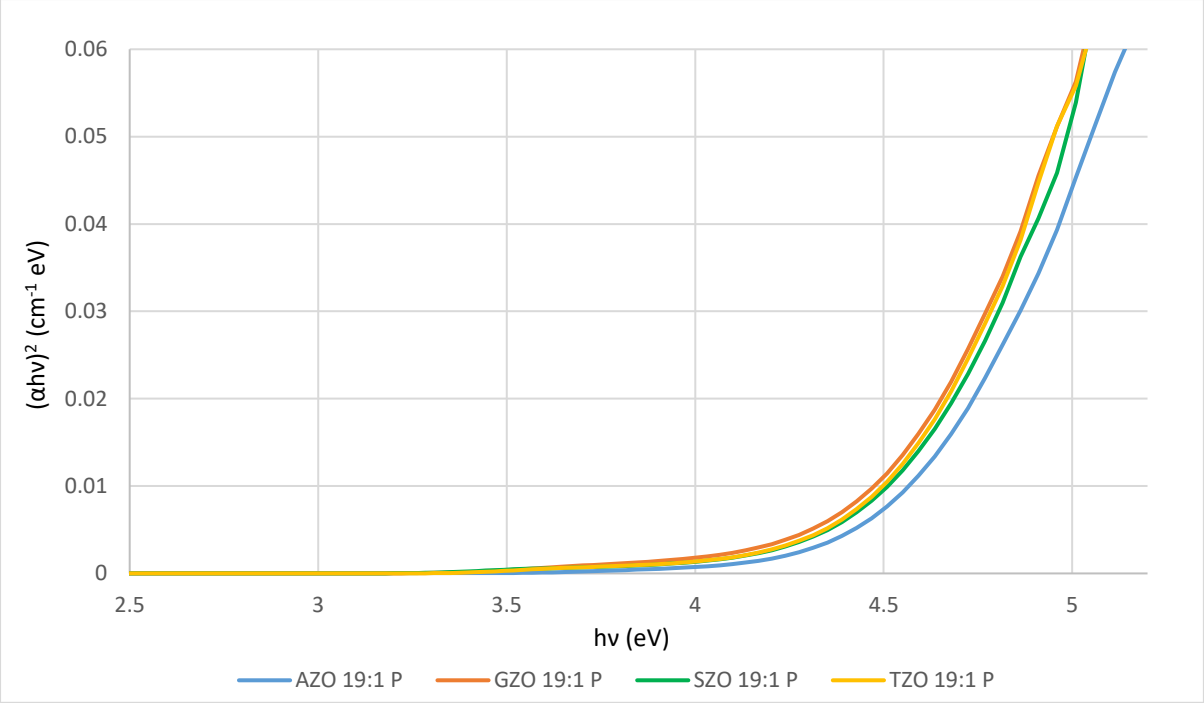

Figure II: Tauc plot for PE-ALD 19:1 AZO, GZO, SZO and TZO on glass substrates

(a)

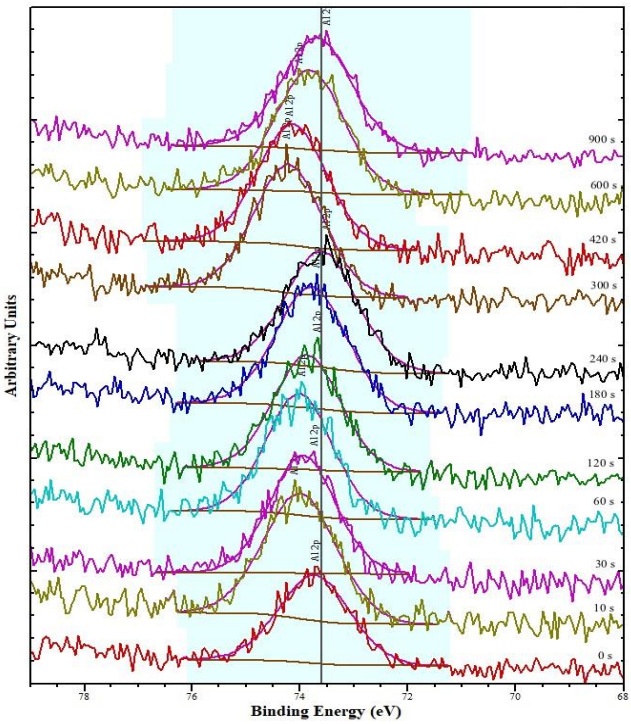

(b)

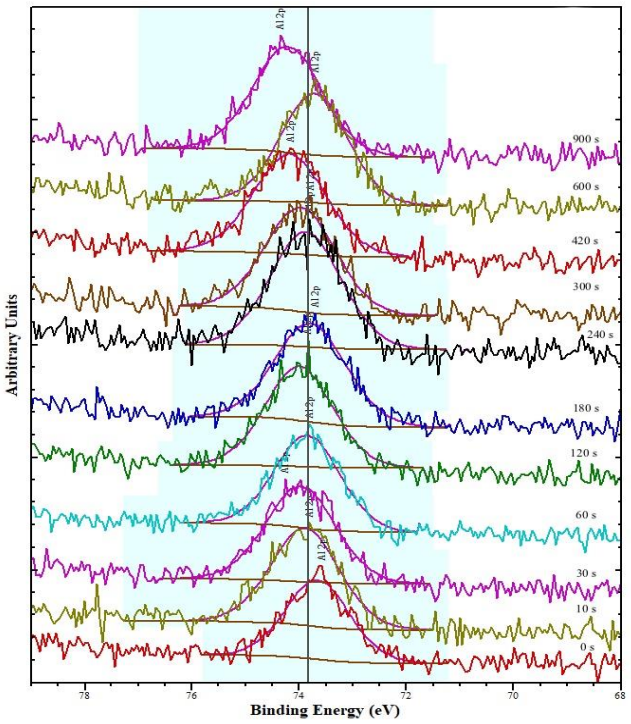

Figure III: XPS spectra of the Al 2p region for (a), thermal and (b), PE-ALD AZO at a depth of 0-36 nm

(a)

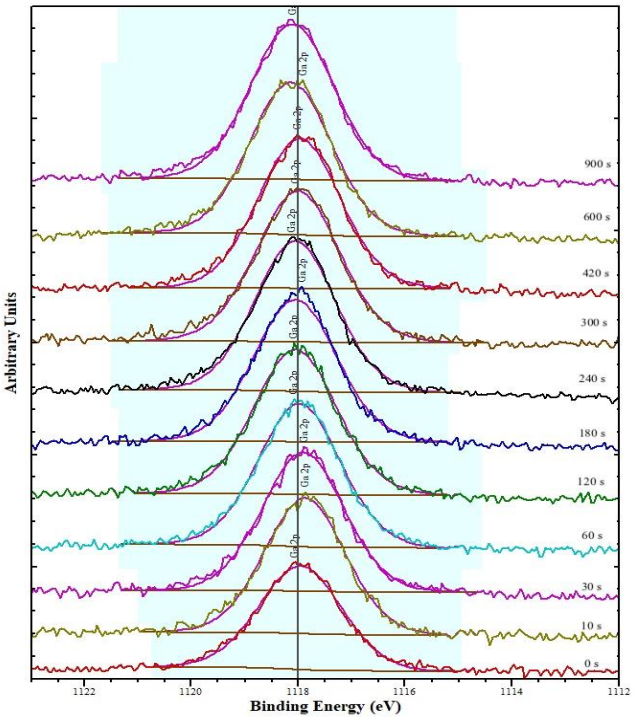

(b)

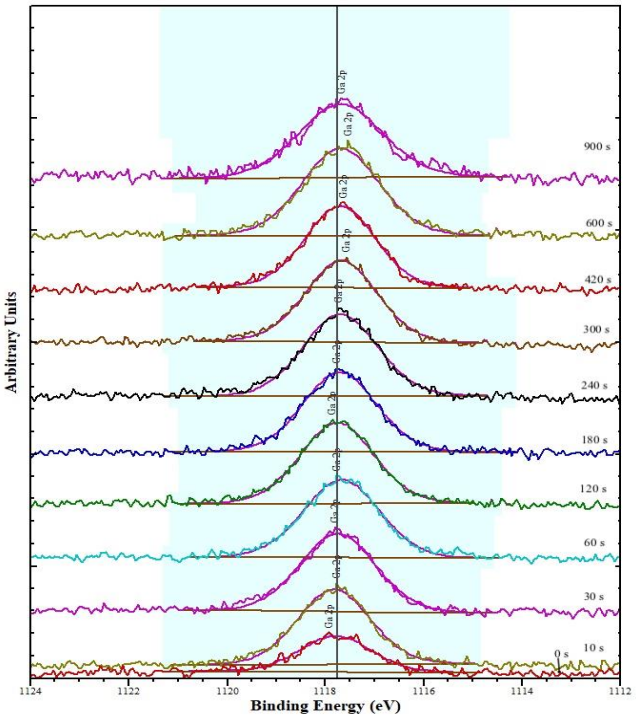

Figure IV: XPS spectra of Ga 2p region for (a), thermal and (b), PE-ALD GZO at a depth of 0-36 nm on Si (100) substrate

(a)

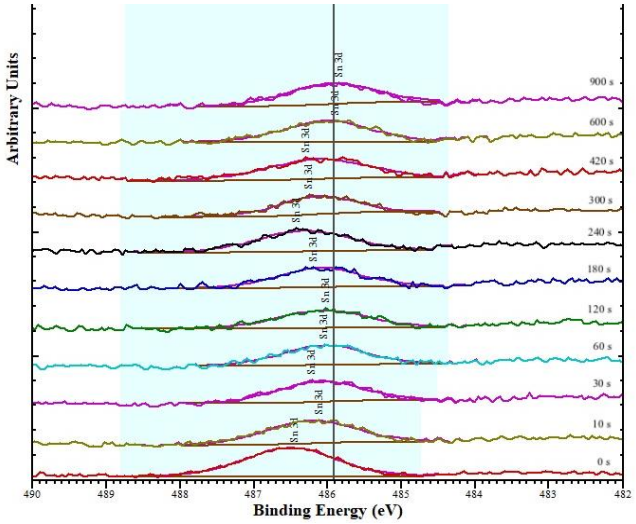

(b)

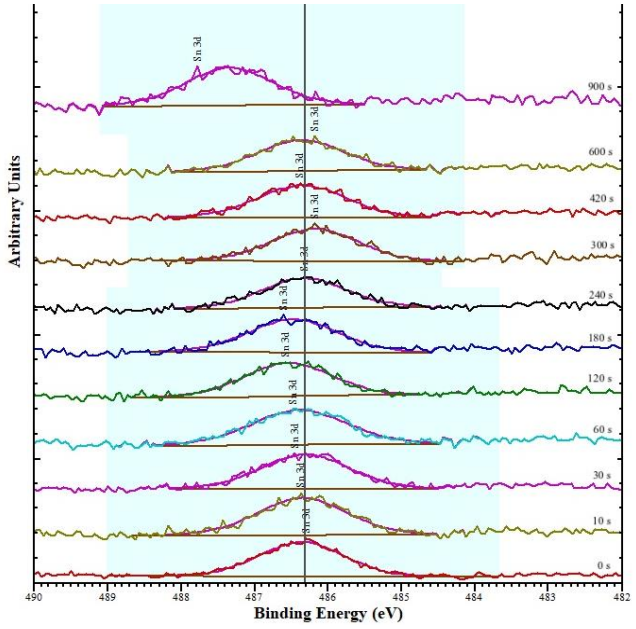

Figure V: XPS spectra of the Sn 3d region for (a), thermal and (b), PE-ALD SZO at a depth of 0-36 nm on Si (100) substrate

(a)

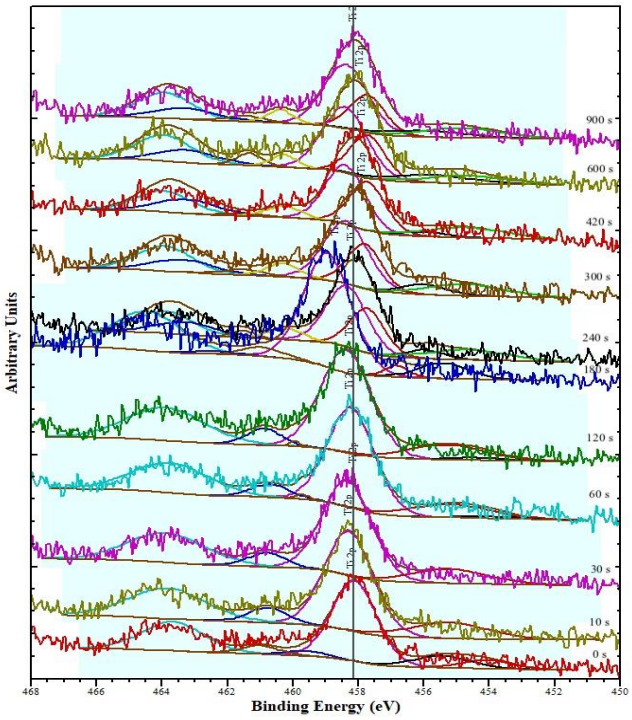

(b)

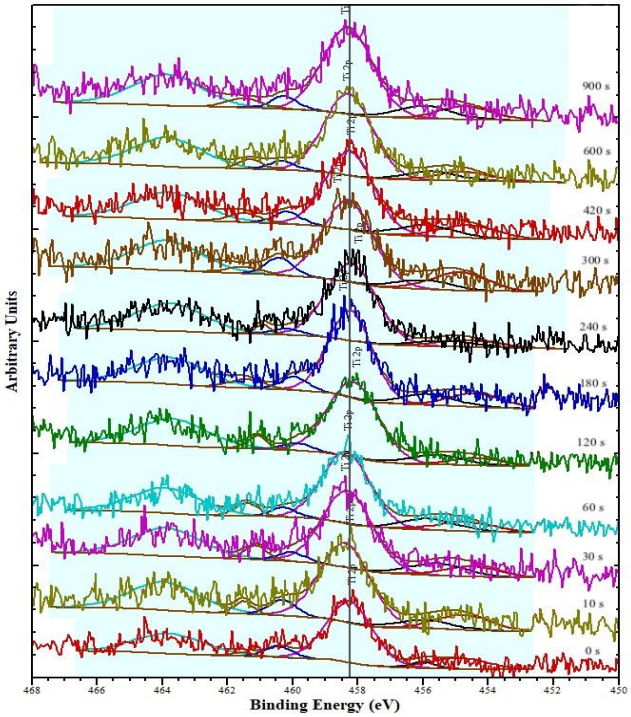

Figure VI: XPS spectra of Ti 2p region for (a), thermal and (b), PE-ALD TZO at a depth of 0-36 nm